THE UNIVERSITY OF ALBERTA

ANALYSIS AND DESIGN OF EXCAVATIONS IN CLAY

by

Lal Samarasekera ©

A THESIS
SUBMITTED TO THE FACULTY OF GRADUATE STUDIES AND RESEARCH
IN PARTIAL FULFILMENT OF THE REQUIREMENTS FOR THE DEGREE
OF DOCTOR OF PHILOSOPHY

Department of Civil Engineering

EDMONTON, ALBERTA
Fall of 1989

THE UNIVERSITY OF ALBERTA

RELEASE FORM

NAME OF AUTHOR Lal Samarasekera

TITLE OF THESIS ANALYSIS AND DESIGN OF EXCAVATIONS IN CLAY

DEGREE FOR WHICH THESIS WAS PRESENTED DOCTOR OF PHILOSOPHY

YEAR THIS DEGREE GRANTED Fall of 1989

Permission is hereby granted to THE UNIVERSITY OF ALBERTA LIBRARY to reproduce single copies of this thesis and to lend or sell such copies for private, scholarly or scientific research purposes only.

The author reserves other publication rights, and neither the thesis nor extensive extracts from it may be printed or otherwise reproduced without the author's written permission.

(SIGNED) L Samarasekera

PERMANENT ADDRESS:
32/55, Sri Sumangala Road North
Katutara North
Sri Lanka

DATED 5th January 1989

THE UNIVERSITY OF ALBERTA

FACULTY OF GRADUATE STUDIES AND RESEARCH

The undersigned certify that they have read, and recommend to the Faculty of Graduate Studies and Research, for acceptance, a thesis entitled **ANALYSIS AND DESIGN OF EXCAVATIONS IN CLAY** submitted by Lal Samarasekera in partial fulfilment of the requirements for the degree of DOCTOR OF PHILOSOPHY in Civil Engineering.

....

Supervisor

....

....

....

....

....

External Examiner

Date 5th January 1989

Dedication

To my father, mother, brothers, teachers and the rest

Abstract

Complex constitutive models have been found capable of accurately predicting soil stress-strain, strength and pore pressure behaviour under laboratory conditions, and the finite element method has provided an accurate numerical approximation for the continuum model. When these two are combined, they seldom yield correspondingly accurate field predictions. This is due to the discrepancies that may arise and get accumulated at different stages; sampling, testing and interpretation, and material and numerical modelling. To avoid some of these problems, a design concept termed Solution Oriented Model is proposed which may improve the accuracy of predictions. It uses field observations to compute a set of factors that make the subsequent predictions more accurate.

A set of simple numerical and material models is used in an uncoupled analysis to study deformation, pore pressure generation and dissipation behaviour and its influence on displacements. The results of the application of this type of analysis to case histories compared reasonably well with observed deformation, pore pressure generation and dissipation.

Using the uncoupled analysis, a parametric study was carried out to investigate the pore pressure generation and dissipation around shallow, supported and unsupported tunnels, constructed in normally consolidated clay. A term Effective Stiffness Ratio was introduced to quantify the

influence of the support system on pore pressure. A similar study was undertaken on unsupported shallow tunnels in overconsolidated clay.

The pore pressure diagrams presented using nondimensional and normalized quantities may be used to estimate the pore pressure around a shallow tunnel. Stiffer supports generate pore pressure that is smaller in magnitude. The pore pressures developed around shallow tunnels constructed in normally consolidated clay tend to be positive, whereas in overconsolidated clay they tend to be negative. Consequently, the stability of a shallow tunnel constructed in overconsolidated clay decreases with time. A method of stability analysis that combines finite element method and limit equilibrium theory is used to study this phenomenon parametrically. Concisely presented nondimensionalized results relate strength, geometry and the time taken for general failure of an unsupported tunnel constructed in overconsolidated clay. These results quantify the deterioration of stability with time which may be utilized to estimate the stand-up time.

Acknowledgement

I am most grateful to Dr. Z. Eisenstein for his guidance and technical as well as moral support throughout this research program.

I wish to Thank Drs. Dave Murray, Terry Hrudey and Dave Chan for their input for my finite element work. Thanks are also due to, Dr. A. V. G. Krishnayya for his help in the modification of his consolidation program, and Ms. Angela Kupper and Arsenio Negro for providing me with detailed data on some of the case histories, and their help in many other ways including Portuguese to English translations. I wish to thank Mr. Alan Gale and Dr. Dave Sego for their input on experimental Soil Mechanics, and Drs. Heinrich Heinz, Andre Chan, Po Tsui, Messrs Richard Wan, Attia Shalaby and M. Vasuvithasan and my other colleagues for their input and help in various ways for this research project. Dr. G. Bandarage helped to/(not to) draw analogies from theoretical Physics, and Dr. Ms. Chandani Senanayake helped me explain myself the relevance/(non relevance) of the structure of water and potential flow in comparison to the structure of soil and plastic potential. Without the help of Ms. Nadine Leenders and Mr. Peter Buttuls, I would never have solved that easily the problems I faced with computer graphics, and Mr. Patrick Collins' textform macros helped in typing the equations, and Ms. Debbie Reinhart helped solve many textformatting problems.

Special thanks should go to Dr. S. Thomson for reading my manuscript and making valuable suggestions, even before he became one of my examiners. I also wish to thank Messrs Bandula Abeysundara, Ravi Kulatunga, M. Skantharajah, Tai Wong, Ms. Emma Crossly, Ms. Indira Ginige, Ms. Leela Kobbekaduwa and Ms. Jo Ann Mackie, Drs. V. C. Epa and Angelo Fernando for helping in various ways in the preparation of this thesis, including proof reading. Thank you Indira for all your delicious food during the couple of weeks leading to the defence, it also provided moral support. Thank you Bandula for proof reading the whole thesis with very short notice; and your suggestions for my presentation were most helpful, not to mention your moral support.

I would also like to thank the examination committee for their valuable suggestions.

The research was supported by the grants awarded to Dr. Z. Eisenstein from National Science and Engineering Council of Canada, and the financial assistance provided by the Department of Civil Engineering in the form of Teaching Assistantships. These grants are acknowledged with gratitude.

Table of Contents

Chapter Page

Dedication iv

Abstract v

Acknowledgement vii

List of Tables xv

List of Figures xvi

List of Symbols xxv

1. INTRODUCTION 1

2. MODERN GEOTECHNICAL ENGINEERING DESIGN 3

2.1 INTRODUCTION 3

2.2 ELEMENTS OF MODERN GEOTECHNICAL ENGINEERING DESIGN 7

2.2.1 MATERIAL MODELS 7

2.2.1.1 CAM CLAY MODEL 8

2.2.1.2 LADE'S MODEL 15

2.2.1.3 DISCUSSION 16

2.2.2 MODELS FOR PARAMETER GENERATION (LABORATORY AND FIELD) 19

2.2.2.1 SAMPLING 20

2.2.2.2 TESTING 20

2.2.2.3 TYPE OF TEST 27

2.2.2.4 INTERPRETATION OF RESULTS (using KINEMATIC and MATERIAL MODELS) 27

2.2.2.5 DISCUSSION 29

2.2.3 NUMERICAL MODELS 31

2.2.3.1 FINITE ELEMENT FORMULATION 32

2.2.3.2 FINITE ELEMENT MESH 34

2.2.3.3 IMPROVING THE MESH 38

2.2.3.4 SELECTION OF THE BOUNDARY 48

2.2.3.5 INITIAL STRESS STATE, CONSTRUCTION SEQUENCE AND SOLUTION TECHNIQUES 49

2.2.3.6 DISCUSSION 51

2.3 SOLUTION ORIENTED MODELS(SOM) 51

3. PORE PRESSURE AND DEFORMATION BEHAVIOUR 59

3.1 INTRODUCTION AND OBJECTIVE 59

3.2 CONCEPTS OF CONSOLIDATION IN A CONTINUUM 59

3.2.1 COUPLED SOLUTION 60

3.2.2 UNCOUPLED SOLUTION 63

3.3 A SIMPLE MODEL FOR PORE PRESSURE BEHAVIOUR AND DEFORMATION 65

3.3.1 Step 1; UNDRAINED BEHAVIOUR 67

3.3.2 Step 2; PORE PRESSURE DISSIPATION 67

3.3.3 Step 3; DISPLACEMENTS DUE TO PORE PRESSURE DISSIPATION 67

3.4 NUMERICAL APPROACH FOR THE SIMPLE MODEL 68

3.4.1 Step 1; UNDRAINED BEHAVIOUR 69

3.4.1.1 HYPERBOLIC MODELS 69

3.4.1.2 PORE PRESSURE PARAMETERS 79

3.4.2 Step 2; PORE PRESSURE DISSIPATION 81

3.4.3 Step 3; DISPLACEMENTS DUE TO PORE PRESSURE DISSIPATION 81

3.5 FINITE ELEMENT FORMULATION 82

3.5.1 VIRTUAL WORK APPROACH FOR EQUILIBRIUM EQUATION 82

3.5.2 VIRTUAL WORK EQUATION FOR DISPLACEMENT FINITE ELEMENT FORMULATION 85

3.5.3 SOLUTION TECHNIQUES 89

3.5.3.1 STEPWISE METHODS 90

3.5.3.2 EQUILIBRIUM ITERATION PROCCEDURE ..93

3.5.3.3 CHOICE OF A SOLUTION TECHNIQUE 96

3.5.4 SOLUTION OF [K]{r}={R} AND STORAGE PROCEDURE 100

3.5.5 VARIATIONAL APPROACH FOR UNCOUPLED CONSOLIDATION 102

3.5.6 FINITE ELEMENT VARIATIONAL FORMULATION FOR UNCOUPLED ANALYSIS 103

3.5.7 CONSOLIDATION FINITE ELEMENTS IN THE TIME DOMAIN 107

3.5.8 CAM CLAY MODEL IN FINITE ELEMENT DISPLACEMENT FORMULATION 109

3.6 VERIFICATION OF FINITE ELEMENT CODES 114

3.6.1 NON LINEAR ELASTIC FINITE ELEMENT MODEL ..115

3.6.2 CAM CLAY FINITE ELEMENT MODEL 117

3.6.2.1 PLANE STRAIN TRIAXIAL STRESS-STRAIN BEHAVIOUR 121

3.6.2.2 PLANE STRAIN SIMPLE SHEAR STRESS-STRAIN BEHAVIOUR 125

3.7 CONDITIONS FOR A RELIABLE SOLUTION 129

4. APPLICATION OF THE SIMPLE MODELS 132

4.1 INTRODUCTION AND OBJECTIVE 132

4.2 METHOD OF ANALYSIS 132

4.3 DISPLACEMENT AROUND A TUNNEL 133

4.3.1 METHOD OF CONSTRUCTION AND INSTRUMENTATION 134

4.3.2 GEOMETRY AND SOIL PROFILE 136

4.3.3 OBSERVATIONS AND PREDICTIONS 136

4.4 PORE PRESSURE AROUND AN EXCAVATION 140

4.4.1 METHOD OF CONSTRUCTION AND INSTRUMENTATION 143

4.4.2 GEOMETRY AND SOIL PROFILE 144

4.4.3 OBSERVATIONS AND PREDICTIONS 144
4.5 SETTLEMENT AND PORE PRESSURE AROUND A TUNNEL ... 146
4.5.1 METHOD OF CONSTRUCTION 149
4.5.2 INSTRUMENTATION 149
4.5.3 GEOMETRY AND SOIL PROFILE 150
4.5.4 OBSERVATIONS AND PREDICTIONS 152
4.6 SUMMARY AND CONCLUSIONS 161
5. PORE PRESSURE BEHAVIOUR AROUND SHALLOW TUNNELS IN CLAY 163
5.1 INTRODUCTION AND OBJECTIVE 163
5.2 CLOSED FORM SOLUTIONS AND LIMITATIONS 165
5.3 NEED FOR NORMALIZATION AND NON-DIMENSIONALIZATION 168
5.3.1 NON-DIMENSIONALIZATION OF PORE PRESSURE .. 169
5.3.2 SPATIAL NON-DIMENSIONALIZATION 170
5.3.3 NON-DIMENSIONALIZATION OF STRENGTH AND MODULUS 172
5.3.4 NON-DIMENSIONALIZED TIME (T) 173
5.3.5 A NON-DIMENSIONAL PARAMETER FOR SUPPORTED TUNNELS, ESR 173
5.4 FINITE ELEMENT ANALYSIS 175
5.4.1 SELECTION OF A MESH 175
5.4.2 ASSUMPTION OF MONOTONICALLY INCREASING STRESS 182
5.4.3 LOAD STEP SIZE AND ITS SIGNIFICANCE 183
5.5 PARAMETRIC STUDY 189
5.5.1 UNSUPPORTED TUNNELS IN NORMALLY CONSOLIDATED CLAY 191
5.5.1.1 STRENGTH AND PORE PRESSURE 192
5.5.1.2 MODULUS AND PORE PRESSURE 196

5.5.1.3 HENKEL'S COEFFICIENT a AND PORE PRESSURE 198

5.5.1.4 IN SITU K_0 AND PORE PRESSURE 199

5.5.1.5 H/D RATIO AND PORE PRESSURE 203

5.5.1.6 TUNNEL DIAMETER (D), γ AND PORE PRESSURE 205

5.5.1.7 PORE PRESSURE DISSIPATION; TIME FACTOR T AND H,D 207

5.5.1.8 PORE PRESSURE DISSIPATION; TIME FACTOR T AND c_v 208

5.5.2 SUPPORTED TUNNELS IN NORMALLY CONSOLIDATED CLAY 217

5.5.2.1 SOIL MODULUS, LINER MODULUS AND PORE PRESSURE 226

5.5.2.2 A_l, I_l, SOIL MODULUS AND PORE PRESSURE 227

5.5.2.3 K_0 AND PORE PRESSURE 227

5.5.2.4 TUNNEL DIAMETER AND PORE PRESSURE 230

5.5.2.5 t/R AND PORE PRESSURE 233

5.5.2.6 FURTHER COMMENTS ON SUPPORTED TUNNELS 233

5.5.3 UNSUPPORTED TUNNELS IN OVERCONSOLIDATED CLAY 235

5.5.3.1 MODULUS AND PORE PRESSURE 253

5.5.3.2 STRENGTH AND PORE PRESSURE 254

5.5.3.3 K_0 AND PORE PRESSURE 257

5.5.3.4 HENKEL'S COEFFICIENT a AND PORE PRESSURE 259

5.5.3.5 H/D AND PORE PRESSURE 262

5.6 PORE WATER PRESSURE DIAGRAMS 264

5.7 SUMMARY AND CONCLUSIONS 273

6. STABILITY EVALUATION OF UNSUPPORTED SHALLOW TUNNELS IN OVERCONSOLIDATED CLAYS USING A NEW APPROACH 281

6.1 TUNNEL STABILITY 281

6.2 INADEQUACY IN CURRENT PRACTICE 284

6.3 NEW APPROACH FOR STABILITY OF SOIL STRUCTURES AND APPLICATION FOR TUNNELS 285

6.4 FACTORS INFLUENCING TUNNEL STABILITY 289

6.5 TIME-STABILITY-STRENGTH (TSS) CURVES FOR ESTIMATING STABILITY VARIATION DUE TO PORE PRESSURE DISSIPATION 290

6.6 SUMMARY AND CONCLUSIONS 300

7. SUMMARY AND CONCLUSIONS 303

BIBLIOGRAPHY 307

APPENDIX A THEORY OF REAL FINITE ELEMENT ANALYSIS 321

APPENDIX B EFFECTIVE STIFFNESS RATIO FORMULATIONS 323

List of Tables

Table Page

4.1 Thunder Bay Tunnel; Material Properties 153

4.2 Observations and Predictions of Pore Pressure Dissipation; Thunder Bay Tunnel 158

5.1 Practical Ranges of Parameters used 260

5.2 Summary of Parametric Analysis on Pore Pressure 274

List of Figures

Figure Page

2.1 Basic Steps of Modern Geotechnical Engineering Design 6

2.2 Critical State Line for Clay 10

2.3 Consolidation of Clay 10

2.4 State Boundary Surface; Cam-Clay Model 13

2.5 Laboratory Results and Cam-Clay Predictions (after Roscoe et al., 1968 : modified) 18

2.6 Lade's Model Predictions and Laboratory Results (after Lade, 1975 : modified) 18

2.7 Influence of Sampling Technique on Unconfined Compression Test Results (after Raymond et al., 1971 : modified) 21

2.8 Influence of Base Friction on UU Test Results (after Duncan et al., 1968 : modified) 23

2.9 The Effects of Membrane on Pore Pressure in CU Triaxial Tests (after Kiekbusch et al., 1977 : modified) 24

2.10 Influence of System Compliance on Stress Ratios to cause Liquifaction (after Martin et al., 1978 : modified) 25

2.11 Influence of Strain Rate on Undrained Stress-Strain Behaviour in a Triaxial Test (after Vaid et al., 1974 : modified) 26

2.12 Comparison of Strength values from Unconfined and Semi-confined Tests (after DeLory et al., 1971 : modified) 28

2.13 Kinematic Models for Interpreting Triaxial Results (after Roscoe et al., 1963 : modified) 30

2.14 Triaxial Stress-Strain Behaviour Interpreted using Different Kinematic Models (after Roscoe et al., 1963 : modified) 30

2.15 Different Quadrilateral Finite Elements 33

Figure Page

2.16 Strain Energies of Lagrangian and Serendipity Elements for same Degrees of Freedom (after Argyris et al., 1973 : modified) 35

2.17 The Influence of the Order of Quadrature on Finite Element Results (after Zienkiewicz, 1977, : modified) 36

2.18 Selective Refinement of Quadrilateral and Triangular Elements 41

2.19 Parabolic Tensile Stress on a Plate 41

2.20 A Typical Finite Element Mesh (after McNeice et al., 1973 : modified) 42

2.21 Optimum Mesh after Seven Iterations (after McNeice et al., 1973 : modified) 42

2.22 Pinched Roller 44

2.23 Grid Using Isoenergetics, 27 dof (after Shephard et al., 1979 : modified) 44

2.24 Grid Using Isoenergetics, 25 dof (after Turcke et al., 1974 : modified) 46

2.25 Grid Using Isostatics, 24 dof (after Turcke, 1979 : modified) 46

2.26 Initial Mesh, 23 dof (after Turcke, 1979 : modified) 47

2.27 Arbitrarily Refined Grid, 37 dof (after Turcke, 1979 : modified) 47

2.28 Finite Element and Closed form Solutions for Surface Settlement (after Girijavallabhan, 1968 : modified) 54

2.29 Concept of Solution Oriented Model 54

3.1 Uncoupled Model for Pore Pressure and Deformation Analysis 66

3.2 FE Models for the Uncoupled Analysis of Pore Pressure and Deformation 70

3.3 Hyperbolic Stress-Strain Relations 72

3.4 Hyperbolic Stress-Strain Curve as a Material Model 75

Figure Page

3.5 A Different Interpretation of the Hyperbolic Model 75

3.6 K_0 Triaxial Stress-Strain Curves 77

3.7 General Hyperbolic Material Model 83

3.8 Body under Equilibrium 83

3.9 Basic Incremental Method and Runge-Kutta Mid-Point Method 95

3.10 Iterative Procedure 95

3.11 Constant Stiffness Iterative Method 97

3.12 Mixed Iterative Approach 97

3.13 Block Solver Technique (after Murray, 1985 : modified) 104

3.14 Consolidation Boundary Value Problem 104

3.15 Closed Form and Finite Element Stress-Strain Solutions using Hyperbolic Models 116

3.16 Cam-Clay Model in Plane Strain (after Chang et al., 1983 : modified) 119

3.17 Three Dimensional Cam-Clay Model 119

3.18 Finite Element and Quasi-Closed form Solutions for Plane Strain Triaxial Test using Cam-Clay Model 122

3.19 Finite Element and Quasi-Closed Form Solutions for Plane Strain Simple Shear Test Using Cam-Clay Model 126

4.1 Sequential Tunnelling Technique and a Typical Instrumented Section (after Negro and Eisenstein, 1981 : modified) 135

4.2 NATM Tunnel; Geometry and Soil Stratigraphy (after Negro and Eisenstein, 1981 : modified) 137

4.3 Finite Element Mesh for NATM Tunnel 139

Figure Page

4.4 Predicted and Observed Surface Settlements; NATM Tunnel 141

4.5 Predicted and Observed Vertical Settlements; NATM Tunnel 142

4.6 Kimola Canal; Geometry, Soil Stratigraphy and Piezometer Configuration (after Kankare, 1969a : modified) 145

4.7 Finite Element Mesh for Kimola Canal 147

4.8 Equivalent Unloading Forces 147

4.9 Predicted Pore Pressure-change Contours and Observed Pore Pressure Changes 148

4.10 Instrumentation at Array 2; Thunder Bay Tunnel (after Belshaw and Palmer, 1978 : modified) 151

4.11 Finite Element Mesh for Thunder Bay Tunnel 154

4.12 Observations and Predictions of Initial Surface Settlements; Thunder Bay Tunnel 156

4.13 Thunder Bay Tunnel; Geometry and Soil Stratigraphy 159

4.14 Piezometers for Long Term Monitoring; Thunder Bay Tunnel (after Belshaw and Palmer, 1978 : modified) 159

4.15 Observed and Predicted Additional Settlements after 20 days; Thunder Bay Tunnel 160

5.1 Unloading Stresses vs Tunnel Depth; $K_0=1$ 171

5.2 Spatial Nom-dimensionalization 171

5.3 Initial Coarse Mesh 177

5.4 Mesh after First Modification 178

5.5 Refined Mesh, Typical Mesh Used in the Study 179

5.6 Mesh for the Expanded Boundary 181

Figure Page

5.7 Stress-Strain Behaviour of Critical Elements during Tunnel Excavation Simulation 184

5.8 Stress-Strain Behaviour of Critical Elements with Half-Load Step Size in Tunnel Excavation Simulation 186

5.9 Material Behaviour of Critical Finite Elements and the Idealized Behaviour 188

5.10 Normalized Pore Pressure Contours for s_u/σ_v=0.4 194

5.11 Normalized Pore Pressure Contours for s_u/σ_v=0.7 194

5.12 Normalized Pore Pressure for E_i/σ_v=200 197

5.13 Normalized Pore Pressure for E_i/σ_v=800 197

5.14 Normalized Pore Pressure for a=0.12 200

5.15 Normalized Pore Pressure for a=0.48 200

5.16 Normalized Pore Pressure for K_0=0.5 202

5.17 Normalized Pore Pressure for K_0=0.8 202

5.18 Normalized Pore Pressure for H/D=1.25 204

5.19 Normalized Pore Pressure for H/D=2.75 204

5.20 Normalized Pore Pressure for γ=10 kN/m^3 206

5.21 Normalized Pore Pressure for D=9m 206

5.22 Normalized Pore Pressure for D=3m 209

5.23 Normalized Pore Pressure for D=3m T=0.001; Unsealed Tunnel 209

5.24 Normalized Pore Pressure for D=3m, T=0.01; Unsealed Tunnel 210

5.25 Normalized Pore Pressure for H/D=1.25, T=0.001; Unsealed Tunnel 210

5.26 Normalized Pore Pressure for H/D=1.25, T=0.01; Unsealed Tunnel 211

5.27 Normalized Pore Pressure for H/D=1.25, T=0.1; Unsealed Tunnel 211

Figure Page

5.28 Normalized Pore Pressure for H/D=1.25, T=0.001; Sealed Tunnel 212

5.29 Normalized Pore Pressure for H/D=1.25, T=0.01; Sealed Tunnel 212

5.30 Normalized Pore Pressure for H/D=1.25, T=0.1; Sealed Tunnel 213

5.31 Normalized Pore Pressure for H/D=2.75, T=0.001; Unsealed Tunnel 213

5.32 Normalized Pore Pressure for H/D=2.75, T=0.01; Unsealed Tunnel 214

5.33 Normalized Pore Pressure for H/D=2.75, T=0.1; Unsealed Tunnel 214

5.34 Normalized Pore Pressure for H/D=2.75, T=0.001; Sealed Tunnel 215

5.35 Normalized Pore Pressure for H/D=2.75, T=0.01; Sealed Tunnel 215

5.36 Normalized Pore Pressure for H/D=2.75, T=0.1; Sealed Tunnel 216

5.37 Unsealed Tunnel in NCC, $\hat{u}$ in (ξ,η), ESR=0, T=0 218

5.38 Unsealed Tunnel in NCC, $\hat{u}$ in (ξ,η), ESR=0, T=0.001 219

5.39 Unsealed Tunnel in NCC, $\hat{u}$ in (ξ,η), ESR=0, T=0.01 220

5.40 Unsealed Tunnel in NCC, $\hat{u}$ in (ξ,η), ESR=0, T=0.1 221

5.41 Sealed Tunnel in NCC, $\hat{u}$ in (ξ,η), ESR=0, T=0.001 222

5.42 Sealed Tunnel in NCC, $\hat{u}$ in (ξ,η), ESR=0, T=0.01 223

5.43 Sealed Tunnel in NCC, $\hat{u}$ in (ξ,η), ESR=0, T=0.1 224

5.44 Normalized Pore Pressure, ESR=10^{-3}, E_1/σ_{1c}=200; E_1 Decreased 228

5.45 Normalized Pore Pressure, ESR=10^{-3}, E_1/σ_{1c}=800; E_1 Increased 228

Figure Page

5.46 Normalized Pore Pressure, ESR=10^{-2}, E_1/σ_{1e}=200; I_1, A_1 Decreased 229

5.47 Normalized Pore Pressure, ESR=10^{-2}, E_1/σ_{1e}=800; I_1, A_1 Increased 229

5.48 Normalized Pore Pressure, ESR=10^{-1}, K_0=0.5 231

5.49 Normalized Pore Pressure, ESR=10^{-1}, K_0=0.8 231

5.50 Normalized Pore Pressure, ESR=10^{-2}, D=3m 232

5.51 Normalized Pore Pressure, ESR=10^{-2}, D=9m 232

5.52 Normalized Pore Pressure, ESR=10^{-1}, t/R=0.03 234

5.53 Normalized Pore Pressure, ESR=10^{-1}, t/R=0.07 234

5.54 Unsealed Tunnel in NCC; $\hat{u}$ in (ξ,η), ESR=10^{-3}, T=0 236

5.55 Unsealed Tunnel in NCC; $\hat{u}$ in (ξ,η), ESR=10^{-3}, T=0.001 237

5.56 Unsealed Tunnel in NCC; $\hat{u}$ in (ξ,η), ESR=10^{-3}, T=0.01 238

5.57 Unsealed Tunnel in NCC; $\hat{u}$ in (ξ,η), ESR=10^{-3}, T=0.1 239

5.58 Sealed Tunnel in NCC; $\hat{u}$ in (ξ,η), ESR=10^{-3}, T=0.001 240

5.59 Sealed Tunnel in NCC; $\hat{u}$ in (ξ,η), ESR=10^{-3}, T=0.01 241

5.60 Sealed Tunnel in NCC; $\hat{u}$ in (ξ,η), ESR=10^{-3}, T=0.1 242

5.61 Unsealed Tunnel in NCC; $\hat{u}$ in (ξ,η), ESR=10^{-2}, T=0 243

5.62 Unsealed Tunnel in NCC; $\hat{u}$ in (ξ,η), ESR=10^{-2}, T=0.001 244

5.63 Unsealed Tunnel in NCC; $\hat{u}$ in (ξ,η), ESR=10^{-2}, T=0.01 245

5.64 Sealed Tunnel in NCC; $\hat{u}$ in (ξ,η), ESR=10^{-2}, T=0.001 246

Figure Page

5.65 Sealed Tunnel in NCC; $\hat{u}$ in (ξ,η), $ESR=10^{-2}$, $T=0.01$ 247

5.66 Unsealed Tunnel in NCC; $\hat{u}$ in (ξ,η), $ESR=10^{-1}$, $T=0$ 248

5.67 Unsealed Tunnel in NCC; $\hat{u}$ in (ξ,η), $ESR=10^{-1}$, $T=0.001$ 249

5.68 Unsealed Tunnel in NCC; $\hat{u}$ in (ξ,η), $ESR=10^{-1}$, $T=0.01$ 250

5.69 Sealed Tunnel in NCC; $\hat{u}$ in (ξ,η), $ESR=10^{-1}$, $T=0.001$ 251

5.70 Sealed Tunnel in NCC; $\hat{u}$ in (ξ,η), $ESR=10^{-1}$, $T=0.01$ 252

5.71 Normalized Pore Pressure, $E_i/\sigma_{1c}^{\frac{1}{2}}=6\ \mathrm{GPa}^{\frac{1}{2}}$ 255

5.72 Normalized Pore Pressure, $E_i/\sigma_{1c}^{\frac{1}{2}}=136\ \mathrm{GPa}^{\frac{1}{2}}$ 255

5.73 Normalized Pore Pressure, $s_u/\sigma_{1c}^{\frac{1}{2}}=10\ \mathrm{kPa}^{\frac{1}{2}}$ 258

5.74 Normalized Pore Pressure, $s_u/\sigma_{1c}^{\frac{1}{2}}=100\ \mathrm{kPa}^{\frac{1}{2}}$ 258

5.75 Normalized Pore Pressure, $K_0=1.25$ 261

5.76 Normalized Pore Pressure, $K_0=1.75$ 261

5.77 Normalized Pore Pressure, $\alpha=-0.2$ 263

5.78 Normalized Pore Pressure, $\alpha=-0.6$ 263

5.79 Normalized Pore Pressure, $H/D=1$ 265

5.80 Normalized Pore Pressure, $H/D=3$ 265

5.81 Unsealed Tunnel in OCC, $\hat{u}$ in (ξ,η), $T=0$ 266

5.82 Unsealed Tunnel in OCC, $\hat{u}$ in (ξ,η), $T=0.001$ 267

5.83 Unsealed Tunnel in OCC, $\hat{u}$ in (ξ,η), $T=0.01$ 268

Figure Page

5.84 Unsealed Tunnel in OCC, $\hat{u}$ in (ξ,η), T=0.1 269

5.85 Sealed Tunnel in OCC, $\hat{u}$ in (ξ,η), T=0.001 270

5.86 Sealed Tunnel in OCC, $\hat{u}$ in (ξ,η), T=0.01 271

5.87 Sealed Tunnel in OCC, $\hat{u}$ in (ξ,η), T=0.1 272

5.88 3-D Image of Pore Pressure around an Unsupported Tunnel in NC Clay 276

5.89 3-D Image of Pore Pressure around a Supported Tunnel in NC Clay 277

5.90 3-D Image of Pore Pressure around an Unsupported Tunnel in OC Clay 278

6.1 Some Failure Mechanisms of Shallow Tunnels 282

6.2 A Simple Failure Mechanism for Shallow Tunnels 287

6.3 Definition of Factor of Safety 287

6.4 A Typical Failure Mode in a Model Test (after Mair, 1979) 293

6.5 Typical Pore Pressure Distributions 293

6.6 Limit Equilibrium Solutions for Different Failure Planes 294

6.7 Time-Stability-Strength (TSS) Curves for K_0=0.8, H/D=1.8 295

6.8 Time-Stability-Strength (TSS) Curves for K_0=1.2, H/D=1.8 298

6.9 Time-Stability-Strength (TSS) Curves for K_0=1.5, H/D=1.8 299

List of Symbols

A_l	Area of cross section, liner
$[B]$	Strain displacement matrix
C_{ijkl}	Constitutive matrix
c_f	Compressibility coefficient of the fluid
c_v	Coefficient of Consolidation
c'	Effective cohesion
dof	Degrees of freedom
D	Diameter of the tunnel
$[D]$	Constitutive matrix
e	Void Ratio
E_i	Initial Young's modulus, soil
E_l	Liner Young's modulus
E_s	Young's modulus, soil
E_t	Tangent Young's modulus
E_{t0}	Tangent Young's modulus with no principal axes rotation
E_{t90}	Tangent Young's modulus with 90^0 principal axes rotation
$E_{t\theta}$	Tangent Young's modulus with θ^0 principal axes rotation
ESR	Effective Stiffness Ratio
F_i	Body force tensor
F_j	Body force tensor(of fluid)
F	Body force vector
$\{F\}$	Nodal loading vector due to body force
$\{F_T\}$	Nodal loading vector due to traction

G_i	Initial shear modulus
h	Total head
H	Height of the overburden above the crown of tunnel, depth of cover
H_c	Depth of Centre of Tunnel below Ground Surface
$[H]$	Coefficient matrix of consolidation; finite elements
I_l	Second moment of area, liner
k_{ij}	Permeability tensor
k_x	Permeability in x direction
k_{xy}	Cross permeability
k_y	Permeability in y direction
K	Bulk Modulus
K_0	Coefficient of earth pressure at rest
$[K]$	Stiffness matrix
L	Length of the Failure Plane
m	Power index, strength
M	Slope of q vs p
$\bar{M}$	$E_s/2(1+\nu)(1-2\nu)$
n	Power index, modulus
n_j	j component of unit normal
$\bar{n}$	Unit normal
OCR	Over consolidation ratio
p_0	p' corresponding to pre-consolidation state
p'	$= \frac{1}{3}(\sigma'_x+\sigma'_y+\sigma'_z)$
p'_r	Defined in Figure 3.14, section 3.5.8
p_i	Internal pressure of the tunnel
P_a	Atmospheric pressure

q	$= \sqrt{\frac{1}{2}[(\sigma_x-\sigma_y)^2 + (\sigma_y-\sigma_z)^2 + (\sigma_z-\sigma_x)^2 + 6\tau_{xy}^2]}$
q_0	Outflow rate at specified boundary
q^0	$\sigma'_v(1-K_0)$
q^{fc}	Strength in compression
q^{fe}	Strength in extension
Q	$= 2(1+\nu)(1-2\nu)\gamma_w/E$
r_i	Displacement at node i
$\{r\}$	Displacement vector
R	Radius of the tunnel
R_i	Nodal Force at Node i
R_f	Failure Ratio
s	Line domain
s_u	Undrained strength
s_{u0}	Undrained strength; compression
s_{u90}	Undrained strength; extension
$s_{u\theta}$	Undrained strength; principal axes rotated by θ^0
s_1	Line boundary where flow is specified
s_2	Line boundary where pore pressures are specified
S	Area domain
S_T	Surface where traction is specified
S_u	Surface where displacements are specified
SOM	Solution Oriented Model
t_l	Thickness of the liner
T	Time factor for the tunnel
T_i	Traction tensor (on the body)
$\vec{T}$	Traction vector
TSS	Time-Stability-Strength

u	Excess pore water pressure
$u(t)$	Pore pressure at time t
u_f	Nodal u values where the values are not fixed
u_s	Nodal u values where the values are fixed
u_i^e	Pore pressure at a node in an element
$\bar{u}_i$	Nodal values of pore pressure in time element i (or ith time step)
u^t	Total pore pressure
$\dot{u}$	$\frac{\partial u}{\partial t}$
$\hat{u}$	Non-dimensionalized and normalized pore water pressure
$\bar{u}$	Nodal pore pressure vector at time t
v	volume
v_i	Fluid flow velocity in i direction
$v_{i,i}$	$\frac{\partial v_i}{\partial x_i}$
$\vec{v}$	Flow velocity
w_i	Displacement in i direction
$w_{k,l}$	$\frac{\partial w_k}{\partial x_l}$
$\dot{w}_{i,i}$	$\frac{\partial w_{i,i}}{\partial t}$
x	x coordinate, x value of vertical failure plane
x_i	x coordinate of node i
y	y coordinate
$\check{y}$	(R^2-x^2) for $x \leq R$ 0 for $x>R$
α	Henkel's pore pressure coefficient
γ	Unit weight of soil
γ_f	Unit weight of fluid

γ_{max}	Maximum Shear strain
γ_w	Unit weight of water
Δ	Area of the triangle
Δt	Time step
$\Delta\sigma_{ij}$	Stress change tensor
$\Delta\sigma_1$	Major principal stress of $\Delta\sigma_{ij}$
$\Delta\sigma_2$	Intermediate principal stress of $\Delta\sigma_{ij}$
$\Delta\sigma_3$	Minor principal stress of $\Delta\sigma_{ij}$
ϵ	Strain
ϵ_{ij}	Strain tensor
η	Non-dimensionalized y coordinate; $q/(p'_r+p')$
κ	Slope of rebound curve on a semi-log plot
λ	Slope of normally consolidated curve on a semi-log plot
ν	Poisson's Ratio, Soil
ν_1	Poisson's Ratio, liner
ξ	Non-dimensionalized x coordinate
σ	Stress
σ_{ij}	stress tensor
σ_h	Horizontal Normal Stress
σ_m	Mean normal Stress
σ_r	Radial stress
σ_v	Vertical Normal Stress
σ_1	Major Principal Stress
σ_3	Minor Principal Stress
σ_θ	Hoop stress around the tunnel
σ'_{xx}	Effective normal stress in x direction

σ'_{yy}	Effective normal stress in y direction
σ'_{zz}	Effective normal stress in z direction
$\overline{\sigma}$	$<\sigma_x \ \sigma_y \ \tau_{xy}>^T$
τ_{max}	Maximum shear stress
ϕ'	Friction angle; effective

1. INTRODUCTION

In geotechnical engineering design, accuracy of prediction may ensure optimum design which implies safety and economy. The accuracy of prediction is especially important (Lambe, 1973) in the case of large projects, such as dams and tunnels because the savings involved may be correspondingly large. For example, conventional design tools such as limit equilibrium methods cannot predict the field behaviour in great detail. To overcome this problem, a large number of sophisticated material models have been developed. Generally, these models can accurately predict the laboratory soil (stress-strain, strength and pore pressure) behaviour. In some cases, these models have been incorporated in finite element techniques that can achieve very high numerical accuracies. Paradoxically, in design, such combinations of numerical and material models do not appear to have a correspondingly greater advantage over the conventional methods (Desai and Christian, 1977; Peck, 1984).

In an attempt to solve this paradox, the basic steps of the modern geotechnical engineering design are reviewed in detail in Chapter 2. A new design concept called Solution Oriented Model (SOM) is introduced to make predictions more accurate. For wide applicability of this approach, the use of simple models is recommended. This in turn raises the question whether simple models can be used to describe complex phenomena. To answer this question, some simple models are proposed to investigate the pore pressure behaviour in clays. These models are applied to field situations to check their performance. The results are generally encouraging.

The proposed models are used in a parametric study to understand the pore pressure behaviour around shallow tunnels. The study included the pore pressure dissipation behaviour and its influence on the overall wall stability of the tunnel.

2. MODERN GEOTECHNICAL ENGINEERING DESIGN

The use of numerical models, such as the finite element methods that incorporate sophisticated material models, is becoming a part of modern geotechnical engineering design. These models are expected to simulate the field behaviour considerably better than the conventional methods and therefore, produce more accurate results. In the sections that follow, the problems involved in the use of the numerical and material models are discussed and possible modifications and alternative concepts are suggested.

2.1 INTRODUCTION

It may be true that for the design of a small retaining wall or even a large earth dam (an earthfill dam 11 miles long, 70 ft. high, containing about 17 million cubic yards of embankment was completed in Ceylon in the year 504 B.C. - USBR, 1977), the theories of geotechnical engineering may not be necessary. However, there is no guarantee that these designs are the most economical for a given safety standard. In geotechnical engineering, in addition to servicebility, safety and economy are primary objectives, and a design employing accurate predictions is likely to reach all these objectives. In order to make more detailed and accurate predictions, the main emphasis has been on the development of accurate material models (DiMaggio et al., 1971; Lade et al., 1975; Finn et al., 1980; Prevost, 1980) and the adaptation of these models to finite element procedures.

When these models (numerical and material) are combined and applied to field situations, they generally do not yield correspondingly accurate predictions. For this reason, they do not have a clear advantage over conventional methods. There are different views on this subject. Referring to modern geotechnical engineering design, Desai and Christian (1977) state:

> Its use as a design tool is somewhat limited; some of the reasons for this minimal design role may be (1) satisfaction with conventional methods; (2) difficulties with older numerical methods: (3) cost; and (4) character of the geotechnical engineer. The last reason can be explained by the fact that most geotechnical engineers enjoy their work precisely because they often design using "engineering judgement" and less reliance on theoretical tools.
>
> Satisfaction with the present state of the art design methods for earth structure interaction is to a degree substantiated by studies of failures of earth retaining systems such as that reported by Sowers and Sowers(1967). They note that few of the failures included in their study could be attributed to inadequacies in conventional earth pressure theory but were largely due to environmental factors. These facts may be accepted at face value; however they do nothing to assure the designer that his conventional design is economical, nor do they ensure that designs for problems beyond the conventional will perform satisfactorily. ... It remains clear, however, that the use of numerical methods should never preclude the generous use of engineering judgement, because while the results obtained may be more detailed and comprehensive, simulations of the capricious elements of nature and man's work are always highly idealized.

This explanation does not answer two fundamental questions. (1) If the modern design is clearly better, why is the geotechnical engineer satisfied with conventional design?

(2) Is it merely the "character" of the geotechnical engineer to often use considerable engineering judgement and rely less on modern design tools, or are there other important reasons? Or, as previously mentioned, could it be possible that the modern design methods have not yet proven to the geotechnical engineer that their predictions in general are more reliable and accurate than conventional methods? The possible answers to these questions are explored in this Chapter. To answer these questions, it is essential to scrutinize closely each step of the modern design. The block diagram shown in Figure 2.1 illustrates concisely the basic steps of the modern geotechnical engineering design procedure.

Samples are obtained from the field and a variety of soil tests are performed; alternatively, field or in situ tests can be done. The results of these tests are used in material and kinematic models to generate soil parameters which, along with the material models, are employed in numerical models, such as finite elements, to predict field behaviour. Ideally, these predictions should match field observations. However, most of the time they do not. This is probably one reason why the geotechnical engineer often uses conventional methods of design, engineering judgement and empiricism, and relies less on more theoretical tools.

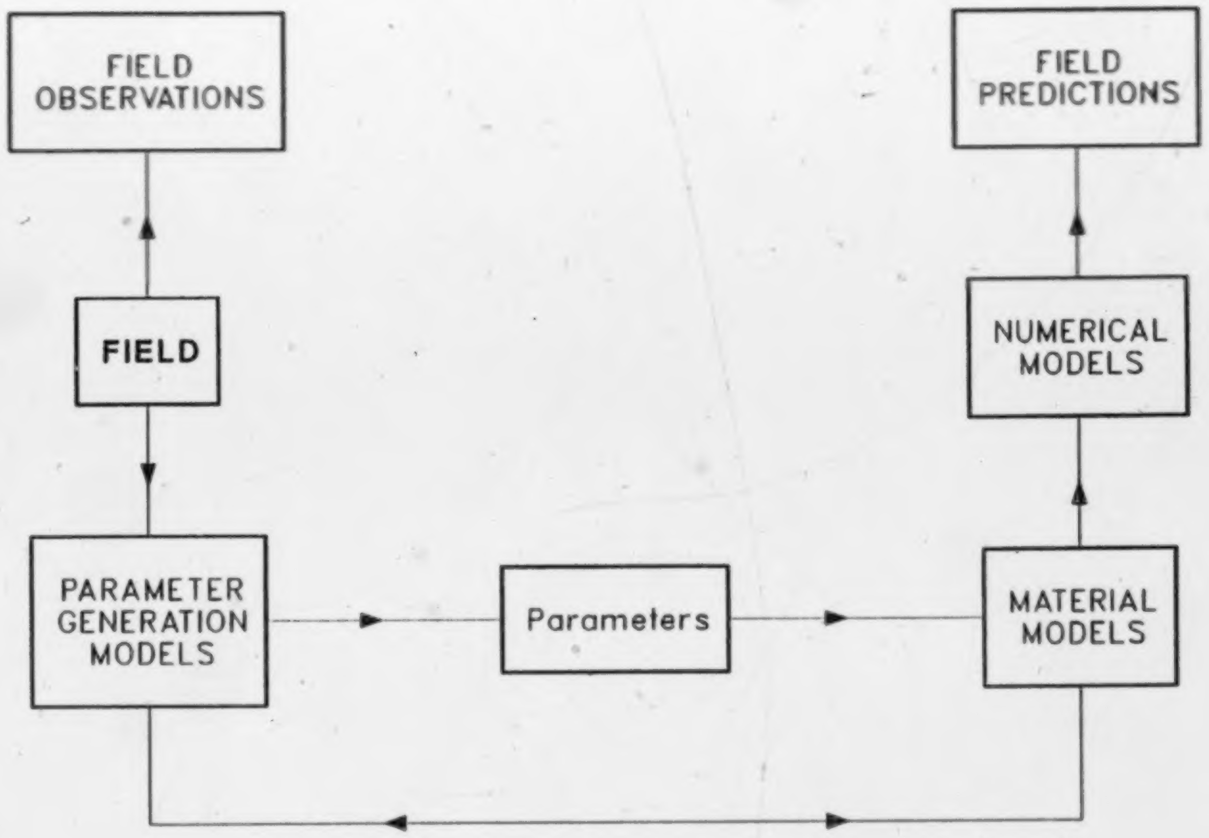
FIELD OBSERVATIONS
FIELD PREDICTIONS
FIELD
NUMERICAL MODELS
PARAMETER GENERATION MODELS
Parameters
MATERIAL MODELS

Figure 2.1 Basic Steps of Modern Geotechnical Engineering Design

2.2 ELEMENTS OF MODERN GEOTECHNICAL ENGINEERING DESIGN

The basic steps of modern geotechnical engineering design (Figure 2.1) were stated in the previous section. In the following sections, each of these steps is scrutinized to gain a better insight into the design procedure and to find reasons for its limited success.

2.2.1 MATERIAL MODELS

Material models form an essential part of geotechnical engineering design. To gain an insight into the material models, it is essential to understand the basic principles involved in their development. In this section, two different models, the Cam-Clay and the Lade's elasto-plastic model, are studied in detail in order to understand the basic principles involved in their development. These two models were chosen because, in many ways, they represent two extremes. For example, the Cam-Clay theory is considered to be based on fundamentals of physics, whereas Lade's model is considered to be merely based on curve fitting of laboratory data. Only five parameters are necessary to define the Cam Clay model and all have a direct geotechnical engineering meaning. On the other hand, to define the Lade's model, 14 parameters are needed and only a few of these have geotechnical engineering meaning.

q = $(\sigma_1 - \sigma_3)$ and

p = $(\sigma'_1 + \sigma'_2 + \sigma'_3)/3$.

Consolidation behaviour is self-explanatory from Figure 2.3. The normally consolidated behaviour is mathematically expressed in the following manner:

$$V = N - \lambda \ln(p) \qquad [2.2]$$

The elastic rebound line or the overconsolidated behaviour can be expressed as follows:

$$V = N_\kappa - \kappa \ln(p) \qquad [2.3]$$

where,

V = 1 + e, e being the void ratio,

λ slope of the normally consolidated line,

κ slope of the elastic rebound line,

N is the value of V when p=1 on the normally consolidated line and

N_κ is the value of V when p=1 on elastic rebound line.

POSTULATE

It is assumed that there are no recoverable shear strains. Therefore, the recoverable energy U can be expressed by the following Equation:

$$U = \frac{\kappa p}{V} \qquad [2.4]$$

Thus, the energy dissipation or the plastic work performed due to a stress increment of ($\delta p, \delta q$) can be expressed as follows:

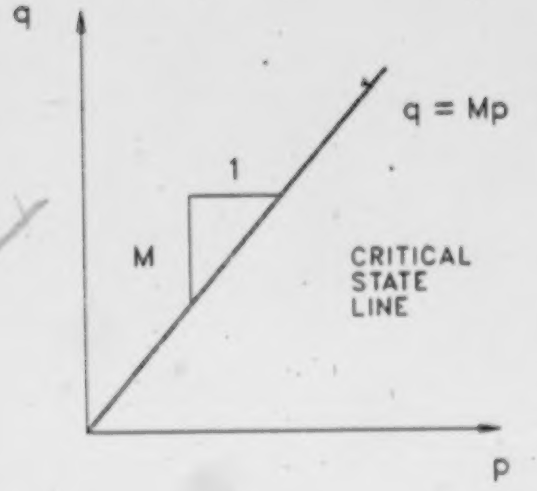
q
q = Mp
1
M
CRITICAL
STATE
LINE
p

Figure 2.2 Critical State Line for Clay

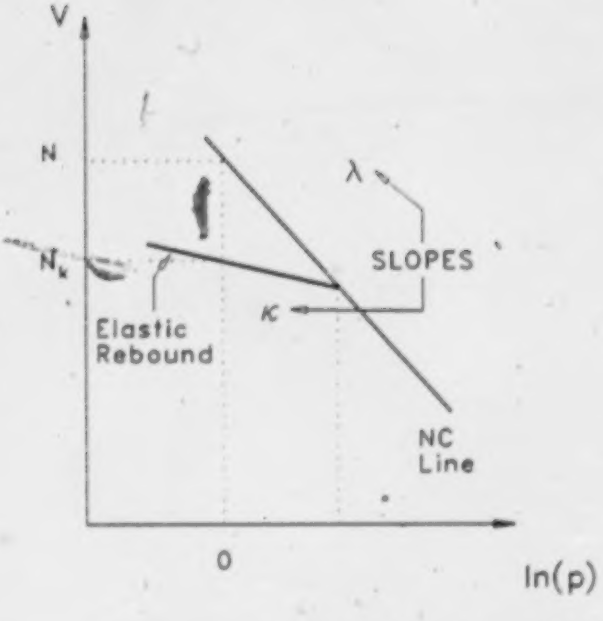
V
N
N_κ
λ
SLOPES
κ
Elastic
Rebound
NC
Line
0
ln(p)

Figure 2.3 Consolidation of Clay

$$\delta w_p = Mp\delta\epsilon_s \qquad [2.5]$$

where,

$\delta\epsilon_s$ is the shear strain.

POSTULATE

Positive work is done by an external agency during the application of a set of stresses:

$$d\sigma_{ij}d\epsilon_{ij} > 0 \qquad [2.6]$$

The net work performed by these stresses over the application and removal of load is either positive or zero:

$$d\sigma_{ij}d\epsilon_{ij}^{p} \geq 0 \qquad [2.7]$$

These are sufficient conditions for the stability of the material and the uniqueness of a solution.

POSTULATE

An existence of a yield surface is assumed.

Using the above concepts, a yield locus can be derived for the Cam-Clay model and can be expressed mathematically as:

$$\frac{q}{p} = M\ln\left[\frac{p_0}{p}\right] \qquad [2.8]$$

where, p_0 is the p value corresponding to the preconsolidated state. The rebound curve which is given by Equation 2.3 is considered to be the projection of the yield curve on (p,V) plane. Therefore, it is possible to obtain a surface which embraces all possible yield curves. This surface can be expressed mathematically in the following manner:

$$\frac{q}{Mp} = [N - V - \lambda \ln(p)]\frac{1}{\lambda - \kappa} \qquad [2.9]$$

Since none of the state points can cross the yield curves, all state points lie on or below this surface. Consequently, it is called the state boundary surface and is shown in Figure 2.4 in (p,V,q) space.

According to Cam-Clay theory, $d\epsilon_v^p/d\epsilon_s=(M-\eta)$, where, $\eta=q/p$. Therefore, for hydrostatic loading, $d\epsilon_v^p$ must be 0. However, the observations of soil consolidation used in the Cam-Clay model clearly show that there is considerable plastic volume change under hydrostatic loading. At the time the model was developed, this inconsistency was successfully explained by both mathematical and physical reasoning. It was pointed out that the energy dissipation takes place due to local plastic shear distortions and under the hydrostatic loading, the local shears are nullified due to the complete randomness of their directions. Therefore, under hydrostatic conditions, $d\epsilon_v^p/d\epsilon_s=(M-\eta)$ is applicable only on a microscopic level and not globally. On the other hand, mathematically, the hydrostatic stress state represents a cusp which is a singularity in the yield curve (Figure 2.4). Therefore, $d\epsilon_v^p/d\epsilon_s=(M-\eta)$ need not necessarily be applicable to the hydrostatic state.

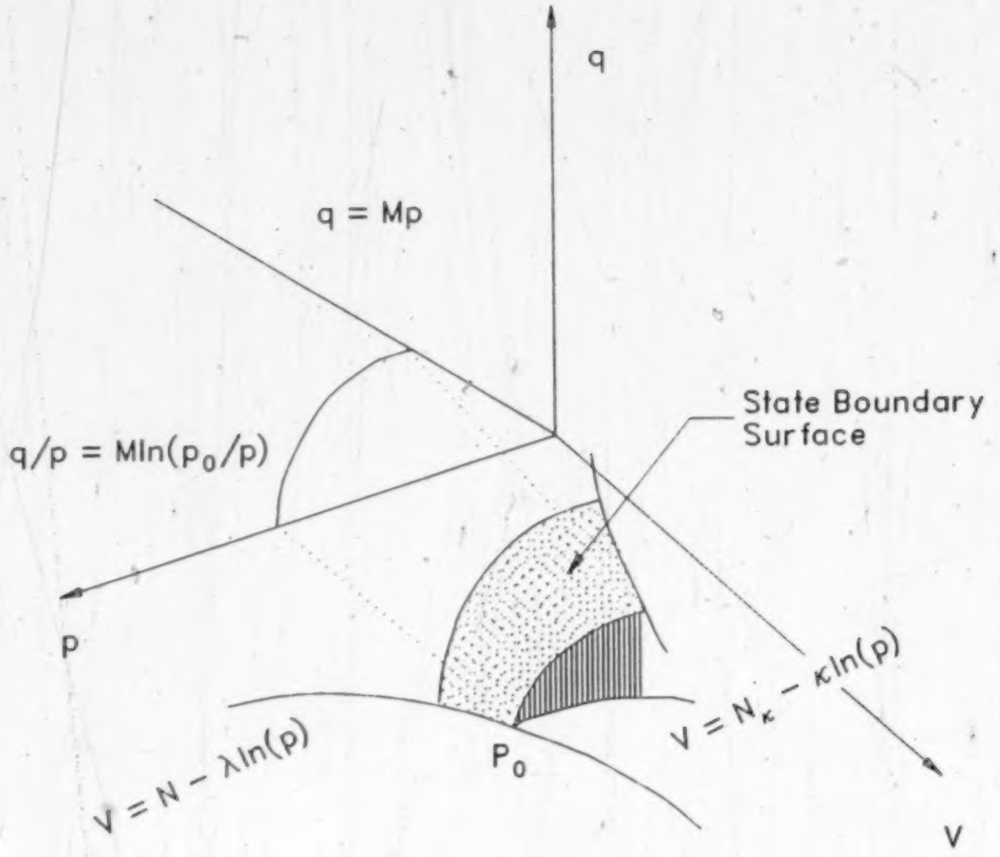
q
q = Mp
State Boundary Surface
$q/p = M\ln(p_0/p)$
p
$V = N_\kappa - \kappa\ln(p)$
$V = N - \lambda\ln(p)$
P_0
V

Figure 2.4 State Boundary Surface; Cam Clay Model

The immediate question is, what this model, which is based on fundamentals of physics, can accomplish? It has the potential of describing almost all aspects of soil behaviour.

It can predict the:

undrained stress path

$$q/Mp = \frac{\lambda}{\lambda-\kappa}\ln(p_0/p) \qquad [2.10]$$

undrained strength

$$s_u/\sigma_c = M/2\ \exp(-\Lambda) \qquad [2.11]$$

where, $\Lambda = \frac{\lambda}{\lambda-\kappa}$ undrained stress-strain relations

$$q/Mp = 1 - \exp(-MV_0\epsilon/\kappa\Lambda) \qquad [2.12]$$

drained strength

$$q_f/\sigma_c = M/(1-M/3) \qquad [2.13]$$

drained stress-strain relations

$$d\epsilon_s^{d}/d\epsilon_s^{u} = \lambda(3 - 2M + 3\Lambda)/\kappa v_d(3 - \eta) \qquad [2.14]$$

coefficient of earth pressure at rest

$$K_0 = (6 - 2M + 3\Lambda)/(6 + 4M - 6\Lambda) \qquad [2.15]$$

and finally, the Cam-Clay model can also predict the relationship between C_c and plasticity index:

$$C_c = 1.34\ PI \qquad [2.16]$$

2.2.1.2 LADE'S MODEL

Following are the basic concepts involved in the development of the Lade's model. This constitutive model was originally developed for sand.

The failure criterion,

$$I_1^3 - K_1 I_3 = 0 \ (K_1 > 27) \qquad [2.17]$$

was found by curve fitting. I_1 and I_3 are the first and third invariants of the effective stress tensor. When an associated flow rule was assumed, using a yield surface of the form given in Equation 2.18, much higher rates of dilation than observed in laboratory tests were predicted.

$$f = I^3{}_1/I_3 - K = 0 \qquad [2.18]$$

Hence, a nonassociated flow rule that assumes a plastic potential of the form given in Equation 2.19 was used to obtain a better fit with the laboratory results.

$$g = I_1^3 - K_2 I_3 \qquad [2.19]$$

By curve fitting laboratory data to Equation 2.20, K_2 and A are evaluated.

$$K_2 = Af + 27(1 - A) \qquad [2.20]$$

The plastic work Equation 2.21 and the parameters a, d and f_t are also obtained by curve fitting from experimental data.

$$(f - f_t) = \frac{w_p}{a + dw_p} \qquad [2.21]$$

where,

w_p is the plastic work corresponding to f and

a is parameter dependent on the confining pressure.

The variation of "a" is fitted into an Equation of the form:

$$a = MP_a\left[\frac{\sigma_3}{P_a}\right]^l \qquad [2.22]$$

where, M and l are obtained using laboratory results and Equation (2.22) (i.e.curve fitting). It can be proved that for the above constitutive model, the plastic strain increments are given by:

$$d\epsilon_{ij}^{p} = \Delta\lambda \frac{\partial q}{\partial \sigma_{ij}} \qquad [2.23]$$

and

$$\Delta\lambda = \frac{dw_p}{3g} \qquad [2.24]$$

In contrast to the Cam-Clay model, Lade's model is fundamentally based on curve fitting. Moreover, unlike the Cam-Clay model, Lade's model is too complex to obtain closed form solutions.

2.2.1.3 DISCUSSION

When the Cam clay model was used to predict the clay behaviour for a simple stress path, predictions deviated significantly from the laboratory results (Figure 2.5). However, the predictions made for complex stress paths using Lade's model compared considerably better with the laboratory results (Figure 2.6). By this time, Cam-Clay developers had already proposed corrections (Burland, 1967) to their energy equation, but the energy equation was the basis of Cam-Clay theory. Before, this energy Equation had been strongly defended using micro structure and mathematical singularities. Burland (1967) proposed the Modified Cam-Clay theory with a new Energy Equation 2.25 to obtain a better correspondence (Figure 2.5) between model predictions and laboratory results.

$$dw_p = \left[(Mpd\epsilon_s)^2 + (pd\epsilon_v^p)^2 \right]^{\frac{1}{2}} \qquad [2.25]$$

It is clear that the energy Equation is an implicit way of incorporating curve fitting in the Cam-Clay theory. This proposition is further reinforced by the manner in which the Modified Cam-Clay model was revised. The Modified Cam-Clay theory was revised by introducing a set of horizontal yield curves to obtain a better tally of predictions with laboratory results (Figure 2.5). In conclusion, both the Cam-Clay and the Lade's constitutive models are different forms of curve fitting for laboratory data. In Cam-Clay model, the curve fitting nature is more implicit than in Lade's model. Generally, material models involve a combination of explicit and implicit curve fitting. This must be emphasized, because in Cam-Clay theory where curve fitting is implicit, the tendency is to consider the Energy Equation to be more fundamental than laboratory results. This appears to be the case when Wei (1981),

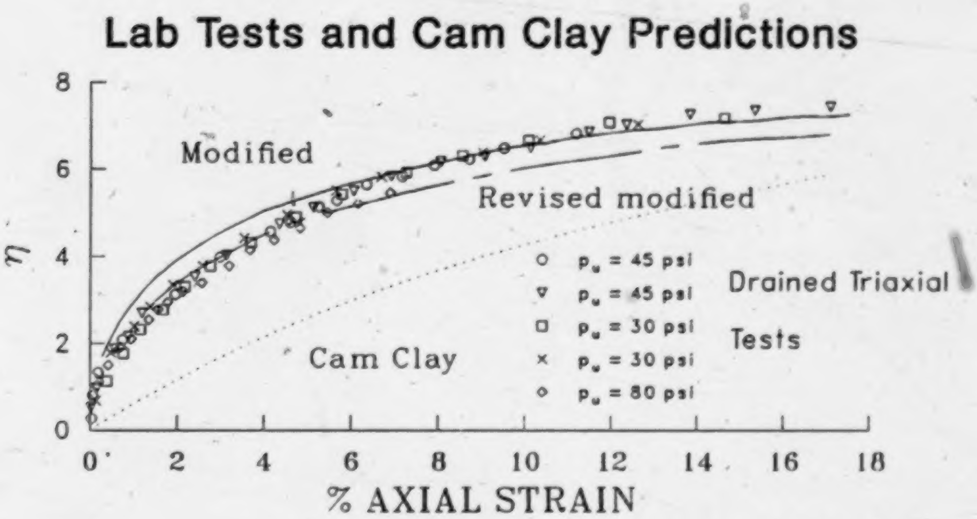

Figure 2.5 Laboratory Results and Cam Clay Predictions

(after Roscoe et al., 1968 : modified)

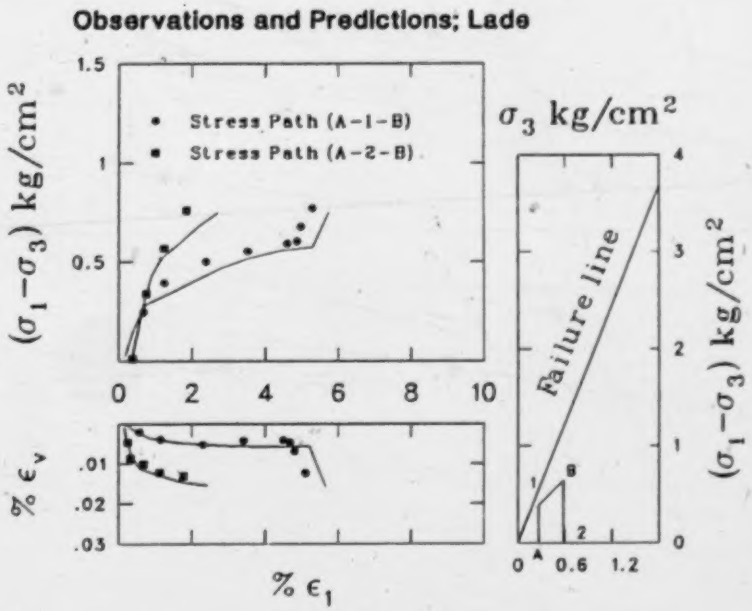

Figure 2.6 Lade's Model Predictions and Laboratory Results

(after Lade, 1975 : modified)

referring to the Cam Clay theory states: "The same expression of yield locus as that previously (Wei, 1964) obtained from test data is derived from the energy equation".

2.2.2 MODELS FOR PARAMETER GENERATION (LABORATORY AND FIELD)

As in conventional design, the determination of material parameters is an essential part of modern design. The laboratory determination of parameters involves three stages; sampling, testing and interpretation of the results. For the field tests however, sampling is not needed. The three stages of parameter determination involve different forms of modeling. Consider, for instance, the triaxial test (considered to be one of the most accurate and reliable tests). The undisturbed samples are brought to the laboratory, then trimmed and samples prepared for the test. Sometimes these samples are tested in different sizes in the triaxial apparatus. In interpreting the triaxial test results, a kinematic model of uniform displacements (hence uniform strain and void ratios) is assumed (Figure 2.13). This kinematic model together with a material model, is used to obtain soil parameters. Although it may not appear explicitly, for many reasons this approach fails to produce parameters that are representative of the field values.

2.2.2.1 SAMPLING

The geotechnical engineer faces a similar problem as the physicist working on particle physics does. The observed is "changed" by the very act of observation. In geotechnical engineering, the act of observation inevitably changes the stress state of the soil, if not the structure as well. This is true in both laboratory and field tests, but the soil properties are stress dependent. Geotechnical engineers realized these facts and they have been using correction factors (e.g. Schmertmann, 1953) for many years. Added to this problem is the sampler-dependent nature of the soil properties. Figure 2.7 shows the stress-strain curves obtained using the same test, on the same material, employing different sampling techniques. The strength difference is up to 300%, whereas the modulus difference is up to 500% for the different sampling techniques.

2.2.2.2 TESTING

In testing soil samples, preparation and mounting are also very important. Depending on the type of soil and the degree of disturbance the sample experiences, the disturbance can have a significant influence on the laboratory parameters. In addition, the tests themselves are generally not capable of producing true soil parameters. Specific examples are given in the paragraphs to follow.

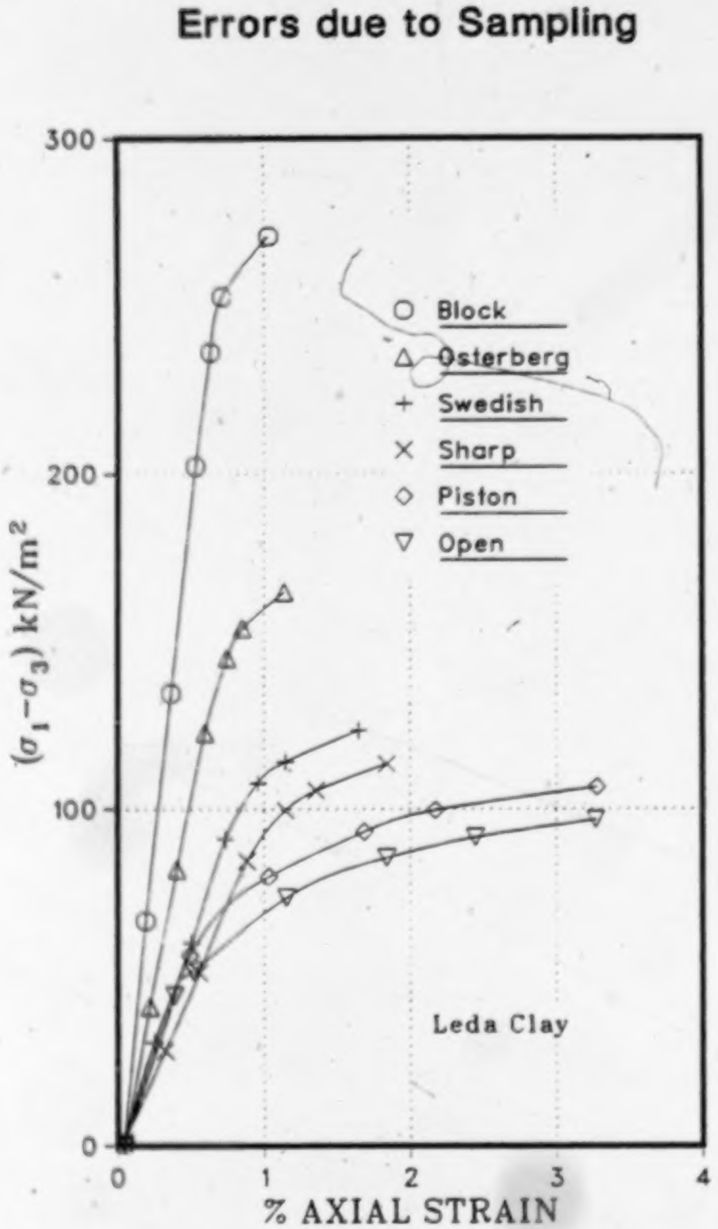

Figure 2.7 Influence of Sampling Technique on Unconfined Compression Test Results

(after Raymond et al., 1971 : modified)

Figure 2.8 shows the difference in triaxial stress-strain curves obtained with lubricated and nonlubricated normal caps. The test results with normal caps yield strengths of about 10% higher than the lubricated caps.

The influence of membrane penetration on the pore pressure generated during a consolidated undrained triaxial test is shown in Figure 2.9. In the preceding undrained test, the rubberized membrane gives up to about 50% higher pore pressure values than the standard normal membrane. The rubber coating was only 0.5 mm thick and its effects were considered to be negligible.

Figure 2.10 shows the influence of system compliance on the stress ratio to cause liquifaction in a cyclic simple shear test. The errors can be up to 150%, depending on the compliance of the system.

The undrained stress-strain curves obtained from a triaxial test depend on the strain rate. Figure 2.11 shows the influence of the strain rate on the stress-strain behaviour of a clay. The strain rates were constant and the pore water pressure equalization was monitored and checked. The strength difference is up to 30% and the modulus difference is up to 200% for different strain rates.

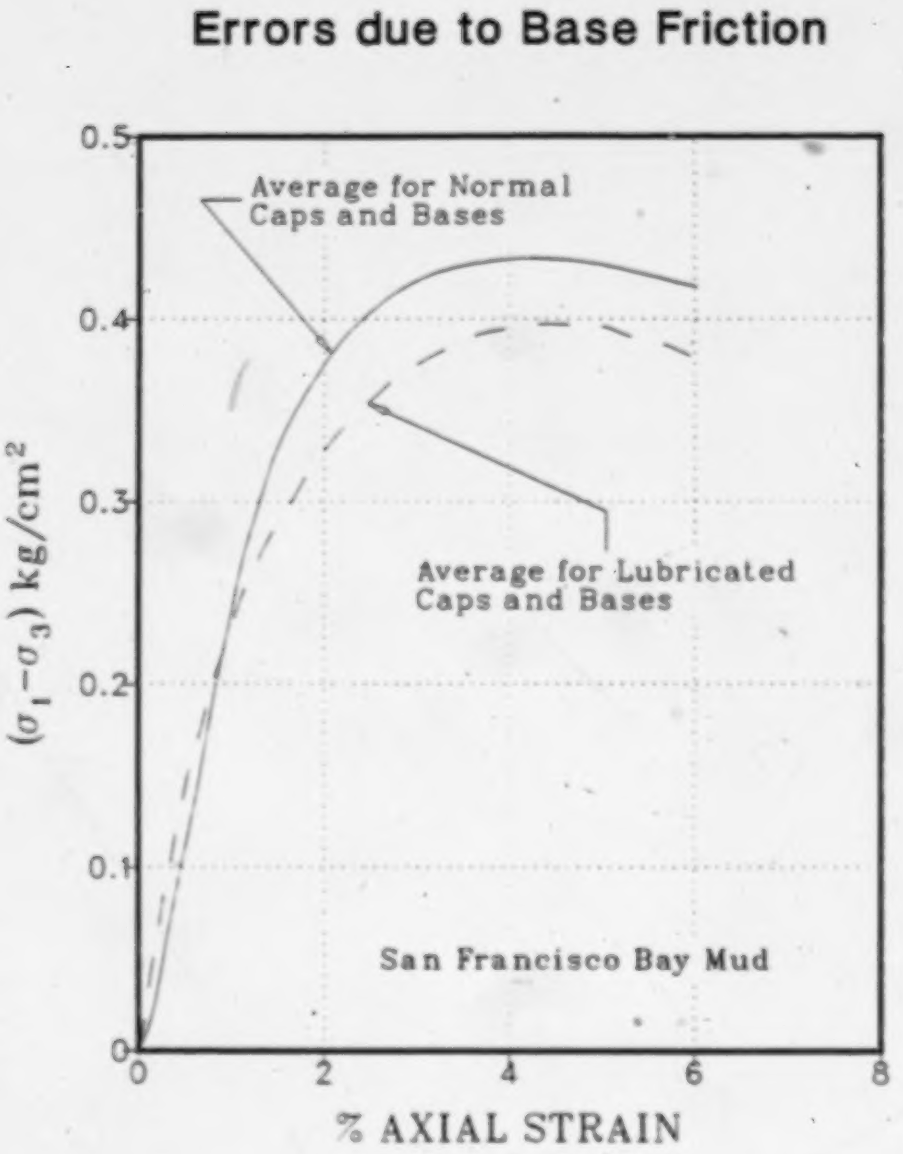

Figure 2.8 Influence of Base Friction on UU Test Results

(after Duncan et al., 1968 : modified)

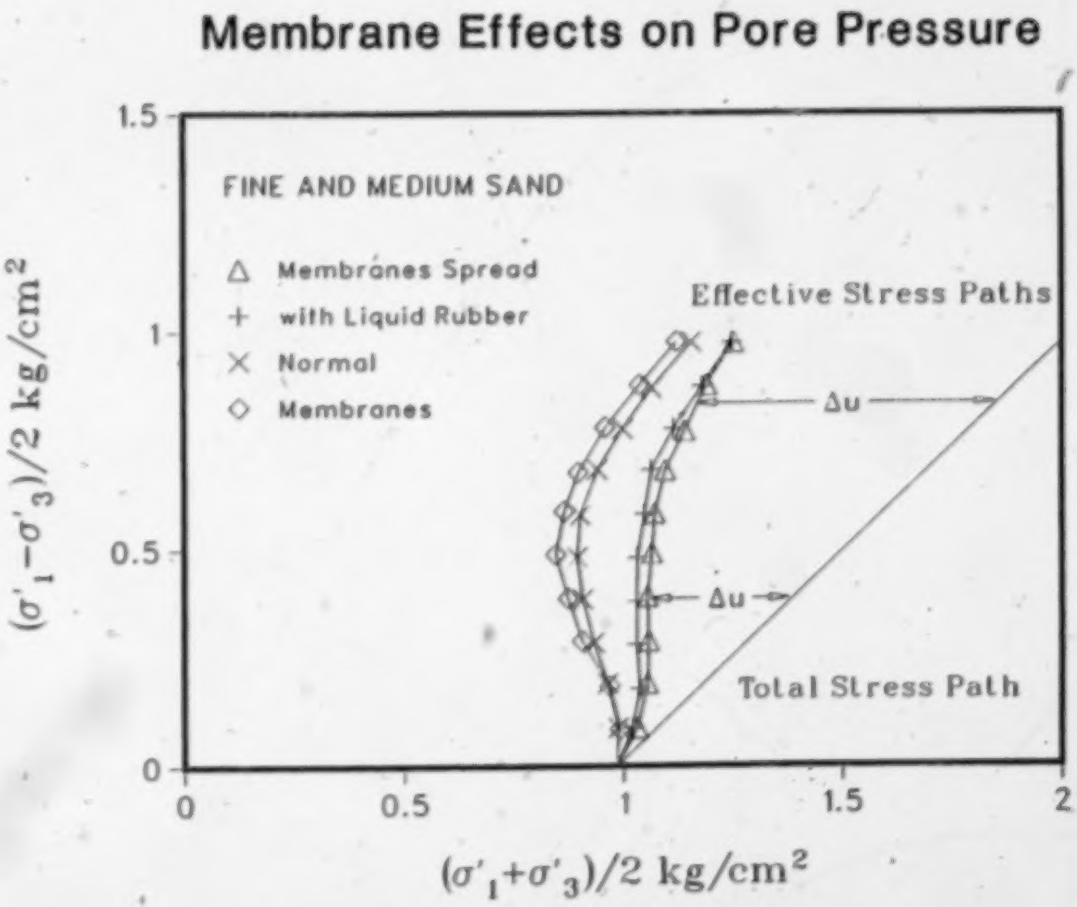

Figure 2.9 The Effects of Membrane on Pore Pressure in CU Triaxial Tests (after Kiekbusch et al., 1977 : modified)

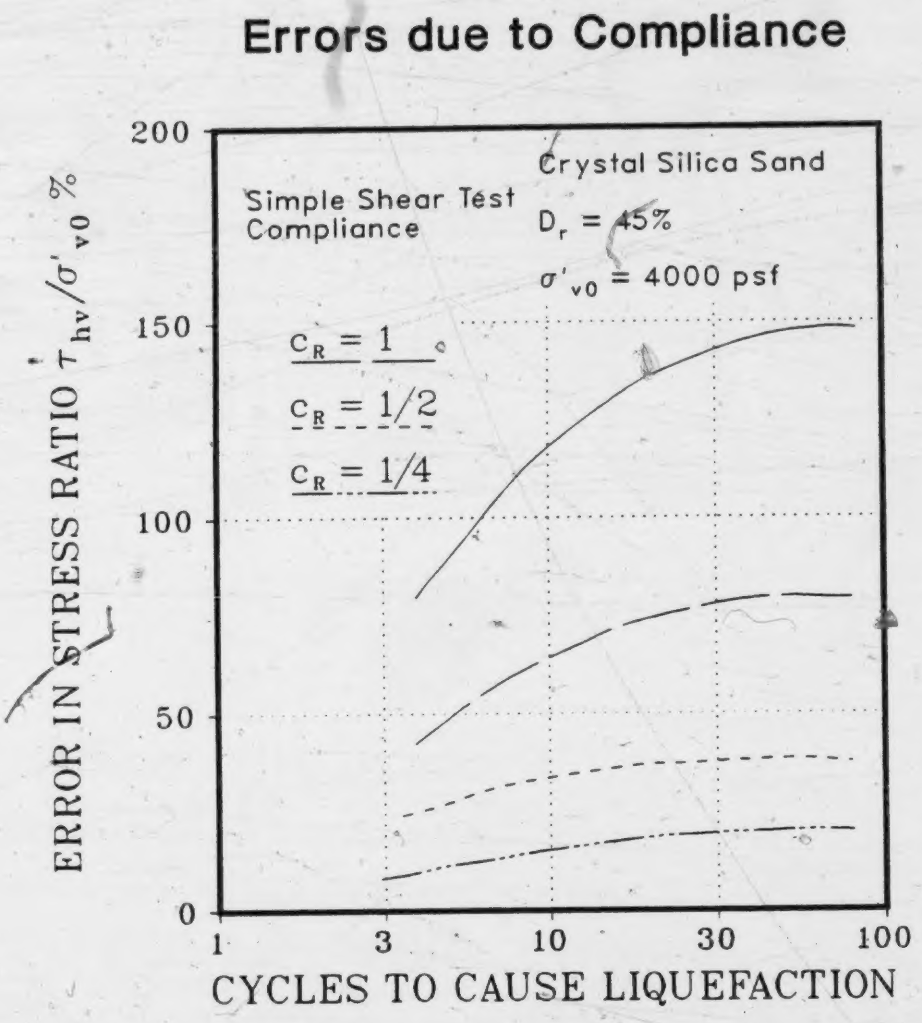

Figure 2.10 Influence of System Compliance on Stress Ratios to cause Liquifaction

(after Martin et al., 1978 : modified)

Undrained Test and Strain Rate

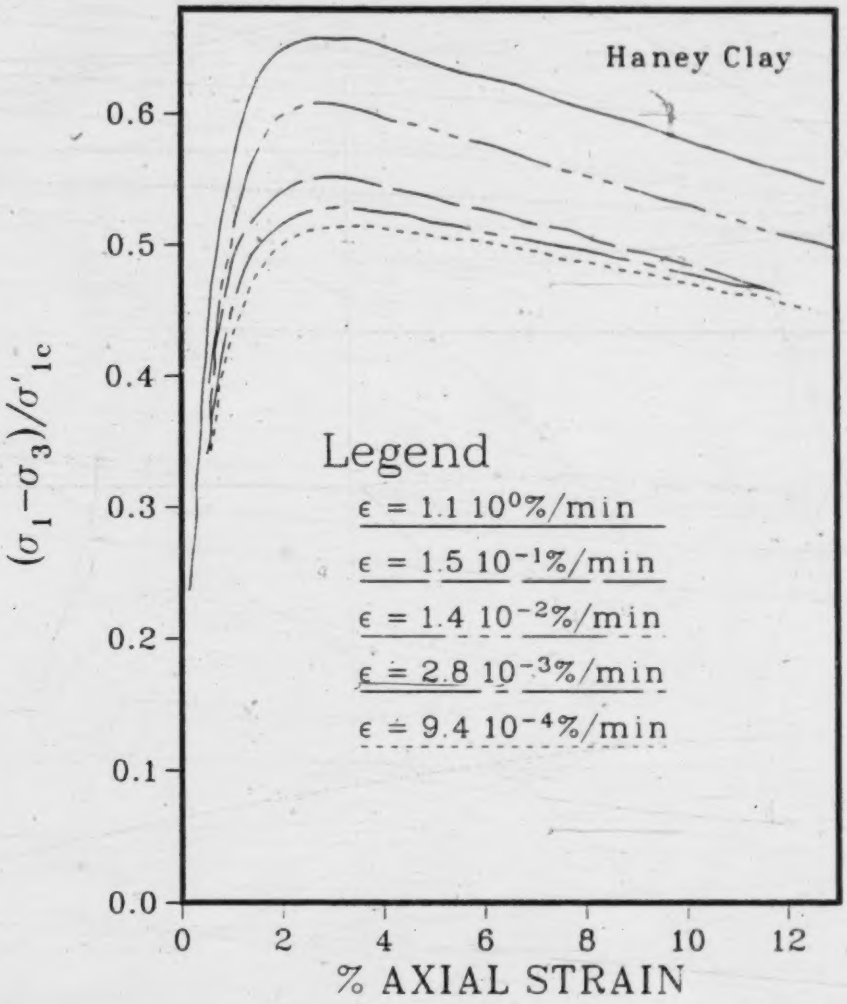

Figure 2.11 Influence of Strain Rate on Undrained Stress-Strain Behaviour in a Triaxial Test (after Vaid et al., 1974 : modified)

2.2.2.3 TYPE OF TEST

The results of semiconfined and unconfined tests are compared in Figure 2.12. These two tests appear to be different, but when the material and kinematic models used to interpret the results are considered, the two tests are identical. However, the strength values from the confined tests are about 10% higher than those obtained from the unconfined test.

2.2.2.4 INTERPRETATION OF RESULTS (using KINEMATIC and MATERIAL MODELS)

As stated previously, the kinematic models are used to interpret the laboratory results and hence obtain the soil parameters. These kinematic models have a significant influence on the parameters obtained and on the interpretation of soil behaviour or developing material models.

Again, the triaxial test is considered. Instead of using a kinematic model of uniform strains (conventional method; Figure 2.13) to interpret the test results, a non-uniform axial strain distribution is utilized. These strains are computed using the observations of displacements at different heights (P, Q, R, S and T in Figure 2.13) of the sample. The strain distributions of a typical extension test are shown in Figure 2.13. In computing the stress, the actual cross-sectional area of the element concerned is employed instead of the uniform cross-section assumed (Figure 2.13) in the conventional

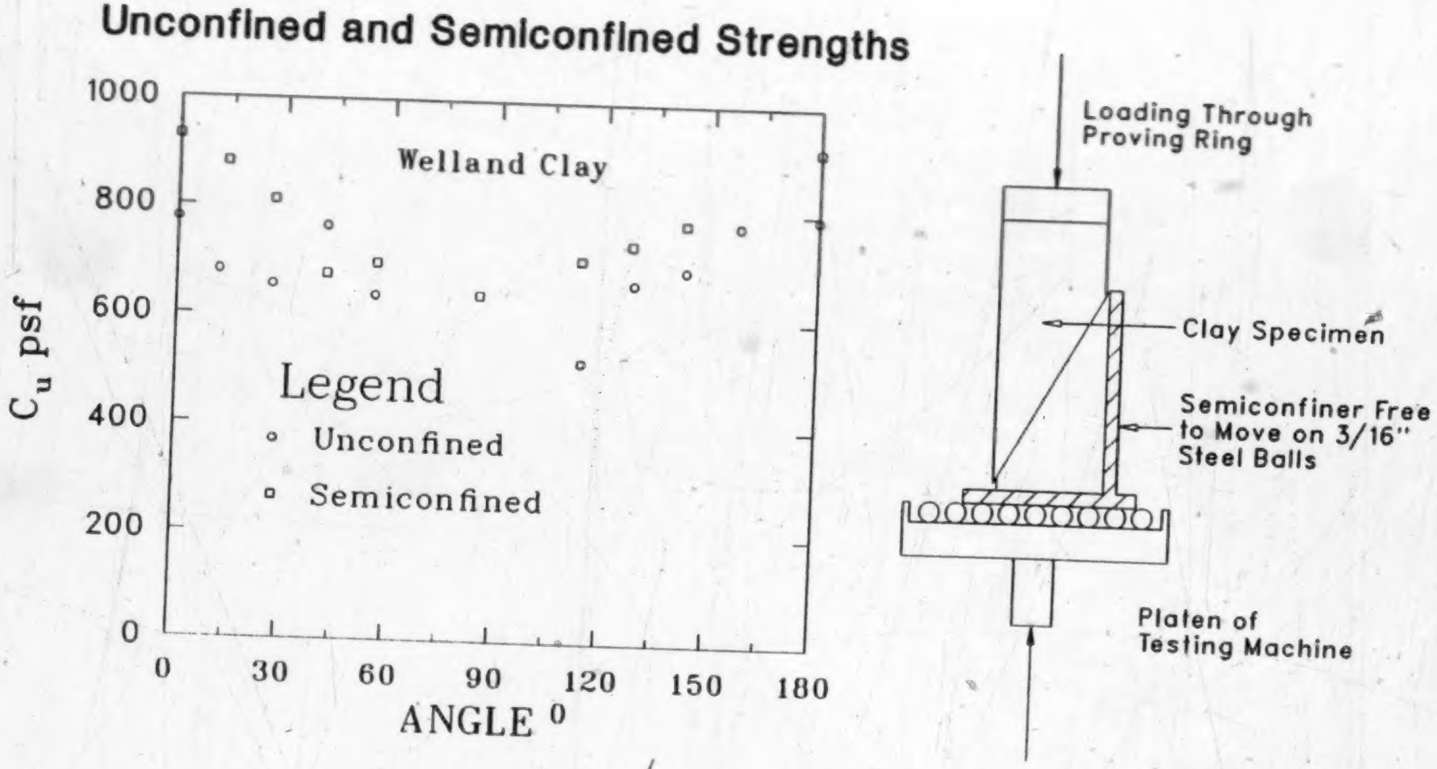

Figure 2.12 Comparison of Strength values from Unconfined and Semi-confined Tests (after DeLory et al., 1971 : modified)

method. The stress-strain curves obtained using this approach are shown in Figure 2.14 and compared with the stress-strain curve produced using the conventional method. The results of the two different interpretations give rise to two entirely different soil behaviours or material models and yield different soil parameters.

2.2.2.5 DISCUSSION

In the previous sections, the factors that may have an influence on the estimated value of the parameters of geotechnical engineering material were discussed. These observations raise the question of which soil test is "good" and produces the "right" parameter values? The answer is important especially when these parameters are used in sophisticated material and numerical models to make field predictions. The answer to the above question probably is: in many cases, using the existing soil tests, it may not be possible to obtain the "right" soil parameters that can make accurate predictions. This fact has been recognized for many years. Ladd (1974) made the statement: "The reason that the present method generally works is that the variations frequently tend to be self compensating." He refers to the variation of a parameter value due to such factors as those pointed out in the above sections. Further, the factor of safety used in geotechnical engineering, to a certain extent accounts for the past experience in a quantitative manner, thereby contributing to the success of design. However,

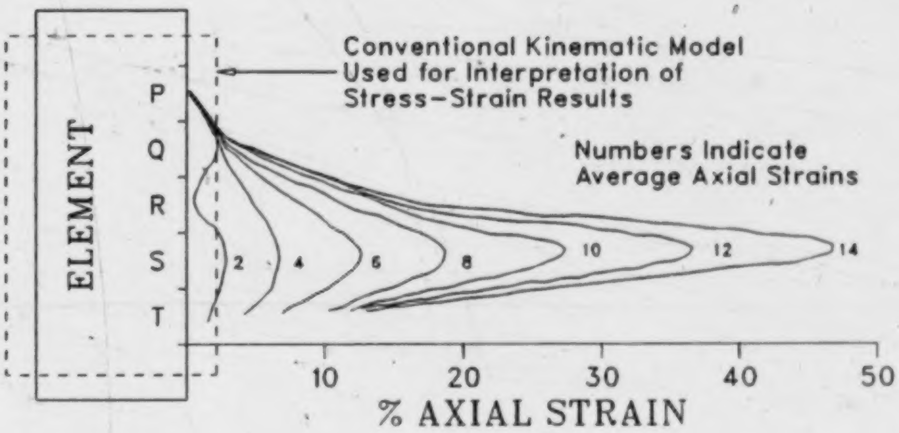

Figure 2.13 Kinematic Models for Interpreting Triaxial Results

(after Roscoe et al., 1963 : modified)

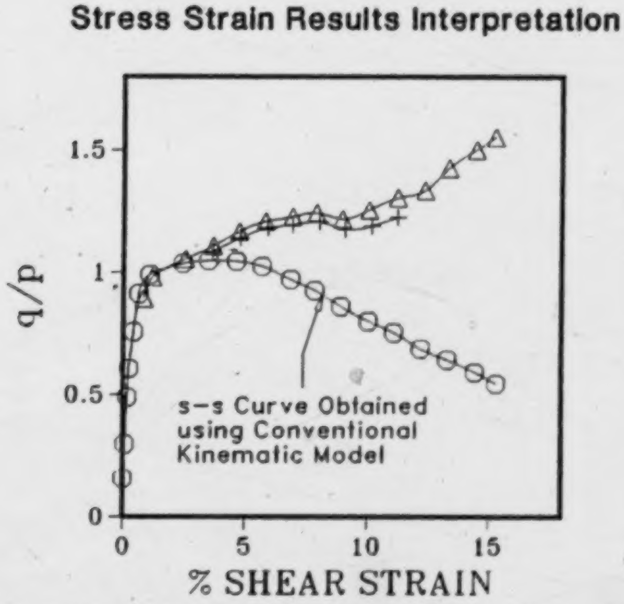

Figure 2.14 Triaxial Stress Strain Behaviour Interpreted using Different Kinematic Models

(after Roscoe et al., 1963 : modified)

a soil test that provides consistent measures of the in situ material properties may be considered a "good" test. In fact, there are many "good" soil tests used in geotechnical engineering practice. This idea is incorporated in the new design approach (SOM) proposed in section 2.3. The preceding observations made for the laboratory tests are also true in principle for the field tests.

2.2.3 NUMERICAL MODELS

It is often not possible to obtain closed form solutions for realistically idealized geotechnical engineering problems. Therefore, numerical methods are the only option available to the design engineer. With the advent of high speed computers and the development of efficient solution techniques, numerical methods are gaining popularity. Numerical methods in general, rapidly produce approximate (as opposed to closed form) solutions. These numerical methods essentially convert a continuum model, which constitutes an infinite number of material points, into a finite number of discrete domains or points. Continuum models are mathematically described either by a variational or a differential mathematical model. Solutions for the discrete models are obtained by appropriately selecting either a finite difference or a piecewise trial function approximation.

The numerical models form an essential part of the modern geotechnical engineering design. The most popular trial function approximation method used in geotechnical engineering is the finite element technique. Hence, the discussion of numerical models will focus on finite element techniques, although the points discussed are relevant in principle to any other numerical technique. In geotechnical engineering design, the finite element models include the finite element formulation (e.g. displacement formulation using constant strain triangles), the mesh pattern (including the boundary), solution technique and the idealized construction sequence. The solution depends to a greater or lesser extent on these factors. In order to have confidence in the results of a finite element analysis, the influence of all the preceding factors must be clearly understood. These factors will be discussed in the following section.

2.2.3.1 FINITE ELEMENT FORMULATION

In addition to many types of finite element formulations, there are different finite element types. Examples of some of the different quadrilateral elements are shown in Figure 2.15. Certain types of formulations and elements are known to be better suited for solving certain types of problems (Kulhawy, 1974). For the elastic case, the performance of the elements are assessed by comparing the rate of convergence using strain energy. The strain energies computed for the

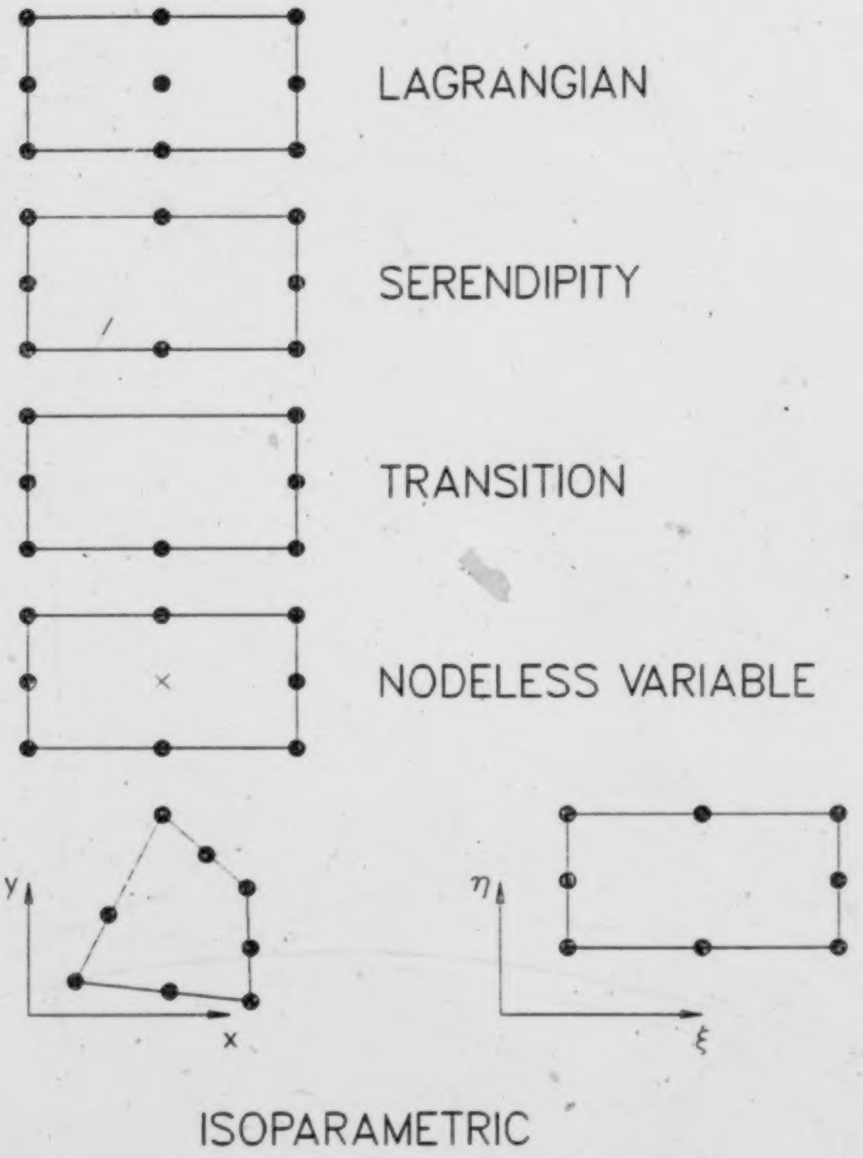
LAGRANGIAN
SERENDIPITY
TRANSITION
NODELESS VARIABLE
y
x
η
ξ
ISOPARAMETRIC

Figure 2.15 Different Quadrilateral Finite Elements

classic problem of a hole in a plate using different types of elements are shown in Figure 2.16. The implications of the strain energy difference are discussed in section 2.2.3.2.

The order of integration used in the element can also have an influence on the finite element solution. Figure 2.17 shows the solutions obtained for the same problem using the same finite element type, but with different orders of integration. Although 3×3 Gauss quadrature integrates the energy Equation exactly, the reduced integration yields better results. Investigation of the type of elements and the number of Gauss points that produce best results is in itself a research problem, and that topic will not be discussed any further in this thesis.

Once the finite element formulation is selected, including the finite element type and order of Gauss quadrature, the choice of mesh becomes the most important item in the subsequent finite element analysis. In the next section, the selection of a finite element mesh will be discussed in detail.

2.2.3.2 FINITE ELEMENT MESH

Having chosen the finite element type and having properly idealized the boundaries, the design engineer selects a mesh pattern for the solution of the problem. The results of a finite element analysis are dependent to a lesser or greater degree on the mesh selected.

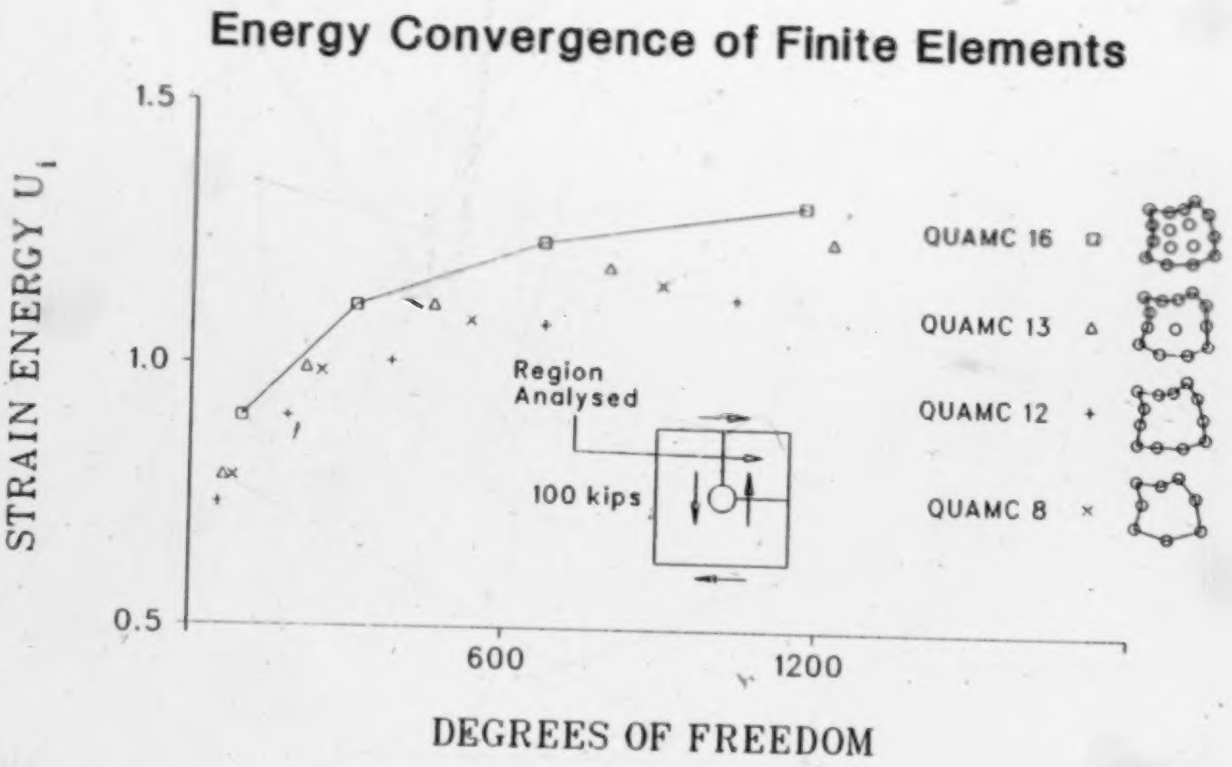

Figure 2.16 Strain Energies of Lagrangian and Serendipity Elements for same Degrees of Freedom

(after Argyris et al., 1973 : modified)

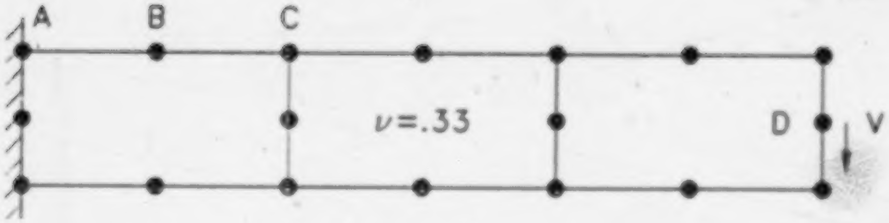

ORDER OF GAUSSIAN INTEGRATION	σ_x at			V at
	A	B	C	D
3×3	105.5	90.0	74.5	-.5084
2×2	108.0	90.0	72.0	-.5114
EXACT	108.0	90.0	72.0	-.5299

Figure 2.17 The Influence of the Order of Quadrature on Finite Element Results

(after Zienkiewicz, 1977, : modified)

Although the selection of mesh is one of the most important steps in a finite element analysis, often the importance is overlooked, or dealt with only arbitrarily. To obtain reliable and accurate results, it is essential that the selected mesh accurately represents the real problem as far as the boundaries, mesh pattern, number of elements and the type of elements are concerned. Usually, the mesh pattern selection is based on intuition and engineering judgement, or the work of other analysts. However, caution must be exercised in the utilization of previous applications; one should understand fully the previous investigator's selection criteria, and most important, must understand how well one's problem relates to the previous investigator's problem. For instance, a finite element mesh that produces accurate results for stresses may not necessarily yield equally accurate results for displacements.

In practice, once a mesh is selected, it is taken for granted that it produces accurate and reliable results. Figure 2.20 shows a typical mesh that was selected for the solution of the problem shown in Figure 2.19. However, when the grid shown in Figure 2.21 was used with the same number of nodes and elements, the computed stress at the center improved by about 70%. For this reason it is very important to have a rational procedure for generating grids that produce accurate and reliable results. The following sections discuss these aspects of the finite element mesh in detail.

2.2.3.3 IMPROVING THE MESH

Basically there are two independent methods of improving a finite element mesh. (i) Refine the mesh, or (ii) Modify the mesh. However, one can use the above two methods in combination to improve the mesh more efficiently.

(i) REFINING

The general refinement includes an existing mesh being modified and refined using certain criteria to get more accurate results. If properly done, this is a very involved and time consuming procedure. On the other hand, one can use a method termed selective refinement where one refines only the parts that are deemed necessary. The procedure must ensure that the elements are not overly elongated. Figure 2.18 shows the standard procedure of such a refinement used for both quadrilateral and triangular elements. In this procedure a single element is refined into four new elements. Although this method appears much simpler and easier than the general refinement, it has some limitations and disadvantages. For instance, one may have to constrain the degrees of freedom at node six with respect to one and three. This can be achieved either by global restraint equations or by the use of transition elements. The use of elements of hierarchical nature (nodal variables for an element of order n constitute a subset of nodal variables for an element of order n+1) may also overcome the problem. There are major disadvantages in this refining procedure. The new mesh is completely dependent on the initial mesh. Only some parts are refined, but the others remain unaltered. This refining procedure is less flexible.

(i) MODIFYING

To obtain more accurate results, the modification of the mesh can be achieved by two methods. The first is the so-called real finite element method and the second is the contouring method.

(a) REAL FINITE ELEMENT ANALYSIS

Consider the variational approach of finite element stress analysis that uses potential energy. In reality, both the nodal displacements and the nodal coordinates are variables. Therefore, in a real minimum value problem, the potential energy has to be minimized with respect to the nodal displacements as well as nodal coordinates. This approach is referred to as a real finite element analysis. The following Equations briefly describe the theory (see Appendix A for details).

$$K_{ij}r_j - R_i = 0 \quad i = 1, n \qquad [2.26]$$

and

$$\frac{1}{2} \langle r \rangle \frac{\partial [K]}{\partial x_j} \{r\} - \frac{\partial \langle R \rangle}{\partial x_j} \{r\} = 0 \quad j = 1, n \qquad [2.27]$$

where,

K_{ij} is the stiffness matrix,

n is the number of degrees of freedom,

r_j nodal displacement vector,

R_i is nodal load vector,

$[K] = K_{ij}$,

$\{r\} = r_j$,

$\langle R \rangle = R_i$ and

x_j's are the nodal coordinates.

In order to apply this theory, the analysis must start with an initial grid and subsequently, the nodal coordinates must be updated until sufficient modification is obtained. For the simple problem shown in Figure 2.19 with the initial grid shown in Figure 2.20, the theory was applied manually by McNeice et al., (1973). Only a certain number of nodes were moved at a time to keep the computational procedure less cumbersome. For example, the node six was kept fixed throughout the entire procedure. After seven iterations, the optimized mesh shown in Figure 2.21 was obtained. In this approach, the nodal coordinates have to be constrained so that the domain boundaries remain intact and the element aspect ratios lie within desired limits. In addition to the system of equations being nonlinear, the investigators have found that these constraints can add severe nonlinearities and also can overconstrain the

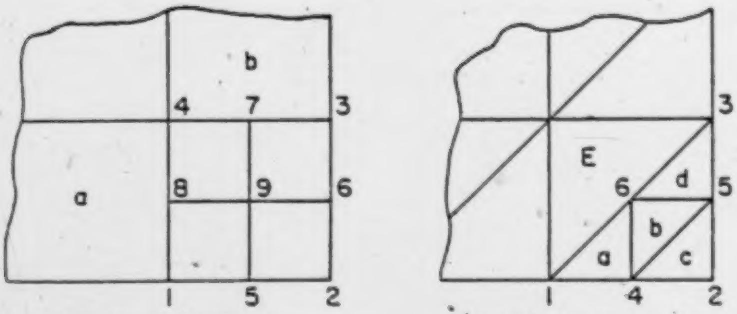
b
4
7
3
a
8
9
6
1
5
2
3
E
6
d
5
b
a
c
1
4
2

a) Scheme for Quadrilateral Elements

b) Scheme for Triangular Elements

Figure 2.18 Selective Refinement of Quadrilateral and Triangular Elements

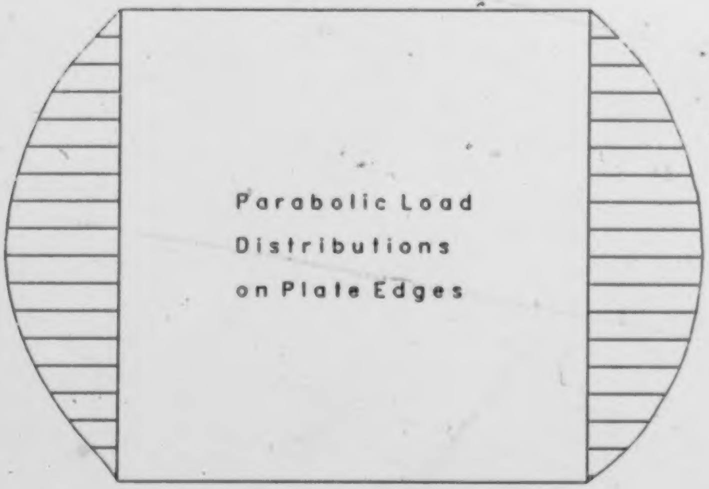
Parabolic Load
Distributions
on Plate Edges

Figure 2.19 Parabolic Tensile Stress on a Plate

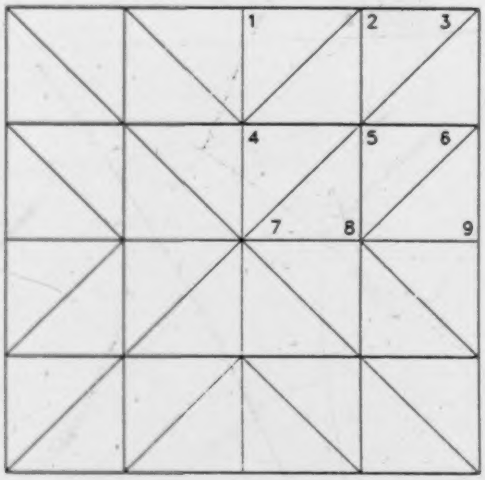

Figure 2.20 A Typical Finite Element Mesh
(after McNeice et al., 1973 : modified)

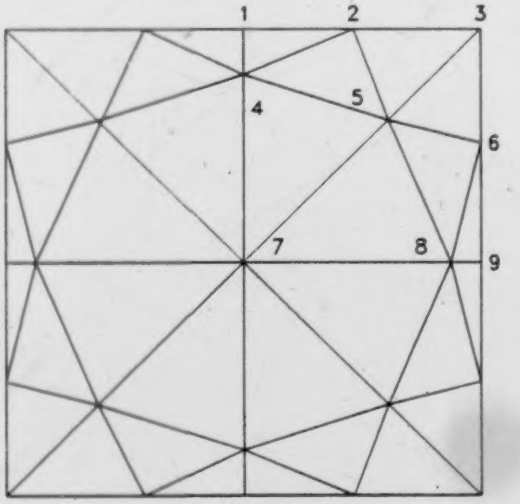

Figure 2.21 Optimum Mesh after Seven Iterations
(after McNeice et al., 1973 : modified)

problem. The solution should be a numerical optimization procedure. Theoretically, by this method it is possible to obtain the best finite element mesh for any given problem with a given number of degrees of freedom. However, Shephard (1979) concluded that even numerical optimization procedures can be unreliable for the severe nonlinearities faced with the solution of such equations. Shephard (1979) also concluded that with all possible efficiency incorporated, optimization procedures are very expensive and unlikely to be proven profitable.

(b) CONTOURING METHOD

In this approach, a set of contours of a selected quantity drawn using an initial trial grid is used as a guideline for the next modification of the mesh. For instance, displacement contours may be used as a guideline to generate an efficient finite element mesh. Isoenergetics, contours of constant strain energy density, have been found to work for stress analysis. Figure 2.23 shows the improved mesh with 27 dof (degrees of freedom) obtained by Shephard et al. (1979) using the isoenergetics of a pinched roller problem shown in Figure 2.22. However, this approach has problems and limitations. For example, Figure 2.24 shows the improved grid obtained by Turcke et al. (1974) using isoenergetics with 25 dof for the same problem. A

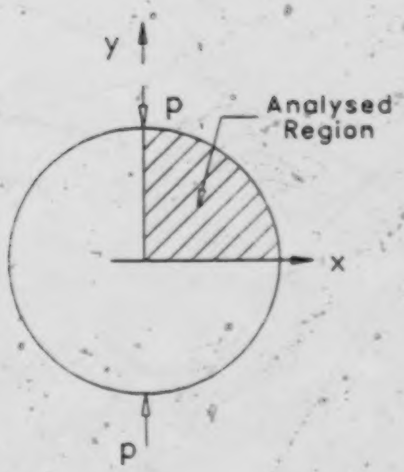
y
p
Analysed Region
x
p

Figure 2.22 Pinched Roller

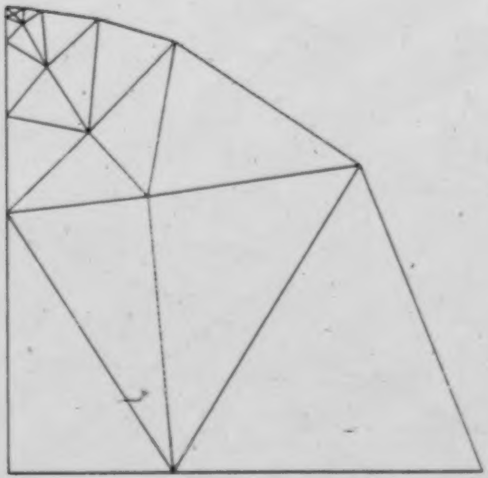

Figure 2.23 Grid Using Isoenergetics, 27 dof

(after Shephard et al., 1979 : modified) significant difference between the two meshes can be observed, although the degrees of freedom are nearly the same. Moreover, when the finite element formulation is not a variational formulation of potential energy in an elastic medium, the applicability of isoenergetics for efficient mesh generation is questionable. That is, isoenergetics may not be the exclusive contouring method of improved grid generation. The mesh patterns of optimized grids appeared to be very similar to the meshes generated (Turcke, 1979) using isostatics, the principal stress trajectories. This seems to overcome the theoretical limitation of the capability of isoenergetics to generate improved meshes. Turcke (op. cit.) found that the meshes generated using isostatics resulted in considerable efficiency. For example, Figure 2.25 shows the grid with 24 dof obtained by Turcke (op. cit.) using isostatics for the pinched roller problem shown in Figure 2.22. The strain energy content of this grid (24 dof) is 40% higher than the initial grid with nearly the same dof (23) arbitrarily chosen (Figure 2.26) and 10% higher than the arbitrarily refined grid (Figure 2.27) having 50% more degrees of freedom (37). Note that McNeice et al. (1973) showed that a 1.48% increase in strain energy may improve the stresses up to about 70%. The use of isostatics in generating efficient mesh patterns is found to be most effective where there are high concentrations of isostatics (Turcke, 1979). In

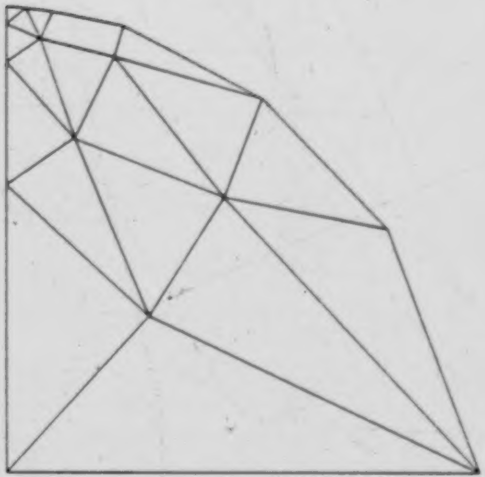

Figure 2.24 Grid Using Isoenergetics, 25 dof

(after Turcke et al., 1974 : modified)

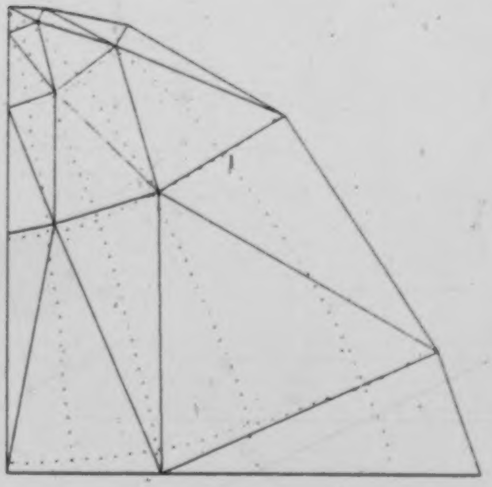

Figure 2.25 Grid Using Isostatics, 24 dof

(after Turcke, 1979 : modified)

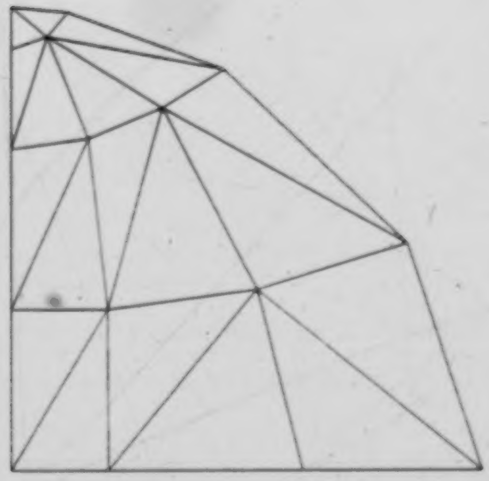

Figure 2.26 Initial mesh, 23 dof

(after Turcke, 1979 : modified)

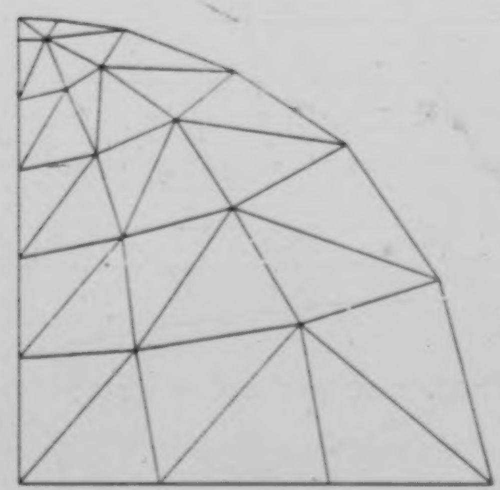

Figure 2.27 Arbitrarily Refined Grid, 37 dof

(after Turcke, 1979 : modified)

general, one can observe certain similarities of contours of displacements, isobars, isochromatics, isostatics and isoenergetics (Turcke et al., 1974). In most cases, in order to obtain exact contours, the accurate solution of the problem is not known initially. Usually, the contours are generated using an initial trial mesh and these contours are used to obtain a more efficient mesh. For these reasons, it is more logical not to spend too much effort and resources in generating a mesh that accurately conforms to a specific guideline. Therefore, while using the above concepts as approximate guidelines, one must use engineering judgement in modifying a mesh, especially when the resulting contour pattern is complex.

This method of mesh improvement is more involved and time consuming compared to selective refinement because the entire mesh must be re-established. The main advantage of this method is that the new mesh is completely independent of the previous mesh, as opposed to the case of selective refinement where the current mesh is completely dependent on the previous grid.

2.2.3.4 SELECTION OF THE BOUNDARY

Depending on the complexity of the geotechnical engineering problem, the idealization of the boundaries itself may be a difficult problem. For instance, when the problem involves semi-infinite boundaries, the selection of the outer boundary essentially becomes an additional problem. One simple and less rigorous solution to this problem is to expand the boundary until the new solution does not change beyond a tolerable limit from the immediately previous solution (Kulhawy, 1974). That is, if the changes of the quantity under consideration do not exceed a predetermined tolerable limit, the selected boundary can be considered to be adequate. It can be clearly seen that this procedure of determining the adequacy of the selected boundary lacks mathematical rigour. However, this is the standard procedure adopted in many numerical techniques to check convergence. Figure 2.28 compares the typical results of a finite element analysis for a semi-infinite problem with its closed form solution. At the center, the finite element settlements are about 20% less than that of the closed form values.

Most finite element methods used in geotechnical engineering incorporate 2-D analysis, but real field situations in general are 3-D. However, the 2-D solutions represent a measure of real 3-D behaviour.

2.2.3.5 INITIAL STRESS STATE, CONSTRUCTION SEQUENCE AND SOLUTION TECHNIQUES

As stated earlier, the constitutive properties of soil are stress dependent, therefore, the final solution of a geotechnical engineering problem depends on the initial stress state used in the analysis. There are two popular methods of determining the initial stress state.

In one approach, the vertical stress, σ_v, is considered to be equal to γz, where z is the depth of the point below the ground surface, and γ is the unit weight of the soil. σ_h is evaluated using an estimate of K_0 obtained from laboratory or field tests, or engineering judgement. The second method is to use a finite element analysis to obtain the initial stresses. For example, in a method known as 'switch-on gravity', the gravity is simulated by applying equivalent gravity loads to the stress free elements using a finite element method. Generally these methods yield different initial stress values, and a difference in the initial stress state usually results in a difference in the final solutions of the finite element analyses.

The other important aspect in the solution of geotechnical engineering problems using finite elements is the simulation of construction sequence. There are two popular methods of idealizing the construction sequence:

(i) the application of load on the final configuration; and

(ii) the change of configuration as construction proceeds.

These two methods may produce different results for the same problem.

Finally, the solution technique employed for the solution of equations may also influence the results.

Some of the solution techniques used with the finite element method are discussed in section 3.5.3.

2.2.3.6 DISCUSSION

As discussed in the preceding sections, a given problem can be solved using a variety of finite element models, which may yield different solutions. However, each model can be expected to produce a consistent measure of the idealized continuum behaviour.

2.3 SOLUTION ORIENTED MODELS(SOM)

Using the detailed discussions made on basic elements of geotechnical engineering design, the following observations may be made.

Modern geotechnical engineering design consists of a chain of models (Figure 2.1). Generally, each link in this chain, when considered as an independent entity produces accurate results. However, as stated earlier, when these links form a chain representing the design process of a field situation, they tend not to make correspondingly accurate predictions. Further, it may be concluded that:

(i) material/constitutive models are curve fitting for laboratory data;

(ii) parameters obtained using laboratory and field tests are at best only a consistent measure of the real properties; and

(iii) numerical models also generally represent a consistent measure of the continuum model.

Furthermore, the continuum model represents only a consistent measure of the real soil behaviour.

These observations raise the question of what can be done under these circumstances to make accurate predictions. As previously mentioned, each link in the design chain represents either a measure of the real soil behaviour or a form of curve fitting to laboratory/field data. Therefore, the logical answer to the question raised earlier is that the curve fitting process must be extended to the entire chain of models taken as a unit. This must be done on a problem to problem basis. The chain of models taken as a single entity is called a Solution Oriented Model(SOM), and accordingly, this new design approach is called the SOM method.

This approach appears similar to the "calibration" and "back analysis" procedures or the methods used to make "class C predictions" in geotechnical engineering. The basic philosophies of the proposed approach and the others mentioned above are fundamentally different. Gioda et al. (1981), Gioda (1985) and Ledesma et al. (1986) cite examples where rigorous theories of optimization and system engineering have been employed for the purpose of "back analysis" and "calibration", although the material models used in many of these cases are over-simplifications. However, the proposed method can accommodate more realistic material models.

The basic concepts of the SOM approach are given below, and are illustrated schematically in Figure 2.29.

In making field predictions the SOM employs a series of models that use a set of parameters, or more precisely, measures of parameters $\phi_1, .. \phi_k, .. \phi_m$. It is known that the predictions are a function of $\phi_1, \phi_2 ...... \phi_m$ which can be expressed mathematically in the form:

$$\text{PREDICTIONS} = \text{SOM}\left[\phi_1, .. \phi_k, .. \phi_m\right] \qquad [2.28]$$

In the SOM approach, it is postulated that,

$$\text{OBSERVATIONS} = \text{SOM}\left[\lambda_1\phi_1, .. \lambda_k\phi_k, .. \lambda_n\phi_n, \phi_{n+1}, .. \phi_m\right] \qquad [2.29]$$

where,

$\lambda_k\phi_k$ is the SOM parameter of the parameter ϕ_k and

λ_k is the SOM factor of the parameter ϕ_k.

For example, ϕ_i may be the strength, or the modulus of the soil.

The following are the basic steps involved in the application of the SOM approach.

1. Select a material testing scheme.
2. Select material models.
3. Select numerical models.
4. Obtain and select the parameters.
5. Obtain initial predictions for the required quantities.
6. If the predictions do not compare reasonably with the observations, using engineering judgement, choose n

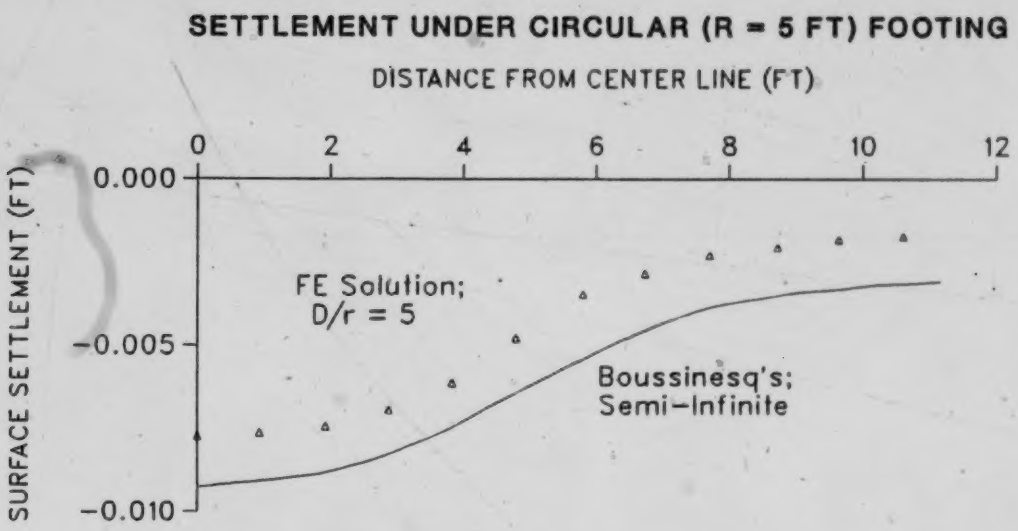

Figure 2.28 Finite Element and Closed form Solutions for Surface Settlement

(after Girijavallabhan, 1968 : modified)

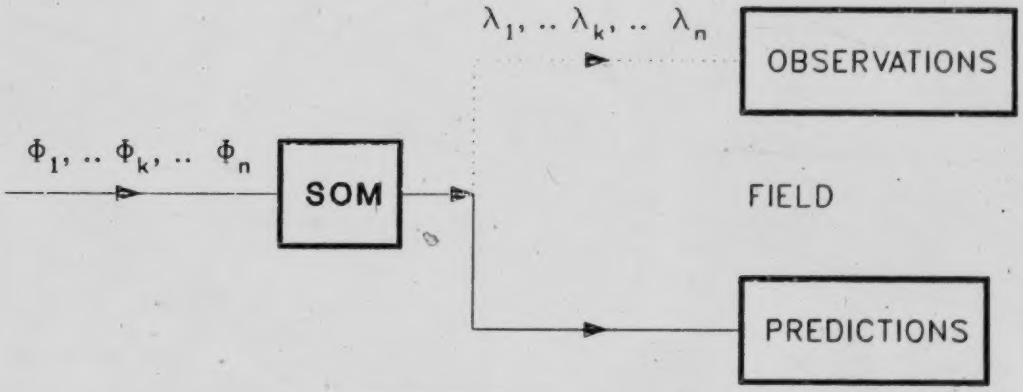
$\lambda_1, .. \lambda_k, .. \lambda_n$
OBSERVATIONS
$\Phi_1, .. \Phi_k, .. \Phi_n$
SOM
FIELD
PREDICTIONS

Figure 2.29 Concept of Solution Oriented Model

number of parameters(ϕ_i's) that need modification and an equal number of observations (o_i's).

7. Compare the observations with the predictions and find λ_k's

8. Then use the above λ_k's and the same SOM to predict the behaviour of similar soils.

The numerical procedure for evaluating λ_k's from the observations is as follows:

$$SOM_1(\lambda_1,\ ..\ \lambda_k,\ ..\ \lambda_n) = O_1 \qquad [2.30]$$

$$SOM_i(\lambda_1,\ ..\ \lambda_k,\ ..\ \lambda_n) = O_i \qquad [2.31]$$

$$SOM_n(\lambda_1,\ ..\ \lambda_k,\ ..\ \lambda_n) = O_n \qquad [2.32]$$

where, (O_1 .. O_i .. O_n) are the selected n observations and (λ_1, .. λ_k, .. λ_n) are the selected n SOM factors for curve fitting. The above set of equations is solved using Newton-Raphson iterative scheme.

Let

$$\bar{\lambda}^{r-1} = (\lambda^{r-1}_1,\ ..\ \lambda^{r-1}_k\ ..\ \lambda^{r-1}_n) \qquad [2.33]$$

and

$$\bar{\lambda}^{r} = \bar{\lambda}^{r-1} + (\Delta\lambda^r_1,\ ..\ \Delta\lambda^r_k\ ..\ \Delta\lambda^r_n) \qquad [2.34]$$

The derivatives can be computed in the following manner.

$$\frac{\partial(SOM)_1}{\partial\lambda_1} =$$

$$\left[SOM_1(\lambda^{r-1}_1+\Delta\lambda^r_1,\ ..\ \lambda^{r-1}_k\ ..\ \lambda^{r-1}_n) - SOM_1(\bar{\lambda}^{r-1})\right]/\Delta\lambda^r_1 \qquad [2.35]$$

$$\frac{\partial(\mathrm{SOM})_i}{\partial\lambda_1} =$$

$$\left[\mathrm{SOM}_i(\lambda^{r-1}_1+\Delta\lambda^r_1,\ ..\ \lambda^{r-1}_k\ ..\ \lambda^{r-1}_n) - \mathrm{SOM}_i(\bar{\lambda}^{r-1})\right]/\Delta\lambda^r_1 \qquad [2.36]$$

$$\frac{\partial(\mathrm{SOM})_n}{\partial\lambda_1} =$$

$$\left[\mathrm{SOM}_n(\lambda^{r-1}_1+\Delta\lambda^r_1,\ ..\ \lambda^{r-1}_k\ ..\ \lambda^{r-1}_n) - \mathrm{SOM}_n(\bar{\lambda}^{r-1})\right]/\Delta\lambda^r_1 \qquad [2.37]$$

The rest of the derivatives can be computed similarly. Then using the Newton-Raphson iterative procedure as shown below, the λ_k's that match the observations can be computed.

$$\frac{\partial(\mathrm{SOM})_i}{\partial\lambda_k}\,\Delta\lambda^{r+1}_k = -\ (\mathrm{SOM})_i(\bar{\lambda}^r) + O_i \qquad [2.38]$$

For obvious reasons, $\bar{\lambda}^0 = (1,\ ..\ 1,\ ..\ 1)$ can be considered to be a reasonably good initial trial solution. In this approach, for determining new λ_k's, n number of extra analyses need to be performed using each of $\lambda^{r-1}_k + \Delta\lambda^r_k$ separately (Equations 2.35 to 2.37). In selecting values for $d\lambda^1_k$'s, engineering judgement should be used such that after one iteration, a reasonably good set of predictions (also good λ_k's) are obtained. If, for some reason, a numerically more accurate set of λ_k's are needed, additional analyses can be performed by changing only the required λ_k's. For the rest of λ_k's the latest values can be used.

The λ_k's depend on the problem, the type of material, and the individual models used in the SOM. For example, they depend on the sampling techniques, the way the samples are prepared, type of soil tests performed, type of material and numerical models used. In many cases, only one or two parameters may need to be considered as SOM parameters. For instance, if only the soil deformations are under study, it is possible that only the modulus need be considered as an SOM parameter. On the other hand if the load capacity of the soil is of interest, it is possible that only the material strength need to be considered as an SOM factor. At this point the geotechnical engineer gets the opportunity to use his past experience and engineering judgement in a rational manner. This is one of the major advantages of the SOM approach. A similar approach has been applied to a particular case of a strutted excavtion by Clough et al. (1976).

Combined with a proper instrumentation procedure, and "design as you construct" approach, the proposed design procedure has the potential of making accurate predictions (c.f. observational method, Peck, 1969). It has the potential for successful use in large projects such as the design and construction of tunnels and dams (section 2.1). The other advantage of the SOM approach is that it allows the engineer to use fairly simple models and yet obtain relatively accurate results. In fact, an attempt must be made to use fairly simple and easily understood material and numerical models to allow greater applicability and efficiency (time and resources) of an SOM. However, it must be noted that by no means is the SOM approach applicable only with simple models. On the contrary, it should be applied as a rational method with all types of models whenever circumstances allow.

As stated in the foregoing paragraph, for greater applicability, an SOM should involve simple and lucid models. This condition raises the question of whether it is possible to use simple and easily understood models to investigate complex soil phenomena. The particular case of a complex phenomenon, pore pressure behaviour in clays, will be discussed in Chapters to follow.

3. PORE PRESSURE AND DEFORMATION BEHAVIOUR

3.1 INTRODUCTION AND OBJECTIVE

The pore pressure behaviour in cohesive soils is a complex phenomenon, for example, the pore pressure behaviour around excavations has hardly been investigated and thus is not very well understood. In this Chapter, the selection of numerical and material models for the investigation of pore pressure behaviour in cohesive soils will be discussed comprehensively. The advantages of using simple, lucid, yet realistic models, are discussed in Chapter 2. The cost efficiency and the fact that more design engineers can use them with better understanding are the primary advantages of using such models. Whether it is possible to develop numerical models satisfying such conditions is discussed in this and the following Chapter. The material models that incorporate such simple concepts as the uncoupled consolidation process, K_0 stress-strain behaviour (K_0 triaxial test), pore pressure parameters and basics of soil plasticity are considered. An effort was made to utilize the above concepts (in material and finite element models) to investigate the pore pressure behaviour in cohesive soils.

3.2 CONCEPTS OF CONSOLIDATION IN A CONTINUUM

The following sections present a discussion of the modeling of the coupled and the uncoupled solutions of the consolidation process in soil.

3.2.1 COUPLED SOLUTION

The soil is assumed to be a continuum. Both in reality and in the idealized continuum model, the consolidation process seems to be a coupled phenomenon. As the pore pressures dissipate with time, there appears to be a coupling among the displacements, stresses and the pore pressures. In the following sections, the basic concepts and assumptions of consolidation processes and their mathematical implications will be presented together with the derivation of governing equations.

The fluid that flows through the continuum is considered compressible. Assuming mass to be conserved, the rate of mass reduction in a control volume must be equal to the rate of mass outflow.

Rate of mass reduction is:

$$\frac{\partial}{\partial t}\left[\rho_w\left(w_{i,i} - \frac{u^t}{c_f}\right)\right] \qquad [3.1]$$

where,

$1/c_f$ = $-d\epsilon_v/du^t$, compressibility coefficient of the pore fluid,

t time,

u^t pore pressure of the fluid,

$w_{i,i}$ = $\sum_{i=1}^{3} \frac{\partial w_i}{\partial x_i}$; volumetric strain (reduction) of soil, in which w_i is the displacement tensor

x_i spatial coordinate and

ρ_w density of water.

The rate of mass outflow is:

$$\rho_w v_{i,i} \qquad [3.2]$$

where,

v_i is fluid flow velocity in the i direction and

$v_{i,i}$ $= \sum_{i=1}^{3} \frac{\partial v_i}{\partial x_i}$.

Since c_f is assumed to be independent of t:

$$\dot{w}_{i,i} - \frac{\dot{u}^t}{c_f} - v_{i,i} = 0 \qquad [3.3]$$

where,

$\dot{u}^t$ $= \frac{\partial u^t}{\partial t}$ and

$\dot{w}_{i,i}$ $= \frac{\partial w_{i,i}}{\partial t}$.

Assuming Darcy's law to be valid,

$$v_i = -k_{ij}(u^t{}_{,j} + \rho_f f_j)/\gamma_f \qquad [3.4]$$

where,

k_{ij} is the permeability tensor,

γ_f is unit weight of the fluid,

ρ_f is the fluid density and

f_j is the body force per unit weight of fluid

For equilibrium,

$$\sigma_{ij,j} + F_i = 0 \qquad [3.5]$$

where,

F_i is the body force tensor and

$\sigma_{ij,j}$ $= \frac{\partial \sigma_{ij}}{\partial x_j}$, in which σ_{ij} is stress tensor.

From the concept of effective stress,

$$\sigma'_{ij} = \sigma_{ij} - u^t\delta_{ij} \qquad [3.6]$$

where, σ'_{ij} is the effective stress tensor.

Stress-strain relations can be written in the form,

$$\sigma'_{ij} = C_{ijkl}\,\epsilon_{kl} \qquad [3.7]$$

where,

C_{ijkl} is the constitutive tensor and

ϵ_{kl} is strain tensor.

Strain-displacement relations for small strains can be written as:

$$\epsilon_{kl} = \frac{1}{2}\,[w_{k,l} + w_{l,k}] \qquad [3.8]$$

Combining Equations 3.5, 3.6, 3.7 and 3.8 yields,

$$[C_{ijkl}\,\frac{1}{2}\,\{w_{k,l} + w_{l,k}\} + u^t\delta_{ij}]_{,j} + F_i = 0 \qquad [3.9]$$

and Equations 3.3 and 3.4 yield,

$$\dot{w}_{i,i} - \frac{\dot{u}^t}{C_\ell} - [k_{ij}\,\{u^t_{,j} + \rho_\ell f_j\}/\gamma_\ell]_{,i} = 0 \qquad [3.10]$$

The governing equations of consolidation in a continuum are given by Equations 3.9 and 3.10. There are four unknowns (w_1, w_2, w_3 and u^t) and four Equations (tensor Equation 3.9 represents three equations). Theoretically, in the general case, with appropriate boundary conditions, these 4 equations can be solved for the four unknowns. It is clear that u^t and w_i are coupled in Equations 3.9 and 3.10, therefore, these governing equations are often referred to as the coupled solution of consolidation. In physical terms, the phenomena of equilibrium and flow through porous media are coupled. Although, theoretically the governing Equations (3.9 and 3.10) are solvable, the general solution is very difficult and there are no existing closed form solutions. However, with realistic simplifications, these equations can be simplified and decoupled, making them more amenable to simpler solution techniques.

3.2.2 UNCOUPLED SOLUTION

The decoupled equations are easier to understand and remain reasonably realistic (see also the discussion on SOM in Chapter 2.). This Section will explain the simplification and the decoupling process of the general equations including the assumptions involved.

In most practical geotechnical engineering situations, the cohesive soil layers remain saturated or nearly saturated. The water is incompressible compared to the soil structure and the body force remains constant. With these assumptions, the governing Equation 3.10 becomes,

$$\dot{w}_{i,i} + [k_{ij}h_{,j}]_{,i} = 0 \qquad [3.11]$$

where, h is the total head.

If the bulk modulus is K, then:

$$w_{i,i} = \frac{1}{3K}\sigma'_{ii} \qquad [3.12]$$

and Equation 3.11 becomes,

$$[k_{ij}h_{,j}]_{,i} + \frac{\partial}{\partial t}\left[\frac{\sigma'_{ii}}{3K}\right] = 0 \qquad [3.13]$$

For the 2-D case, and assuming k_{xy} to be zero, which is reasonable in practice, Equation 3.13 becomes,

$$\frac{\partial}{\partial x}\left[k_x \frac{\partial h}{\partial x}\right] + \frac{\partial}{\partial y}\left[k_y \frac{\partial h}{\partial y}\right] +$$

$$\frac{\partial}{\partial t}\left[\frac{\sigma'_{xx}+\sigma'_{yy}+\sigma'_{zz}}{3K}\right] = 0 \qquad [3.14]$$

When plane strain conditions and elasticity are assumed, Equation 3.14 becomes:

$$\frac{\partial}{\partial x}\left[k_x \frac{\partial h}{\partial x}\right] + \frac{\partial}{\partial y}\left[k_y \frac{\partial h}{\partial y}\right] + \frac{\partial}{\partial t}\left[\frac{\{\sigma_{xx}+\sigma_{yy}-2u^t\}(1+\nu)}{3K}\right] = 0 \qquad [3.15]$$

For most practical cases the soil moduli are found to be independent of time, hence Equation 3.15 becomes,

$$\frac{\partial}{\partial x}\left[k_x \frac{\partial h}{\partial x}\right] + \frac{\partial}{\partial y}\left[k_y \frac{\partial h}{\partial y}\right] = \frac{2(1+\nu)}{3K}\frac{\partial u^t}{\partial t} - \frac{(1+\nu)}{3K}\frac{\partial}{\partial t}[\sigma_{xx}+\sigma_{yy}] \qquad [3.16]$$

This equation must be solved with the equilibrium Equations given in 3.9 or 3.5. It is clear that even with a significant degree of simplification, coupling of the two sets of equations still exists. If the total stresses are assumed not to change with time, $\frac{\partial}{\partial t}\{\sigma_{xx} + \sigma_{yy}\}$ vanishes, and hence the governing Equation 3.16 becomes,

$$\frac{\partial}{\partial x}\left[k_x \frac{\partial h}{\partial x}\right] + \frac{\partial}{\partial y}\left[k_y \frac{\partial h}{\partial y}\right] = \frac{1}{\bar{M}}\frac{\partial u^t}{\partial t} \qquad [3.17]$$

where, $\bar{M}=E_s/2(1+\nu)(1-2\nu)$.

This completely decouples the two phenomena, equilibrium and flow through porous media. Mathematically, it decouples the two sets of Equations (3.9 and 3.10), and makes it possible to solve the consolidation Equation (3.10) independently. This assumption was recommended by Terzaghi (1943) and has been applied to several practical cases by Davis et al. (1972). Also, Eisenstein et al. (1977) successfully used an uncoupled approach to analyse pore pressure and deformation behaviour during the construction of a dam. This simplification based on practical considerations, renders the governing equations amenable to simpler solution techniques, yet retains the significant and important realities of the physical processes. Recently Yamagami et al. (1985) compared the results of an uncoupled solution with that of a coupled solution. In terms of stress paths, soil movements and time dependent behaviour, the results of the two approaches matched remarkably well.

The next Section explores the possibility of using the uncoupled solution to examine pore pressure behaviour.

3.3 A SIMPLE MODEL FOR PORE PRESSURE BEHAVIOUR AND DEFORMATION

The decoupled approach simplifies the mathematical model of the coupled pore pressure phenomenon to a great extent. It allows the engineer to perform a stress analysis and make consolidation computations more independently. This independence has many advantages typical of geotechnical engineering practice. One of the most important advantages is that it allows the "engineering judgement" to be used at different stages of the decoupled process. A procedure that can be used with the above simplified concepts to examine the pore pressure behaviour and deformation is outlined in the following three steps. This procedure is illustrated in the block diagram shown in Figure 3.1. Eisenstein et al.

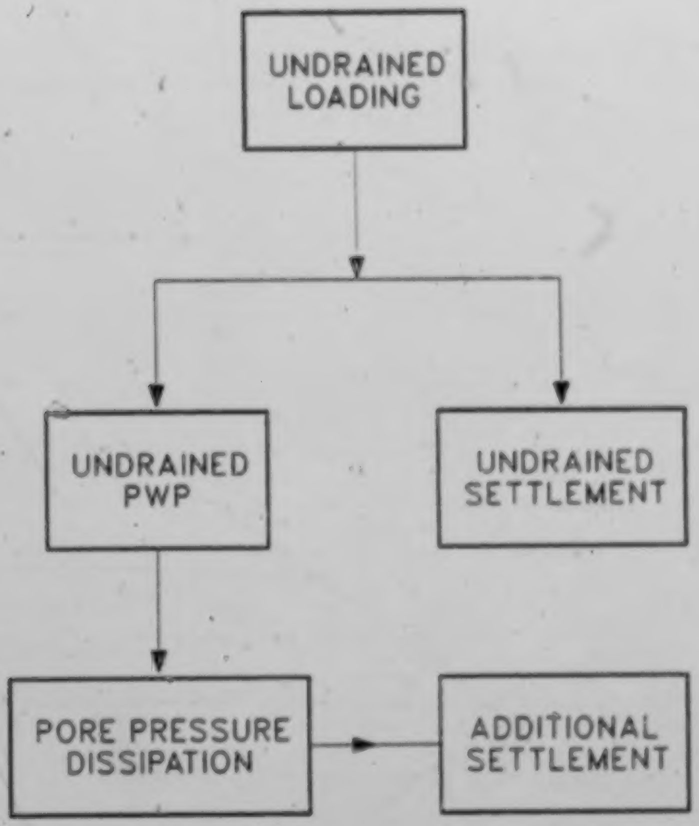
UNDRAINED LOADING
UNDRAINED PWP
UNDRAINED SETTLEMENT
PORE PRESSURE DISSIPATION
ADDITIONAL SETTLEMENT

Figure 3.1 Uncoupled Model for Pore Pressure and Deformation Analysis

(1976) introduced the fundamentals of this procedure and applied it to the analysis of consolidation in the cores of earth dams. Eisenstein et al. (1977) made further applications of this uncoupled theory to earth dams.

3.3.1 Step 1 UNDRAINED BEHAVIOUR

The initial loading/unloading (excavation/fill) is considered undrained. The total stress changes due to this undrained loading are computed using the equilibrium equations and the appropriate boundary conditions. These results provide the initial or undrained displacements (settlement or heave) and total stresses. The initial total stress changes are used with the pore pressure coefficients to evaluate initial pore pressure.

3.3.2 Step 2 PORE PRESSURE DISSIPATION

Over time, these initial pore pressures dissipate. The pore pressure at a given time can be computed using the initial pore pressure and suitable boundary conditions in the uncoupled consolidation equation.

3.3.3 Step 3 DISPLACEMENTS DUE TO PORE PRESSURE DISSIPATION

The pore water pressure dissipation gives rise to a change in pore pressures which, in turn, results in effective stress changes. Effective stress changes cause additional displacement, either settlement or heave, depending on whether the change is positive or negative.

Knowing the boundary conditions, the decoupled governing equations can be solved to obtain pore pressure dissipation. Using these results, a stress analysis can be performed to evaluate the displacements due to the changes in effective stress.

The closed form solutions of these equations are still difficult even for an ordinary geotechnical engineering problem, unless it is oversimplified to a degree that the oversimplification may become unrealistic. To solve these equations more readily, a numerical procedure can be implemented.

3.4 NUMERICAL APPROACH FOR THE SIMPLE MODEL

The simplified approach of the three steps noted in the preceding sections is not readily amenable to closed form analysis, hence a practical option is a numerical approach. However, this raises an important and a fundamental question: 'Can numerical approaches retain the reality of the geotechnical engineering situation (which closed form analysis cannot), and yet be simple enough to be widely applicable?'. This research has found that the finite element approach is one solution, and other possible solutions have not been explored in this thesis. The following steps describe the proposed numerical procedure that is considered to achieve the above objectives. These are essentially the three general steps of the simple model described previously except that specific details of the proposed numerical approach are provided. Figure 3.2 illustrates the steps of the numerical procedure.

3.4.1 Step 1 **UNDRAINED BEHAVIOUR**

The undrained loading (fill/excavation), uses a finite element analysis that incorporates a nonlinear hyperbolic stress-strain model. A total stress analysis is performed. This procedure yields both the initial settlement and the initial total stresses. A finite element program originally developed by Kulhawy et al. (1969) was modified for this purpose. Using these total stress changes in the Henkel's (1960) pore pressure formula given below, the initial pore pressures due to the undrained loading can be obtained.

$$\Delta u = \frac{1}{3}[\Delta\sigma_1+\Delta\sigma_2+\Delta\sigma_3] + a[(\Delta\sigma_1-\Delta\sigma_2)^2 + (\Delta\sigma_2-\Delta\sigma_3)^2 + (\Delta\sigma_3-\Delta\sigma_1)^2]^{\frac{1}{2}} \qquad [3.18]$$

where a is the Henkel's pore pressure coefficient and $\Delta\sigma_i$'s are the principal values of the stress-change tensor $\Delta\sigma_{ij}$. The soil is assumed to be saturated. The stress-strain model in this finite element procedure incorporates a modification of the widely used hyperbolic model which has some limitations. The modifications which are discussed below overcome these limitations reasonably well.

3.4.1.1 HYPERBOLIC MODELS

The hyperbolic stress-strain model was derived by Kondner (1963) using the conventional triaxial test results. The results are generally interpreted in the

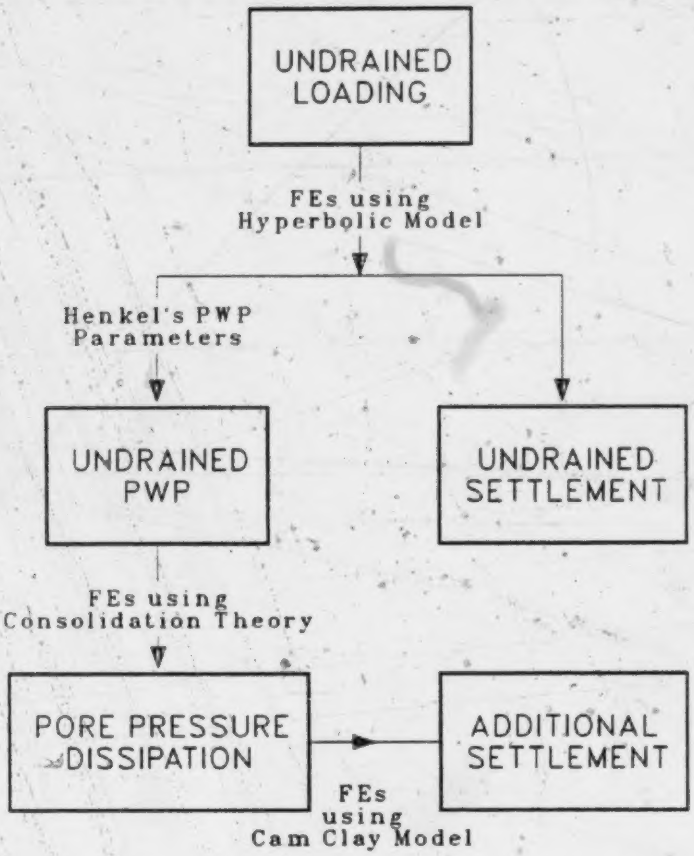
UNDRAINED LOADING
FEs using Hyperbolic Model
Henkel's PWP Parameters
UNDRAINED PWP
UNDRAINED SETTLEMENT
FEs using Consolidation Theory
PORE PRESSURE DISSIPATION
ADDITIONAL SETTLEMENT
FEs using Cam Clay Model

Figure 3.2 FE Models for the Uncoupled Analysis of Pore Pressure and Deformation

form of a stress-strain material model (Figure 3.3). Usually, this model is expressed in the following mathematical form.

$$\sigma = \frac{\epsilon}{b + d_i\epsilon} \qquad [3.19]$$

where, b and d_i are material properties, σ and ϵ are stress and strain respectively. It can be shown, that 1/b is the initial Young's modulus and $1/d_i$ is an idealized compressive strength which corresponds to an infinite strain. However, in practice, this idealized strength can never be attained. Hence, to relate this asymptotic value to a practically defined strength (using ultimate stresses or allowable strains) a failure ratio R_f has been introduced. Using the failure ratio, the hyperbolic relations can be written in the following form,

$$\sigma = \frac{\epsilon}{b + d\epsilon R_f} \qquad [3.20]$$

In this case, 1/d is a practical value, reciprocal of the real strength, as opposed to a completely theoretical quantity d_i.

If this triaxial stress-strain curve (Figure 3.3) is interpreted as a general stress-strain relation, some ambiguities arise. For example, in a general 2-D stress-strain situation, the modulus does not appear to depend uniquely on ϵ. That is, the stress-strain curve shown in Figure 3.3 may not be considered as a consistent material model. To overcome this inconsistency, a

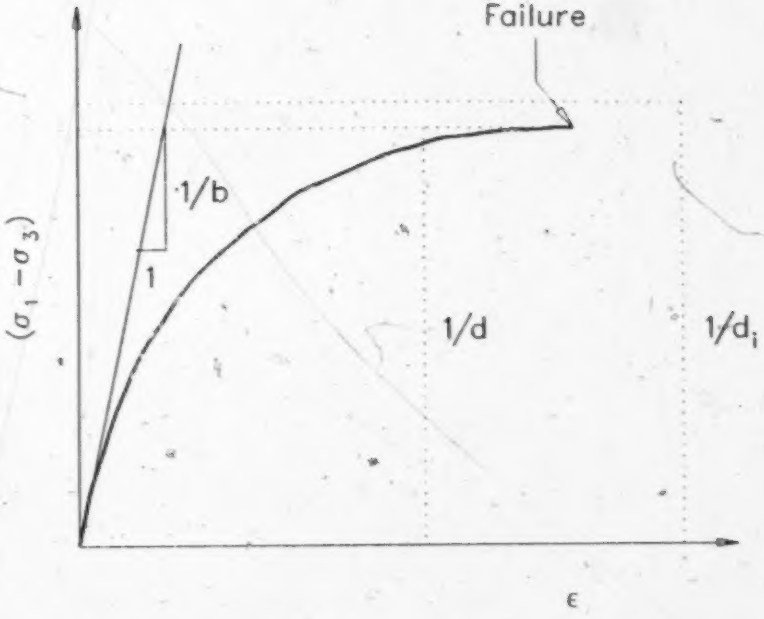

Figure 3.3 Hyperbolic Stress-Strain Relations

different interpretation has been given by researchers such as Desai et al. (1977). The results of the triaxial test are plotted on the maximum shear stress and maximum shear strain plane (Figure 3.4). The mathematical model is as given below:

$$\tau_{max} = \frac{\gamma_{max}}{b + d\gamma_{max}/R_f} \qquad [3.21]$$

This is considered to be a stress-strain material model. However, there is a difficulty in considering τ_{max} vs γ_{max} curve as a material model of stress-strain. It is clear that the γ_{max} and τ_{max} planes in a nonlinear elastic material do not coincide. Hence, defining a shear modulus relating these two quantities is not consistent with the general concept of shear modulus. The stress-strain curve obtained from the triaxial test alone may not be considered as a stress-strain material model. Important assumptions are required in order to convert this simple triaxial stress-strain curve to a stress-strain material model. In a different interpretation, instead of considering the stress-strain curve as a material model, only the modulus is defined as a material model. It is assumed that the tangent modulus is dependent only on the initial conditions (before the undrained loading) and the stress level during loading. The stress level is broadly defined as $(\sigma_1-\sigma_3)/2s_u$. On this basis, a consistent material model can be derived from the hyperbolic triaxial stress-strain curve and is presented mathematically in the following form:

$$E_t = E_i[1 - \frac{(\sigma_1-\sigma_3)R_f}{2s_u}]^2 \qquad [3.22]$$

where,

s_u is the undrained strength

E_i is the initial Young's modulus and

E_t is the current tangent modulus.

The graphical representation of this material model is shown in Figure 3.5.

There are other limitations in the widely used hyperbolic stress-strain model. For instance, it assumes that the rotation of the principal axes has no influence on the tangent modulus of the material. It also assumes that the stress-strain behaviour in extension is identical to the stress-strain behaviour in compression. However, in some soils (Vaid et al., 1974) these two behaviours can be considerably different (Figure 3.6). Finally, the widely used hyperbolic model disregards the difference between the isotropically consolidated and the K_0 consolidated triaxial stress-strain behaviour. Using experimental results, Vaid et al. (1974) showed (Figure 3.6) this difference for a typical cohesive material which can produce a significant error in the prediction of displacement. During simple shear and extension stress-strain behaviour of a soil, the rotation of principal axes takes place. In most geotechnical engineering problems, the loading/unloading gives rise to stress changes as well as rotation of principal axes.

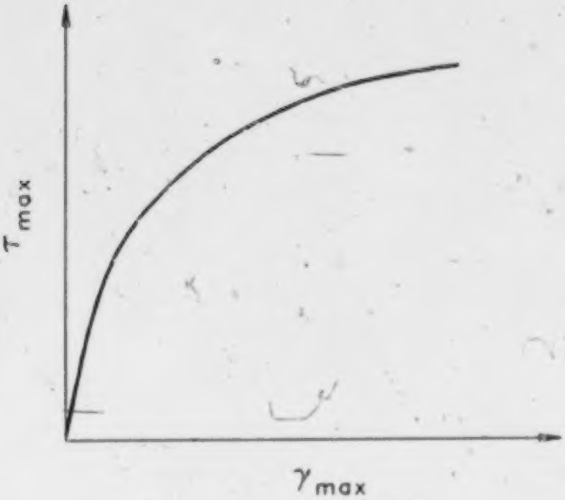
τ_{max}
γ_{max}

Figure 3.4 Hyperbolic Stress-Strain Curve as a Material Model

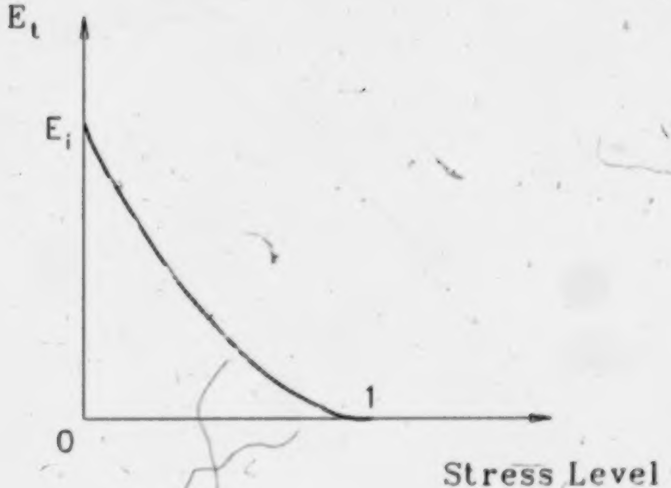
E_t
E_i
1
0
Stress Level

Figure 3.5 A Different Interpretation of the Hyperbolic Model

Duncan et al. (1969) proposed a sinusoidal square variation to estimate what is called an apparent modulus due to rotation of principal axes. Simon et al. (1974) suggested a similar variation for the change in undrained strength due to rotation of principal axes. The same concepts were used to interpolate the strength and the modulus for rotation of principal axes in our analysis. The mathematical equations that describe these concepts are:

$$E_{t\theta} = E_{t0} - [E_{t0}-E_{t90}]\mathrm{Sin}^2\theta \qquad [3.23]$$

$$s_{u\theta} = s_{u0} - [s_{u0}-s_{u90}]\mathrm{Sin}^2\theta \qquad [3.24]$$

where, $E_{t\theta}$ and $s_{u\theta}$ denote the tangent modulus and strength corresponding to a θ degree rotation of principal axes. Vaid et al. (1981) also found a very important stress-strain behaviour. They found that the K_0 consolidated triaxial stress-strain curves can be represented using hyperbolic curves, if the origins of the two hyperbolic segments (one for compression and one for extension) are located at the K_0 stress state (Figure 3.6). These hyperbolic stress-strain curves can be expressed mathematically using the following equations.

For compression,

$$q - q^0 = \frac{\epsilon}{1/E_i+R_{fc}\epsilon/(q^{fc}-q^0)} \qquad [3.25]$$

For extension,

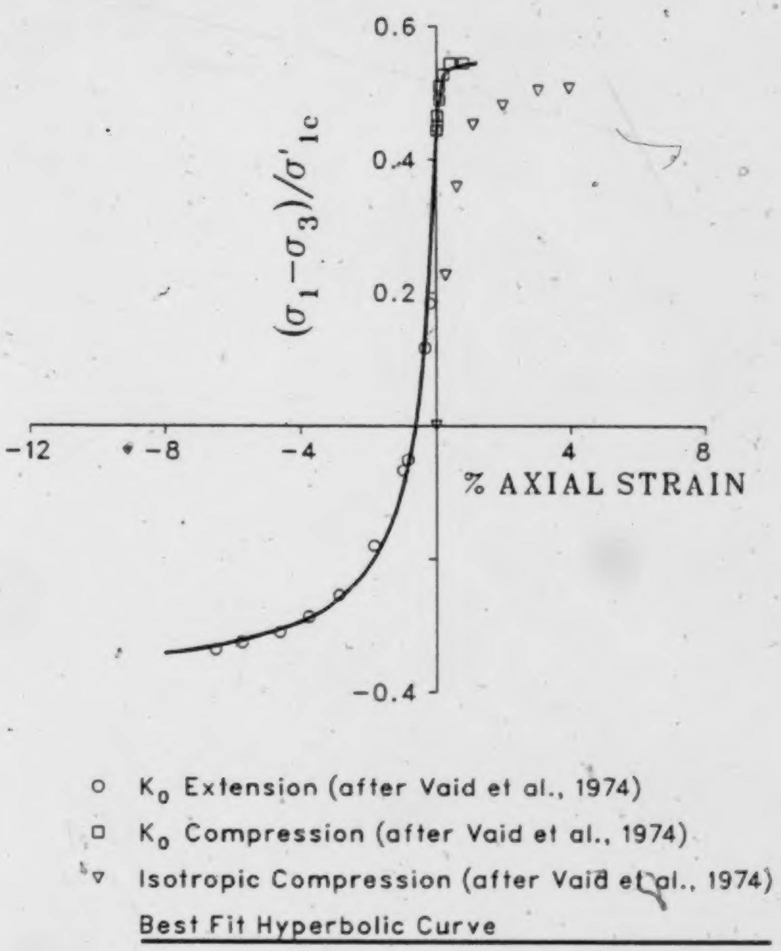

Figure 3.6 K_0 Triaxial Stress-Strain Curves

$$q^0 - q = \frac{\epsilon}{1/E_i + R_{fe}\epsilon/(q^{fe}+q^0)} \qquad [3.26]$$

where,

q = $(\sigma_y - \sigma_x)$,

q^0 = $\sigma_v'(1-K_0)$,

q^{fc} is compression strength and

q^{fe} is extension strength.

Using the consistent material model concepts discussed initially and the findings of Duncan et al. (1969), Simon et al. (1974) and Vaid et al. (1981), a more realistic stress-strain material model for cohesive clays has been obtained (Samarasekera, 1982), see also, Clough et al. (1981) for a similar approach. This consistent material model can be expressed using Equations 3.23 and 3.24 together with the following Equations:

$$E_{t0} = E_i[1-R_{fc}(q-q^0)/(q^{fc}-q^0)]^2 \text{ for } q \geq q^0 \qquad [3.27]$$

$$E_{t0} = E_i[1-R_{fe}(q^0-q)/(q^{fe}+q^0)]^2 \text{ for } q < q^0 \qquad [3.28]$$

$$E_{t90} = E_i[1-R_{fe}(q^0+q)/(q^{fe}+q^0)]^2 \qquad [3.29]$$

where,

E_{t0} is tangent modulus for no principal axes rotation and

E_{t90} is tangent modulus for 90^0 principal axes rotation.

The tangent modulus is assumed to be dependent only on the stress level (e.g. for $\theta=90^0$, stress level is $[(q^0+q)/(q^0+q_{te})]$). This stress-strain material model is shown graphically in Figure 3.7.

It is important to note that the basic concepts of this material model are fairly simple and easily understood, yet realistic as far as the soil stress-strain behaviour is concerned. Hence, it was decided that the constitutive model (Equations 3.23, 3.24, 3.27, 3.28 and 3.29) be used as the material model in the proposed finite element analysis.

3.4.1.2 PORE PRESSURE PARAMETERS

One of the simplest pore pressure formulas was developed by Skempton (1954) which, although well known and widely used, has significant limitations. This formula was developed mainly for triaxial stress situations (using triaxial test results) where two principal stresses are equal. The Skempton formula can be expressed as:

$$\Delta u = B\left[\Delta\sigma_3 + A\{\Delta\sigma_1-\Delta\sigma_3\}\right] \qquad [3.30]$$

Even for a triaxial situation, this formula creates problems and ambiguity. The first ambiguity arises from the lack of a clear definition for $\{\Delta\sigma_1-\Delta\sigma_3\}$. Is $\{\Delta\sigma_1-\Delta\sigma_3\}$, the change in the difference of major and minor principal stresses; the difference of the changes in major and minor principal stresses; the difference in major and minor principal stresses in the stress-change tensor $\Delta\sigma_{ij}$? There are no clear answers to these questions. It is imperative that these questions be answered before attempting to apply the formula to general 2-D or 3-D stress states. When the rotation of principal axes take place, more ambiguity occurs. Also, doubts arise concerning the applicability of the same pore pressure coefficients for different stress paths. These doubts are confirmed by the fact that even for the triaxial situation, the Skempton parameter A, for compression is different from the value for extension. This formula also developed mainly for triaxial stress states, does not take into account the influence of the intermediate principal stress on pore presure generation.

However, the Henkel formula (Equation 3.18) overcomes these problems and ambiguities, but is as simple as the Skempton formula. In the Henkel formula, there is no ambiguity about the stress change or the stress system change (rotation of principal axes). It also takes into account the influence of the intermediate principal stress on the pore pressure. Using experimental results, Henkel (1960) showed that the pore pressure parameter for both compression and extension is nearly the same in his formula. For these reasons, the Henkel pore pressure model was used in estimating the pore pressure generated due to the initial undrained loading.

3.4.2 Step 2 PORE PRESSURE DISSIPATION

As mentioned in the preceding sections, the computation of pore pressure dissipation with time can be achieved using the uncoupled consolidation theory which is a simpler but realistic approach. A two dimensional finite element model was adopted for solving the governing equations. The elasticity of the continuum has been assumed in this formulation. A finite element program, originally developed by Krishnayya (1973), was modified for this purpose.

3.4.3 Step 3 DISPLACEMENTS DUE TO PORE PRESSURE DISSIPATION

This step consists of computing the settlements due to pore pressure dissipation. As explained before, the settlements are computed by taking the pore pressure change as an additional equivalent force. For cases such as tunnels, stress reversals can occur (Negro, 1988) due to the pore pressure dissipation. An elasto-plastic material model can account for these stress reversals reasonably well. The Modified Cam-Clay model is a good choice for this purpose since it simulates the soil behaviour reasonably accurately. One of the main advantages of using the uncoupled consolidation theory is that the design engineer is free to select different realistic and practical models for the analysis of different stages of soil behaviour in a geotechnical engineering problem. Depending on the required accuracy and reliability of the necessary results, the engineer can select these models using the past experience and engineering judgement.

3.5 FINITE ELEMENT FORMULATION

The following sections discuss briefly the procedure adopted in the formulation of finite element models used in the numerical analysis. The finite element formulations for the uncoupled solution in the form of equilibrium and consolidation will be discussed in the sections that follow.

3.5.1 VIRTUAL WORK APPROACH FOR EQUILIBRIUM EQUATION

The virtual work approach for solving equilibrium equations has a wider applicability than, for example, the variational approaches that use potential energy. Hence the virtual work approach was used.

According to the principle of virtual work, for any kinematically admissible displacement field, the amount of external work done by the equilibrating forces is equal to the internal virtual work. Therefore (Figure 3.8),

$$\int_v \sigma_{ij}\delta\epsilon_{ij}dv = \int_v F_i\delta w_i dv + \int_{S_T} T_i\delta w_i dS \qquad [3.31]$$

where,

F_i	is body force tensor,
S_T	is surface where traction is specified,
T_i	is the traction force,
v	is volume domain,

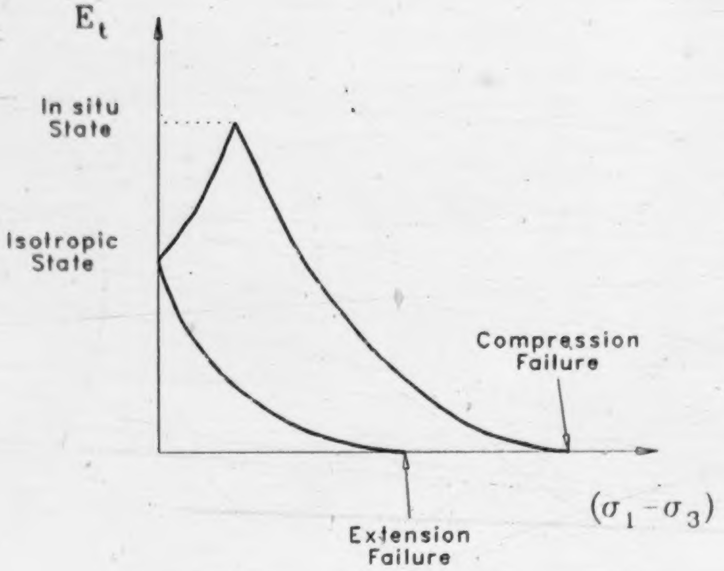

Figure 3.7 General Hyperbolic Material Model

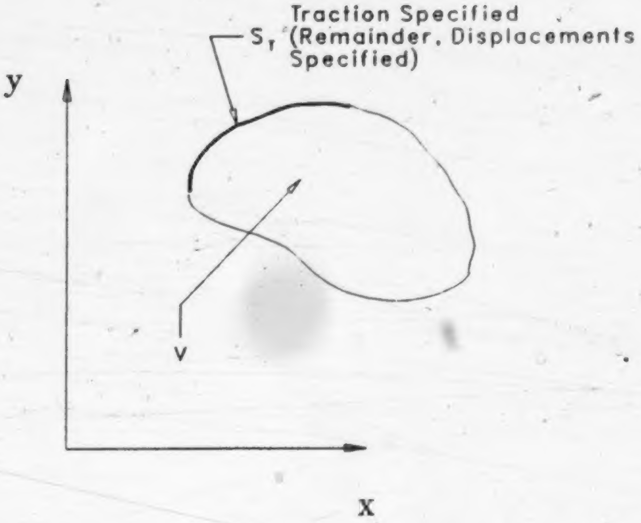
Traction Specified
S_T (Remainder, Displacements Specified)
y
V
x

Figure 3.8 Body under equilibrium

δw_i is an admissible arbitrary virtual displacement field,

σ_{ij} is the stress tensor and

$\delta\epsilon_{ij}$ is the corresponding strain tensor.

The RHS becomes,

$$\int_v \sigma_{ij}\,\frac{1}{2}\,\{\delta w_{i,j} + \delta w_{j,i}\}dv \qquad [3.32]$$

$$\int_v \sigma_{ij}\delta w_{i,j}dv \qquad [3.33]$$

$$\int_v \{\sigma_{ij}\delta w_i\},_j dv - \int_v \{\sigma_{ij}\},_j \delta w_i dv \qquad [3.34]$$

$$\int_S \sigma_{ij}n_j\delta w_i dS - \int_v \{\sigma_{ij}\},_j \delta w_i dv \qquad [3.35]$$

Hence Equation 3.31 becomes,

$$\int_v \{\sigma_{ij,j} + F_i\}\delta w_i dv + \int_{S_T} \{T_i - \sigma_{ij}n_j\}\delta w_i dS = 0 \qquad [3.36]$$

Since δw_i is arbitrary, the above Equation implies,

$$\sigma_{ij},_j + F_i = 0 \text{ on } v \qquad [3.37]$$

$$\sigma_{ij}n_j - T_i = 0 \text{ on } S_T \qquad [3.38]$$

These two Equations, with the kinematic boundary conditions, (also known as essential boundary conditions where, displacements are specified on S_u) form the well known equilibrium boundary value problem. That is, the virtual work equation implies equilibrium. One major advantage of the virtual work principle is that it does not require the continuum to be elastic.

3.5.2 VIRTUAL WORK EQUATION FOR DISPLACEMENT FINITE ELEMENT FORMULATION

Once the type of finite element formulation (e.g. displacement formulation using virtual work) is selected, selection of finite element type and solution technique becomes important. The finite element types and the solution techniques used in this thesis are discussed in the following sections (see also Chapter 2 on selection of finite element type). A four node bilinear isoparametric element was used. The displacement formulation assumes a distribution for the displacement field in a finite element. For this case,

$$u_x = <\phi_1\ \phi_2\ \phi_3\ \phi_4>\{\overline{u}_x\} \qquad [3.39]$$

$$u_y = <\phi_1\ \phi_2\ \phi_3\ \phi_4>\{\overline{u}_y\} \qquad [3.40]$$

where,

u_x is displacement field in x direction,
u_y is displacement field in y direction,
$\{\overline{u}_x\}$ is nodal displacement vector in x direction and
$\{\overline{u}_y\}$ is nodal displacement vector in y direction.

For isoparametric transformation,

$$x = <\phi_1\ \phi_2\ \phi_3\ \phi_4>\{\overline{x}\} \qquad [3.41]$$

$$y = <\phi_1\ \phi_2\ \phi_3\ \phi_4>\{\overline{y}\} \qquad [3.42]$$

where,

$\{\overline{x}\}$ is nodal x coordinate vector and
$\{\overline{y}\}$ is nodal y coordinate vector.

The shape functions:

$$\phi_i = \frac{1}{4}(1+\xi_i\xi)(1+\eta_i\eta) \qquad [3.43]$$

where, ξ_i and η_i are nodal coordinates of the transformed element in (ξ,η) space (Figure 2.25). For the continuous displacement field used, the virtual work Equation given in 3.31 can be written in the following manner for the finite element discretization:

$$\Sigma\int_{v_e} <\delta q>[N]^T\{F\}dv + \Sigma\int_{S_T} <\delta q>[N]^T\{T\}dS =$$

$$\Sigma\int_{v_e} <\delta q>[B]^T\{\bar{\sigma}\}dv \qquad [3.44]$$

where,

$<\delta q>$ is nodal displacement vector due to an arbitrary displacement field,

$\{T\}$ is traction force vector and

$\{F\}$ is body force vector.

$$[N] = \begin{vmatrix} <\phi> & 0 \\ 0 & <\phi> \end{vmatrix} \qquad [3.45]$$

where, $<\phi> = <\phi_1 \ \phi_2 \ \phi_3 \ \phi_4>$.

$$\begin{vmatrix} \epsilon_x \\ \epsilon_y \\ \gamma_{xy} \end{vmatrix} = [B]\{q\} \qquad [3.46]$$

$\{q\}$ is displacement vector due to the applied load and

$$[B] = \begin{vmatrix} \frac{\partial<\phi>}{\partial x} & 0 \\ 0 & \frac{\partial<\phi>}{\partial y} \\ \frac{\partial<\phi>}{\partial y} & \frac{\partial<\phi>}{\partial x} \end{vmatrix} \qquad [3.47]$$

$$\left|\begin{matrix}\dfrac{\partial}{\partial x}\\ \dfrac{\partial}{\partial y}\end{matrix}\right| = [J]^{-1}\left|\begin{matrix}\dfrac{\partial}{\partial \xi}\\ \dfrac{\partial}{\partial \eta}\end{matrix}\right| \qquad [3.48]$$

$$[J] = \left|\begin{matrix}\dfrac{\partial}{\partial \xi}\\ \dfrac{\partial}{\partial \eta}\end{matrix}\right| <x\ \ y> \qquad [3.49]$$

$$\{\overline{\sigma}\} = \left|\begin{matrix}\sigma_x\\ \sigma_y\\ \tau_{xy}\end{matrix}\right| \qquad [3.50]$$

The constitutive relation can be written in the form,

$$\{\overline{\sigma}\} = [D]\{\overline{\epsilon}\} \text{ and} \qquad [3.51]$$

$$\{\overline{\epsilon}\}^T = <\epsilon_x\ \ \epsilon_y\ \ \gamma_{xy}> \qquad [3.52]$$

where, [D] is the constitutive matrix. For instance, in incremental analysis (Section 3.5.3.1), [D] consists of tangent moduli and the stresses and strains become increments. For our case, 2-D plane strain, [D] is:

$$[D] = \frac{E_t}{(1+\nu_t)(1-2\nu_t)}\left|\begin{matrix}1-\nu_t & \nu_t & 0\\ \nu_t & 1-\nu_t & 0\\ 0 & 0 & (1-2\nu_t)/2\end{matrix}\right| \qquad [3.53]$$

The Equation 3.44 becomes,

$$\Sigma\int_{v_e}<\delta q>[N]^T\{F\}dv + \Sigma\int_{S_T}<\delta q>[N]^T\{T\}dS =$$

$$\Sigma\int_{v_e}<\delta q>[B]^T[D][B]\{q\}dv \qquad [3.54]$$

$$\int_{v_e}[B]^T[D][B]dv = \int_{v_e^*}[B]^T[D][B]J\,dv^* = [k^e] \qquad [3.55]$$

where,

$[k^e]$ is the element stiffness matrix and

v^e is v in the transformed $\{\xi, \eta\}$ space.

Usually, the above integral is numerically evaluated using the Gaussian quadrature. In this analysis, 2×2 Gaussian quadrature was used. If the summations in Equation 3.54 are performed and the quantities are referred to a global coordinate system, the Equation becomes,

$$<\delta r>[K]\{r\} = <\delta r>\{F_b\} + <\delta r>\{F_T\} \qquad [3.56]$$

where,

$\{F_b\}$ is the nodal load vector due to body force,

$\{F_T\}$ is the nodal load vector due to traction and

$\{r\}$ is the displacement vector with respect to a global coordinate system.

The displacement vector consists of free nodes and those where displacements are specified. In other words, $<r>$ can be written in the form $<r^f\ r^s>$,

where,

$<r^f>$ is the displacement vector of the free nodes and

$<r^s>$ is the vector of specified displacements.

Hence, the kinematically admissible displacement vector becomes, $<\delta r^f\ 0>$.

[K] can be written in the form,

$$[K] = \begin{vmatrix} K^{ff} & K^{fs} \\ K^{sf} & K^{ss} \end{vmatrix} \qquad [3.57]$$

Hence the virtual work Equation 3.56 becomes,

$$<\delta r^f\ 0>\left[[K^{ff}]\{r^f\} + [K^{fs}]\{r^s\}\right] = <\delta r^f\ 0>\{F_b\} + <\delta r^f\ 0>\{F_T\} \qquad [3.58]$$

This Equation is valid for arbitrary $<\delta r^f>$, hence it yields,

$$[K^{ff}]\{r^f\} + [K^{fs}]\{r^s\} = \{F_b^f\} + \{F_T^f\} \qquad [3.59]$$

where,

$\{F_b^f\}$ is body force vector on free nodes and

$\{F_T^f\}$ is traction force vector on free nodes.

For our case $\{r^s\} = \{0\}$, therefore, the equilibrium equations reduce to,

$$[K^{ff}]\{r^f\} = \{F_b^f\} + \{F_T^f\} \qquad [3.60]$$

In the above system of equations, $[K^{ff}]$, $\{F_b^f\}$ and $\{F_T^f\}$ are known. This system of equations is solved and the unknown displacement vector $\{r^f\}$ is computed. The strains, and hence the stresses are then computed using Equations 3.46 and 3.51, respectively. The solution of this system of equations are discussed in the following sections.

3.5.3 SOLUTION TECHNIQUES

The problem under discussion has nonlinear material properties. The solution of such nonlinear problems is achieved in finite element analysis using two basic techniques, namely, the stepwise methods and the iterative procedures. The stepwise or the incremental technique has an apparent advantage that the numerical simulation can be made to correspond with the actual construction sequence. Since many geotechnical engineering constructions are completed in a step-by-step manner, it is easier for the geotechnical engineer to relate the above numerical model to the actual construction process in the field (see also the concepts of SOM in Chapter 2).

3.5.3.1 STEPWISE METHODS

The stepwise methods can be subdivided into two major categories. These are referred to as the basic incremental approach and the Runge-Kutta approach. These methods are discussed in the following sections.

(i) BASIC INCREMENTAL METHOD

In this method the nonlinear constitutive behaviour is simulated using an "incremental finite element analysis". The basis of the incremental analysis is to subdivide the total load into sufficiently small increments so that it is reasonable to assume that within a load increment, the material behaviour is linearly elastic. Although not always true, these load increments are usually equal. The procedure is schematically shown in Figure 3.9. To compute the corresponding displacement increments for the current load step, the stiffness matrix is computed using the tangent moduli values that correspond to the stress-strain state at the end of the previous load increment. That is,

$$[K]_i = [K\{R_{i-1}, r_{i-1}\}] \qquad [3.61]$$

$$\{R_{i-1}\} = \sum_{j=1}^{i-1} \{\Delta R_j\} \qquad [3.62]$$

$\{r_{i-1}\}$ is computed using Equation 3.65. The total load:

$$\{R\} = \sum_{j=1}^{m} \Delta\{\Delta R_j\} \qquad [3.63]$$

where, m is the number of load steps. The finite element equilibrium equations can be written as:

$$[K]_i\{\Delta r\}_i = \{\Delta R\}_i \qquad [3.64]$$

where,

$\{\Delta r\}_i$ is the displacement increment corresponding to $\{\Delta R\}_i$ and

$\{\Delta R\}_i$ is i^{th} load increment.

Equation 3.64 is solved for the incremental displacements $\{\Delta r\}_i$. Knowing the incremental displacements, the incremental stresses and strains can be computed using Equations 3.46 and 3.51. The total displacements can be computed as follows:

$$\{r_i\} = \sum_{j=1}^{i} \{\Delta r_j\} \qquad [3.65]$$

Similarly, the total stresses and strains can be computed by summing their incremental values as in the case of displacements. Note, however, that this solution continually deviates from the so called exact solution (Figure 3.9). It is clear that the deviation can be reduced by increasing the number of load increments which in turn increases the computational costs. However, to obtain more accurate results a better approach would be to use the Runge-Kutta techniques.

(ii) MID-POINT RUNGE-KUTTA METHOD

The mid-point Runge-Kutta method can be considered as a major improvement of the basic incremental method. This approach, in addition to improving the numerical accuracy of the results, retains the simplicity of the basic incremental method.

The principle underlying this approach is to compute the stress state corresponding to the half-load step increment using the moduli corresponding to the previous stress state. It can be mathematically expressed as a matrix equation in the following manner.

$$[K]_{i-1}\{\Delta r\}_{i-\frac{1}{2}} = \{\Delta R_i/2\} \qquad [3.66]$$

Using $\{\Delta r\}_{i-\frac{1}{2}}$, the stress state corresponding to the half-load step increment is computed. Using these stresses, the moduli values corresponding to the half-load step increment are obtained, hence the stiffness matrix $[K]_{i-\frac{1}{2}}$ can be evaluated. Employing this stiffness matrix in load displacement equations for the full-load step, the displacements corresponding to the full-load step increment are computed:

$$[K]_{i-\frac{1}{2}} \{\Delta r\}_i = \{\Delta R_i\} \qquad [3.67]$$

Using these incremental displacements, as before, the incremental strains and hence incremental stresses are computed (using Equations 3.46 and 3.51). Then the stress, strain and displacement states corresponding to the i^{th} load step can be computed by summing the respective incremental values as in the basic incremental method (Section 3.5.3.1(i)). The same procedure is repeated for all load steps. Figure 3.9 shows schematically the mid-point Runge-Kutta approach and compares this with the basic incremental method.

3.5.3.2 EQUILIBRIUM ITERATION PROCCEDURE

In principle, the iterative procedure is the same as the Newton-Raphson approach of solving nonlinear equations. This procedure of solving problems with nonlinear material behaviour involves the application of the full load $\{R\}$ in one step. In this case, for the first iteration it is not possible to use the correct modulus (Figure 3.10) of the nonlinear elastic body. Therefore, the computed displacements (hence strains and stresses) are only approximate. It is also clear from Figure 3.10 that under these circumstances, the loads computed from these stresses, $\{R_e\}_{i-1}$, and the actual applied loads $\{R\}$ will be out of balance by $\{R_i\}$, where,

$$\{R_i\} = \{R\} - \{R_e\}_{i-1} \qquad [3.68]$$

This out of balance force $\{R\}_i$ will be used to compute a correction $\{\Delta r\}_i$ for the displacements.

$$[K]_i\{\Delta r\}_i = \{R_i\} \qquad [3.69]$$

where $[K]_i$ is the stiffness matrix computed using the tangent moduli corresponding to the stress state at the previous iteration (Figure 3.10). The incremental stresses and strains can be computed from the displacements. The procedure is repeated until a satisfactory degree of convergence is achieved. Figure 3.10 shows this procedure schematically. The corrected displacements are computed by summing the incremental values as:

$$\{r\}_i = \{r\}_{i-1} + \{\Delta r\}_i \qquad [3.70]$$

where, $\{r\}_i$ is the ith corrected displacement vector. The incremental stresses and strains are similarly summed to obtain corrected stresses and strains respectively.

The computation of the stiffness matrix using tangent moduli for each iteration can be very expensive especially when the required number of iterations for convergence is large. Therefore, in a modification of this method, instead of changing the stiffness matrix for every iteration, the initial stiffness matrix is used for all iterations. It can be clearly seen that this modification increases the number of iterations required for reaching a given degree of convergence (Figure 3.11). In order to overcome this problem, this method is further modified, yet the basic principle remains the same. In this modification, the total load is subdivided into smaller load steps, and iterations

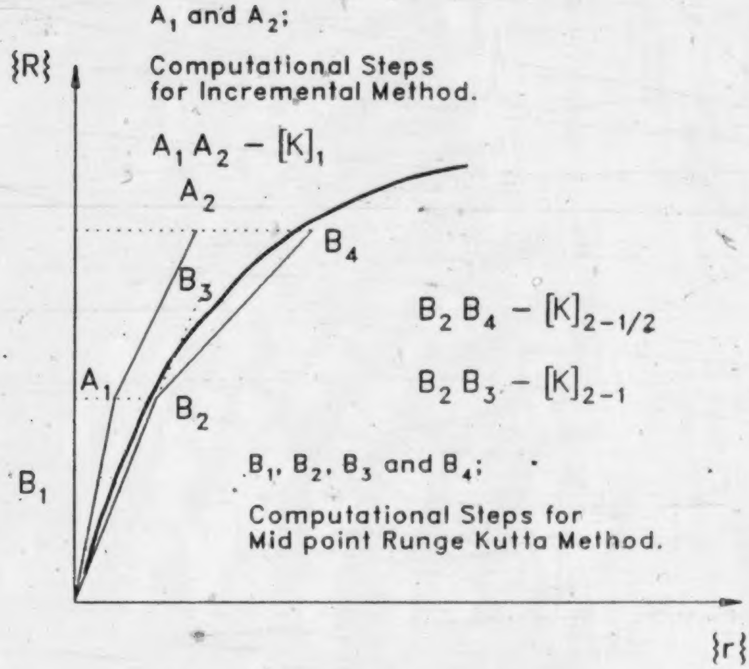
A$_1$ and A$_2$;
Computational Steps for Incremental Method.
A$_1$ A$_2$ – [K]$_1$
{R}
A$_2$
B$_4$
B$_3$
B$_2$ B$_4$ – [K]$_{2-1/2}$
A$_1$
B$_2$ B$_3$ – [K]$_{2-1}$
B$_2$
B$_1$
B$_1$, B$_2$, B$_3$ and B$_4$;
Computational Steps for Mid point Runge Kutta Method.
{r}

Figure 3.9 Basic Incremental Method and Runge-Kutta

Mid-Point Method

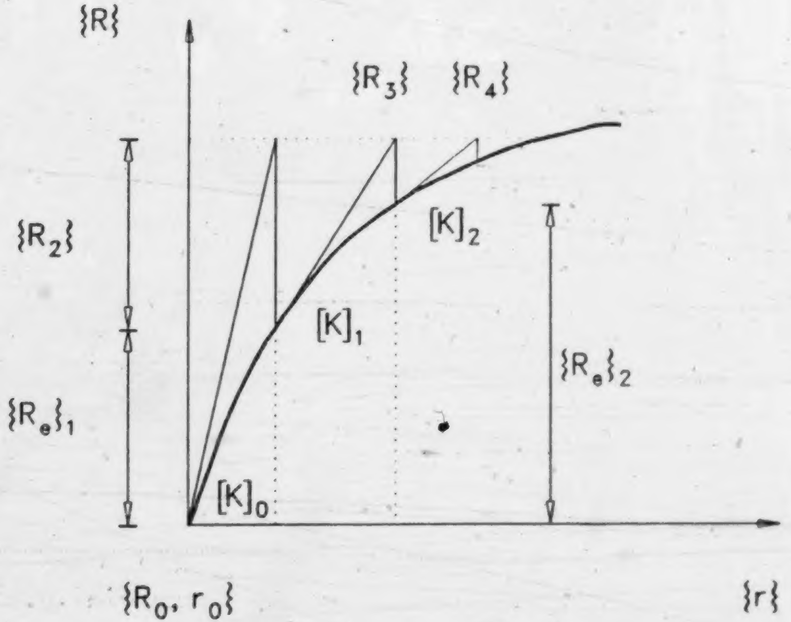
{R}
{R$_3$}
{R$_4$}
{R$_2$}
[K]$_2$
[K]$_1$
{R$_e$}$_2$
{R$_e$}$_1$
[K]$_0$
{R$_0$, r$_0$}
{r}

Figure 3.10 Iterative Procedure

are used for each load step. Within a load step, the constant stiffness matrix computed using the tangent moduli corresponding to the stress state at the end of the previous load step is used. This technique is a combination of iterative and incremental approaches, and is referred to as the mixed iterative method (Figure 3.12).

3.5.3.3 CHOICE OF A SOLUTION TECHNIQUE

In selecting a solution technique, several legitimate questions were raised. If the basic incremental method were used, there is a possibility that the answers will not be sufficiently accurate and that the stress-strain behaviour of the elements will stray considerably from the real stress-strain curves. It is clear that the basic incremental technique can pose problems with respect to numerical accuracy, especially when the size of the load step is large or the strains are large. However, there were different views on the need for using the equilibrium iteration approach. There was no disagreement on the numerical accuracy of the equilibrium iteration method. It was also noted that the proposed finite element analysis is basically applicable for small strains, and therefore, for large strains it may not be very reliable, whatever the solution technique is.

As explained in Chapter 2, the solution technique is merely one link in the complete chain of geotechnical

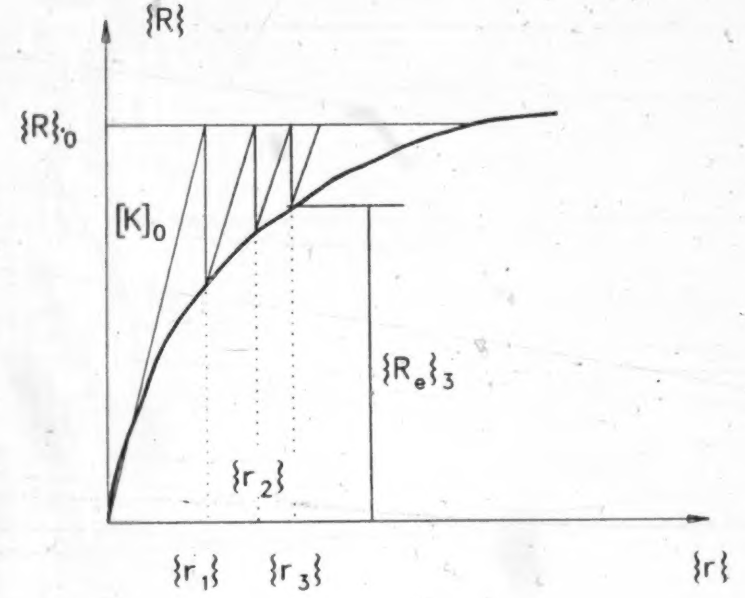
{R}
{R}$_0$
[K]$_0$
{R$_e$}$_3$
{r$_2$}
{r$_1$}
{r$_3$}
{r}

Figure 3.11 Constant Stiffness Iterative Method

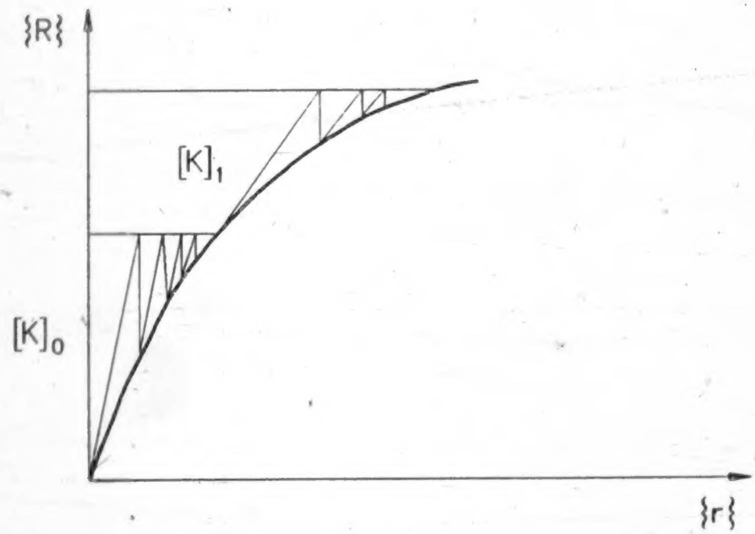

Figure 3.12 Mixed Iterative Approach

engineering design. Therefore, the question of accuracy must be addressed globally. Ideally, the accuracy of each link of the design chain must be nearly the same.

In reality each soil element has a different stress-strain curve. Often, the number of samples taken is not sufficient to represent this scatter accurately. Further, in practice, even for the few samples one has, in a finite element analysis one usually uses the average material parameters. The accuracy of the numerical procedure should be comparable with the accuracy of the other links of the design chain.

A compromise was reached on the basis of the above facts and the concepts of SOM approach (explained in Chapter 2) such as, simplicity, reality and economy. It was decided that the Mid-point Runge-Kutta method was acceptable. It was also decided that if the geotechnical engineer finds it necessary, the accuracy of the numerical procedure be checked with the accuracy of the other links of the design chain. For example, the accuracy of the numerical procedure can be checked with the accuracy of the material properties used. That is, the selected size of the load step for the mid-point Runge-Kutta method must provide sufficiently accurate numerical results. In order to achieve this, the load steps must be halved and the quantities under study (stresses, strains, displacements etc.) must be compared to check whether they fall within the required accuracy (see Section 5.4.3). This procedure has the added advantage that, when the load steps are equal, the consecutive results can be used in Richardson's extrapolation formula. Using this formula, it is possible to obtain a numerically more accurate value for a given quantity. For example, if the settlement δ_p at point P is required to a better accuracy, the Richardson's formula can be applied as follows. For load step size ΔP1, the computed deflection δ_p^1 can be written as,

$$\delta_p^1 = \delta_p + K(\Delta P1)^n$$

where, δ_p is the more accurate value of the deflection and K is an unknown factor.
For load step size ΔP2, the computed deflection δ_p^2 can be written as,

$$\delta_p^2 = \delta_p + K(\Delta P2)^n$$

As in the standard Richardson's extrapolation formula, n can be assumed to be equal to 2, and hence δ_p can be computed. However, the value of n need not be assumed to compute δ_p. If a third trial is made with a different load step size, the values of both δ_p as well as n can be calculated.

It is possible to find the stress-strain behaviour that the finite elements follow during the numerical loading. These stress-strain curves in general, deviate from the theoretical stress-strain curves of the element material. For an economical and reliable numerical solution, these deviations should not exceed the expected scatter of the stress-strain curves of the real soil. With a restricted budget, the advantage of the above compromise solution technique cannot be overemphasized.

3.5.4 SOLUTION OF [K]{r}={R} AND STORAGE PROCEDURE

From the detailed description of the solution techniques, stepwise and iterative, it is clear that both procedures require the solution of a set of linear simultaneous equations of the form, [K]{r}={R}, where, {R} is the known load vector and {r} is the unknown displacement vector. There are two basic approaches to solving this type of a system of simultaneous equations for the displacement vector {r}. One method is the iterative approach where successive improvements are made to a set of initial trial values (of the unknown displacements) until a required convergence accuracy is attained. This method has been applied to large systems of equations resulting from 3-D finite element analysis. However, with the improvement of computing capabilities, direct methods have proven more efficient and reliable (Felippa et al., 1970, White, R. N., 1963 and Schakade, 1969). The solution technique incorporated in our finite element analysis is the second approach, the direct elimination approach. In our case, the Gaussian elimination technique has been used and is suitable to the solution of equilibrium equations. The coefficient matrix of the system of equations is symmetric and banded. Furthermore, it is positive definite, and thus, eliminates the need for pivoting (Desai, C. S. and Abel, J. F.). The major advantage of not having to pivot the system (pivoting destroys the banded nature of the matrix) is the storage saving which leads to cost savings. In addition, the symmetry and the banded nature of the matrix are also used in saving a large volume of storage. One of these storage saving procedures used in the Gaussian elimination is called the block solver approach and has been employed in the finite element program used. The basic steps involved in the block solver are as follows (see also, Figure 3.13). Since the coefficient matrix (N×N) is symmetric and banded (band width 2B-1), only (approximately) a half of the elements(B×N) need storage. Then, this B×N matrix is divided into B×B blocks, starting from the top. At a given time, two of these blocks are taken into the high speed storage. Then the elimination of the top block (B×B) can be completed, because the Gaussian elimination of B rows can influence only B rows below the last row of the top block. The rest of the elements is kept in peripheral storage which in our case is the tape. Once the Gaussian elimination is performed on a B×B block, that block is transferred to a second tape and the elimination of the following B×B block begins. This process is continued block by block until the complete B×N coefficient matrix is Gaussian eliminated. When using B×B blocks, if there is still a problem of high speed storage, using additional tapes, the same technique can be extended to reduce the required storage to 2×B. That is, one block will be 1×B instead of B×B.

3.5.5 VARIATIONAL APPROACH FOR UNCOUPLED CONSOLIDATION

As derived in section 3.2.2, (Equation 3.17) the uncoupled theory can be expressed as follows:

$$\frac{\partial}{\partial x}\left[k_x \frac{\partial h}{\partial x}\right] + \frac{\partial}{\partial y}\left[k_y \frac{\partial h}{\partial y}\right] = \frac{1}{\bar{M}} \frac{\partial u^t}{\partial t} \qquad [3.71]$$

where, $\bar{M}=E_s/2(1+\nu)(1-2\nu)$.

At steady state,

$$\frac{\partial}{\partial x}\{k_x \frac{\partial}{\partial x}\left[\frac{\partial u_{ss}}{\partial x}\right]\} + \frac{\partial}{\partial y}\{k_y \frac{\partial}{\partial y}\left[\frac{\partial u_{ss}}{\partial y}\right]\} = 0 \qquad [3.72]$$

where, u_{ss} is the steady state pore pressure, and

$$u^t = u + u_{ss} \qquad [3.73]$$

where, u is the excess pore pressure. Therefore, Equations 3.71 and 3.72 yield,

$$\frac{\partial}{\partial x}\left[k_x \frac{\partial u}{\partial x}\right] + \frac{\partial}{\partial y}\left[k_y \frac{\partial u}{\partial y}\right] = \frac{\gamma_w}{\bar{M}} \frac{\partial u}{\partial t} \qquad [3.74]$$

This equation and the boundary conditions form the simplified uncoupled solution. This form of equation is known as the governing equation of consolidation under Rendulic conditions.

For the variational formulation, the following functional must be considered (Figure 3.14):

$$\Omega = \int_S \left[\frac{1}{2}\{(k_x \frac{\partial u}{\partial x})^2 + (k_y \frac{\partial u}{\partial x})^2\} + \frac{\gamma_w}{\bar{M}} \frac{\partial u}{\partial t} u\right] dS + \int_{s_1} q_0 u ds \qquad [3.75]$$

For a change in u of δu at time t,

$$\delta\Omega = \int_S \left[k_x \frac{\partial u}{\partial x} \frac{\partial\{\delta u\}}{\partial x} + k_y \frac{\partial u}{\partial y} \frac{\partial\{\delta u\}}{\partial y} + \frac{\gamma_w}{\bar{M}} \frac{\partial u}{\partial t} \delta u \right] dS + \int_{s_1} q_0 \delta u ds \qquad [3.76]$$

After simplification, rearrangement and using Stokes' theorem, the Equation becomes,

$$\delta\Omega = - \int_S \left[\frac{\partial}{\partial x} \{k_x \frac{\partial u}{\partial x}\} + \frac{\partial}{\partial y} \{k_y \frac{\partial u}{\partial y}\} - \frac{\gamma_w}{\bar{M}} \frac{\partial u}{\partial t} \right] \delta u dS + \int_{s_1} \left[q_0 - \bar{v}.\bar{n} \right] \delta u ds \qquad [3.77]$$

For Ω to be an extremum at time t,

$$\frac{\partial}{\partial x} \left[k_x \frac{\partial u}{\partial x} \right] + \frac{\partial}{\partial y} \left[k_x \frac{\partial u}{\partial y} \right] - \frac{\gamma_w}{\bar{M}} \frac{\partial u}{\partial t} = 0 \qquad [3.78]$$

$$\text{and } q_0 - \bar{v}.\bar{n} = 0 \qquad [3.79]$$

This proves that the above functional yields the governing equations of consolidation and the boundary conditions. Note that the function u is selected such that it satisfies the essential boundary conditions. The following sections discuss how the above functional was used in the finite element formulation.

3.5.6 FINITE ELEMENT VARIATIONAL FORMULATION FOR UNCOUPLED ANALYSIS

A simple finite element type consisting of three nodes with a linear pore pressure distribution was used, i.e.:

$$\hat{u} = \sum_{i=1}^{3} \zeta_i \hat{u}_i \qquad [3.80]$$

where,

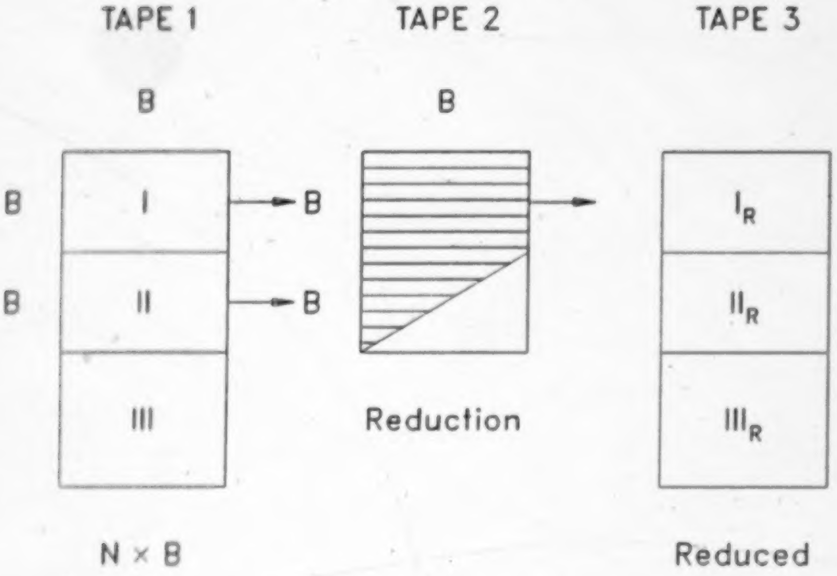
TAPE 1
TAPE 2
TAPE 3
B
B
B
I
B
B
II
B
III
Reduction
I_R
II_R
III_R
N × B
Reduced

Figure 3.13 Block Solver Technique

(after Murray, 1985 : modified)

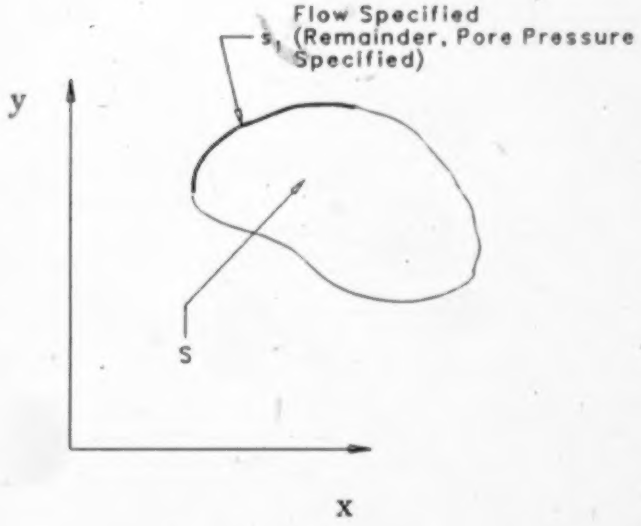
Flow Specified
s_1 (Remainder, Pore Pressure Specified)
y
s
x

Figure 3.14 Consolidation Boundary Value Problem

$\mathring{U}$ is the element pore pressure,

$\mathring{u}_i$ is the nodal pore pressure at node i of an element and

ζ_i's are the interpolation functions (natural coordinates).

$$\frac{\partial}{\partial x} = \frac{1}{\Delta}\sum_{i=r}^{3} b_i \frac{\partial}{\partial \zeta_i} \qquad [3.81]$$

$$\frac{\partial}{\partial y} = \frac{1}{\Delta}\sum_{i=1}^{3} a_i \frac{\partial}{\partial \zeta_i} \qquad [3.82]$$

where,

$a_1 = x_3 - x_2$, $b_1 = y_2 - y_3$,

$a_2 = x_1 - x_3$, $b_2 = y_3 - y_1$,

$a_3 = x_2 - x_1$, $b_3 = y_1 - y_2$ and

Δ is the area of the element.

Therefore,

$$\frac{\partial u}{\partial x} = \frac{1}{\Delta}\sum_{i=1}^{3}\left[b_i \mathring{u}_i\right] \qquad [3.83]$$

$$\frac{\partial u}{\partial y} = \frac{1}{\Delta}\sum_{i=1}^{3}\left[a_i \mathring{u}_i\right] \qquad [3.84]$$

Variational formulation of uncoupled consolidation given in Equation 3.75 is:

$$I = \int_s \left[\frac{1}{2} \{k_x \frac{\partial u}{\partial x} \}^2 + \{k_y \frac{\partial u}{\partial x} \}^2 + \frac{\gamma_w}{\bar{M}} \frac{\partial u}{\partial t} u\right]dS + \int_{s_1} q_0 u ds \qquad [3.85]$$

Since the $\mathring{U}$'s are continuous across the elements, the total integral can be written as a summation of the element integrals:

$$I = \Sigma I_e \qquad [3.86]$$

Substituting the assumed pore pressure distribution into

Equation 3.85 yields,

$$I_e = \frac{1}{8\Delta^2}\int_s \langle\mathring{u}\rangle\left[k_x\{b\}\langle b\rangle + k_y\{a\}\langle a\rangle - \langle\mathring{u}\rangle\{\zeta\}\frac{\partial}{\partial t}\langle\zeta\rangle\{\mathring{u}\}\right]dS + \langle\mathring{u}\rangle\{P_e\} \qquad [3.87]$$

where,

$$\langle\mathring{u}\rangle\{P_e\} = \int_s \langle\mathring{u}\rangle\{\zeta\}q_0 ds \text{ and}$$

$$\int_s \left[\langle\mathring{u}\rangle\{\zeta\}\frac{\partial}{\partial t}\langle\zeta\rangle\{\mathring{u}\}\right]dS = \langle\mathring{u}\rangle[C]\{\dot{u}\}$$

If the summation is made in global coordinates,

$$I = \frac{1}{2}\langle u\rangle[H]\{u\} - \langle u\rangle[C]\{\dot{u}\} + \langle u\rangle\{P\} \qquad [3.88]$$

where,

$$\dot{u} = \frac{\partial u}{\partial t}\ .$$

As in the case of virtual work formulation, there are free nodes and those nodes where the value of u is specified. Therefore, Equation 3.88 can be written as:

$$I = \frac{1}{2}\langle u_f\ u_s\rangle[H]\begin{vmatrix}u_f\\u_s\end{vmatrix}\ \langle u_f\ u_s\rangle[C]\begin{vmatrix}\dot{u}_f\\\dot{u}_s\end{vmatrix} + \langle u_f\ u_s\rangle\begin{vmatrix}P_f\\P_s\end{vmatrix} \qquad [3.89]$$

where,

u_f is pore pressure at free nodes and

u_s is specified pore pressure.

Note that $\{\dot{u}_s\} = \{0\}$, hence

$$\delta I = \langle\delta u_f\ 0\rangle[H]\begin{vmatrix}u_f\\u_s\end{vmatrix} - \langle\delta u_f\ 0\rangle[C]\begin{vmatrix}\dot{u}_f\\0\end{vmatrix} + \langle\delta u_f\ 0\rangle\begin{vmatrix}P_f\\P_s\end{vmatrix} \qquad [3.90]$$

It is clear that $\langle\delta u_s\rangle=\langle 0\rangle$. Note also that [H] can be written in the following form:

$$[H] = \begin{vmatrix}H^{ff} & H^{fs}\\H^{sf} & H^{ss}\end{vmatrix} \qquad [3.91]$$

From the variational principle, for an arbitrary $<\delta u_f>$, δI must be zero. That is,

$$<\delta u_f>[H^{ff}]\{u_f\} + [H^{fs}]\{u_s\} - [C]\{\dot{u}_f\} - \{P_f\}] = 0 \qquad [3.92]$$

Since $<\delta u_f>$ is arbitrary,

$$[H^{ff}]\{u_f\} - [C]\{\dot{u}_f\} + [H^{fs}]\{u_s\} - \{P_f\} = 0 \qquad [3.93]$$

This is the first stage of the finite element formulation of consolidation. The second stage, the finite element formulation in the time domain, is discussed in the following sections.

3.5.7 CONSOLIDATION FINITE ELEMENTS IN THE TIME DOMAIN

There are several finite element approaches that can handle the time domain of the uncoupled consolidation theory. The weighted residual approach is the simplest and the most straightforward method. This approach was implemented in the numerical procedure used. The governing finite element Equation 3.93 derived in the previous Section can in general be written in the form,

$$[H]\{u\} + [C]\{\dot{u}\} + \{g\} = 0 \qquad [3.94]$$

Since time is an independent variable, the discretization of u in the time domain can be done in the following manner.

$$\overline{u} = \Sigma N_i \overline{u}_i \qquad [3.95]$$

where,

$\overline{u}$ is the nodal pore pressure vector at time t,

$\overline{u}_i$ is the nodal pore pressure vector in time element i (or ith time step) and

N_i's are the shape functions and are the same for each component of vector $\overline{u}_i$ and, therefore, are scalars.

The general weighted residual finite element equation can be written as:

$$\int_0^t w_j\Big[[C]\{\overline{u}_i\dot{N}_i\} + [H]\{\overline{u}_iN_i\} + \{g\}\Big]dt = 0 \qquad [3.96]$$

where, w_j is the weighting function. For a typical element of length Δt with nodal values $\overline{u}_i$ and $\overline{u}_{i+1}$, the linear shape functions can be written in the form,

$$N_i = 1-\xi$$

$$N_{i+1} = \xi$$

$$0\leq\xi\leq1$$

$$\dot{N}_i = -\frac{1}{\Delta t}$$

$$\dot{N}_{i+1} = +\frac{1}{\Delta t}$$

Therefore, the weighted residual Equation becomes,

$$\int_0^1 w_j\Big[[C]\{-\overline{u}_i\frac{1}{\Delta t} + \overline{u}_{i+1}\frac{1}{\Delta t}\}$$

$$+ [H]\{\overline{u}_i(1-\xi) + \{\overline{u}_{i+1}\xi\} + \{g\}\Big]d\xi = 0 \qquad [3.97]$$

OR

$$\Big[\frac{1}{\Delta t}[C] + [H]\theta\Big]\overline{u}_{i+1} + \Big[[H](1-\theta) - \frac{1}{\Delta t}[C]\Big]\overline{u}_i +$$

$$\overline{g} = 0 \qquad [3.98]$$

where,

$$\theta = \int_0^1 w_j\xi d\xi \Big/ \int_0^1 w_j d\xi \text{ and}$$

$$\overline{g} = \int_0^1 w_j\{g\}d\xi \Big/ \int_0^1 w_j d\xi.$$

In our case, $w_j=1$ for $0\leq t\leq\Delta t$, thus θ becomes $\frac{1}{2}$. This is equivalent to the Crank-Nicolson approach of finite differences. The important implication of the choice of this weighting function is that the system of equations is unconditionally stable. Similar to the equilibrium equations, the coefficient matrix of these consolidation equations is symmetric and banded, therefore, a storage procedure similar to that described in section 3.4.4 can be used in the solution process. The same Gaussian elimination technique has also been used for the solution of the equations. Since the soil properties are assumed to be independent of time, and linear elasticity is assumed, the problems of solving the equilibrium equations with nonlinear soil properties do not arise in this case. Only one solution is necessary for each time element. However, certain guidelines were followed in selecting the size of the time element for reliable results (see section 3.6).

3.5.8 CAM CLAY MODEL IN FINITE ELEMENT DISPLACEMENT FORMULATION

As explained in the foregoing sections, Cam-Clay model was used for computing the displacements due to the dissipation of pore pressure. The details of the Cam-Clay model are given in section 2.2.1.1. The finite element types, the integration points and the solution techniques used here are the same as described for the hyperbolic model in sections 3.5.1 to 3.5.4. The major difference is in the formulation of the constitutive matrix. This formulation of the constitutive matrix for the modified Cam-Clay Model is as follows. It must be noted that all Cam-Clay parameters can be obtained using one isotropic consolidation and swelling test, and one conventional triaxial compression test.

(i) PLASTIC BEHAVIOUR

Chang et al. (1983) approximated the Modified Cam Clay yield function for plane strain conditions as (Figure 3.16):

$$\left[\frac{M^2+\eta^2}{M^2}\right](p'_r+p') - (p'_r+p'_0) = 0 \qquad [3.99]$$

where,

p' $= \frac{1}{3}(\sigma'_x+\sigma'_y+\sigma'_z)$,

q $= \sqrt{\frac{1}{2}\left[(\sigma_x-\sigma_y)^2 + (\sigma_y-\sigma_z)^2 + (\sigma_z-\sigma_x)^2 + 6\tau_{xy}{}^2\right]}$,

η $= \frac{q}{p'_r+p'}$,

p'_r is defined in Figure 3.16,

p' is the octahedral normal effective stress,

M is defined in Equation 3.100,

q is the octahedral shear stress and

p'_0 is the p' corresponding to the pre-consolidation pressure.

The failure is defined by the critical state of the soil. Therefore, the failure conditions are given by

$$q = M(p' + p'_r) \qquad [3.100]$$

When $q<Mp'+p'_r$, for an appropriate stress increment, stable work hardening occurs and the yield surface expands. For an

outward probing stress increment, if $q \geq Mp' + p'_r$, then the soil reaches critical state, or unstable strain softening takes place with the collapsing of the yield surface. The proposed finite element analysis cannot be used to model the strain softening behaviour. The hardening rule in this case is,

$$e = e_a - \lambda \log(p'_0) \qquad [3.101]$$

where,

e_a is the void ratio that corresponds to a unit p' and

λ is the approximate constant slope of the virgin consolidation curve on a semi-log plane.

The Cam-Clay model employs an associated flow rule. Although there are some constitutive models that use nonassociated flow rules, the models that use associated flow rules have given reliable results in the past (Johnston et al., 1983). They have the added advantage of providing a symmetric stiffness matrix which can reduce the storage and computational cost by a considerable amount. The Cam-Clay yield function can be expressed in the following general manner.

$$F(\sigma_{ij}, p'_0) = 0 \qquad [3.102]$$

For consistency condition,

$$\frac{\partial F}{\partial \sigma_{ij}} d\sigma_{ij} + \frac{\partial F}{\partial p'_0} dp'_0 = 0 \qquad [3.103]$$

For the Cam clay theory,

$$d\varepsilon^p_v = \frac{\lambda-\kappa}{p'_0(1+e)} dp'_0 \qquad [3.104]$$

where,

κ is the slope of isotropic swelling curve on a semi-log plane and

$d\varepsilon^p_v$ is plastic volume strain.

Substituting for dp'_0 in 3.103 yields:

$$\frac{\partial F}{\partial \sigma_{ij}} d\sigma_{ij} + \frac{\partial F}{\partial p'_0} \frac{p'_0(1+e)}{\lambda-\kappa} d\varepsilon^p_v = 0 \qquad [3.105]$$

But,

$$d\varepsilon^e_{kl} = d\epsilon_{kl} - d\varepsilon^p_{kl} \text{ and} \qquad [3.106]$$

$$d\sigma_{ij} = C^e_{ijkl}(d\epsilon_{kl} - d\varepsilon^p_{kl}) \qquad [3.107]$$

where,

$d\varepsilon^e_{kl}$ is elastic strain tensor and

C^e_{ijkl} is elastic constitutive tensor.

The Cam clay model uses an associated flow rule and therefore,

$$d\varepsilon^p_{ij} = \psi \frac{\partial F}{\partial \sigma_{ij}} \qquad [3.108]$$

Substitution of 3.106, 3.107 and 3.108 in 3.105 yields,

$$\frac{\partial F}{\partial \sigma_{ij}} C^e_{ijkl}\left[d\epsilon_{kl} - \psi \frac{\partial F}{\partial \sigma_{kl}}\right] + \frac{\partial F}{\partial p'_0} \frac{p'_0(1+e)}{\lambda-\kappa} \psi \frac{\partial F}{\partial \sigma_{kk}} = 0 \qquad [3.109]$$

hence,

$$\psi = \frac{\partial F}{\partial \sigma_{ij}} C^e_{ijkl} d\epsilon_{kl} \Big/ \left[\frac{\partial F}{\partial \sigma_{ij}} C^e_{ijkl} \frac{\partial F}{\partial \sigma_{kl}} - \frac{\partial F}{\partial p'_0} \frac{p'_0(1+e)}{\lambda-\kappa} \frac{\partial F}{\partial \sigma_{kk}}\right] \qquad [3.110]$$

Equations 3.107 and 3.108 yield,

$$d\sigma_{ij} = C^e_{ijkl}\left[\left(d\epsilon_{kl} - \psi \frac{\partial F}{\partial \sigma_{kl}}\right)\right] \qquad [3.111]$$

Substituting for ψ from 3.110 in 3.111 yields the elastoplastic constitutive matrix given below.

$$\mathcal{C}^{ep}_{ijkl} = \mathcal{C}^{e}_{ijkl} - \mathcal{C}^{e}_{ijrs} \frac{\partial F}{\partial \sigma_{rs}} \frac{\partial F}{\partial \sigma_{pq}} \mathcal{C}^{e}_{pqkl} /$$

$$\left[\frac{\partial F}{\partial \sigma_{pq}} \mathcal{C}^{e}_{pqrs} \frac{\partial F}{\partial \sigma_{rs}} - \frac{\partial F}{\partial p'_0} \frac{p'_0(1+e)}{\lambda - \kappa} \frac{\partial F}{\partial \sigma_{kk}} \right] \qquad [3.112]$$

For the Cam clay model, and the plane strain conditions:

$$\frac{\partial F}{\partial \sigma_x} = \frac{2\sigma_x - \sigma_y - \sigma_z}{M^2(p' + p'_r)} + \frac{M^2 - \eta^2}{3M^2} \qquad [3.113]$$

$$\frac{\partial F}{\partial \sigma_y} = \frac{2\sigma_y - \sigma_z - \sigma_y}{M^2(p' + p'_r)} + \frac{M^2 - \eta^2}{3M^2} \qquad [3.114]$$

$$\frac{\partial F}{\partial \sigma_z} = \frac{2\sigma_z - \sigma_x - \sigma_y}{M^2(p' + p'_r)} + \frac{M^2 - \eta^2}{3M^2} \qquad [3.115]$$

$$\frac{\partial F}{\partial \tau_{xy}} = \frac{6\tau_{xy}}{M^2(p' + p'_r)} \text{ and} \qquad [3.116]$$

(ii) ELASTIC BEHAVIOUR

Inside the yield surface, the modified Cam-Clay model assumes nonlinear elastic behaviour.

The bulk modulus K is defined as:

$$\frac{dp'}{d\epsilon_v} = - \frac{dp'}{de}(1 + e) \qquad [3.117]$$

For the isotropic rebound curve of soil:

$$\frac{dp'}{de} = - \frac{p'}{\kappa} \qquad [3.118]$$

Therefore, the bulk modulus,

$$K = \frac{p'}{\kappa}(1 + e) \qquad [3.119]$$

where,

κ is the slope of the rebound curve on a semi-log scale, e is the void ratio,

p' is the mean normal effective stress and

ϵ_v volumetric strain.

It has been found (Johnston et al., 1983) that a Poisson's ratio value of 0.3 for clays gives satisfactory results, and this value was used in the finite element formulation. For the case of plane strain, the elastic matrix can be written in the following manner:

$$[C^e] = \frac{E}{(1+v)(1-2v)} \begin{vmatrix} 1-v & v & v & 0 \\ v & 1-v & v & 0 \\ v & v & 1-v & 0 \\ 0 & 0 & 0 & (1-2v)/2 \end{vmatrix} \qquad [3.120]$$

for the strain vector $<\epsilon_x\ \epsilon_y\ \epsilon_z\ \tau_{xy}>$, where,

E is the Young's modulus and

v is the Poisson's ratio.

Only the normally and lightly overconsolidated clay behaviour can be simulated accurately using this programme because it does not use a separate yield surface for overconsolidated clays.

3.6 VERIFICATION OF FINITE ELEMENT CODES

The final part of a numerical scheme is the coded program. It is essential that this program be verified and tested as much as possible before being used to solve practical problems to obtain reliable results.

The verification was carried out in two stages. In stage one, the results of the program obtained for simple and small (small enough to permit hand calculations) meshes were compared with hand calculations. This verification attempts to ensure that the coded program performs the computations that are expected of it by the programmer. The second stage compares the results with possible closed form solutions or those close to them. These verifications attempt to ensure that the theory has been applied properly in the numerical procedure. The following sections present the cases of such verifications. Hand calculations are not presented.

3.6.1 NON LINEAR ELASTIC FINITE ELEMENT MODEL

The finite element model discussed in sections 3.5.1, 3.5.2 and 3.5.3 uses the nonlinear hyperbolic stress strain model. Closed form solutions obtained using the hyperbolic model are nonexistent and impossible even for very simple geotechnical engineering problems. It is only possible to obtain closed form solutions for extremely simple cases, such as those described below. The closed form solution of the plane strain behaviour of a typical soil sample shown in Figure 3.15 (a) was obtained using the hyperbolic theory described in section 3.4.1.1 The sample is K_0 (=0.77) consolidated and has a width to height ratio of 2:1. The s_u/σ_{1c} values for compression and extension were 0.6 and 0.4, respectively. The normalized initial modulus, E_i/σ_{1c} was 3000, failure ratio R_f was 0.9 and the vertical consolidation stress σ_{yc} was 300 kN/m^2. The closed form

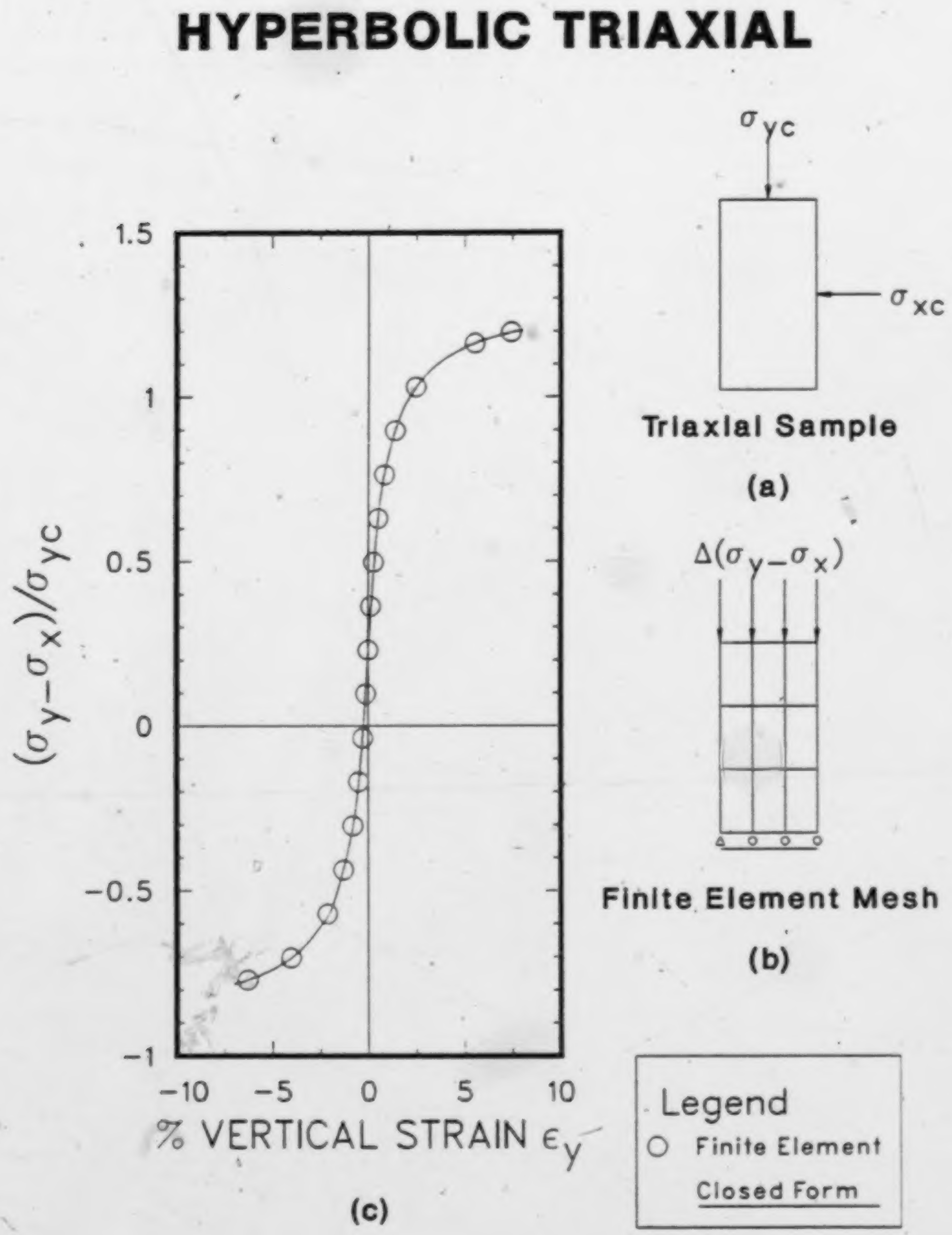

Figure 3.15 Closed Form and Finite Element Stress-Strain Solutions using Hyperbolic Models

solution obtained (using Equations 3.25 and 3.26) for the stress-strain behaviour of this sample in both (plane strain) compression and extension is shown in Figure 3.15 (c).

For finite element analysis, the soil sample was discretized as shown in Figure 3.15 (b). Using the proposed finite element model, the stress-strain behaviour in both compression and extension for the soil sample was simulated. The vertical load was increased in equal steps to simulate the compression test. The plane strain triaxial conditions were simulated with the boundary conditions shown in Figure 3.15 (b). The extension behaviour was simulated by unloading (the vertical load) the element with equal load steps. In both cases, the load steps were halved until a required accuracy (see also section 3.5.3.3) in the stress-strain results was obtained. Equal (except for the last step) steps of 16 load increments/reductions yielded satisfactory results for both compression and extension and are presented in Figure 3.15(c). As expected, the agreement between the closed form and finite element results are very satisfactory.

3.6.2 CAM CLAY FINITE ELEMENT MODEL

Using Roscoe et al.'s (1968) simplifications given below, it is possible to obtain quasi-closed form solutions for the simplest cases of plane strain triaxial and plane strain simple shear situations. Since this approach is different from the finite element approach, it is suitable for the verification of the finite element code. For the triaxial case, with the usual notation, the Cam-Clay yield curve can be expressed as:

$$\frac{p'}{p'_0} = \frac{M^2}{(M^2+\eta^2)} \qquad [3.121]$$

This Equation when expressed in terms of z and r (Figure 3.17(a)) becomes,

$$\frac{z}{z_0} = \frac{M^2}{M^2+9r^2/2z^2} \qquad [3.122]$$

where for the triaxial case,

z = $\sqrt{3}p$; projected distance along the space diagonal of the stress point and

r = $\sqrt{\frac{2}{3}}q$; perpendicular distance to the space diagonal from the stress point.

The above form was used to derive the general three dimensional Cam-Clay model. The solid of revolution of the triaxial Cam-Clay model along the space diagonal is considered to generate the general three dimensional Cam-Clay model (Figure 3.17(b)). However, in the general three dimensional case,

z = $\frac{1}{\sqrt{3}}(\sigma'_1+\sigma'_2+\sigma'_3)$,

r = $\frac{1}{\sqrt{3}}[(\sigma_1-\sigma_2)^2+(\sigma_2-\sigma_3)^2+\sigma_1-\sigma_2)^2]^{\frac{1}{2}}$ and

M^* = $\sqrt{\frac{2}{3}}M$.

and, therefore the general three dimensional yield surface becomes,

$$f = (M^{*2}+6)[\sigma_1'^2 + \sigma_2'^2 + \sigma_3'^2] + 2(M^{*2}-3)[\sigma'_1\sigma'_2 + \sigma'_2\sigma'_3 + \sigma'_3\sigma'_1] -$$

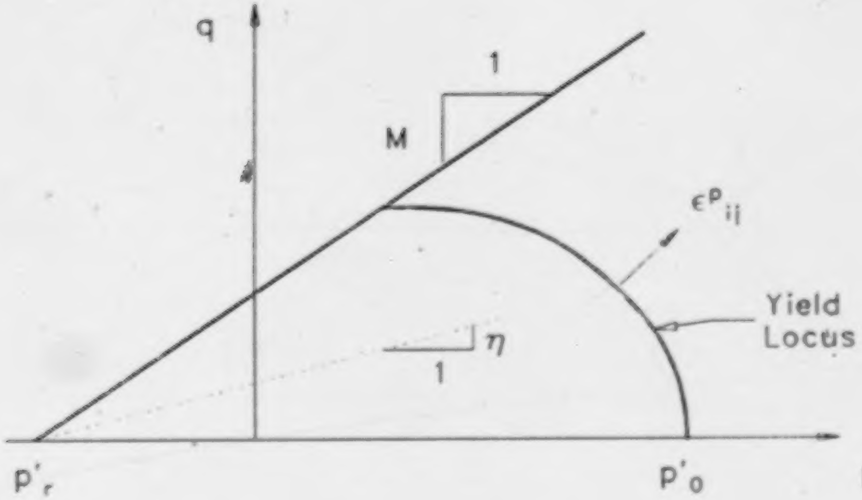
q
1
M
ϵ^p_{ij}
Yield Locus
η
1
p'_r
p'_0
p'

Figure 3.16 Cam-Clay Model in Plane Strain

(after Chang et al., 1983 : modified)

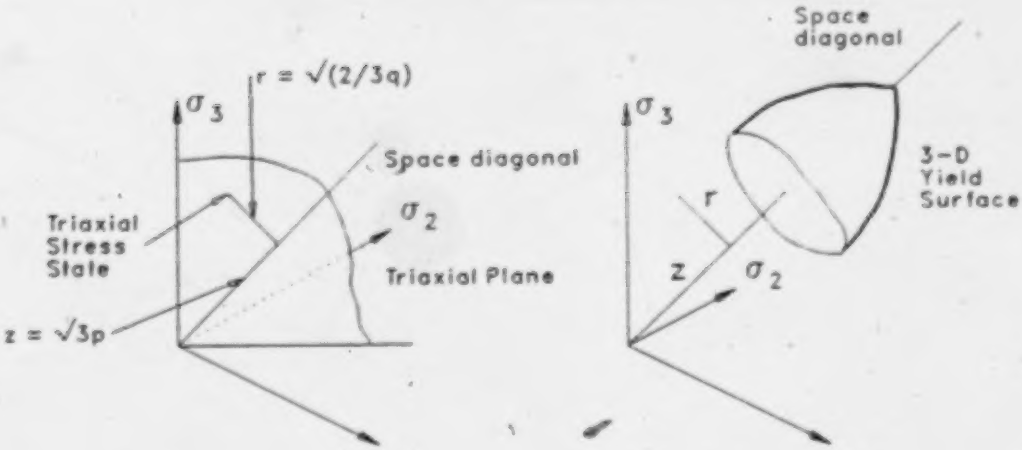
$r = \sqrt{(2/3q)}$
σ_3
Space diagonal
Triaxial Stress State
σ_2
Triaxial Plane
$z = \sqrt{3p}$
σ_1
(a)
Space diagonal
σ_3
3-D Yield Surface
r
z
σ_2
σ_1
(b)

Figure 3.17 Three Dimensional Cam-Clay Model

$$3M^{*2}p_0[\sigma'_1 + \sigma'_2 + \sigma'_3] = 0 \qquad [3.123]$$

For cases where, κ is negligible compared to λ, the plane strain conditions yield,

$$\frac{\partial f}{\partial \sigma'_2} = 0 \qquad [3.124]$$

which implies,

$$\sigma'_2 = \frac{3M^{*2}p_0 - 2(M^{*2}-3)(\sigma'_1+\sigma'_3)}{2(M^{*2}+6)} \qquad [3.125]$$

Hence the plane strain yield curve projected on (σ'_1, σ'_2) becomes,

$$2(M^{*2}+3)(\sigma'^2_1+\sigma'^2_3) - 3M^{*2}p_0(\sigma'_1+\sigma'_3) + 2(M^{*2}-3)\sigma'_1\sigma'_3$$
$$- \frac{M^{*2}p_0}{4} = 0 \qquad [3.126]$$

In (s,t) space, the yield locus becomes,

$$6M^{*2}s^2+2(M^{*2}+6)t^2 - 6M^{*2}p_0 s - \frac{M^{*2}p_0}{4} = 0 \qquad [3.127]$$

where,

$$s = \frac{\sigma'_1+\sigma'_3}{2} \text{ and}$$
$$t = \frac{\sigma'_1-\sigma'_3}{2}.$$

When further simplified, the yield curve becomes,

$$(\eta')^2 = \left[\frac{s_0}{s}\Theta - 1\right] \frac{M^2}{3(A-1)^2} \qquad [3.128]$$

where,

$$\eta' = \frac{t}{s},$$

$$A = 1+\sqrt{(1+M^{*2}/9)} \text{ and}$$

$$\Theta = \left[\frac{M^2 s_0}{9A^2 s} + \frac{2}{A}\right].$$

When $t=0$, $s=s_0$.

For most soils, $0.7<M<1.2$, and, in this range, $2.028<A<2.078$, $1<\frac{s_0}{s}<2$ and $0.999<\theta<1.038$. Hence, the yield locus can be approximated to,

$$\frac{s}{s_0} = \frac{(M/\sqrt{3})^2}{(M/\sqrt{3})^2 + \eta'^2} \quad (A=2,\ \theta=1) \qquad [3.129]$$

3.6.2.1 PLANE STRAIN TRIAXIAL STRESS-STRAIN BEHAVIOUR

The simplified yield locus derived for plane strain conditions by Roscoe et al. (1968) is utilized to obtain the stress-strain behaviour of a typical soil sample shown in Figure 3.18 (a). As in the nonlinear elastic case, the soil sample has a height to width ratio of 2 and the soil parameters chosen are: $\lambda = 0.16$, $M = 0.9$, $e_0 = 1.0$, $\nu = 0.3$, $\kappa = 0.0032$ and $\sigma_{yc} = 300$ kN/m^2. For consistency, K_0 was computed using the following Equation derived from Cam-Clay theory.

$$\eta_{K_0}^2 + 3\left[1-\frac{\kappa}{\lambda}\right]\eta_{K_0} - M^2 = 0 \qquad [3.130]$$

$$K_0 = \frac{3 - \eta_{K_0}}{2\eta_{K_0} + 3} \qquad [3.131]$$

Solution of these two Equations yields, $K_0 = 0.77$ and this value was used in the computations that follow. From Equation 3.129:

$$-\frac{ds}{dt} = \frac{1}{\Psi} = \frac{2\eta'}{(M/\sqrt{3})^2-\eta'^2} \qquad [3.132]$$

From energy considerations, the following Equation can be derived.

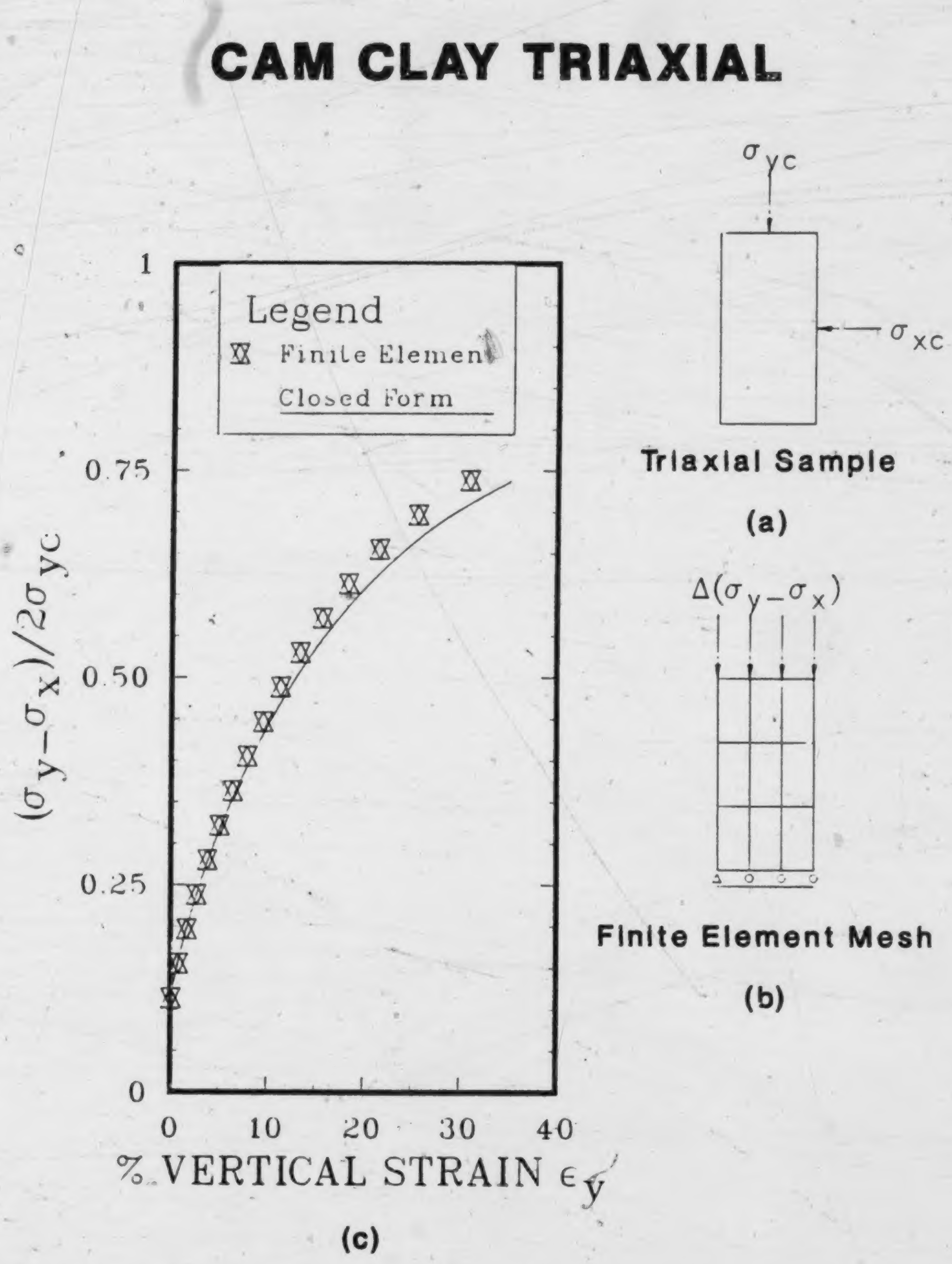

Triaxial Sample

(a)

Finite Element Mesh

(b)

(c)

Figure 3.18 Finite Element and Quasi-Closed form Solutions for Plane Strain Triaxial Test using Cam-Clay Model

$$-\frac{ds}{dt} = \frac{d\gamma}{dv} \qquad [3.133]$$

where,

$$\delta v = \delta\epsilon_1 + \delta\epsilon_3 \qquad [3.134]$$

and

$$\delta\gamma = \delta\epsilon_1 - \delta\epsilon_3. \qquad [3.135]$$

The preceding simplified concepts will be used to obtain a quasi-closed form solution (numerical) for the stress-strain behaviour under triaxial plane strain conditions. In this numerically simulated plane strain triaxial test, the stresses are increased (decreased for extension) in steps. For a given stress increment, let δs and δt be the corresponding increments in s and t.

Let

$s_2 = s_1 + \delta s$

$t_2 = t_1 + \delta t$

$\eta_2 = \eta_1 + \delta\eta$

$s = s_1 + \frac{\delta s}{2}$

$t = t_1 + \frac{\delta t}{2}$ and

$\eta = \eta_1 + \frac{\delta\eta}{2}$.

By analogy, (from the modified Cam-Clay theory for triaxial conditions)

$$\delta v = \frac{\lambda}{1 + e}(\Omega\delta\eta' + \frac{\delta s}{s}) \qquad [3.136]$$

where,

$$\Omega = \frac{2\eta'}{(M/\sqrt{3})^2 + \eta'^2}.$$

Void ratio e and η' are known from the initial conditions for the first load step and from the previous load step for the subsequent load steps. Hence δv can be computed from Equation 3.136.

$$e = e_1 - (1 + e)\delta v/2 \qquad [3.137]$$

The value of e may be computed to a greater accuracy by employing the FORTRAN Equation 3.137 for iterations. The following Equation is used to compute $\delta\gamma$. The value of Ψ is computed using Equation 3.132.

$$\delta\gamma = \frac{1}{\Psi}\delta v \qquad [3.138]$$

Using Equations 3.134 and 3.135, $\delta\epsilon_1$ and $\delta\epsilon_3$ are computed. The above process is repeated for each step. For greater numerical accuracy, iterations were used for each step until the required convergence in void ratio was achieved (Equation 3.137). The stress increments were also halved and the results were compared with the full increment results (section 3.5.3.3) to check the accuracy. For the soil sample under consideration, using the known initial conditions, the stress-strain curve in compression was obtained as explained above. The results shown in Figure 3.18(c) were obtained using 20 steps of load increments.

The soil sample was discretized as shown in Figure 3.18(b). As in the preceding case, the boundary conditions shown in Figure 3.18(b) simulate the plane strain triaxial test. Using the finite element analysis described in section 3.5.8, the stress-strain relation was obtained for compression conditions. As outlined in the preceding Section, the compression test was simulated by increasing the load by equal steps. Until the required accuracy was obtained, the load steps were also halved and the results were compared with that of full-load step results. With equal (except for the last step) steps of 16 the compression test simulation yielded satisfactory results. These results shown in Figure 3.18 (c), are compared with the quasi-closed form solution obtained previously. As expected, the two sets of results are very close. The slight deviation is probably due to approximations made in the closed form solution.

3.6.2.2 PLANE STRAIN SIMPLE SHEAR STRESS-STRAIN BEHAVIOUR

The plane strain simple shear test was simulated, and the finite element and the quasi-closed form results were compared. In the drained simple shear apparatus under consideration, the vertical normal stress σ'_y, remains unaltered during the test. Furthermore, the horizontal normal strain ϵ_x, remains zero. A typical soil sample used in the simple shear test is shown in Figure 3.19(a). The same sample was used in the numerical simulations of the simple shear test. It had an approximate length to height ratio of 3. The soil parameters used were the same as those used in the

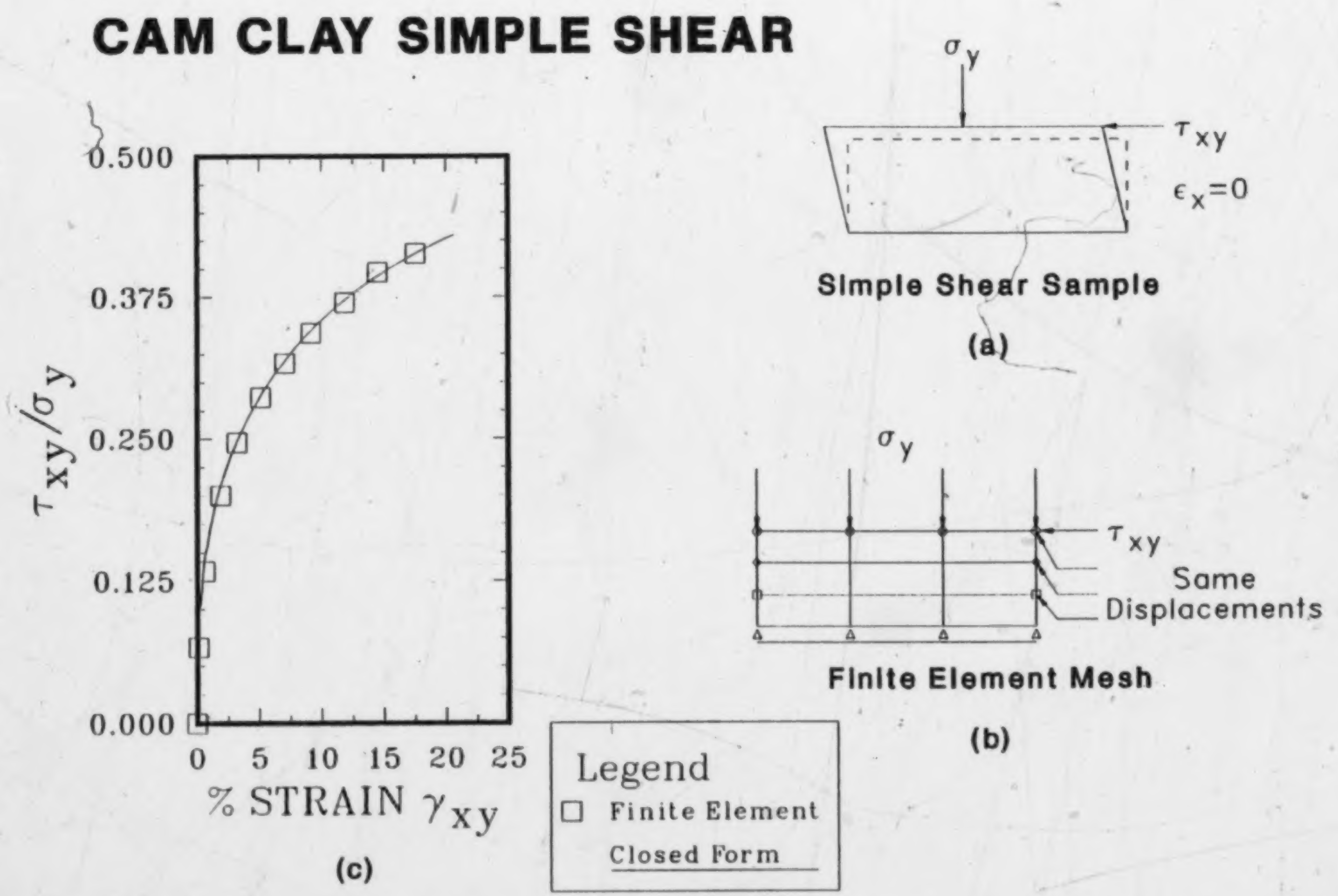

Figure 3.19 Finite Element and Quasi-Closed form Solutions for Plane Strain Simple Shear Test using Cam Clay Model

previous Section. The procedure used to evaluate K_0 in the previous section was also used. This procedure is consistent with the Cam-Clay theory. The following procedure was adopted to obtain the quasi-closed form solution for the stress-strain behaviour of the above sample under plane strain simple shear conditions.

The simple shear test was simulated by increasing the horizontal shear stress τ_{xy}. As in the case of plane strain triaxial test explained in the previous Section, the load increments were made in equal steps. For a given stress change, let the corresponding increment in η' be $\delta\eta'$. Let the current state be denoted by the subscript 1 and the following state by 2.

Let

$$\eta'_2 = \eta'_1 + \delta\eta'$$

$$\eta' = \eta'_1 + \frac{\delta\eta'}{2}$$

By making the assumption that principal stress directions and strain increments coincide for simple shear conditions, Roscoe et al. (1968) found that:

$$t_2 = \sigma'_y 2\eta'_2 / \left[2 + \frac{M^2}{3} - \eta_2^2\right] \qquad [3.139]$$

(s and t are defined at Equation 3.127)

By definition of η' (Equation 3.128):

$$s_2 = \frac{t_2}{\eta'_2} \qquad [3.140]$$

Therefore, s_2 can be computed. Roscoe et al. (1968) also showed that for plane strain simple shear,

$$\tau_{yx2} = \sigma'_y\sqrt{4\eta_2'^2-(M^2/3-\eta_2'^2)^2}/[2+M^2/3-\eta_2'^2] \qquad [3.141]$$

The above Equation yields the shear stress. From Equation 3.136 δv can be computed as follows.

$$\delta v = \frac{\lambda}{1+e}\left[2\eta'\delta\eta'/(\frac{M^2}{3}+\eta'^2) + \frac{\delta s}{s}\right] \qquad [3.142]$$

$$e = e - \delta v(1+e)/2 \qquad [3.143]$$

The above FORTRAN Equation and iterations may be used for computation of e to a greater accuracy.

From Equation 3.138,

$$\delta\gamma = \delta v 2\eta'/\left[\frac{M^2}{3} - \eta'^2\right] \qquad [3.144]$$

This Equation yields the value of δγ and the average quantities are computed as shown below.

$$\tau_{yx} = \frac{1}{2}\{\tau_{yx1}+\tau_{yx2}\} \qquad [3.145]$$

$$s = \frac{1}{2}\{s_1+s_2\} \qquad [3.146]$$

$$\delta\gamma_{yx} = \frac{\tau_{yx}}{t}\delta\gamma \ \tau_{yx} \qquad [3.147]$$

The complete process was repeated until the required stress or strain state was reached. The initial stress state was obtained as outlined in the preceding Section. As in the previous Section, iterations were used for computing e for each stress increment. The stress increment steps were halved and the procedure was repeated until the required numerical accuracy was obtained. Equal steps of 30 stress increments were used to get satisfactory results. Figure 3.19(c) shows this quasi-closed form solution obtained for the stress-strain behaviour of the soil sample.

The finite element analysis explained in section 3.5.8 was used in the simulation of the simple shear test. The same soil sample was discretized as shown in Figure 3.19(b) for the finite element analysis. This finite element mesh simulates the kinematic and stress boundary conditions used in the closed form solution of the previously discussed simple shear test. As in the plane strain triaxial test explained in the previous Section, in this finite element analysis, the simple shear loading was simulated by increasing the load by small steps. As previously explained, the numerical accuracy of the finite element solution was checked by halving the load steps. Increments of 20 equal steps (except for the last step) yielded satisfactory results and are plotted in Figure 3.19(c). The two plots, finite element and closed form solutions compare well.

3.7 CONDITIONS FOR A RELIABLE SOLUTION

To obtain reliable results from the finite element models mentioned in section 3.5, an appropriate mesh size (also in t space) and a suitable size for the load step must be selected (see also sections 3.5.3.3 and 5.4.2).

The nonlinear stress analysis performed using the finite element model that used the hyperbolic model, assumed that the stress points underwent monotonic stress changes during loading or unloading. Since a stress reversal can significantly alter the modulus, if the validity of this assumption is in doubt for a particular problem, it is necessary to check the results to see if in fact the assumption is violated. To verify this assumption using the numerical results, only certain critical elements may be selected. Engineering judgement is used in determining these critical elements. Note also the suggestions made in section 3.5.3.3 on the selection of the load step size for a reliable solution (see section 5.4.3 for applications).

For the consolidation finite element analysis, $\theta = \frac{1}{2}$ ensures unconditional stability. That is, even if the value of Δt is large, the method will produce stable solutions. However, a realistic description of the consolidation process needs smaller time steps. Since there are no specific quantitative bounds for Δt, one has to select Δt in a rational way. Desai et al. (1977) recommend a trial and error procedure until the required "accuracy" is achieved. One can also use engineering judgement and past experience to reduce the number of trials. Using their numerical results, some researchers have determined the bounds for Δt for reliable solutions for particular problems. For instance, if the results are to be reliable for a three layer system where there is sand between two clay layers, Desai et al. (1977) found that for $k_r \leq 10^4$ and $E_r \leq 10^4$, Δt must be such that $\frac{c_v \Delta t}{\Delta x^2 + \Delta y^2} \leq 5 \times 10^{-3}$. Δx and Δy are the average mesh sizes and Δt is the average time increment. E_r and k_r are the modulus and the permeability ratios respectively.

Although these formulas and intuition suggest that the smaller time steps produce more numerically accurate solutions, some researchers have recently found that this is not necessarily true. Vermeer et al. (1981) showed that for reliable numerical solutions of the uncoupled consolidation equation, Δt must also have a lower bound. For the one-dimensional case and for elements with linear pore pressure variations, Vermeer et al. (1981) showed that, when,

$$\Delta t \geq \frac{1(\Delta h)^2}{6\,\theta c_v} \qquad [3.148]$$

the numerical results are reliable, where, Δh is a typical mesh size near the draining boundary. Vermeer et al. (1981) argue that the above results are applicable to both two and three-dimensional problems. They suggest that intuition be used in generalizing this formula to two or three-dimensions.

4. APPLICATION OF THE SIMPLE MODELS

4.1 INTRODUCTION AND OBJECTIVE

In Chapter 2, the importance and the need to use simple numerical and material models in the design of large geotechnical engineering projects were explained. Such simple models that could analyse the deformation and pore pressure behaviour in soil masses were proposed in Chapter 3 which also presented the details of these models. They can be used to estimate movements and pore pressures in soils due to various types of geotechnical engineering construction. These models can be used to compute the initial pore pressure and deformation due to undrained construction. Furthermore, they can be used to estimate the pore pressure dissipation behaviour with time and the additional soil movements due to pore pressure dissipation. These models were used in predicting the behaviour of three well documented case histories. The field observations of these case histories were compared with the predictions. The objective of these applications was to see how the chosen numerical and material models perform, and not to use the predictions as a proof of the models employed.

4.2 METHOD OF ANALYSIS

What follows is a very brief account of the methodology. The construction is assumed to be undrained. The initial deformations are computed using a finite element method which employs an improved version of the widely used hyperbolic material model. The undrained soil parameters are used in this step of the analysis. Using the stress changes computed at the end of undrained construction, and the Henkel's three dimensional pore pressure formula, the initial pore pressures are evaluated. The pore pressure dissipation with time is then estimated using the initial pore pressures and a finite element model that employs uncoupled consolidation theory. To estimate the consolidation settlement due to pore pressure dissipation, the dissipated pore pressure values are used in a finite element analysis that employs the Cam-Clay model. In this analysis drained parameters must be used.

4.3 DISPLACEMENT AROUND A TUNNEL

The displacements around a water tunnel in Sao Paulo, Brazil, have been observed. The details of the construction and observations are given by Negro and Eisenstein (1981). Three different tunnelling techniques were used to discern the suitability of the methods as far as the economy and deformation control capability are concerned. An attempt has been made to predict the displacements of the part of the tunnel where the NATM construction was used. The displacements were predicted using the simple models described in the preceding section. These predictions were compared with the observations.

4.3.1 METHOD OF CONSTRUCTION AND INSTRUMENTATION

As stated in section 4.3, three different tunnelling methods have been employed on an experimental basis. One was full-face excavation with circular steel segmented lining plates erected immediately behind the face. In the second method the face was protected by a berm and horse shoe steel ribs and timber lagging were erected immediately behind the face. The third method utilized the New Austrian Tunnelling Method (NATM), also known as the Sequential Tunnelling Technique. In this method, the excavation proceeded in three steps, the heading followed by the bench and invert (Figure 4.1). Shotcreting of the exposed walls to a thickness of 10 to 13 centimeters followed immediately. A 10×10 cm wire mesh was also used with shotcreting. Neither ribs nor anchors were used. In all three methods the excavation was carried out by hand.

Surface settlement was measured using settlement monuments, whereas the settlement at various depths was measured using magnetic extensometers. Tunnel roof settlement was measured by levelling techniques. The part of the tunnel that used Sequential Tunnelling Technique had three out of five instrumented sections. Figure 4.1 shows a typical instrumented section. Each section had three rows of five surface settlement monuments and one to three bore holes containing about eight magnetic extensometers. These extensometers were placed above the crown and below the invert.

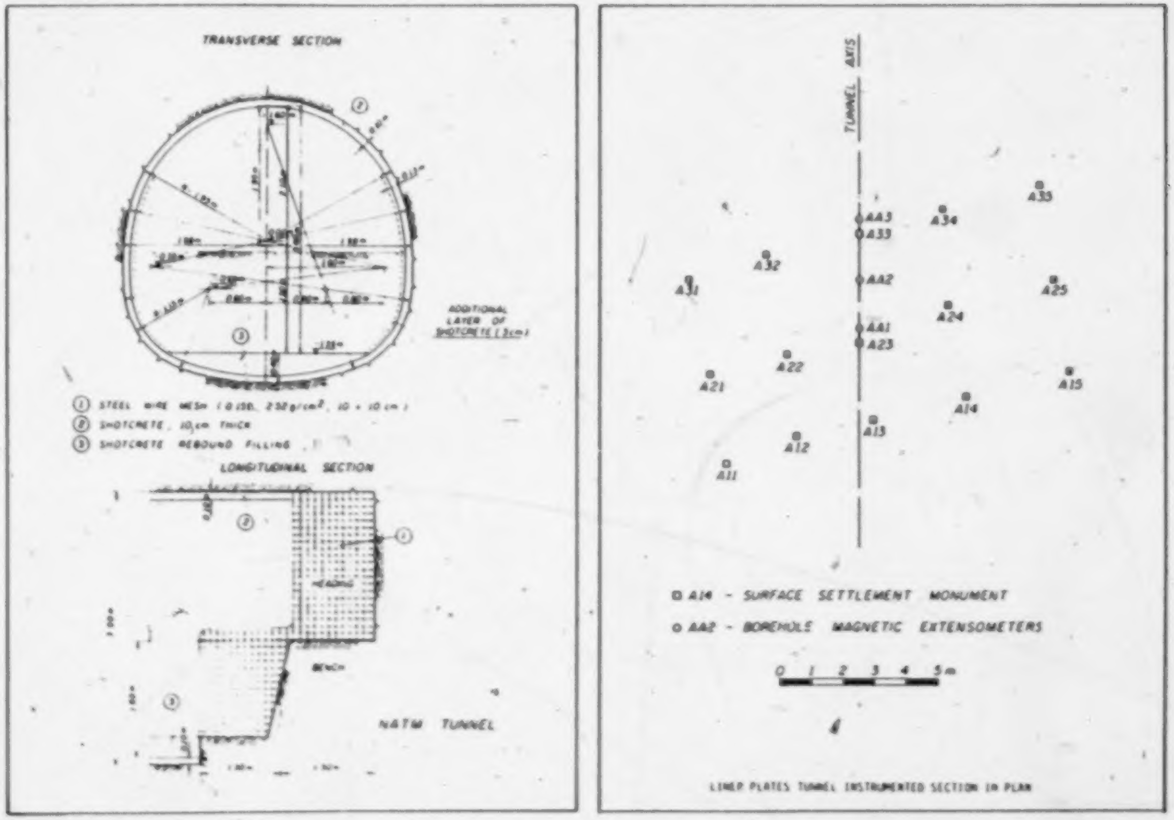
TRANSVERSE SECTION
①
②
③
ADDITIONAL LAYER OF SHOTCRETE (3cm)
① STEEL WIRE MESH (Ø 150, 2.52 g/cm², 10 × 10 cm)
② SHOTCRETE, 10 cm THICK
③ SHOTCRETE REBOUND FILLING
LONGITUDINAL SECTION
HEADING
BENCH
NATM TUNNEL
TUNNEL AXIS
A11
A12
A13
A14
A15
A21
A22
A23
A24
A25
A31
A32
A33
A34
A35
AA1
AA2
AA3
□ A14 - SURFACE SETTLEMENT MONUMENT
○ AA2 - BOREHOLE MAGNETIC EXTENSOMETERS
0 1 2 3 4 5m
LINER PLATES TUNNEL INSTRUMENTED SECTION IN PLAN

Figure 4.1 Sequential Tunnelling Technique and a Typical Instrumented Section (after Negro and Eisenstein, 1981 : modified)

4.3.2 GEOMETRY AND SOIL PROFILE

The soil stratigraphy around NATM portion of the tunnel consisted two major strata, tertiary soft clay underlain by tertiary clayey sand (Figure 4.2). The diameter of the tunnel was approximately 4m, and the depth of cover was 6.3 m. The tunnel was constructed in the tertiary clayey sand layer. The ground water table was below the tunnel invert.

4.3.3 OBSERVATIONS AND PREDICTIONS

A two dimensional numerical model cannot simulate exactly the three dimensional nature of the above three construction procedures. The Sequential Tunnelling Technique appears to be the easiest one to numerically simulate using the models described in section 4.2 and Chapter 3. As stated earlier, three of five instrumented sections were within the tunnel section that used the Sequential Tunnelling Technique. Due to these two reasons, only the movements due to the Sequential Tunnelling Technique were predicted and compared with the observations. Although no stress reversals were expected during the undrained tunnel excavation, a considerable amount of principal axes rotation take place in the soil mass in the vicinity of the tunnel. The laboratory test results (Kupper, 1983) indicate that the K_0 consolidated soil has a higher strength in compression than in extension. It must be noted that the hyperbolic material model employed in our finite element procedure accounts for these factors (section 3.4.1.1).

NATM TUNNEL

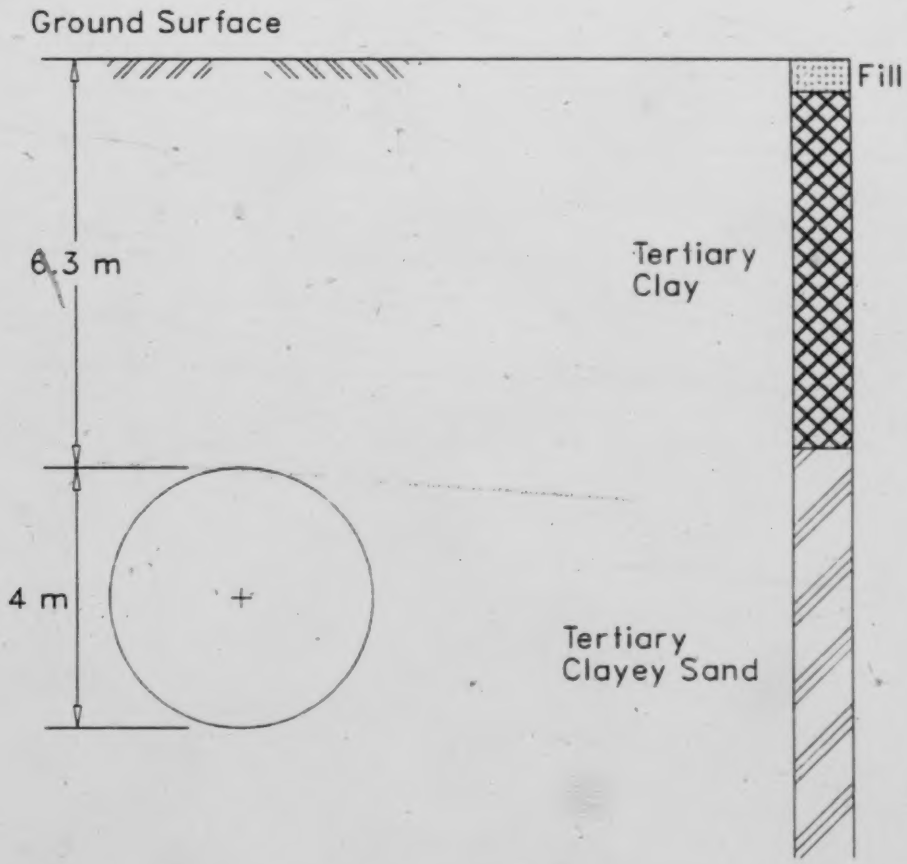
Ground Surface
Fill
6.3 m
Tertiary
Clay
4 m
Tertiary
Clayey Sand

Figure 4.2 NATM Tunnel; Geometry and Soil Stratigraphy (after Negro and Eisenstein, 1981 : modified)

Before proceeding to the numerical computations, it was necessary to obtain the appropriate parameters describing the material models. A comprehensive laboratory testing program was carried out by Kupper (1983) for determining the material behaviour of these clays. Negro et al. (1981) also provides the parameters obtained from both laboratory and field tests.

For the finite element analysis a mesh similar to that shown in Figure 4.3 was used. The factors pointed out in section 5.4.1 were used in developing this mesh. Since the shotcreting was done immediately after the excavation, in the numerical simulation the lining was considered to be in place from the start of the excavation. The results obtained in section 5.4.3 were used in the selection of the size of the load step, and the excavation was simulated in 10 equal load steps. The initial stresses were estimated using K_0 and the excavation was simulated by reducing the in situ stresses at the tunnel periphery. The tunnel was assumed to exist fully from the very begining of the stress reduction.

The parameters obtained from different laboratory tests differed from each other and from the parameters obtained from field tests. The strength parameters obtained from laboratory tests were used in the finite element analysis. The variation of both the strength and modulus with depth fitted best to a square root distribution. The soil moduli computed from the pressure meter test results were used. The $s_u/\sigma_{1c}^{\frac{1}{2}}$ for compression was 380 $(\mathrm{kPa})^{\frac{1}{2}}$ and a value

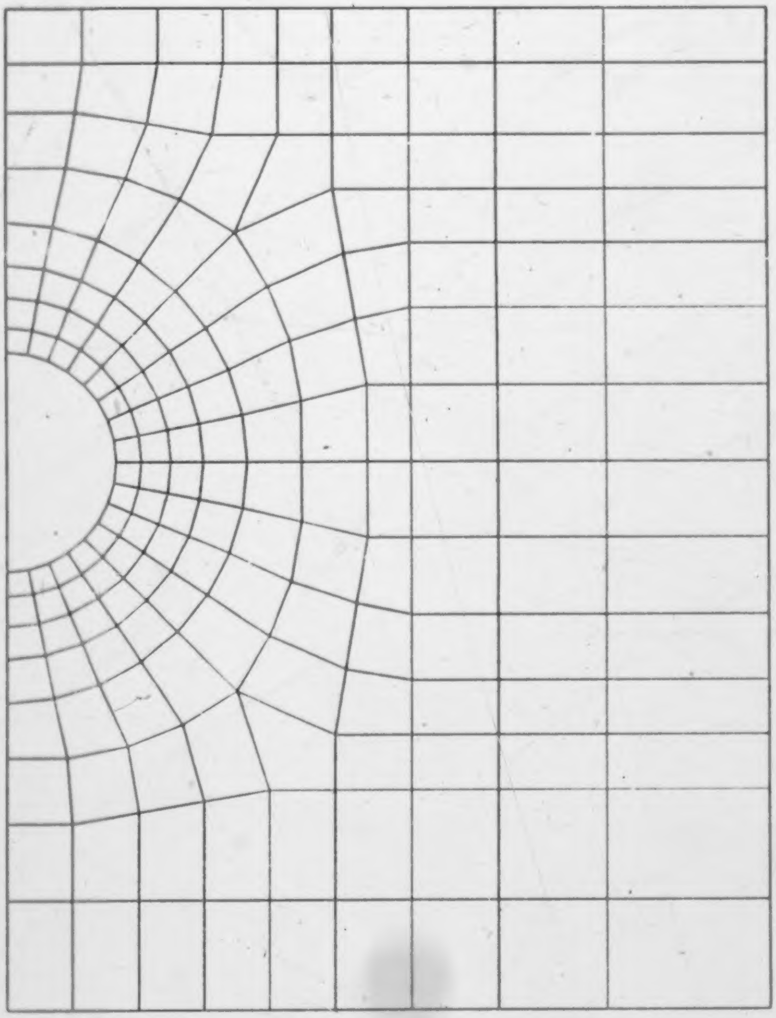

Figure 4.3 Finite Element Mesh for NATM Tunnel

of 300 $(kPa)^{\frac{1}{2}}$ was estimated for extension. The published data presented only an average modulus computed from the pressure meter test results at each depth. The $E_i/\sigma_{1c}^{\frac{1}{2}}$ computed from the pressure meter test was 5000 $(kPa)^{\frac{1}{2}}$. The other parameters used in the finite element analysis were: $K_0=0.8$, $\gamma=15.7$ kN/m^3 and $R_f=0.9$.

The average pressure meter modulus is always less than the initial modulus of the soil. Not surprisingly, when the pressure meter modulus was increased by 25% and used as the initial modulus, the predictions matched the observations more closely. When the value of the shotcrete modulus was varied from its minimum 2 MPa to the maximum 30 MPa, the resulting change in surface settlement above the crown was about 6%. In the final analysis the average modulus of the 10 cm shotcrete was taken to be 15 MPa. Figures 4.4 and 4.5 compare the observations and predictions of the initial soil movements due to the excavation of the tunnel. The surface settlements are shown in Figure 4.4, whereas the soil movements with depth are shown in Figure 4.5. In general, the predictions compare reasonably well with the observations.

4.4 PORE PRESSURE AROUND AN EXCAVATION

The Kimola floating canal is located in central Finland about 120 km northeast of Helsinki. The details of this case history are given by Kankare (1969a and 1969b). The excavation of the canal started in the winter of 1962 and

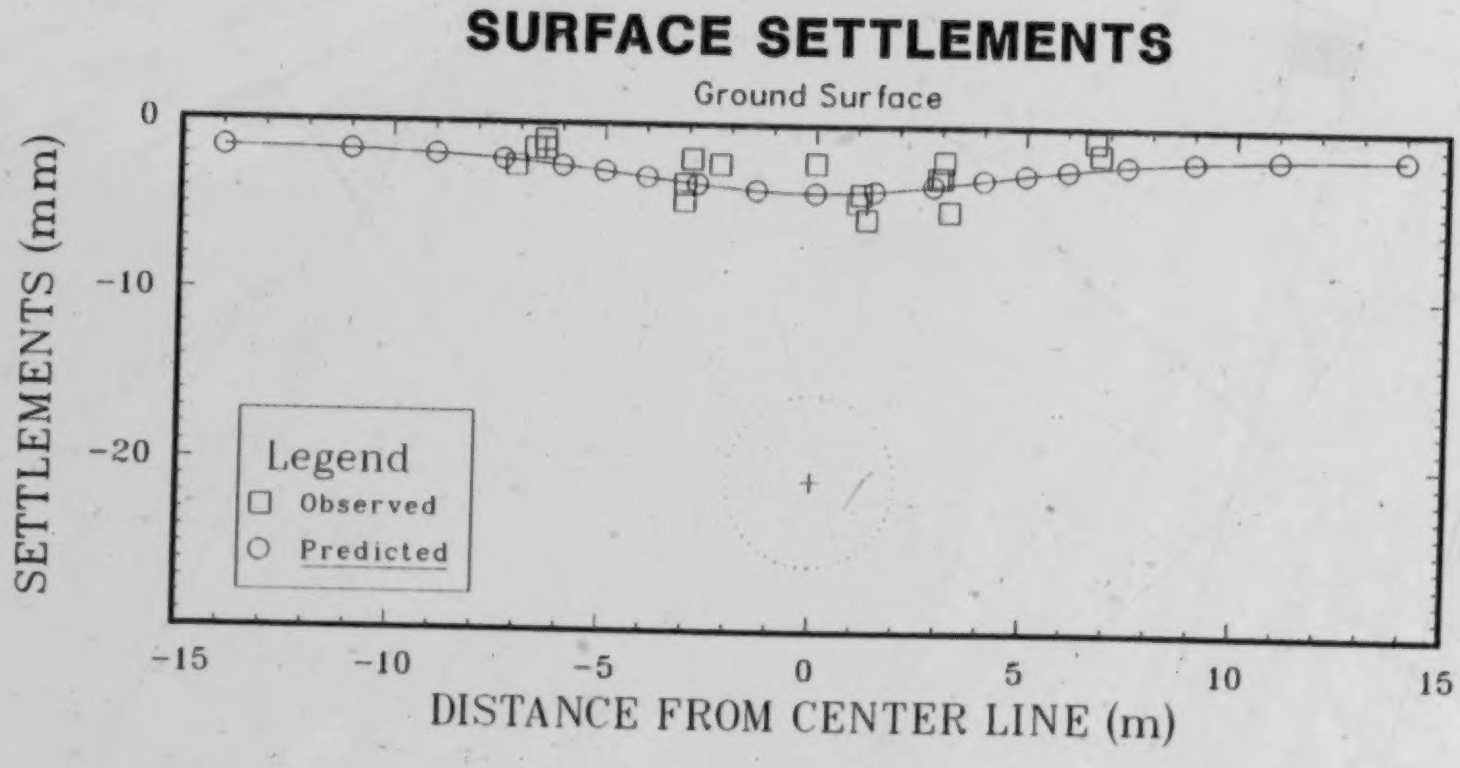

Figure 4.4 Predicted and Observed Surface Settlements; NATM Tunnel

VERTICAL DISPLACEMENTS

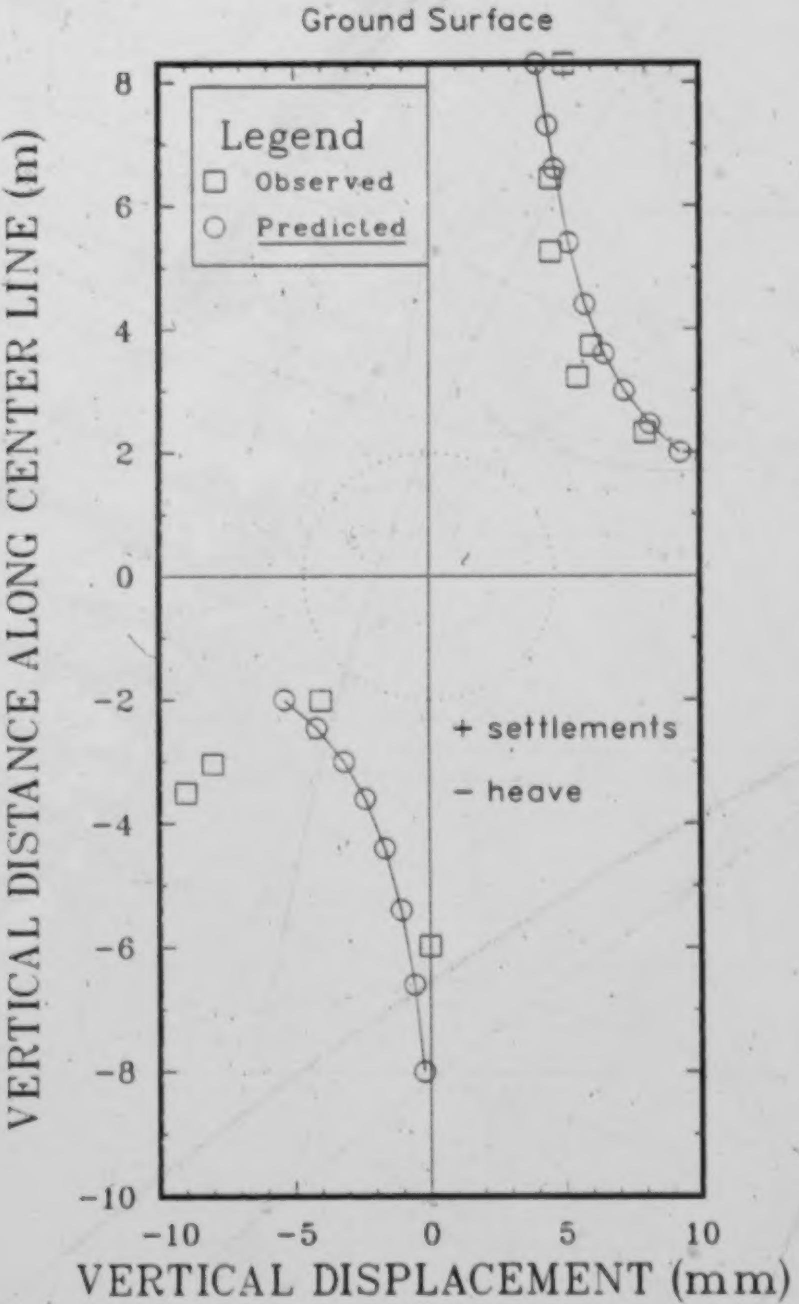

Figure 4.5 Predicted and Observed Vertical Settlements; NATM Tunnel

continued through the summer of 1966. The slopes were in slightly to highly overconsolidated clay. Following a series of slope failures which occurred in 1963, a detailed investigation was started which included measurements of pore pressure in certain locations. In the following sections, some of these observed pore pressures are compared with the predictions made by the model described in section 4.2.

4.4.1 METHOD OF CONSTRUCTION AND INSTRUMENTATION

In the failure area where the canal was instrumented, the excavation was done in two stages. A certain time after excavation, this instrumented section failed. In the winter of 1963, the first stage of excavation (to an elevation of 67 m) was completed. In the second stage the canal was excavated from an elevation of 67 m to 61.9 m which was completed in January 1965. Keeping water away from the canal, the excavation was carried out using drag lines.

At station 52+70, several piezometers were installed (Figure 4.6). Piezometers used were the Geonor type with bronze filter tips. The filter tip had an area of 226 cm^2 and a diameter of 3.3 cm. These were pushed into the slope using steel tubes having a diameter of 3.4 cm. Mercury manometers similar to those used in the old triaxial apparatus were employed. These manometers were installed in a cabin at 67 m level. Pore pressure measurements were continued from 13 July 1964 until the slope failed on 3

November 1965 destroying the instrumentation.

4.4.2 GEOMETRY AND SOIL PROFILE

The geometry, soil profile and the piezometer locations are shown in Figure 4.6. The excavation from 67 m to 61.9 m had side slopes of 2 horizontal to 1 vertical. The soils are glacial deposits in a long and narrow valley and consist of lightly to heavily overconsolidated clay down to a level of about 60 m . Below this level is till (Figure 4.6).

4.4.3 OBSERVATIONS AND PREDICTIONS

The excavation which was completed in less than a week was considered rapid enough to provide undrained conditions. As in the previous case history, no stress reversals were expected during the excavation. However, significant rotation of principal axes were expected. The nonlinear material model described in section 4.2 can accommodate these conditions reasonably well. The Henkel's three dimensional pore pressure formula used in the analysis can describe the pore pressure generation accurately.

For the stress and pore pressure analysis, the soil parameters published by Kankare (1969 a and b) and Eigenbrod (1972) were used. Kankare (1969 a and b) provides the vane shear strength variation with depth. From these results s_u/σ_{1c} was computed to be 0.6 in compression. An estimated E_i/σ_{1c} value of 400, R_f of 0.9 and s_u/σ_{1c} of 0.5 in extension were also used. The bulk density was 20 kN/m^3. Henkel pore

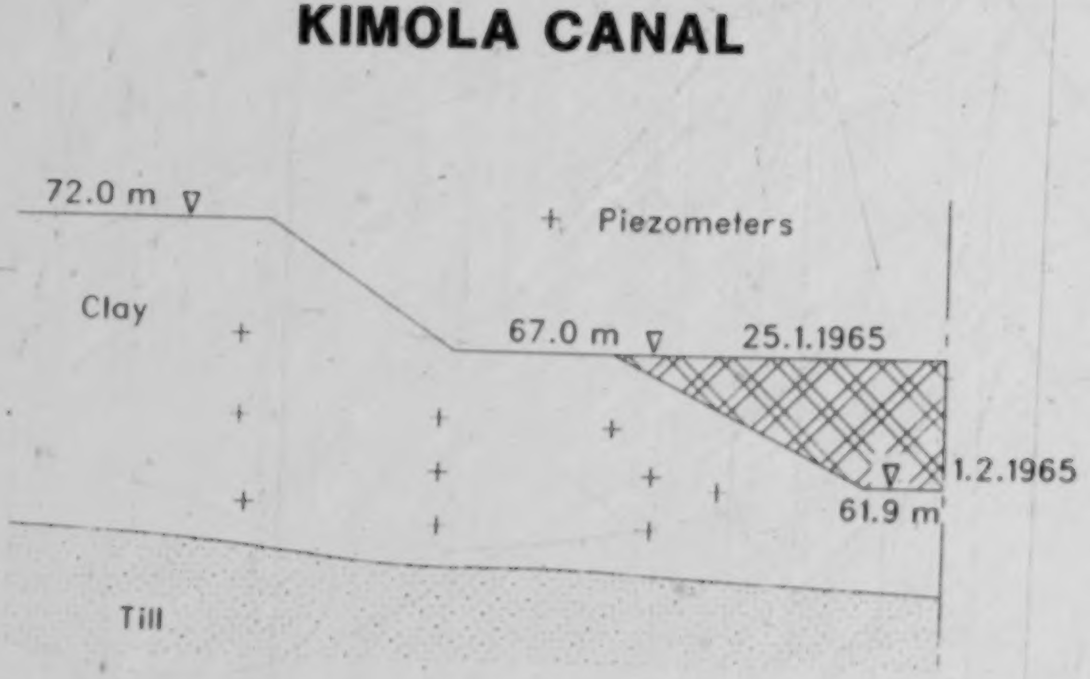
KIMOLA CANAL
72.0 m
+ Piezometers
Clay
67.0 m
25.1.1965
1.2.1965
61.9 m
Till

Figure 4.6 Kimola Canal; Geometry, Soil Stratigraphy and Piezometer Configuration (after Kankare, 1969a : modified)

pressure coefficient of -0.024 and K_0=1.0 were used by Eigenbrod (1972). These parameters were also used in this analysis.

The finite element mesh used for the stress and pore pressure analysis is shown in Figure 4.7. The excavation was simulated by using unloading forces equivalent to the in situ stresses. The computation of equivalent vertical and horizontal forces are illustrated in Figure 4.8. These forces were applied in 10 equal steps to obtain the initial stress changes. As discussed in section 4.2, these stress changes were used in Henkel's 3-D formula to compute the initial pore pressure changes. The predicted contours of initial pore pressure changes are shown in Figure 4.9 and are compared with the observations. The observations compare well with the predictions and the average deviation is about 10%. It must be noted that all pore pressure contours turn towards the center line of the canal with increasing depth and these parts of the contours are not shown in Figure 4.9.

4.5 SETTLEMENT AND PORE PRESSURE AROUND A TUNNEL

In the city of Thunder Bay, a sewer tunnel was constructed using a tunnel boring machine in 1976. The construction and the observation of this tunnel are explained in greater detail by Palmer and Belshaw (1980). It was the first construction of a tunnel using such a technique in Canada. Since the subsoil conditions were known to be difficult, a comprehensive field instrumentation

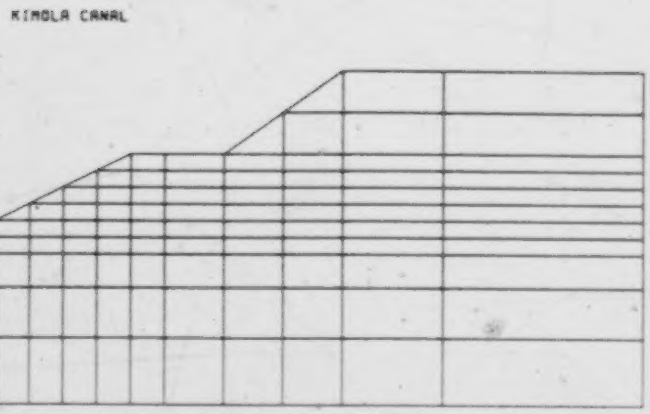
KIMOLA CANAL

Figure 4.7 Finite Element Mesh for Kimola Canal

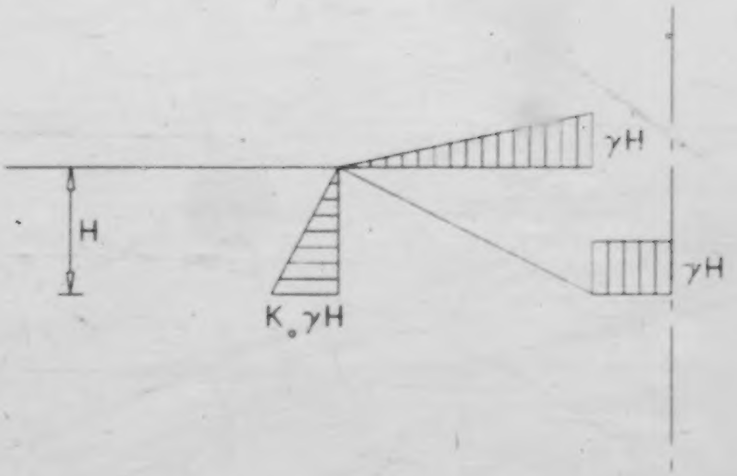

Figure 4.8 Equivalent Unloading Forces

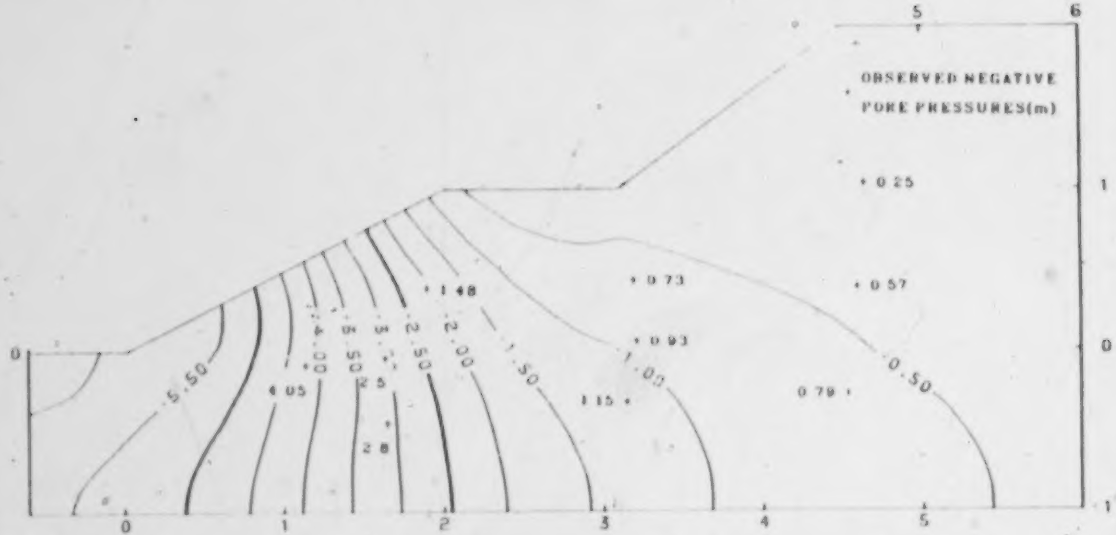

Figure 4.9 Observed Pore Pressures and Predicted Pore Pressure Contours

program was undertaken. Some of these observations are compared with the predictions made using the numerical model described in section 4.2.

4.5.1 METHOD OF CONSTRUCTION

The tunnel excavated by full-face tunnel boring machine used unbolted, precast and segmented lining. A specially designed erector arm lifted and erected the segments of lining. The tunnelling machine used the completed lining as a reaction. As the construction proceeded, a clay grout was injected into the tailpiece void. Construction rates of 29 m of finished tunnel in 8 hours, were achieved in soft to firm clay.

4.5.2 INSTRUMENTATION

Since it was the first time a tunnel boring machine was used in Canada and the ground conditions were difficult, instrumentation to monitor deformations and pore pressures was installed. An instrument installation was made at a section which was constructed at the start, and this section is called Array 1 in the literature. Since this instrumentation was satisfactory, a second set of instrumentation was installed to provide more detailed information about the changes in ground movements and pore pressures with time. This second set of instrumentation is called Array 2 in the literature.

Almost all deformation instruments and piezometers in Array 2 were installed as much as possible within one cross-section. The piezometers were installed only to one side of the line of symmetry of the tunnel cross-section. The surface settlements along the center line were monitored every 6 m for 24 m either side of Array 2. This helped to verify whether the selected cross-section for detailed instrumentation represented typical behaviour of the tunnel. The layout of the instruments that monitored the deformations and pore pressures are shown in Figure 4.10. The piezometers that monitored the long term pore pressure are shown in Figure 4.14. One ring of the tunnel lining was instrumented with pressure cells, stress meters and piezometers. This was located approximately under settlement auger #4. More details of the instrumentation are given in Palmer and Belshaw (1980).

4.5.3 GEOMETRY AND SOIL PROFILE

The subsoil conditions of Array 2 is shown in Figure 4.13. The surface consists of a thin (0.9m) peat layer underlain by silty sand. Below the the silty sand, grey silty clay forms the first 5 m of the cohesive deposits. The strata below the grey silty clay consists of silty clay to clay layers. Layers of silt or fine sand were found sparsely distributed in this deposit. The tunnel geometry at Array 2 is also shown in Figure 4.13. The construction of the tunnel was approximately 10 m below the ground surface and through

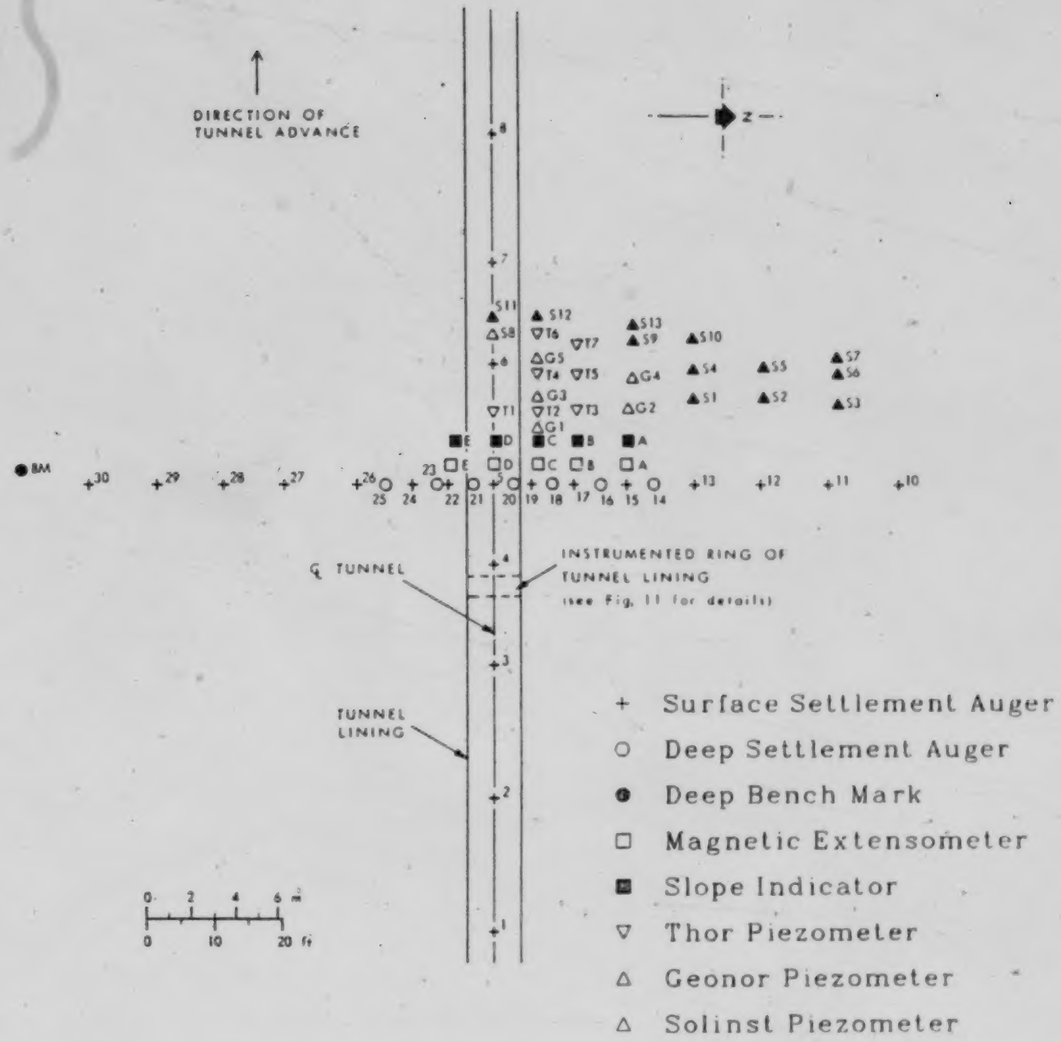
DIRECTION OF TUNNEL ADVANCE
Z
℄ TUNNEL
INSTRUMENTED RING OF TUNNEL LINING (see Fig. 11 for details)
TUNNEL LINING
BM
0 2 4 6 m
0 10 20 ft
+ Surface Settlement Auger
○ Deep Settlement Auger
● Deep Bench Mark
□ Magnetic Extensometer
■ Slope Indicator
▽ Thor Piezometer
△ Geonor Piezometer
▲ Solinst Piezometer

Figure 4.10 Instrumentation at Array 2; Thunder Bay Tunnel (after Belshaw and Palmer, 1978 ; modified)

soft clay. The tunnel has a mined diameter of 2.47 m, the outer diameter of the completed lining is 2.38 m, and the inner diameter is 2.16 m.

4.5.4 OBSERVATIONS AND PREDICTIONS

The observations at Array 2 were selected for comparisons with the predictions. As before, the numerical models described in section 4.2 were utilized to make the predictions. The suitability of this numerical model for the stress analysis around tunnels is discussed in section 4.3.3. The finite element mesh shown in Figure 4.11 was used in the analysis and the excavation was simulated in 10 equal unloading steps. The selection of the size of the load step and a suitable finite element mesh for tunnels are also mentioned in section 4.3.3. The rate of construction was about 19 m of completed tunnel per 8 hr. This rate was assumed to provide initial undrained conditions.

Ng (1984) carried out a series of laboratory and field tests on materials from the same site. The parameters derived from these tests are summarized in Table 4.1. The strength and moduli values showed some scatter. Upper and lower bounds could be found for these quantities. The upper bounds were used in the finite element stress and displacement analysis. The predicted initial surface settlements are shown in Figure 4.12. Two dimensional and undrained conditions have been assumed in making these predictions. These assumptions imply that the tunnel had

Table 4.1 Thunder Bay Tunnel; Material Properties

QUANTITY	SILTY SAND	SILTY CLAY	VARVED CLAY
γ kN/m^3	20.0	16.2	19.0
K_0	0.5	0.75	0.53
E_i/σ_v	100-240	100-240	100-240
s_u/σ_v	0.32-0.20	0.32-0.20	0.32-0.20
$s_{ue}/_{uc}$	0.7	0.7	0.7
R_f	0.9	0.9	0.9
A_f	0.7	0.7	0.7
k_x cm/s	1.0E-07	7.0E-08	15.0E-06
k_y cm/s	1.0E-07	4.0E-08	5.0E-06
m_v kPa^{-1}	0.5E-04	3.0E-04	0.5E-04
λ	0.043	0.326	0.087
κ	0.004	0.065	0.017
M	1.25	1.25	1.25
e_0	0.78	1.43	0.78
ν	0.33	0.40	0.33
OCR	1.0	1.4	1.8

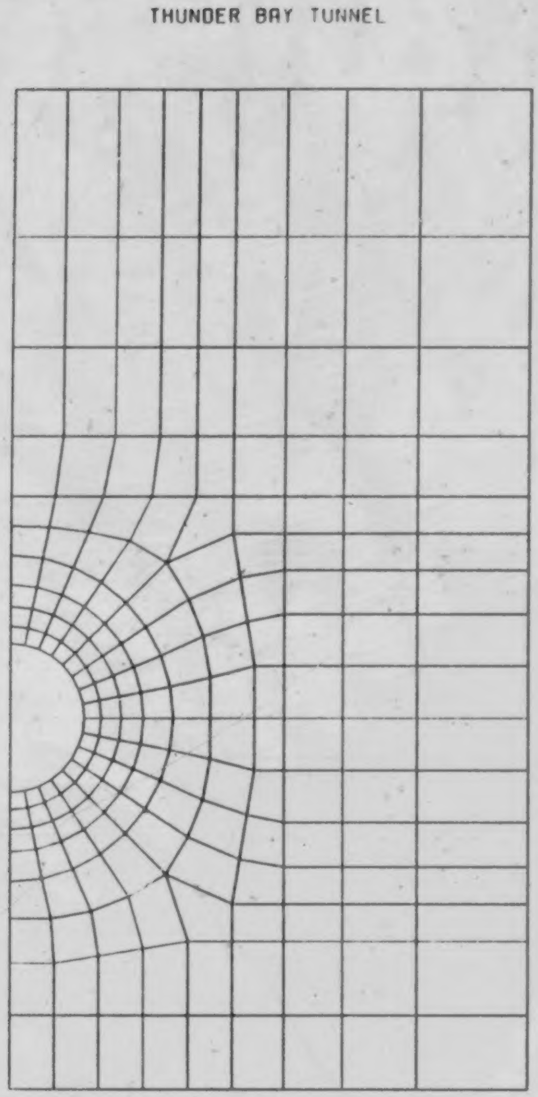
THUNDER BAY TUNNEL

Figure 4.11 Finite Element Mesh for Thunder Bay Tunnel

been excavated instantly to a distance far enough from the instrumented section, so that the 3-D face effects on settlements are insignificant. Theoretically, this distance is infinite, but practically it is a few tunnel diameters. For the elastic case, Ranken and Ghaboussi (1975) found this length to be about two tunnel diameters. It has been reported (Heinz, 1983) that when yielding occurs, this distance tends to increase. In our case, this distance was assumed to be three to four tunnel diameters. That is, when the tunnel excavation proceeded to a length of about 7.5 m to 10 m from the instrumented section, the face effects were assumed to be insignificant. This length will be referred to as the significant length of the tunnel. For our case, the significant length was chosen to be 9.8 m because after 6.7 m the next surface settlement recording had been made when the tunnel excavation proceeded to a distance of 9.8 m from the instrumented section. While the excavation proceeds to a length such that the face effects become negligible, the consolidation settlements due to pore pressure dissipation could continue to accumulate. The time taken to excavate the tunnel to its significant length was about four and a half hours. These observations (corrected for consolidation; explained in the following paragraphs) and predictions of the initial settlement are compared in Figure 4.12. The observations tend to be larger than the predictions in the mid-section of the settlement profile.

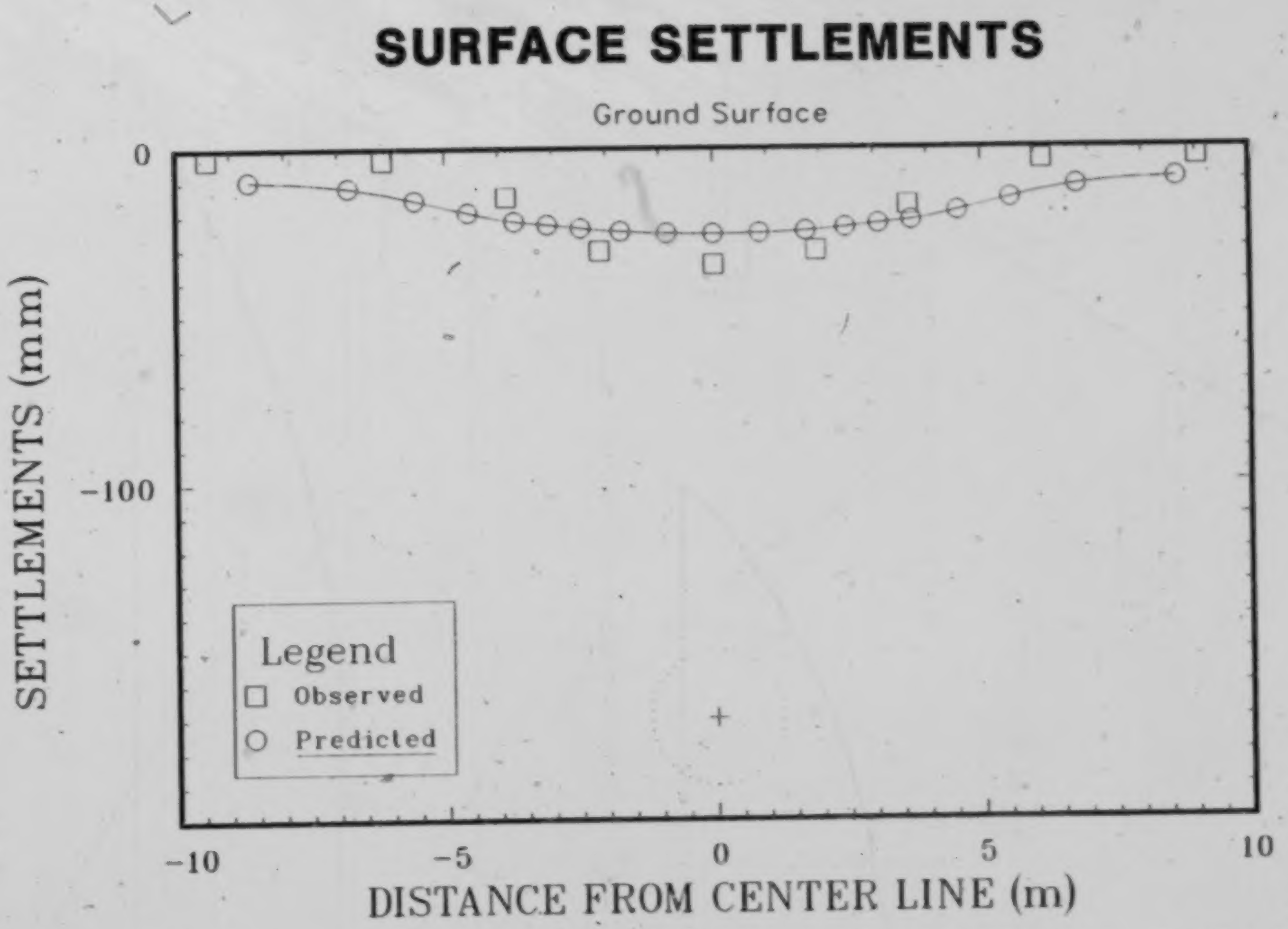

Figure 4.12 Observations and Predictions of Initial Surface Settlements; Thunder Bay Tunnel

The pore pressure dissipation behaviour was analysed using the finite element model that incorporates the uncoupled consolidation theory (Chapter 3). The field pore pressures were recorded at close time intervals until the tunnel face reached a distance of about 10 m from the instrumented section. The recordings that followed had been made after periods of 3 days, 19 days and 10 months. As in the case of settlement, the pore pressure dissipation in the initial stages can be influenced to a considerable extent by the three dimensional face effects. Unlike settlement, it may take longer for the 3-D pore pressure effects to die down because of the slow diffusion process. Nevertheless, these 3-D effects were assumed to have died down before 3 days. Therefore, it is meaningful to compare the 3 day and 19 day 2-D pore pressure predictions with the field pore pressures. These observations and predictions are shown in Table 4.2, and the location of piezometers is shown in Figure 4.14. The observations and predictions compare reasonably well for the pore pressures.

As described in section 4.2, these pore pressure values were used to compute the consolidation settlements. The finite element procedure used in this analysis employs the Cam-Clay model (section 3.5.8). Unlike the hyperbolic model, the Cam-Clay model can accommodate the expected stress reversals reasonably well. The observed and computed additional settlements after a period of 20 days are shown in Figure 4.15. They compare reasonably well.

Table 4.2 Observations and Predictions of Pore Pressure Dissipation; Thunder Bay Tunnel

PIEZOMETER (kPa)	3 Day Pore Pressure		19 Day Pore Pressure	
	Predicted	Observed	Predicted	Observed
T_1	-45	-50	-20	-35
T_2	-10	5	-5	0
T_3	10	10	-2	4
T_4	-30	-35	-20	-30
T_5	15	25	-1	10
T_6	-30	-35	-15	-15
T_7	-5	-10	-5	0

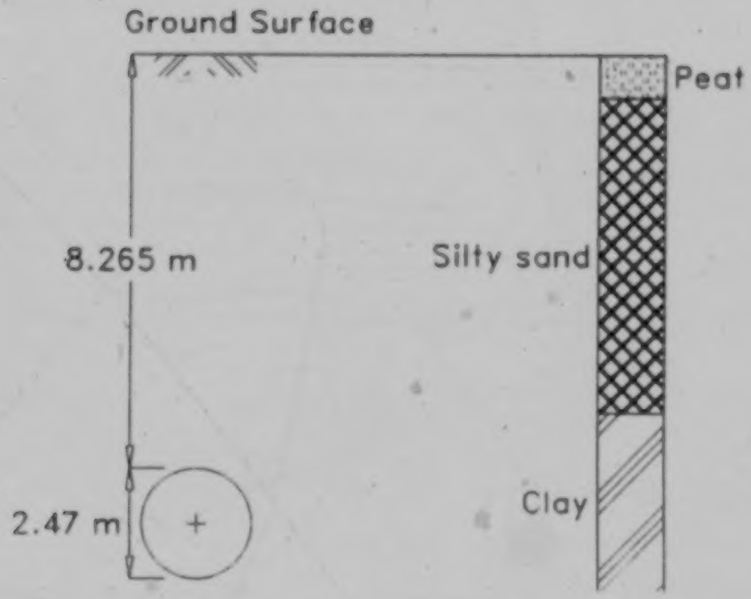
Ground Surface
Peat
8.265 m
Silty sand
2.47 m
Clay

Figure 4.13 Thunder Bay Tunnel; Geometry and Soil Stratigraphy

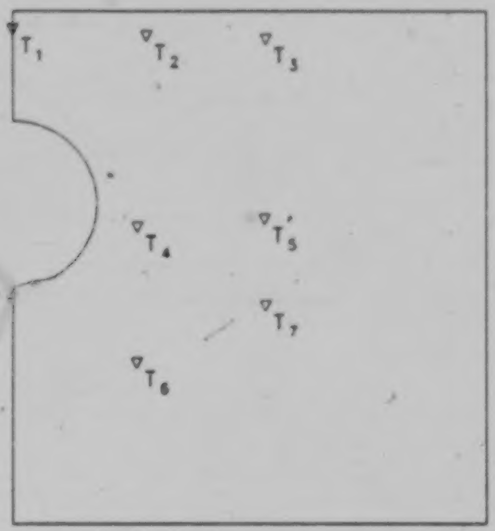
T_1
T_2
T_3
T_4
T_5
T_7
T_6

Figure 4.14 Piezometers for Long Term Monitoring; Thunder Bay Tunnel

(after Belshaw and Palmer, 1978 : modified)

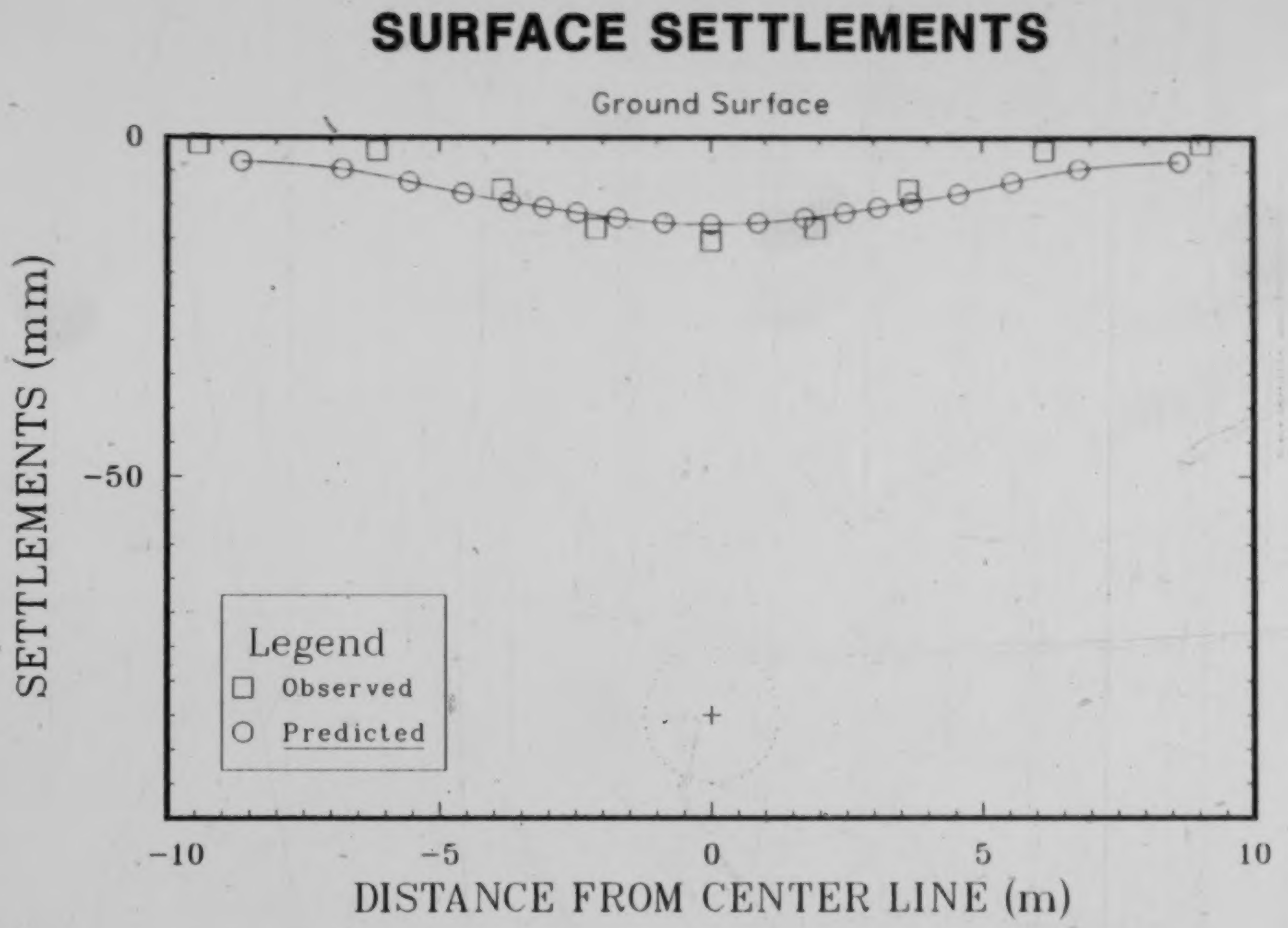

Figure 4.15 Observed and Predicted Additional Settlements after 20 days; Thunder Bay Tunnel

4.6 SUMMARY AND CONCLUSIONS

A 2-D finite element model employing a nonlinear hyperbolic material model was used to predict the initial soil movements and stresses. Using the change in stresses and 3-D Henkel formula, the initial pore pressures were predicted. A 2-D finite element model incorporating the uncoupled consolidation theory uses the initial pore pressures to predict the pore pressure dissipation behaviour with time. Using these pore pressures in a finite element procedure that employs the Cam-Clay material model, the soil movements due to pore pressure dissipation were predicted. The details of these numerical and material models are given in Chapter 3.

The observed soil movements around a tunnel constructed using the Sequential Tunnelling Technique, was compared with the predictions. The observations compare reasonably well with the predictions. The initial pore pressures observed around a canal excavated in an overconsolidated clay were compared with the predictions. The observations agree very well with the predictions. For a second tunnel constructed using a tunnel boring machine, the initial settlements were predicted. Using the computed initial pore pressures, the pore pressure dissipation behaviour was predicted. The pore pressure observations made at two different times after the excavation were compared with the predictions. The computed additional settlements due to pore pressure dissipation were also compared with the observations. All these predictions agree reasonably well with the observations.

The above results show the capabilities of the simple models chosen, in predicting deformations, pore pressure generation and dissipation behaviour and the influence of pore pressure dissipation on deformation. The analyses also showed the importance of the selection of appropriate soil parameters in making reasonably accurate predictions.

5. PORE PRESSURE BEHAVIOUR AROUND SHALLOW TUNNELS IN CLAY

5.1 INTRODUCTION AND OBJECTIVE

The construction of shallow tunnels in large cities for various purposes has been practiced for many years. Because of the development in improved tunneling technology and equipment, it is becoming more feasible and popular. In recent years, a considerable amount of research has been carried out on:

(a) controlling the tunnel stability,

(b) ground movement around the tunnels,

(c) magnitude of the tunnel support pressures.

However, until recently, very little research has been done on pore pressure generation and dissipation around tunnels and its influence on tunnel performance. In general the study of consolidation around excavations has been limited by the complexity of the problem. Johnston and Clough (1983) used a coupled analysis to investigate the influence of various factors on time dependent response (due to consolidation) of tunnels constructed in clays. To simulate construction, they used a different model from that used in this thesis. Finno and Clough (1985) applied these concepts to a case history to evaluate the time dependent soil response to earth pressure balance tunneling.

In Chapter 4 some case histories were analysed using the material and numerical models previously described. The initial settlement and pore pressure dissipation around a

tunnel constructed using a tunnel boring machine were predicted. The influence of pore pressure dissipation on long term deformation was estimated. The same models were also used to predict the deformation behaviour of a NATM tunnel and the pore pressure changes of a canal excavation. Generally, the predictions were satisfactory. The material and numerical models used were very simple and easily understood (c.f. SOM approach, Chapter 2).

Nevertheless, the above procedure involves considerable computational effort and time. Therefore, the use of such an approach for preliminary designs may not always be economical. For this reason, an attempt was made to develop approximate design diagrams or a form of a classification system that would provide a quick and easy reference for estimating or understanding the pore pressure generation and dissipation behaviour around shallow tunnels in both normally and overconsolidated clays. To accomplish this, it is imperative that an in-depth study be pursued. A parametric finite element study was undertaken for this purpose using the model described in Chapter 3. However, before starting a comprehensive numerical study, it is essential that the closed form solutions obtained for pore water pressure behaviour around tunnels be examined. Even the simplest closed form solution can be used to help understand the pore pressure behaviour around tunnels in a very broad sense. And more importantly, these solutions can be used to interpret properly the large volume of numerical results obtained in a parametric study.

5.2 CLOSED FORM SOLUTIONS AND LIMITATIONS

Many closed form solutions have been published for the analysis of tunnel excavations. Among these, the elasto-plastic approach is one of the most realistic and is well established and widely used. The closed form solutions have proven useful within their limitations. However, one cannot over-emphasize the importance of the limitations of these theories, when compared with the real situations and real soil behaviour. There is hardly any published research on pore pressure behaviour around any type of excavation. Except for the work published by Clough et al. (1981), closed form solutions on pore water pressure behaviour around tunnels are virtually nonexistent. An outline of Clough et al.s' (1981) elasto-plastic closed form solution follows.

The plastic zone is bounded by the plastic radius R_p which is given by (with usual notation):

$$R \exp\left[\frac{\sigma_v - p_i - s_u}{2s_u}\right] \qquad [5.1]$$

in the plastic region, the radial stress, σ_r is,

$$p_i + 2s_u \ln\left[\frac{r}{R}\right] \qquad [5.2]$$

and the tangential stress σ_θ is,

$$p_i + 2s_u + 2s_u \ln\left[\frac{r}{R}\right] \qquad [5.3]$$

and the third normal stress σ_y is,

$$p_i + s_i + 2s_i \ln\left[\frac{r}{R}\right] \qquad [5.4]$$

In the elastic region:

$$\sigma_r = \sigma_v - s_u\left[\frac{R}{r}\right]^2 \exp\left[\frac{\sigma_v - p_i - s_u}{s_u}\right] \qquad [5.5]$$

$$\sigma_\theta = \sigma_v + s_u\left[\frac{R}{r}\right]^2 \exp\left[\frac{\sigma_v - p_i - s_u}{s_u}\right] \qquad [5.6]$$

and the third normal stress, $\sigma_y = \sigma_v$. Using Henkel's (1960) pore pressure generation formula, Δu can be expressed as:

$$\frac{1}{3}(\Delta\sigma_1 + \Delta\sigma_2 + \Delta\sigma_3) + a[(\Delta\sigma_1 - \Delta\sigma_2)^2 + (\Delta\sigma_2 - \Delta\sigma_3)^2 + (\Delta\sigma_3 - \Delta\sigma_1)^2]^{\frac{1}{2}} \qquad [5.7]$$

Hence, the pore water pressure in the plastic region becomes:

$$p_i - \sigma_v + s_u\left(1 + 2\ln\left[\frac{r}{R}\right] + a\sqrt{6}\right) \qquad [5.8]$$

and in the elastic region, the expression for pore pressure becomes

$$a\sqrt{6}\,s_u\left[\frac{R}{r}\right]^2 \exp\left[\frac{\sigma_v - p_i - s_u}{s_u}\right] \qquad [5.9]$$

Virtually all these elasto-plastic closed form solutions, including the one presented above, are obtained using major simplifying assumptions. Some of these assumptions can be far reaching.

The material is assumed to be isotropic and the strength and modulus are assumed to be homogeneous. In reality, both in normally and overconsolidated clays, the modulus and strength vary with the depth to a greater or lesser extent. Heinz (1984) showed that the form of modulus distribution with depth can have a significant influence on the surface settlement above the tunnel. Often, hydrostatic initial stress conditions are assumed. However, depending on the value of K_0, the K_0 initial stress state can be considerably different from the hydrostatic state. The unloading stresses due to excavation are usually assumed to be uniform. Even for the hydrostatic initial stress situation, this assumption is not valid, especially when the tunnel is shallow. Figure 5.1 shows a shallow tunnel where the stress relief at the invert is twice as large as at the crown. These closed form solutions completely ignore the nonlinearity of the stress-strain behaviour of soil before failure.

Developing a closed form solution to overcome these limitations is virtually impossible. On the other hand, the major advantage of a proper finite element analysis is that it can overcome all these limitations. Therefore, the finite element procedure described in Chapter 3 was used in a comprehensive parametric study to understand the pore pressure behaviour around shallow tunnels. Any realistic parametric study of pore pressure behaviour around tunnels necessarily involves a large number of parameters. A very large volume of results can be obtained by varying the parameters, but a comprehensive parametric study warrants such a variation and thus the large volume of results is inevitable. It is not possible to use such a large volume of results directly to understand the pore pressure behaviour around tunnels. Furthermore, utilizing all these results as design diagrams or as a classification system (one objective of the study), is impractical. For these reasons, a comprehensive non-dimensionalization and normalization procedure was thought to be an essential part of the proposed parametric study. The sections that follow will discuss and explore possible non-dimensionalization and normalization procedures.

5.3 NEED FOR NORMALIZATION AND NONDIMENSIONALIZATION

As discussed in the previous section, a non-dimensionalization and normalization procedure is necessary to develop simple design diagrams or a classification system to study a complex phenomenon influenced by a large number of variables. The pore pressure behaviour around tunnel excavations is an example of such a complex phenomenon. The use of non-dimensionalized quantities and a proper normalization procedure reduces considerably the number of parameters that need to be displayed in the form of charts, diagrams or a classification system. This is a virtual necessity, if design diagrams or a classification system are to have any practical value or significance. As discussed above, a concisely presented set of results also makes it easier to understand a complex physical phenomenon that involves a large number of variables. The proposed non-dimensionalization and normalization procedure will be discussed in detail in this and the sections to follow. The major factors that govern the pore pressure generation and dissipation behaviour will be identified. The general principles of geomechanics and the closed form solution presented in the previous section will be used as a guideline in this task.

5.3.1 NON-DIMENSIONALIZATION OF PORE PRESSURE

If the water table is at the ground surface or well below the tunnel invert, the pore pressure generated around a tunnel is dependent on the stress change of the soil due to the excavation, which in turn depends on the magnitude of the stress relief. The magnitude of stress relief is determined by the initial in situ stresses around the tunnel before the excavation. Therefore, the pore pressure change can be considered to depend on σ_v and σ_h, or the coefficient of earth pressure at rest K_0 and on σ_v, where, σ_v and σ_h are the vertical and horizontal in situ effective stresses, respectively. That is, the stress relief, and thus the pore pressure can be influenced by the tunnel geometry (depth of cover H and the tunnel diameter D), the soil unit weight γ and K_0. In addition to the pore pressure coefficient a, the soil strength s_u and the modulus E_s may influence the pore pressure generation.

The initial pore pressure is directly influenced by the initial in situ stress, therefore, the pore pressure can be non-dimensionalized intuitively as $u/\gamma H_c$, where, H_c is the depth of tunnel axis below the ground surface.

5.3.2 SPATIAL NON-DIMENSIONALIZATION

A proper non-dimensionalization of spatial coordinates is one of the most important steps in developing concise pore pressure diagrams. If an efficient and realistic spatial non-dimensionalization procedure cannot be developed, each geometry must have a separate pore pressure diagram. A separate diagram for each geometry makes the possibility of developing concise design diagrams or a classification system impractical. A spatial non-dimensionalization procedure was developed to overcome these problems. In the following non-dimensionalization procedure, (x,y) coordinates are non-dimensionalized into (ξ,η) (Figure 5.2).

For $y<0$,

$$\xi = x/R \quad \eta = y/R \qquad [5.10]$$

For $y\geq0$,

$$\xi = x/R \quad \eta = y/[\{(R - H_c/2)/(H_c - \hat{y})\}(H_c - y) + H_c/2] \qquad [5.11]$$

where,

$$\hat{y} = (R^2 - x^2)^{1/2} \text{ for } x<R$$

$$\hat{y} = 0 \text{ for } x\geq R$$

Under this non-dimensionalization procedure, any given circular tunnel geometry in (x,y) plane becomes a unique circle of unit radius, center lying two units below the ground surface in (ξ,η) space (Figure 5.2). Mathematically, this can be considered as a coordinate transformation. Note also that the variables H and D can be split into H/D and D. It is expected that this spatial non-dimensionalization will

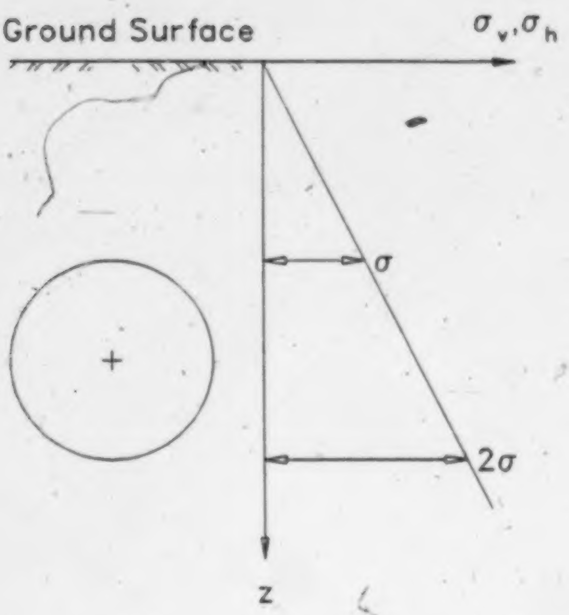
Ground Surface
σ_v, σ_h
σ
2σ
z

Figure 5.1 Unloading Stresses vs Tunnel Depth; $K_0=1$

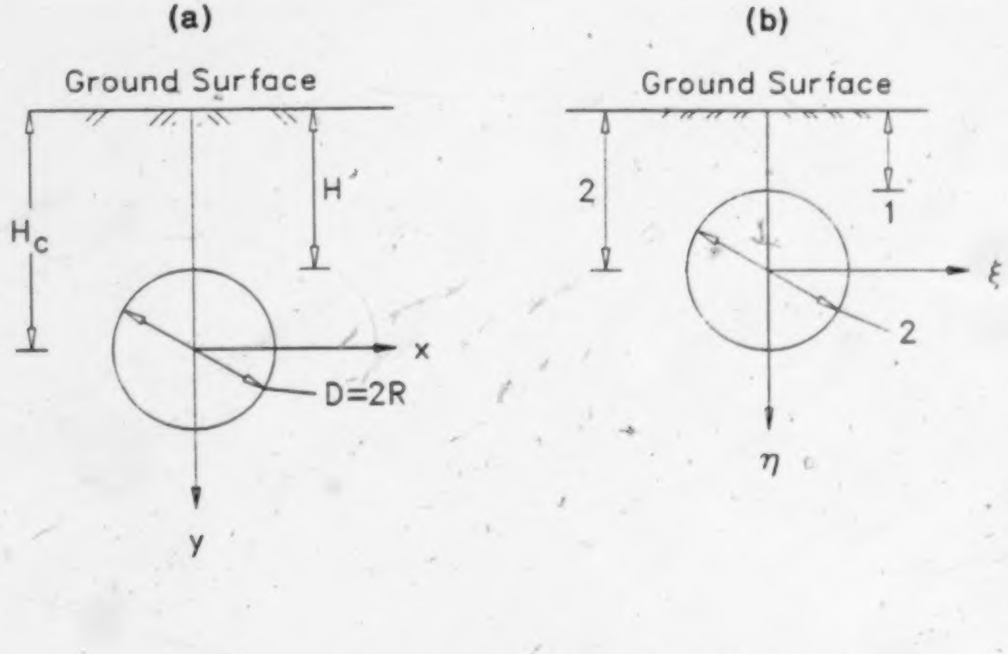
(a)
Ground Surface
H_c
H
x
D=2R
y
(b)
Ground Surface
2
1
ξ
2
η

Figure 5.2 Spatial Nondimensionalization

normalize the pore water pressure with respect to geometry and provide approximately the same pore pressure diagram as far as the geometry is concerned.

5.3.3 NON-DIMENSIONALIZATION OF STRENGTH AND MODULUS

The pore water pressure developed around a tunnel excavation depends on the stress changes. The stress changes, however, may depend on the soil strength, soil modulus and the stress relief. As explained in the previous sections, the stress relief can be characterized by the σ_v and K_0 values around the tunnel before the excavation. The soil modulus depends on the initial stress history, stress state and the current stress level. Since the stress relief around the tunnel can be characterized by σ_v and K_0, the stress level is also determined by K_0 and σ_v. On the basis of the above facts, E_s/σ_v and s_u/σ_v can be considered to be the basic non-dimensional units characterizing the soil modulus and strength in this problem. However, on considering both normally and overconsolidated soil behaviour, the strength and modulus can be non-dimensionalized in a more general form, $(s_u/\sigma_v)(\sigma_v/P_a)^m$ and $(E_s/\sigma_v)(\sigma_v/P_a)^n$, where, P_a is the atmospheric pressure. This approach has the added advantage that these quantities in most cases become soil properties representing normally and overconsolidated clays (sections 5.5.1 and 5.5.3). They will be referred to as the normalized modulus and the normalized strength respectively.

5.3.4 NON-DIMENSIONALIZED TIME (T)

The generation of initial pore pressure is an important first step in examining the general pore pressure behaviour around tunnels. The second step is to examine the pore pressure dissipation behaviour with time. It was postulated that the rate of pore pressure dissipation depends on H and D (Figure 5.2) as far as the tunnel geometry is concerned, and on c_v as far as the material properties are concerned. It can also be argued that while the pore pressure at a given time may be a decreasing function of the coefficient of consolidation c_v and D, it is an increasing function of the depth of cover H. On this basis, a non-dimensionalized time factor of the form given below was proposed.

$$T = c_v t/H^2(D/H)^n \qquad [5.12]$$

This time factor is assumed to take into account the influence of geometry (including the boundary conditions) and the soil properties on the rate of pore water pressure dissipation around a tunnel.

5.3.5 A NON-DIMENSIONAL PARAMETER FOR SUPPORTED TUNNELS, ESR

As discussed previously, pore pressures are generated around a tunnel during excavation due to the change in stress field caused by the excavation process. However, the changes in stress are determined by the strain field, more precisely, by the distribution of the relative values of the strains. Moreover, the relative strains are dependent on the stiffness distribution of the soil mass. It is reasonable to assume that in a very broad sense, in supported tunnels the relative strains are also dependent on the stiffness of the ground relative to the liner. Hence, the pore pressure generated around a supported tunnel is dependent on the ratio of the ground stiffness to the liner stiffness.

It is very difficult to quantify this broad meaning of relative stiffness into simplistic non-dimensionalized quantities. Nevertheless, the following non-dimensionalized quantity for the relative stiffness called the Effective Stiffness Ratio (ESR) was postulated:

Effective Stiffness Ratio,

$$\mathrm{ESR} = \frac{\text{Characteristic strain of the ground}}{\text{Characteristic strain of the liner}} \qquad [5.13]$$

This can be shown equal to:

$$\{2(1-\nu^2)(3-K_0)E_l/(1-\nu_l^2)E_sR\}/\{(1+K_0)/A_l+(1-K_0)R^2/6I_l\} \qquad [5.14]$$

where,

A_l	is cross sectional area of liner,
E_l	is Young's modulus of liner,
I_l	is second moment of area of liner,
R	is radius of the tunnel,
ν	is Poisson's ratio of soil and
ν_l	is Poisson's ratio of liner.

The derivation of this equation is given in Appendix B.

5.4 FINITE ELEMENT ANALYSIS

As stated in section 5.2, closed form solutions oversimplify the continuum model and have many limitations. A finite element analysis overcomes virtually all of these limitations and is, therefore, the most suitable. However, it must be noted that there are different degrees of sophistication and complexity in finite element analyses. Therefore, a reasonable balance has to be reached among the degree of sophistication, complexity, economy and the numerical accuracy of the required solution of a given problem (pore pressure around tunnels in this case). It is also essential that the underlying assumptions and simplifications in the numerical procedure be realistic and acceptable to a reasonable degree. For instance, the selected mesh and the size of the load steps should yield reasonably accurate (numerically) and reliable results. These aspects of the finite element procedure selected (described in Chapter 3) for this parametric study will be discussed in the following sections. This discussion will be specifically related to the problem under consideration, viz., pore pressure behaviour around tunnels.

5.4.1 SELECTION OF A MESH

To obtain numerically reliable results, it is imperative that the mesh selected for the finite element analysis be reasonably accurate and reliable. That is, it must represent properly and to a reasonable degree the idealized continuum, as far as the boundary, the mesh pattern, the number and the type of elements are concerned. However, as pointed out in section 2.2.3.3, it is not possible to select such a mesh in one trial. As discussed in that section, the initial mesh was selected using engineering judgement and is shown in Figure 5.3. In modifying the mesh, along with engineering judgement, the pore water pressure contours obtained for the initial mesh were used (see section 2.2.3.3). Using the modified mesh, the analysis was repeated and the initial pore pressure contours were re-drawn. This first modified mesh is shown in Figure 5.4. For a finite element mesh to be reliable and accurate, it is essential that the grid is sufficiently refined. To ensure that the mesh is reasonably refined, it is necessary to further refine the existing mesh and check whether the change in the computed results are within a required numerical accuracy (Kulhawy, 1974). This is especially true of complex but important problems where no similar analysis has been performed to generate reliable meshes. The author is not aware of any such published work on pore pressure behaviour around tunnels. Therefore, the first modified mesh was refined (Figure 5.5) using engineering judgement and the pore pressure contours obtained using the same mesh (after first modification). The new pore pressure values were compared with the pore pressures obtained using the previous mesh. The maximum deviation in pore pressure was about 5%.

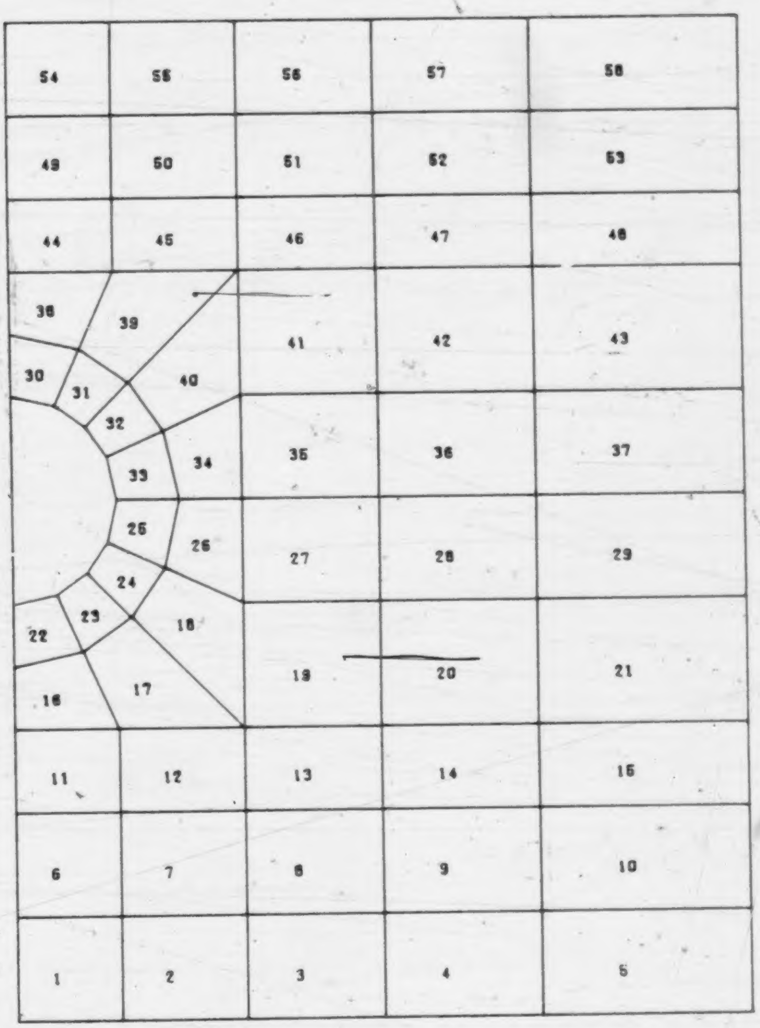
54
55
56
57
58
49
50
51
52
53
44
45
46
47
48
38
39
41
42
43
30
31
40
32
33
34
35
36
37
25
26
27
28
29
24
23
18
22
19
20
21
16
17
11
12
13
14
15
6
7
8
9
10
1
2
3
4
5

Figure 5.3 Initial Coarse Mesh

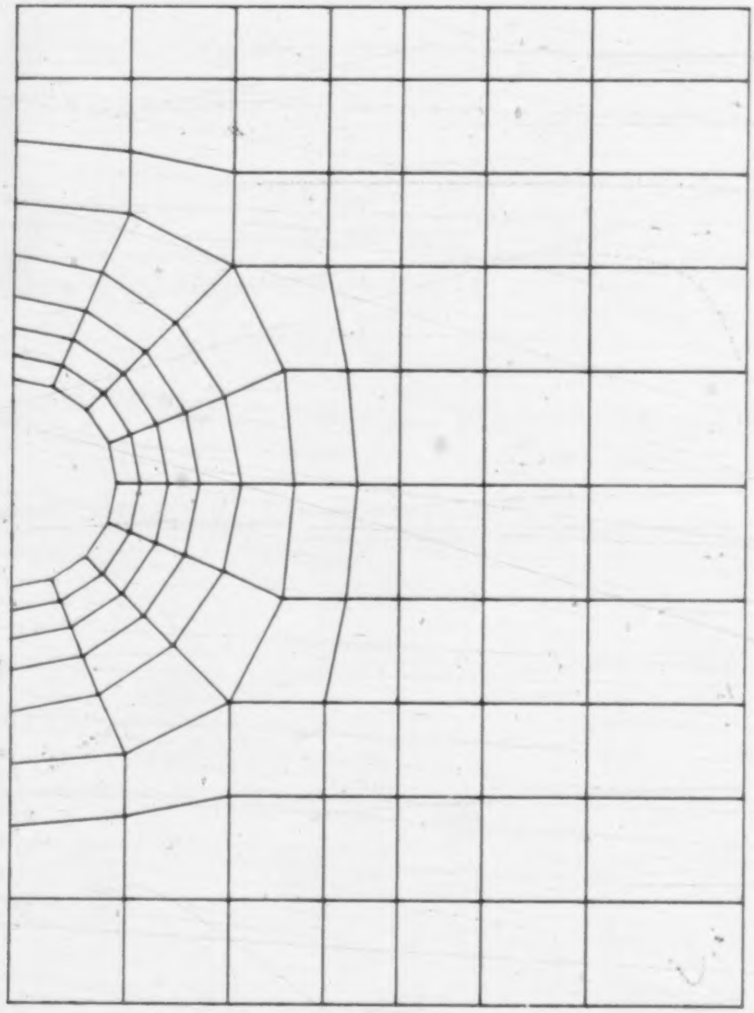

Figure 5.4 Mesh after First Modification

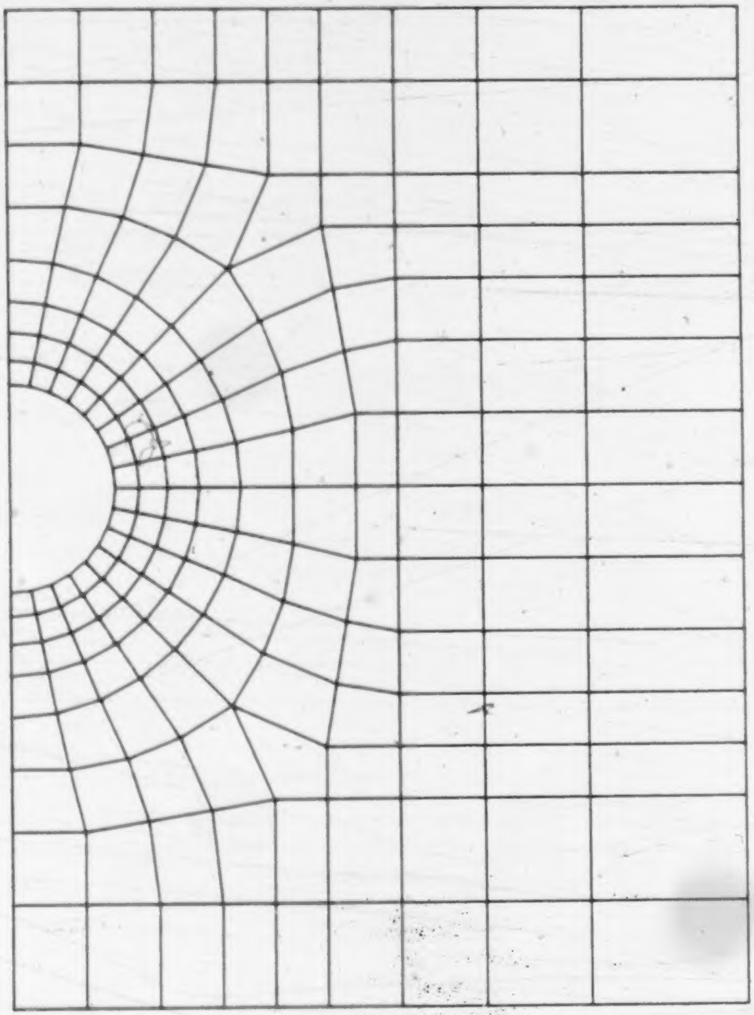

Figure 5.5 Refined Mesh, Typical Mesh Used in the Study

The boundaries must be represented properly for the mesh to be numerically accurate. The idealized problem consists of a semi-infinite continuum, therefore, it is necessary to select a boundary that represents the semi infinite continuum reasonably accurately. To satisfy this condition, the existing boundary was expanded by about 25% and the corresponding mesh is shown in Figure 5.6. It is essential that the rest of the grid be kept unchanged during this process. The pore pressure values were compared with pore pressure values corresponding to the previous mesh (Figure 5.5). The maximum deviation in pore pressures was about 2%. These results also show that the influence of the stress relief is negligible at a depth beyond two and a half diameters and at a horizontal distance beyond three and a half diameters from the center. Kulhawy (1974) obtained similar results for a circular opening. On the basis of these results, the mesh shown in Figure 5.5 will be used as a typical mesh for the parametric studies in the following Chapters. Heinz (1984) studied the influence of boundaries on deformations around tunnels. He found that when the distance to the lateral boundary is greater than about four diameters and the distance to the rigid base is greater than 2.2 diameters from the center, the increase in these distances had only a slight effect on the computed deformations. His results show that this is especially true when the soil modulus increases with depth in some form.

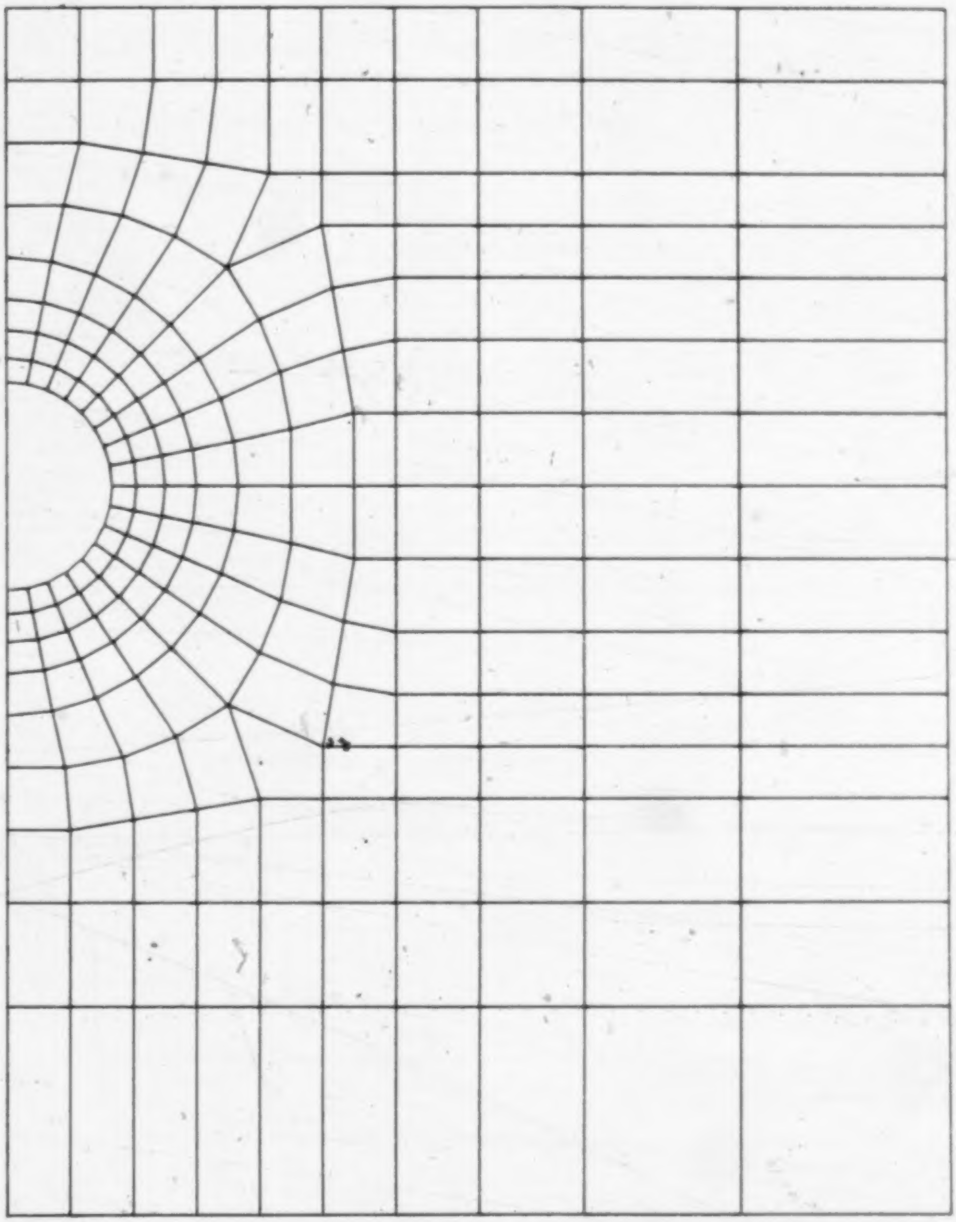

Figure 5.6 Mesh for the Expanded Boundary

5.4.2 ASSUMPTION OF MONOTONICALLY INCREASING STRESS

As pointed out, pore pressure generation is directly related to the stiffness distribution (modulus of a point relative to the others) of the soil mass. In our finite element analysis that incorporates a nonlinear hyperbolic material model, it is assumed that the stresses in every finite element (in the mesh) change monotonically and there are no stress reversals. However, if there are stress reversals, the stiffness of the soil will be much greater than when there are only monotonic stress changes. Depending on the assumption made, the corresponding stiffness distribution and hence the deformations can be significantly different (Heinz, 1984), consequently, the pore pressure distribution will change. The above assumption, unlike the general assumptions, can be verified after the stress analysis is performed (see also section 3.7). It is possible to check whether in fact there were stress reversals during the numerical simulation of the tunnel construction. Due to the importance of this assumption, it was decided to verify it in every case, for critical soil elements (author used engineering judgement and intuition in selecting critical elements).

The typical results obtained for the following case are given in subsequent figures. The tunnel geometry was $H/D=1.6$ and $D=20$ FT. The soil properties chosen were $E_i/\sigma_{1c}=500$, $s_u/\sigma_{1c}=0.5$ and $a=0.3$. The excavation of the tunnel was simulated by unloading the soil mass in ten equal load steps. A finite element mesh very similar to that shown in Figure 5.3 was used. The stress-strain behaviour followed by the three critical elements 22, 25 and 30 (Figure 5.3) with continuing tunnel excavation (continued stress relief) is shown in Figures 5.7 (a), (b) and (c) respectively. It is clear that in these critical elements the stresses change monotonically with continued excavation. These three elements were thought to be the most probable elements that would violate the assumption. It was found however, that these elements represent the typical behaviour of all other elements in the mesh. In other words, this analysis justified the original assumption of monotonic stress changes. As explained earlier, it is important that this assumption is not violated significantly during the numerical simulation. It must also be noted that this behaviour was very typical of all other tunnel excavations simulated in this Chapter.

5.4.3 LOAD STEP SIZE AND ITS SIGNIFICANCE

As discussed in section 3.5.3.3, the choice of a sufficiently small load step is essential to obtain reliable stress and displacement results from the proposed finite element analysis. However, there are no guidelines for determining a sufficiently small load step for a given problem, nor have there been any studies to determine the size of the load step that yields numerically reliable results for the problem of tunnel excavation. An

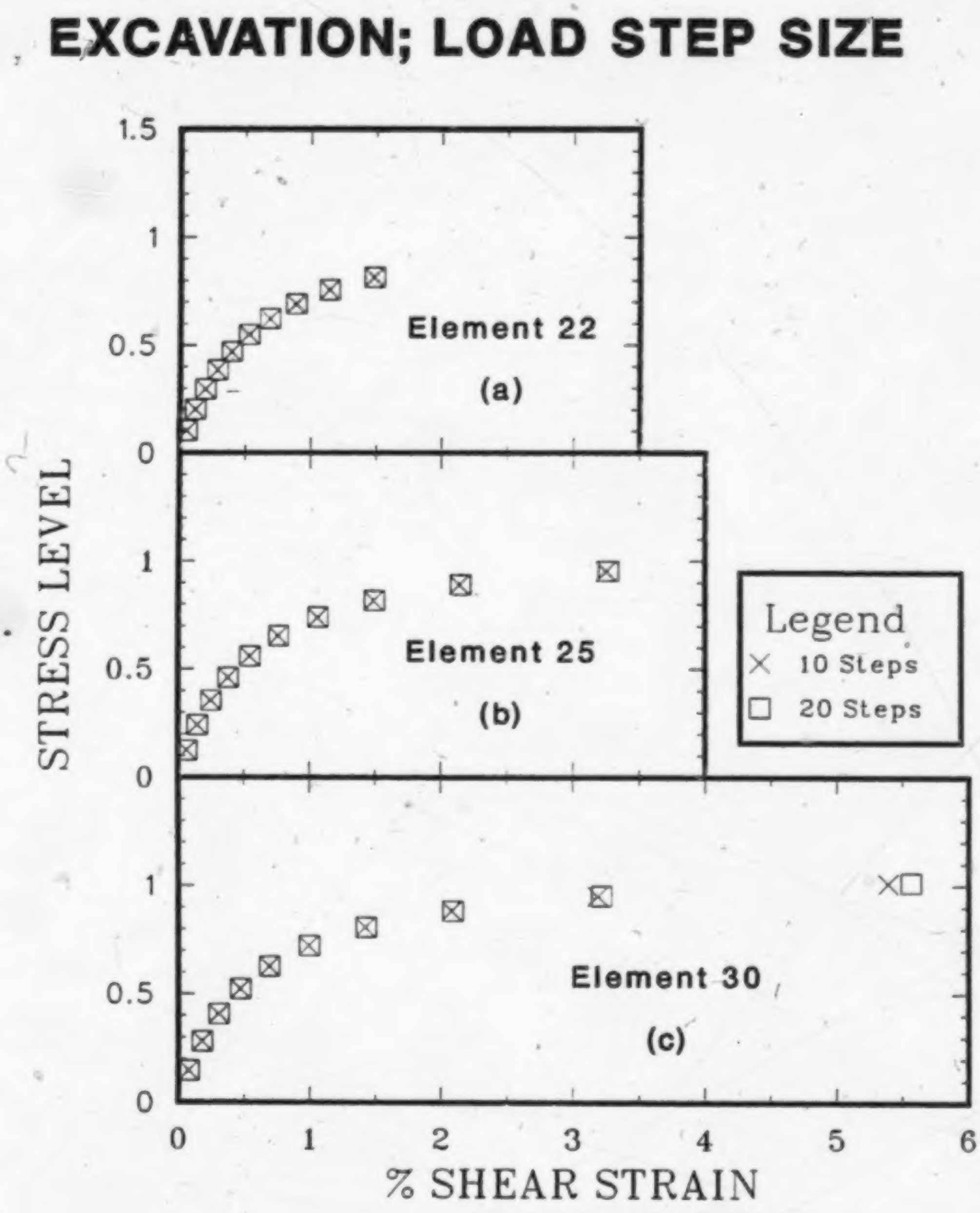

Figure 5.7 Stress-Strain Behaviour of Critical Elements during Tunnel Excavation Simulation

approximate, yet very practical and simple method proposed in section 3.5.3.3 to check whether the chosen load steps are sufficiently small, was applied herein. In this procedure, the finite element analysis is repeated with the load steps halved and the required results (usually the stresses and the strains) of every element in the mesh are compared with the full load step results. If the differences in these results are not acceptable, the load steps are further subdivided until satisfactory results are obtained. In a more practical approach, only a few critical elements (chosen by engineering judgement and intuition) are selected and the results of these elements are compared.

The tunnel excavation simulation described in section 5.4.2 was used. Employing the same mesh (Figure 5.3), the excavation was simulated by 20 equal load steps (i.e. half of the previous load step size). These results were compared with the results obtained in the previous analysis (section 5.4.2) using 10 equal load steps. Figures 5.8 (a), (b) and (c) compare the results for elements 22, 25 and 30 (Figure 5.3) respectively. The deviations in the above stress-strain results were considered insignificant. As in the foregoing section, the elements chosen were considered to be the critical elements. However, the behaviour of the critical elements was found to represent the typical behaviour of other elements in the mesh. These results show that the finite element results obtained using 10 equal load steps are satisfactory. It must also be noted that these results

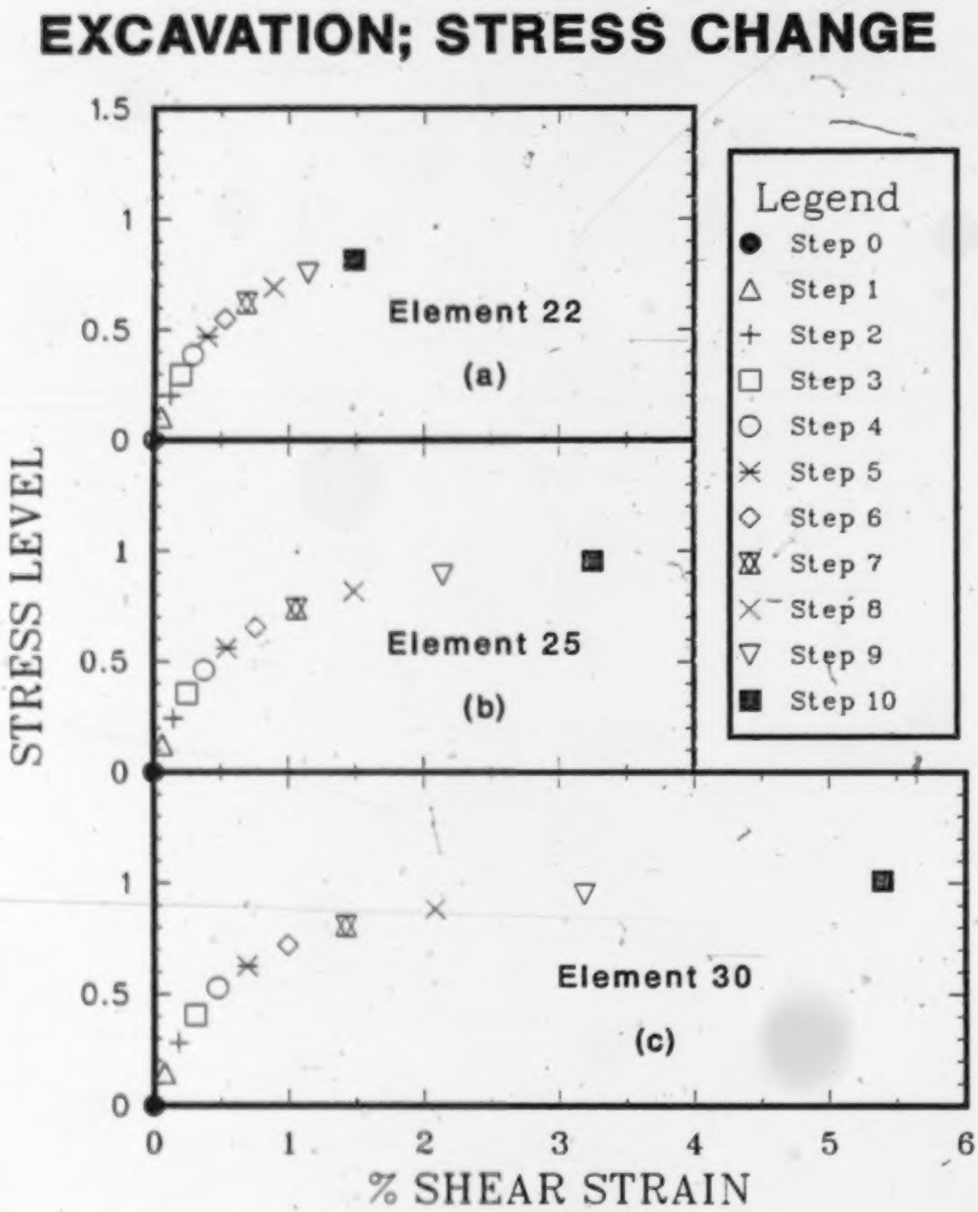

Figure 5.8 Stress-Strain Behaviour of Critical Elements with Half-Load Step Size in Tunnel Excavation Simulation

are typical for this problem and it was found that all other (numerical) tunnel excavation simulations considered in this Chapter yielded similar results.

One other approach proposed in section 3.5.3.3 was applied to verify the adequacy of the size of the selected load step. The basic principle behind this approach is to check how closely the material behaviour that is followed by the finite elements compare with the idealized material behaviour that they are expected to follow. Although theoretically each element has to be checked for its behaviour, as before in a more practical approach, only the critical elements in the mesh were checked.

The tunnel excavation simulation described previously was employed. The finite element mesh used is shown in Figure 5.3. Ten equal load steps were used in this analysis. As before, the elements 22, 25, and 30 were chosen to be the critical elements. The idealized material behaviour that should be followed by these elements was obtained using the hyperbolic model described in section 3.4.1.1. This is plotted in Figure 5.9 which also shows the material behaviour followed by the finite elements 22, 25 and 30 (Figure 5.3). The finite element behaviour obtained using 10 equal load steps compare remarkably well with the idealized material behaviour. On this basis, the selected load step size is satisfactory. It must also be noted that this behaviour is typical of all other elements in the mesh. The fact that all elements closely follow the expected material

FEA AND MATERIAL MODEL

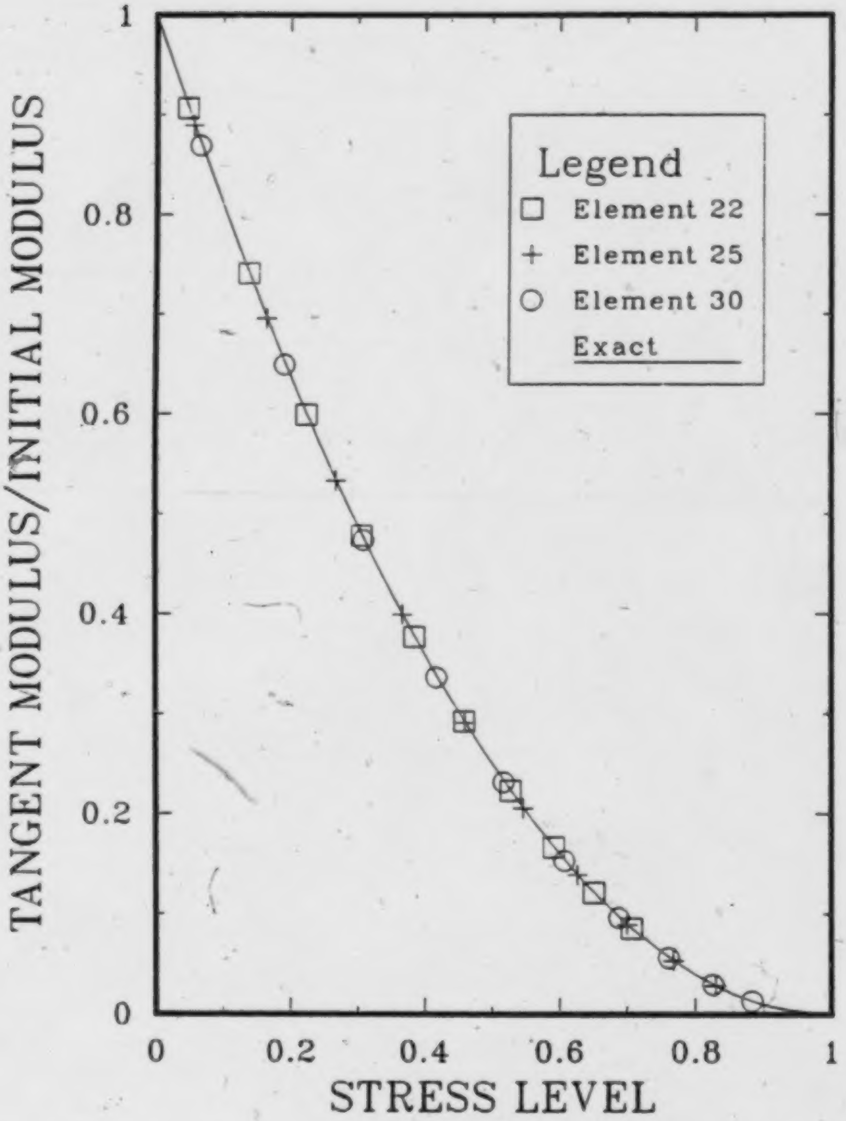

Figure 5.9 Material Behaviour of Critical Finite Elements and the Idealized Behaviour

behaviour is a verification of the consistency of the material model used in this finite element analysis.

5.5 PARAMETRIC STUDY

In the following sections, a comprehensive parametric study will be undertaken in order to understand the pore pressure behaviour around shallow tunnels. An attempt was also made to use these results to develop simple design diagrams or a classification system for estimating pore pressures. The parametric study will be performed on shallow tunnels constructed in both normally and overconsolidated clays. Unsupported as well as supported tunnels will be analysed. The influence of the variation of each parameter (mentioned in section 5.3) on generation and dissipation of pore pressures around tunnels will be examined. These results are essential to understand the pore pressure behaviour around tunnels and to justify the non-dimensionalization and normalization procedures proposed in section 5.3. These results will also be used to further normalize the pore pressures in order to obtain a concise set of pore pressure diagrams describing general pore pressure behaviour. It was decided to restrict the study to the practical ranges of the parameters. By restricting the study to practical ranges of the parameters, pore pressure diagrams can be further simplified and a significant amount of time and resources can be saved. Since the study was restricted to shallow tunnels, it is necessary to have a clear definition of a shallow tunnel. There are two definitions. Eisenstein (1984) defined a shallow tunnel as a tunnel where the difference in boundary conditions above and below the tunnel produce distinctly different displacement fields above and below the tunnel. Atkinson (1977) defined a tunnel producing measurable deformations appearing on the surface as a shallow tunnel. Both these definitions can be interpreted in many different ways and thus can be subjective. Therefore, in certain situations, these definitions may be ambiguous. After carefully examining the published work of Peck, et al. (1972), Mohraz, et al. (1975) Davis et al. (1980) and this study, the author proposed a more precise as well as a practical definition. A tunnel where $H/D<3$ (or $H_c/D<3.5$) is defined as a shallow tunnel. However, in practice, when $H/D<1$, the cut and cover procedure often becomes more economical. On this basis, the study was restricted to shallow tunnels where $1<H/D<3$.

As stated in section 5.2, a finite element analysis is the most realistic available approach for the proposed parametric study. The details of the finite element analysis used for this parametric study are given in Chapter 3. In this parametric study each parameter was varied within its practical range, keeping all the others at their average values. Then the variation of the normalized and non-dimensionalized pore pressure distributions with each parameter was compared with that corresponding to the average parameters. The deviations were computed as a percentage of the largest magnitude of the pore pressure corresponding to the average parameters. This approach is expected to give more realistic numbers for assessing the pore pressure deviations. The maximum deviations were then estimated. It was observed that this maximum deviation had more of a mathematical significance than a practical one. Therefore, a more practical and realistic approach was used in estimating the maximum percentage deviations. A quantity called 95% probable maximum deviation was defined. It is the lower bound of the maximum deviation of 95% of the area of a zone of influence. By examining the pore pressure distribution for different parameters, the zone of influence for pore pressure around shallow tunnels constructed in both normally and overconsolidated clays was considered to be an area bounded by one horizontal and two vertical lines, a diameter below the invert and two diameters away from the spring lines respectively. In our parametric analysis, in addition to these probable percentage deviations, the normalized pore pressure distributions themselves are presented to enable making a complete comparison.

5.5.1 UNSUPPORTED TUNNELS IN NORMALLY CONSOLIDATED CLAY

Before starting a detailed parametric study on tunnels in normally consolidated clay, it is essential to understand the normally consolidated clay behaviour.

In a typical normally consolidated clay, both the strength and modulus increase with depth. The variation is found to be approximately linear (Ladd, et al. (1974)) with depth. That is, s_u/σ_v and E_s/σ_v are approximately constant for a given soil and they can be considered as soil properties. The importance of using the practical ranges of parameters (especially when there are large number of parameters involved) cannot be over emphasized.

In the following section, a comprehensive parametric study will be carried out using the practical ranges of parameters given in Table 5.1 for normally consolidated clay. The variation of pore pressure behaviour will be compared with the pore pressure behaviour corresponding to average parameter values, namely, $H/D = 1.8$, $E_i/\sigma_v=500$, $s_u/\sigma_v=0.5$, $K_0=0.65$, and $D=6$ m .

5.5.1.1 STRENGTH AND PORE PRESSURE

The variation of initial pore pressure generation with soil strength is investigated in this section. The strength of a normally consolidated clay can be characterized by s_u/σ_v (section 5.5.1), therefore, the pore pressure variation with strength can be investigated by varying s_u/σ_v. The investigation was restricted to the practical range of strength values for normally consolidated clays (Table 5.1) from the lower limit of s_u/σ_v of 0.3 to the upper limit of 0.7. While varying the strength, all the other parameters were kept at average values (section 5.5.1). The pore pressure values obtained were normalized in different ways and the distributions were compared. First, the expression given in equation 5.9 was used to normalize the pore pressures. When simplified and approximated, the normalization factor for this expression becomes, $1/(s_u/\sigma_v+\sigma_v/s_u)$, but the results were not encouraging. A normalizing factor of the form $1/(\lambda_1 + \lambda_2 s_u/\sigma_v)$ was postulated. By trial and error, it was found that, for $\lambda_1 = 1$ and $\lambda_2 = 0$, the normalized pore pressure diagrams produced the least deviation from that corresponding to average parameter values. For s_u/σ_v less than 0.4, substantial local failure was observed at the periphery of the tunnel. The material model and the finite element formulation used are not expected to simulate the failure very accurately. Therefore, $s_u/\sigma_v=0.40$, was selected as the lower bound of strength for which the proposed finite element procedure is reliable. The normalized pore pressure distributions corresponding to $s_u/\sigma_v=0.40$, 0.45, 0.55 0.60, 0.65, and 0.70 were computed and compared with that corresponding to $s_u/\sigma_v=0.5$. The extreme deviations took place for the extreme values, namely, $s_u/\sigma_v=0.4$ and 0.7. The percentage pore pressure deviations were computed as explained in section 5.5. The 95% probable maximum pore pressure deviations corresponding to $s_u/\sigma_v=0.4$ and 0.7 are approximately 5% and 10%, respectively. Figure 5.10 shows the normalized pore pressure diagram corresponding to $s_u/\sigma_v=0.4$ and Figure 5.11 for $s_u/\sigma_v=0.7$.

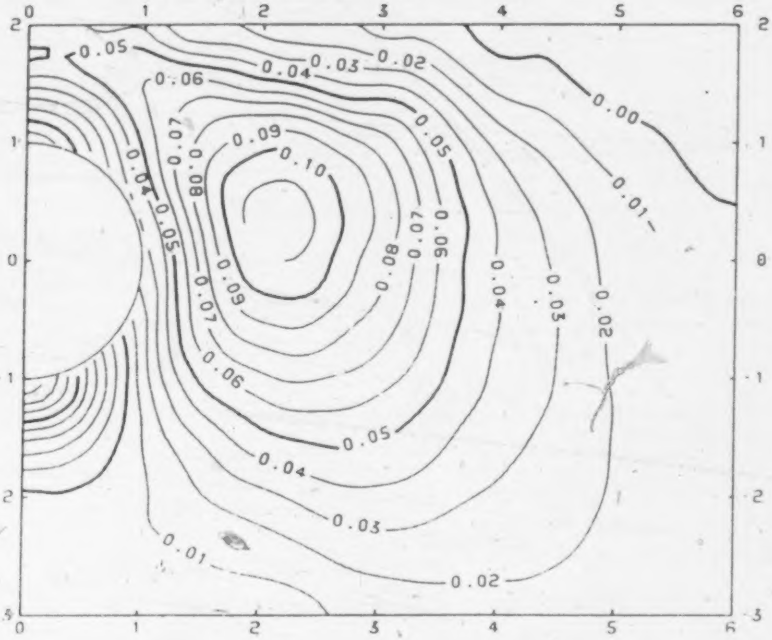

Figure 5.10 Normalized Pore Pressure Contours for $s_u/\sigma_v=0.4$

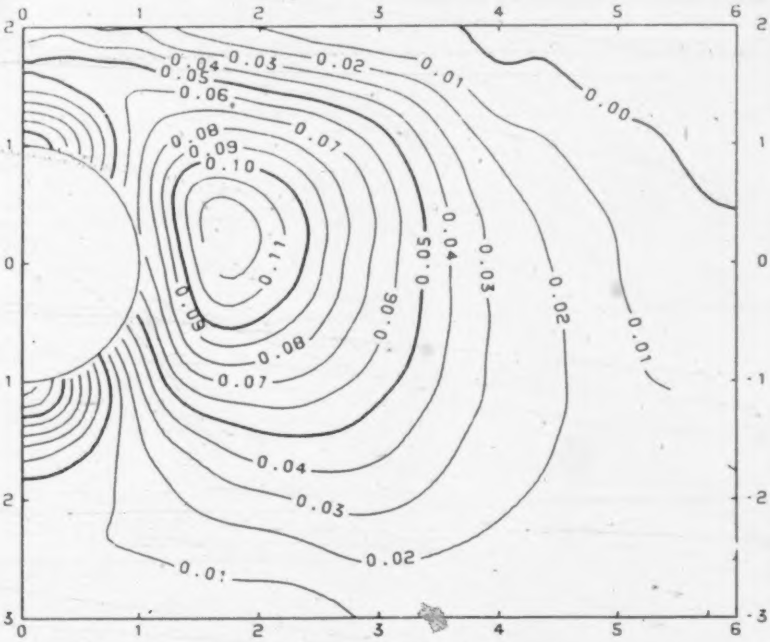

Figure 5.11 Normalized Pore Pressure Contours for $s_u/\sigma_v=0.7$

For s_u/σ_v greater than 0.4, the initial pore pressure seems to be less sensitive to changes in strength. This behaviour is not very surprising in stiffer clays that have higher strength values. Since the differences in stress levels are smaller in clays having higher strength values, the stress changes due to the excavation of the tunnel is not sensitive to the changes of strength. The pore pressures are caused by the stress changes, therefore, this insensitivity is reflected in the initial distribution of the pore pressure. Moreover, the results show that the highest pore pressure value generated around a tunnel excavation tends to slightly increase with increasing strength. This is compatible with the arching process. For higher strength values, the stress level (stress/strength) around the periphery of the tunnel is smaller. Hence the redistribution of loads are lesser and the arching loads tend to be larger. The pore pressure generation is directly related to the stress change, and therefore, the positive maximum pore pressure tends to increase with the increasing strength. It can also be observed that the peak (point of maximum positive pore pressure) moves very slightly, horizontally, towards the center of the tunnel as the strength increases. This is also compatible with the arching process that occurs around a tunnel. As the strength decreases, the zone of a given stress level expands away from the tunnel. With the spread of this zone away from the tunnel, the peak also moves away from the tunnel.

5.5.1.2 MODULUS AND PORE PRESSURE

The influence of modulus variation on pore pressure generation around a tunnel is investigated in this section. As stated in section 5.5.1, the modulus of a normally consolidated clay can be characterized by E_s/σ_v. In hyperbolic models, E_s/σ_v can be characterized by E_i/σ_v (see section 3.4.1.1). Therefore, the pore pressure variation with modulus can be investigated by varying E_i/σ_v. The initial pore pressure corresponding to various E_i/σ_v values were computed and the pore pressure distributions were obtained. The modulus values E_i/σ_v were varied from 200 to 800, which are within a practical range (Table 5.1). The normalized pore pressures for E_i/σ_v=200 and 800 were compared with the pore pressure values corresponding to the average parameters (section 5.5.1) and there was no deviation. Figures 5.12 and 5.13 show the normalized pore pressure diagrams on (ξ,η) plane for E_i/σ_v=200 and 800 respectively. This behaviour is not unexpected and it agrees with the fact that the strain ratios do not depend very much on the value of E_i/σ_v, rather they depend on the form of the modulus variation (Heinz, op. cit.), that is, the stress changes are not sensitive to the changes in E_i/σ_v. However, the pore pressure changes are directly related to the stress changes, and thus,

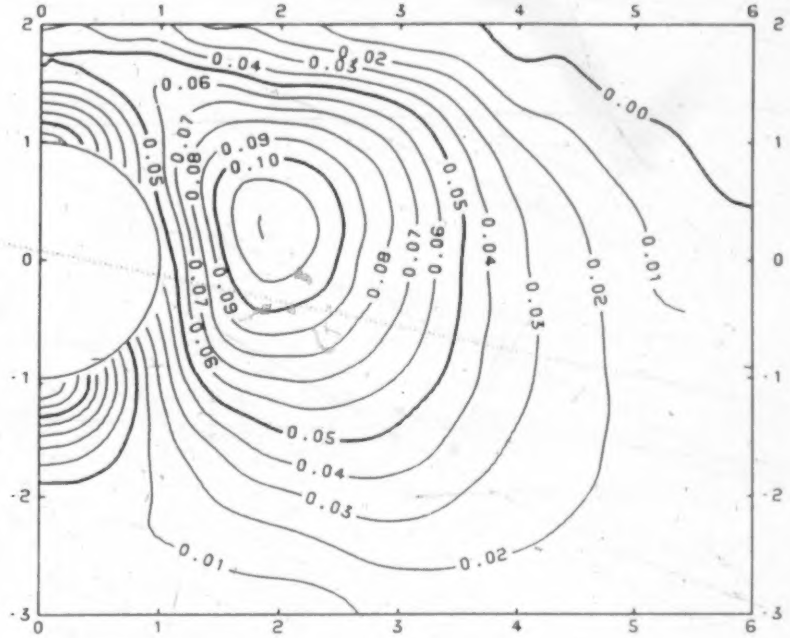

Figure 5.12 Normalized Pore Pressure for E_i/σ_v=200

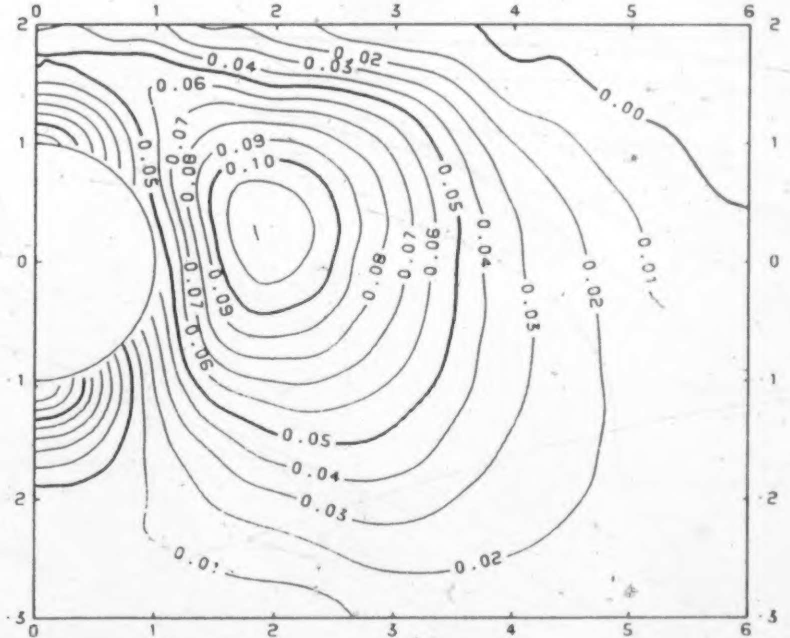

Figure 5.13 Normalized Pore Pressure for E_i/σ_v=800

the pore pressure changes cannot be sensitive to E_i/σ_v changes. This can be seen in the results.

5.5.1.3 HENKEL'S COEFFICIENT a AND PORE PRESSURE

The initial pore pressure generation is directly influenced to a large extent by the pore pressure coefficients. For the reasons given in section 3.4.1.2, the Henkel pore pressure coefficient was employed in this analysis. As before, keeping all the other parameters at their average values (section 5.5.1), the Henkel's pore pressure coefficient was varied and the initial pore pressures were computed. As explained in section 5.5, a practical range of a was selected for the analysis. Consequently, the pore pressure coefficient was varied from 0.12 to 0.48 (0.12, 0.2, 0.3, 0.4 and 0.48) (Table 5.1). Several attempts were made to normalize these pore water pressure values with respect to the pore pressure coefficient. The closed form solution (Clough, et al., 1981) for the elastic region (Equation 5.9) shows that $1/a$ is the normalization factor. However, when $1/a$ was used as the normalization factor, the normalized pore pressure results differed considerably for different a values. A normalization factor of the form $1/(\lambda_1 + \lambda_2 a)$ was attempted, and by trial and error, it was determined that the best results can be obtained for $\lambda_2=10$ and $\lambda_1=1$. Figures 5.14 and 5.15 show the normalized pore pressure diagrams corresponding to Henkel coefficient 0.12 and 0.48

respectively. The deviation of pore pressure values from the values corresponding to average parameters (section 5.5.1) was estimated. The extreme deviations occurred for extreme a values. The 95% probable maximum deviation (defined in section 5.5) of normalized pore pressure for a=0.48 is about 6%, whereas for 0.12 it is about 10%.

In general, with increasing a the pore pressure increases and the peak tends to move slightly towards the center of the tunnel.

5.5.1.4 IN SITU K_0 AND PORE PRESSURE

This section examines the effects of K_0 on the initial pore pressure generation around tunnels. The development of a normalization procedure with respect to K_0 is more difficult, as there are no simple closed form solutions for K_0 conditions that can be used as a guideline in the normalization process. Pore pressure generation is directly influenced by the shear stresses generated and the change in normal stresses due to unloading, and these two factors are directly related to K_0. It was postulated that the pore pressure can be normalized with respect to K_0 within its practical range by a factor of the form, $1/(\lambda_1+\lambda_2K_0)$. Finite element analyses were performed for different K_0 values, 0.50, 0.55, 0.60, 0.70, 0.75 and 0.80, keeping all the other parameters at average values (section 5.5.1). The normalized pore pressure values were compared with the

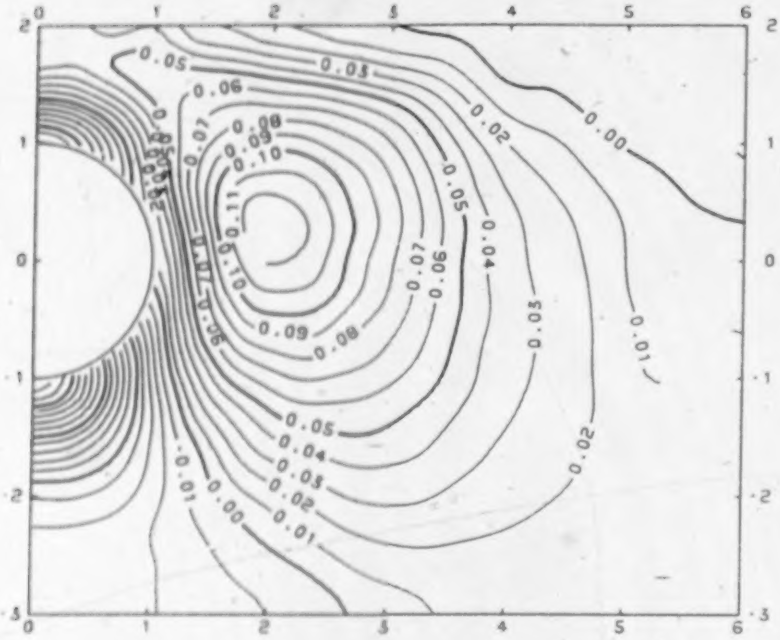

Figure 5.14 Normalized Pore Pressure for a=0.12

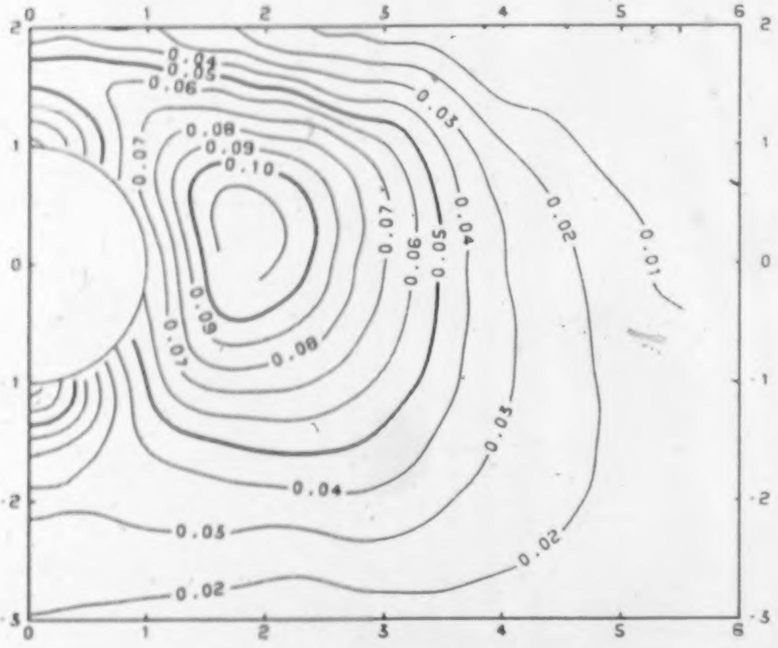

Figure 5.15 Normalized Pore Pressure for a=0.48

values obtained for the average parameters. The range of K_0=0.5 to 0.8 is the practical range (Table 5.1) for normally consolidated clays. The deviations of the normalized pore pressures for different K_0 values from the values corresponding to average parameters were computed as explained in section 5.5. The best results were obtained for λ_2=-0.6 and λ_1=1. The extreme deviations took place for the extreme values of K_0. The 95% probable maximum deviation (defined in section 5.5) for K_0=0.5 is about 5%, and for 0.8 is 4%. The Figures 5.16 and 5.17 show the normalized pore pressure contours for K_0=0.5 and 0.8, respectively.

As K_0 increases in the practical range, the pore pressure tends to decrease. But there appears to be no substantial movement of the peak (point of maximum pore pressure). The change in K_0 has two countervailing effects on the generation of pore pressure. First, any increase in K_0 increases the magnitude of stress relief, which tends to create higher negative pore pressures. This effect is counterbalanced by the fact that higher K_0 leads to a greater degree of arching, which in turn tends to produce higher positive pore pressures. Increased values of K_0 also cause increased shear stress levels that tend to increase the pore pressure. In this case, the effects that tend to decrease the pore pressure with increasing K_0 appear to dominate.

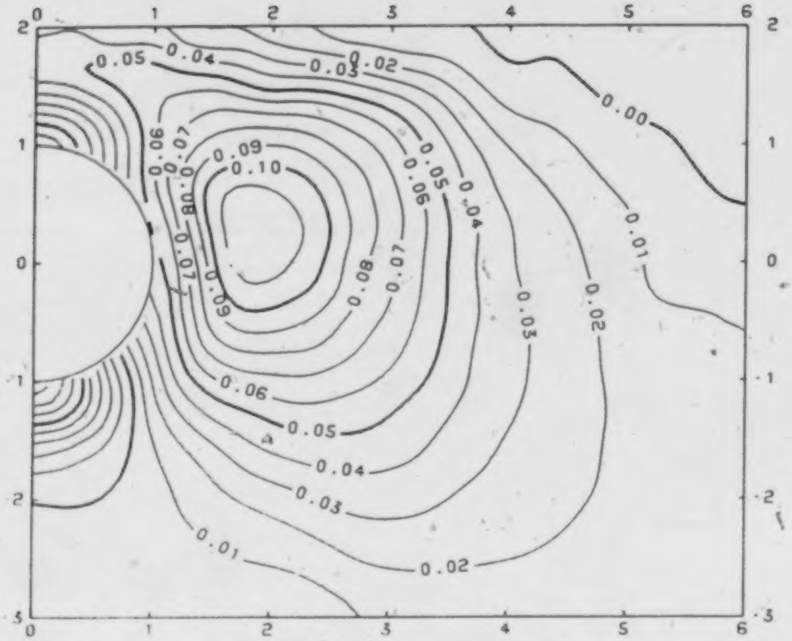

Figure 5.16 Normalized Pore Pressure for K_0=0.5

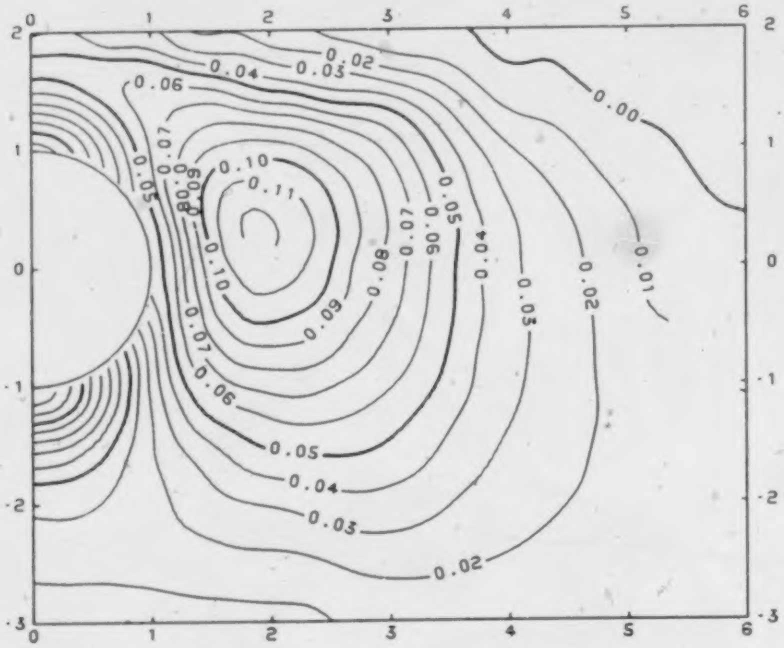

Figure 5.17 Normalized Pore Pressure for K_0=0.8

5.5.1.5 H/D RATIO AND PORE PRESSURE

In this section, the variation of initial pore pressure with H/D ratio is examined, where H is the depth of cover and D is the tunnel diameter. Furthermore, the usefulness of the proposed coordinate non-dimensionalization when H/D varied is investigated. The H/D ratio was kept within the limits of shallow tunnel definition (section 5.5), namely, 3>H/D>1. Also, the D values were kept within their practical range (Table 5.1). The initial pore pressure values were computed for H/D values, 1.25, 1.50, 1.60, 1.70, 1.90, 2.00, 2.25 and 2.75, keeping all the other parameters at their average values (section 5.5.1). The normalized pore pressure distributions in (ξ,η) plane were compared with the pore pressures corresponding to the average parameters. It must be noted that in this case, the deviations were compared at the grid points that were used to draw the pore pressure contours, as opposed to the nodal points of the finite element mesh that were used in the other cases. The percentage deviations were computed as explained in section 5.5. The extreme deviations occurred for the extreme values of H/D. The 95% probable maximum deviation (defined in section 5.5) for H/D=1.25 was 7%, whereas the maximum deviation for H/D=2.75 was 8%. Figures 5.18 and 5.19 show the normalized pore pressure diagrams for H/D=1.25 and 2.75, respectively.

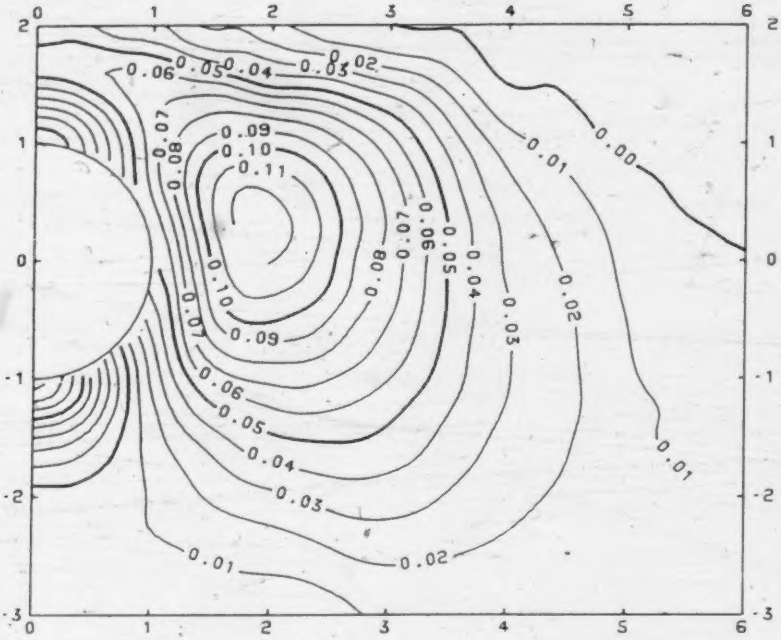

Figure 5.18 Normalized Pore Pressure for H/D=1.25

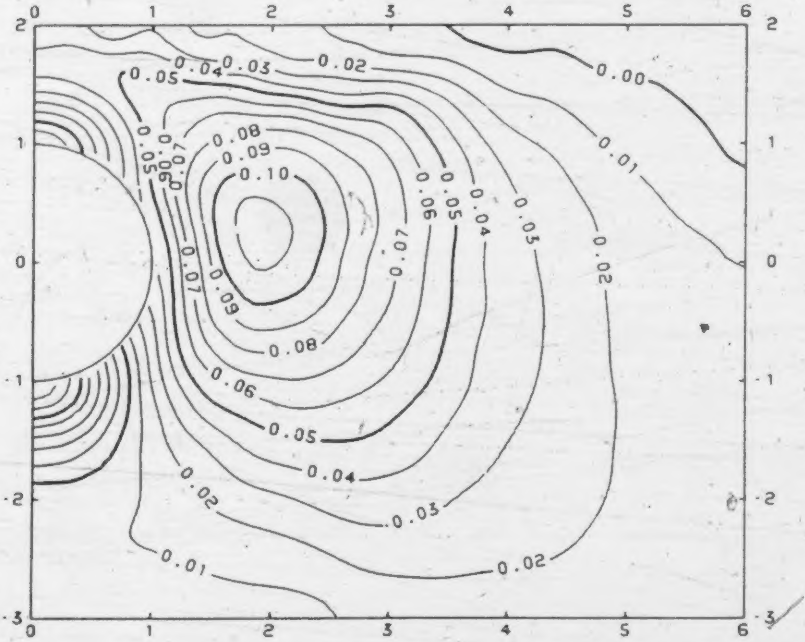

Figure 5.19 Normalized Pore Pressure for H/D=2.75

In general, with increasing H/D, the normalized pore pressures tend to increase slightly but there appears to be no substantial movement of the peak (point of maximum pore pressure).

5.5.1.6 TUNNEL DIAMETER (D), γ AND PORE PRESSURE

The influence of soil unit weight, γ, and the tunnel diameter, D, on the initial pore pressure generation are discussed in this section. It is expected that $u/\gamma H_c$ normalization will take into account these two effects. In attempting to investigate these effects numerically, as before, keeping all the other parameters at their average values (section 5.5.1), the γ value was halved to 10 kN/m^3. The normalized pore pressures were compared with the pore pressures corresponding to average parameters. As expected, no difference was found. The pore pressure diagram corresponding to $\gamma=10$ kN/m^3 is shown in Figure 5.20.

The tunnel diameter was changed, keeping all the other parameters at average values. The practical range of tunnel diameters fall between 3 m and 9 m (Table 5.1). The normalized pore pressure values obtained for D=3 m and 9 m were compared with those corresponding to the average parameters. Again, no deviation was found. Figures 5.21 and 5.22 show the normalized pore pressure diagrams corresponding to tunnel diameters 9 m and 3 m, respectively.

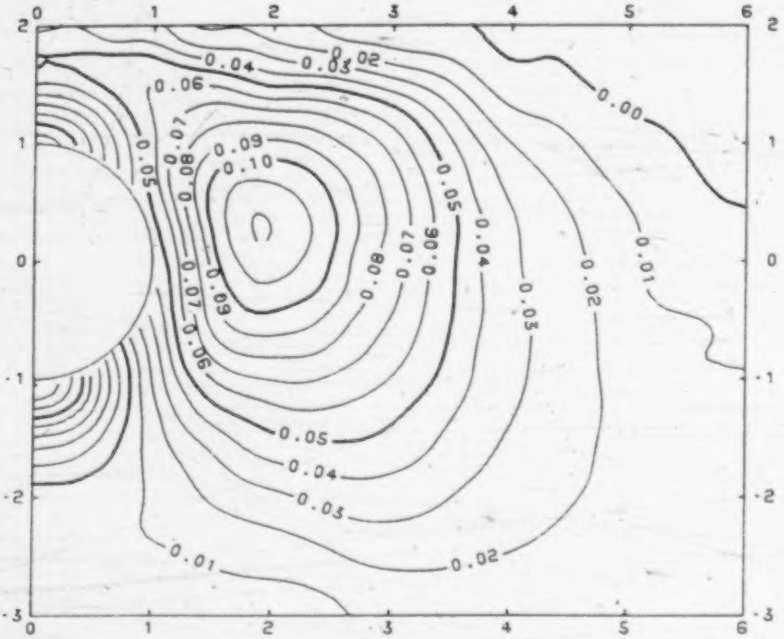

Figure 5.20 Normalized Pore Pressure for $\gamma=10$ kN/m^3

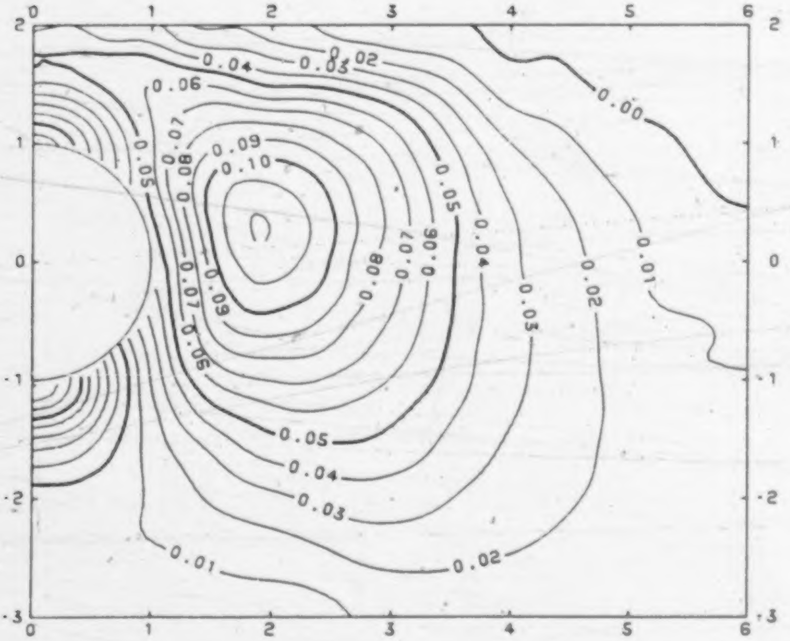

Figure 5.21 Normalized Pore Pressure for D=9m

5.5.1.7 PORE PRESSURE DISSIPATION; TIME FACTOR T AND H,D

The influence of various factors on initial pore pressure generation was investigated in the previous sections. In this section the influence of different parameters on pore pressure dissipation behaviour with time is investigated. As discussed in section 5.3.4, the time factor can be expressed in the form, $T = \frac{c_v t}{H^2}\left[\frac{D}{H}\right]^n$. In order to verify the validity of the time factor for the dissipation of the pore pressure, the following analysis was undertaken. For different D, H/D and n values, the pore pressure distributions for given T values were obtained and compared with the distribution corresponding to the average parameters (section 5.5.1). After a large number of trials, it was found that n=0 yields the best fit. The basic procedure employed is as follows.

In all cases, keeping all the other parameters the same, the value of the tunnel diameter D was changed in the practical range from 3 to 9 m. The pore pressure distribution at certain time factors was computed for each of the different diameters in both sealed and unsealed tunnels. Then, these pore pressure distributions were compared in (ξ,η) plane with the pore pressures corresponding to average parameters. As expected, at every time factor, the pore pressure distributions were found to be the same for all tunnel diameters. This was true for both sealed and unsealed tunnels. For T=0.001 and T=0.01, Figures 5.23 and 5.24 show the normalized pore pressure distribution around an unsealed tunnel of diameter 3m, whereas Figures 5.38 and 5.39 show the normalized pore pressure distribution of a tunnel having a diameter of 6m.

Similarly, the influence of H/D on the pore pressure dissipation was investigated. The pore pressure values at given time factors were computed for H/D values, 1.25, 1.50, 1.60, 1.70, 2.00, 2.25, 2.50 and 2.75, for both sealed and unsealed tunnels. In a sealed tunnel no flow was allowed at the periphery of the tunnel whereas in an unsealed tunnel the change in pore pressure was assumed to be zero. The normalized pore pressures on (ξ,η) plane for different H/D ratios were compared for the same time factor. The percentage deviations were estimated as described in section 5.5. The 95% probable maximum deviation (defined in section 5.5) remained within 10% for both sealed and unsealed tunnels. Figures 5.25 to 5.36 show the normalized pore pressure diagrams for the extreme cases, namely, H/D = 1.25 and 2.75 at T=0.001, 0.01 and 0.1 in both sealed and unsealed tunnels.

5.5.1.8 PORE PRESSURE DISSIPATION; TIME FACTOR T AND c_v

The coefficient of consolidation affects the rate of pore pressure dissipation. It is necessary to investigate whether this influence was properly taken into account in the previously defined (section 3.1.4)

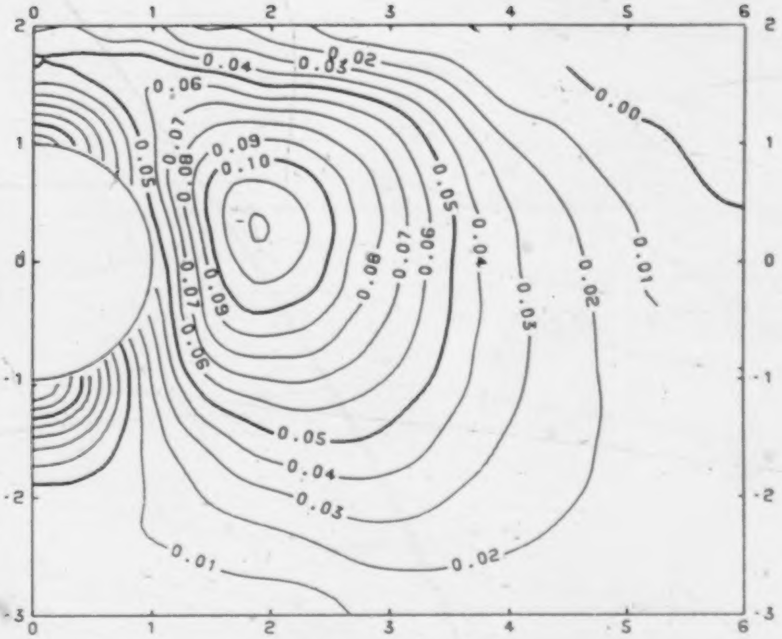

Figure 5.22 Normalized Pore Pressure for D=3m

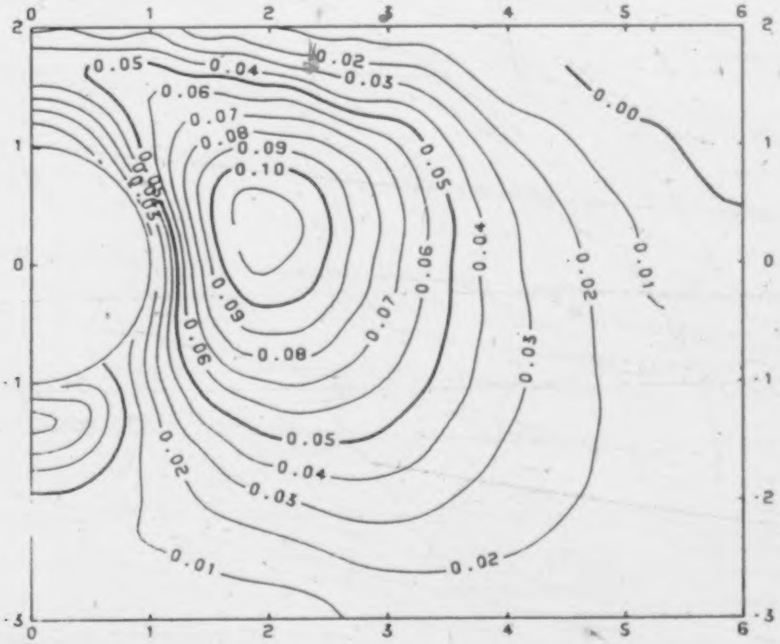

Figure 5.23 Normalized Pore Pressure for D=3m T=0.001;

Unsealed Tunnel

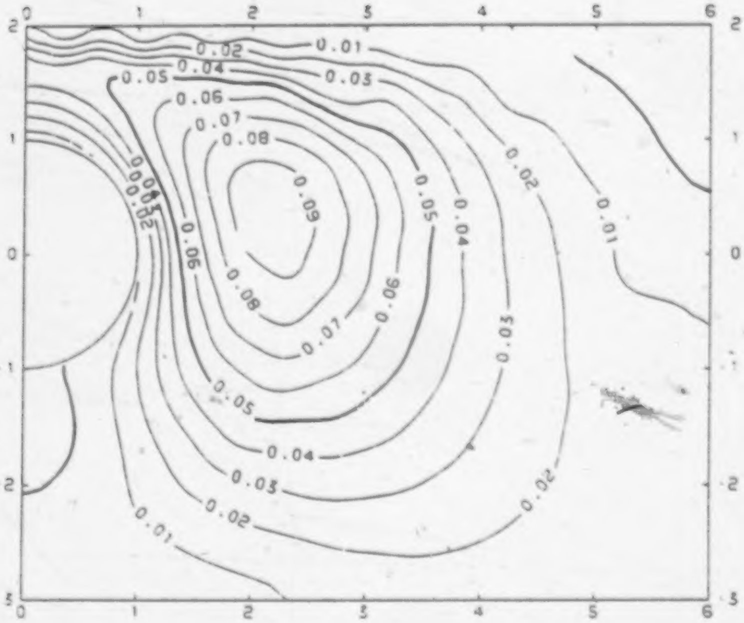

Figure 5.24 Normalized Pore Pressure for D=3m, T=0.01; Sealed Tunnel

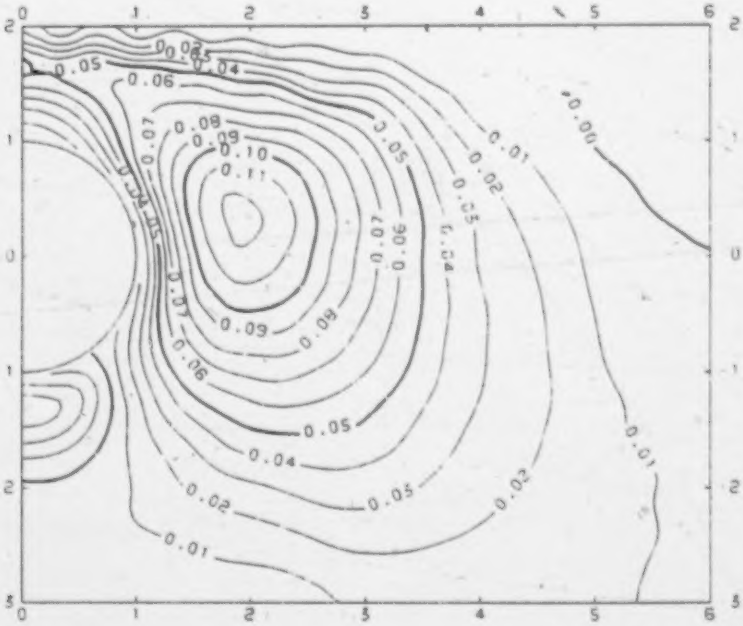

Figure 5.25 Normalized Pore Pressure for H/D=1.25, T=0.001; Unsealed Tunnel

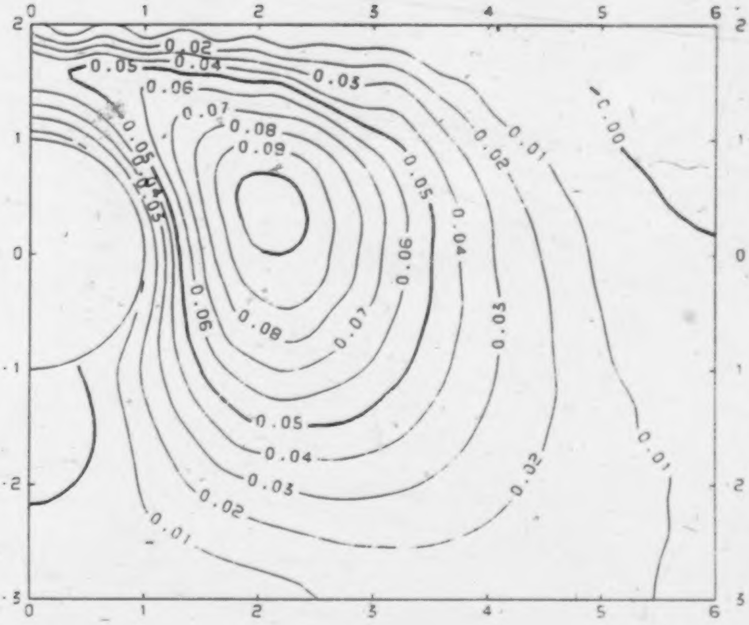

Figure 5.26 Normalized Pore Pressure for H/D=1.25, T=0.01; Unsealed Tunnel

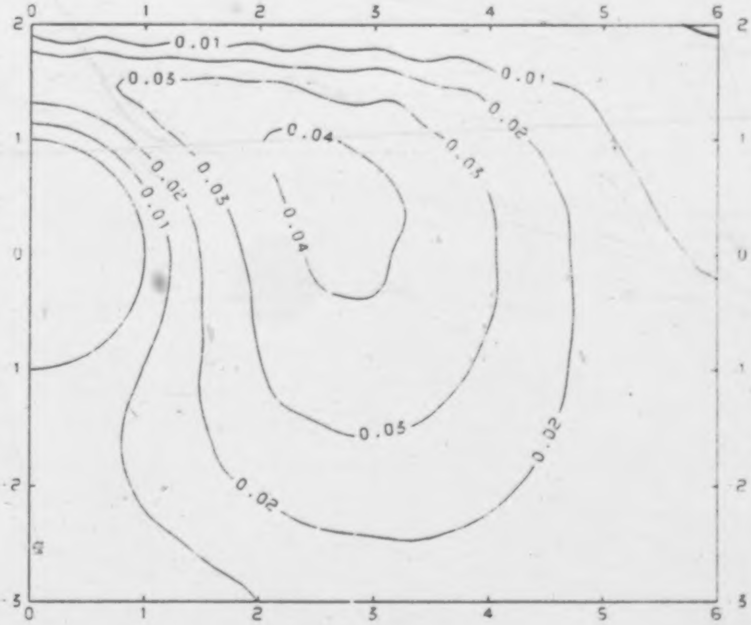

Figure 5.27 Normalized Pore Pressure for H/D=1.25, T=0.1; Unsealed Tunnel

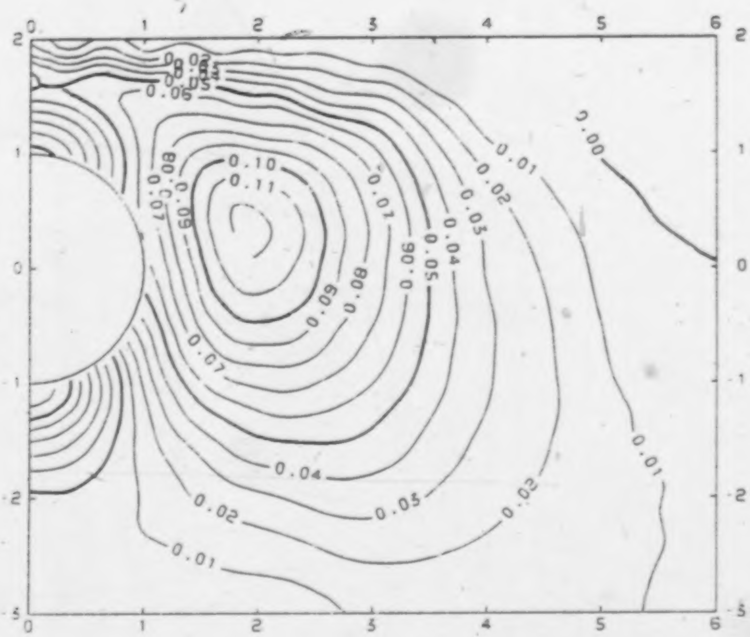

Figure 5.28 Normalized Pore Pressure for H/D=1.25, T=0.001; Sealed Tunnel

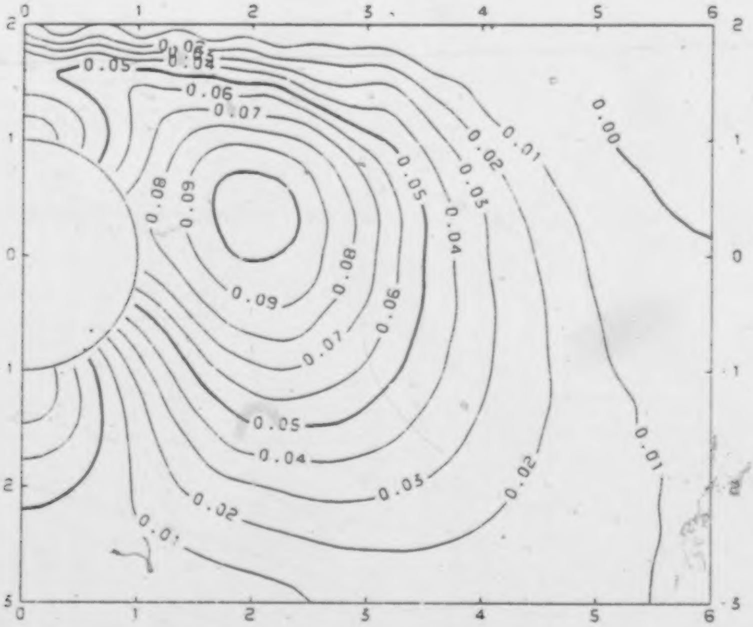

Figure 5.29 Normalized Pore Pressure for H/D=1.25, T=0.01; Sealed Tunnel

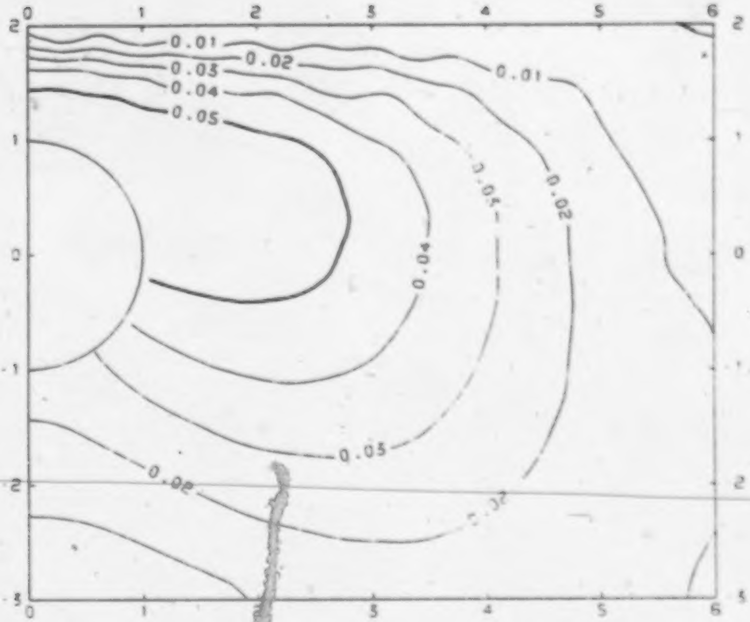

Figure 5.30 Normalized Pore Pressure for H/D=1.25, T=0.1; Sealed Tunnel

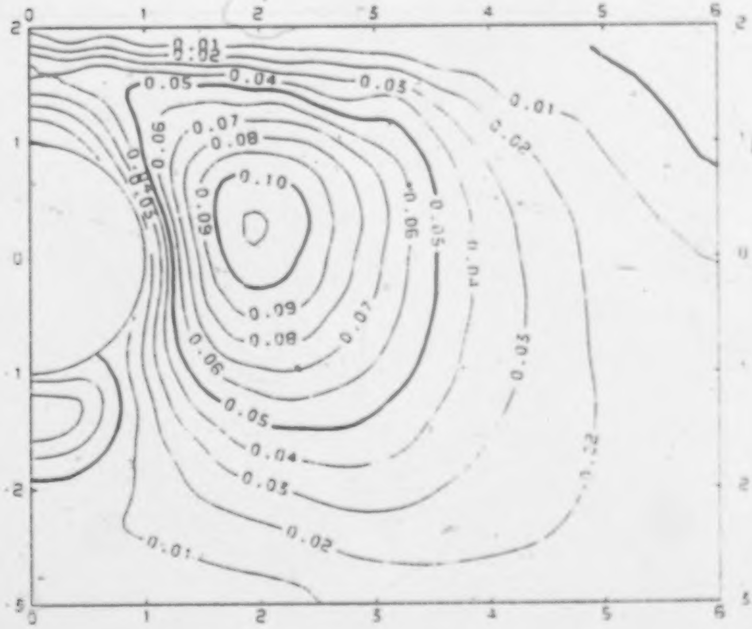

Figure 5.31 Normalized Pore Pressure for H/D=2.75, T=0.001; Unsealed Tunnel

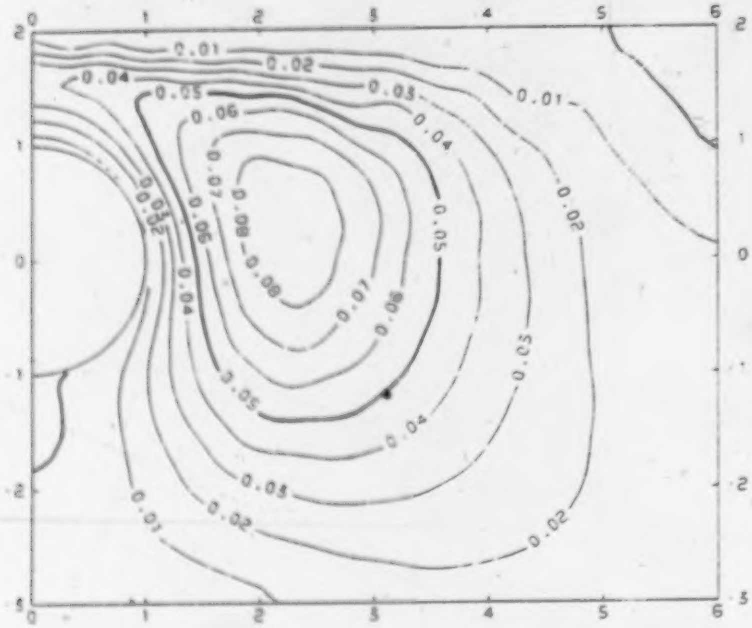

Figure 5.32 Normalized Pore Pressure for H/D=2.75, T=0.01; Unsealed Tunnel

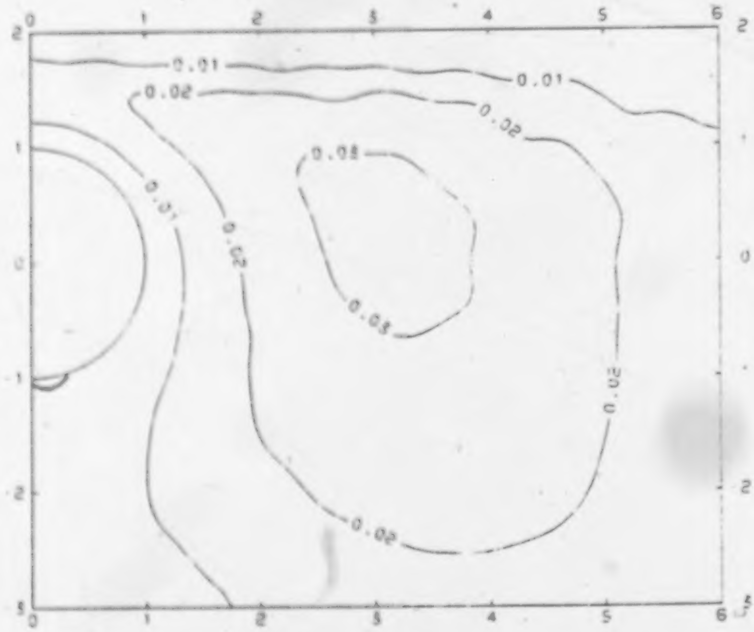

Figure 5.33 Normalized Pore Pressure for H/D=2.75, T=0.1; Unsealed Tunnel

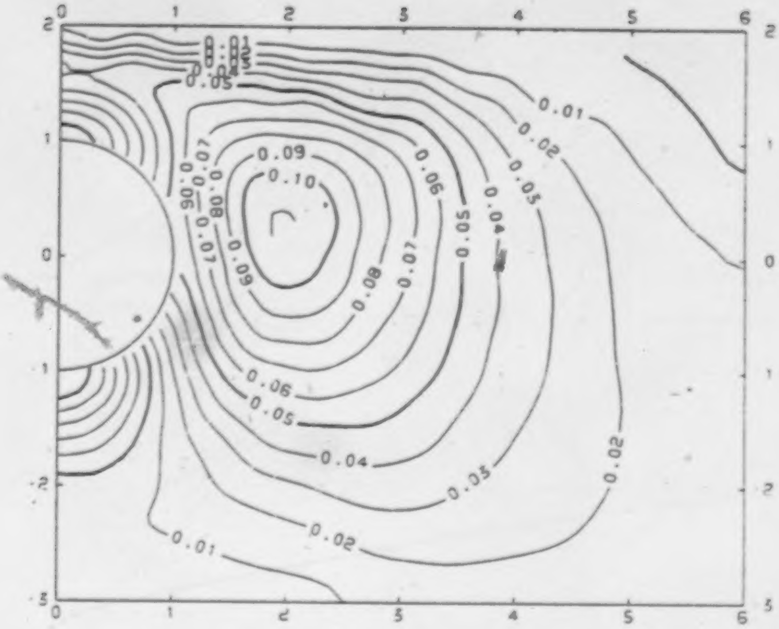

Figure 5.34 Normalized Pore Pressure for H/D=2.75, T=0.001; Sealed Tunnel

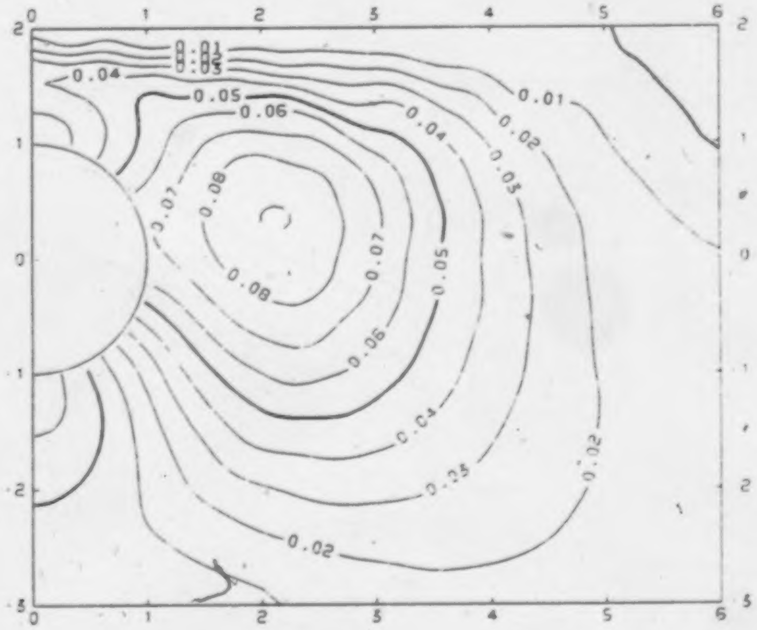

Figure 5.35 Normalized Pore Pressure for H/D=2.75, T=0.01; Sealed Tunnel

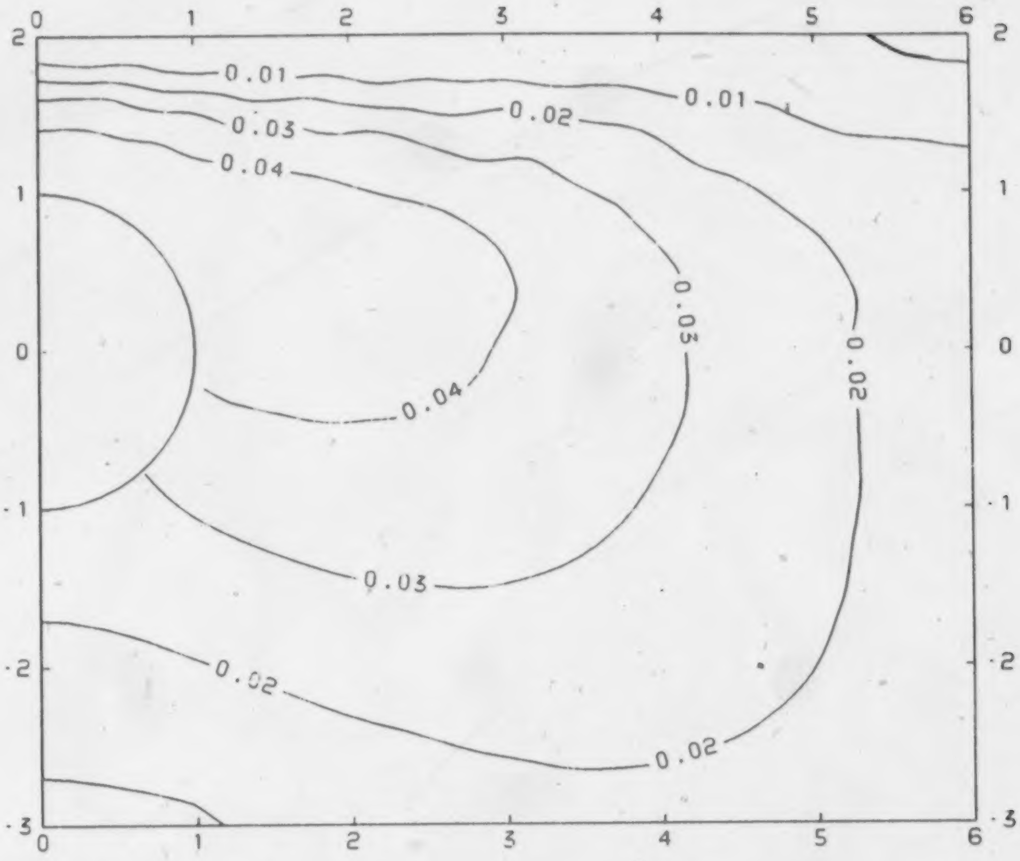

Figure 5.36 Normalized Pore Pressure for H/D=2.75, T=0.1; Sealed Tunnel

time factor T. The pore pressure dissipation analysis was performed for various c_v values within the range given in Table 5.1, keeping all the other parameters at their averages (section 5.5.1). The pore pressure distributions obtained for given T values were compared. The comparisons show that the distributions are the same. This behaviour can also be seen when the governing equations are examined. The results obtained in this and the previous sections justify the time factor postulated to study the dissipation behaviour of pore pressures around tunnels.

The time factor depends on the governing equation (Equation 3.74) and the boundary conditions. If T is the time factor for a given set of boundary conditions, the pore water pressure at any time can be expressed in the form

$$u = u(x,y,T) \qquad [5.15]$$

For the case of a tunnel with both sealed and unsealed conditions, the time factor was found to be $c_v t/H^2$.

5.5.2 SUPPORTED TUNNELS IN NORMALLY CONSOLIDATED CLAY

In the following sections, the influence of the tunnel support system on pore pressure generation will be examined. As discussed in section 5.5, to make the results of a parametric study more useful, less confusing and less cumbersome, it is essential that the practical ranges of these parameters be found and used whenever possible.

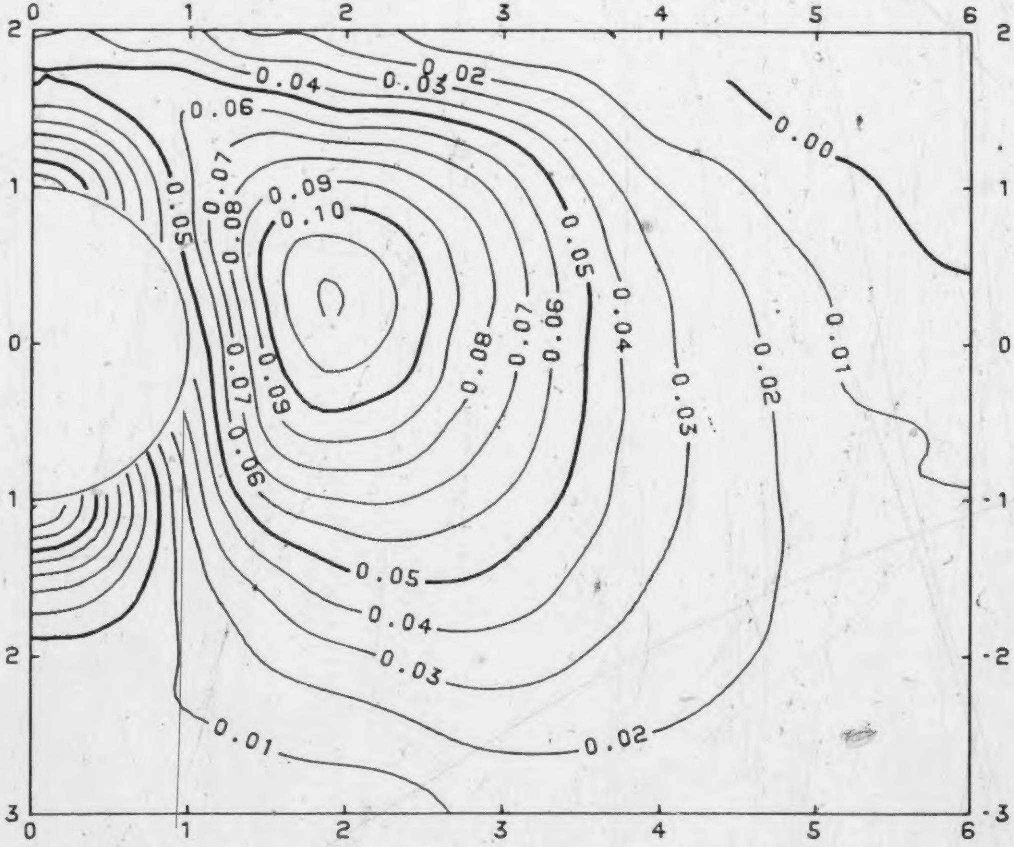

Figure 5.37 Unsealed Tunnel in NCC, $\hat{u}$ in (ξ,η), ESR=0, T=0

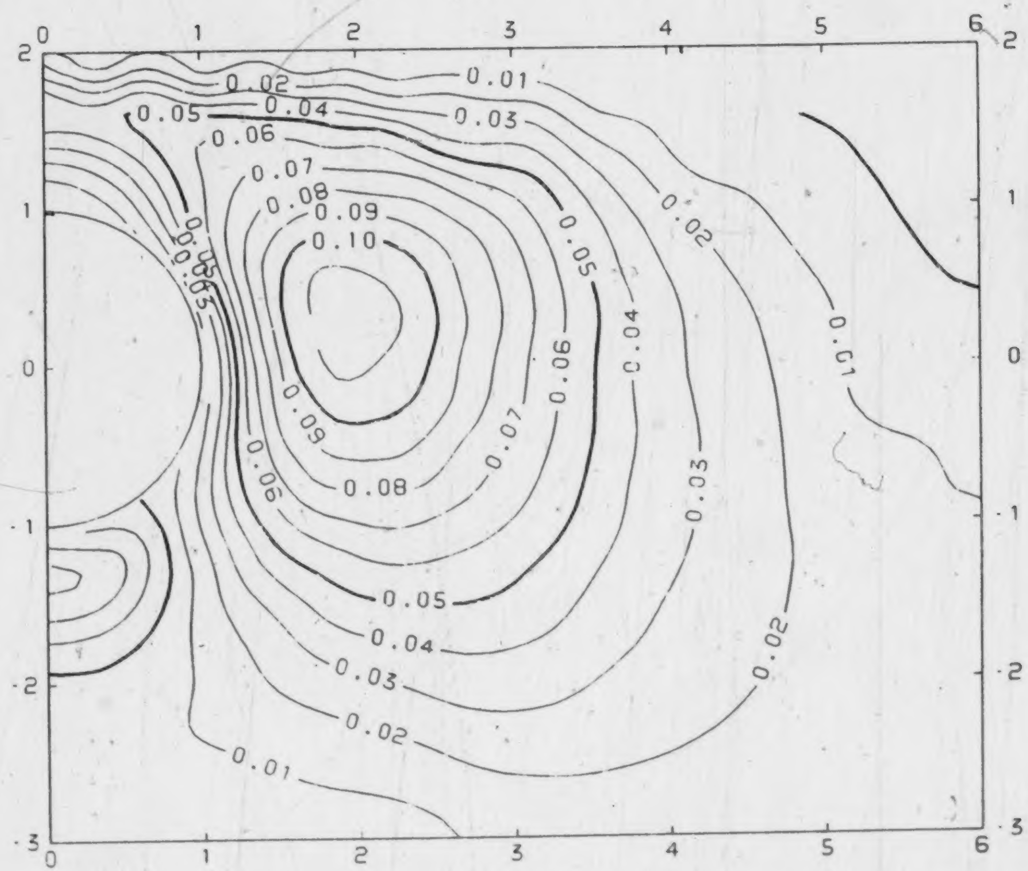

Figure 5.38 Unsealed Tunnel in NCC, $\hat{u}$ in (ξ,η), ESR=0, T=0.001

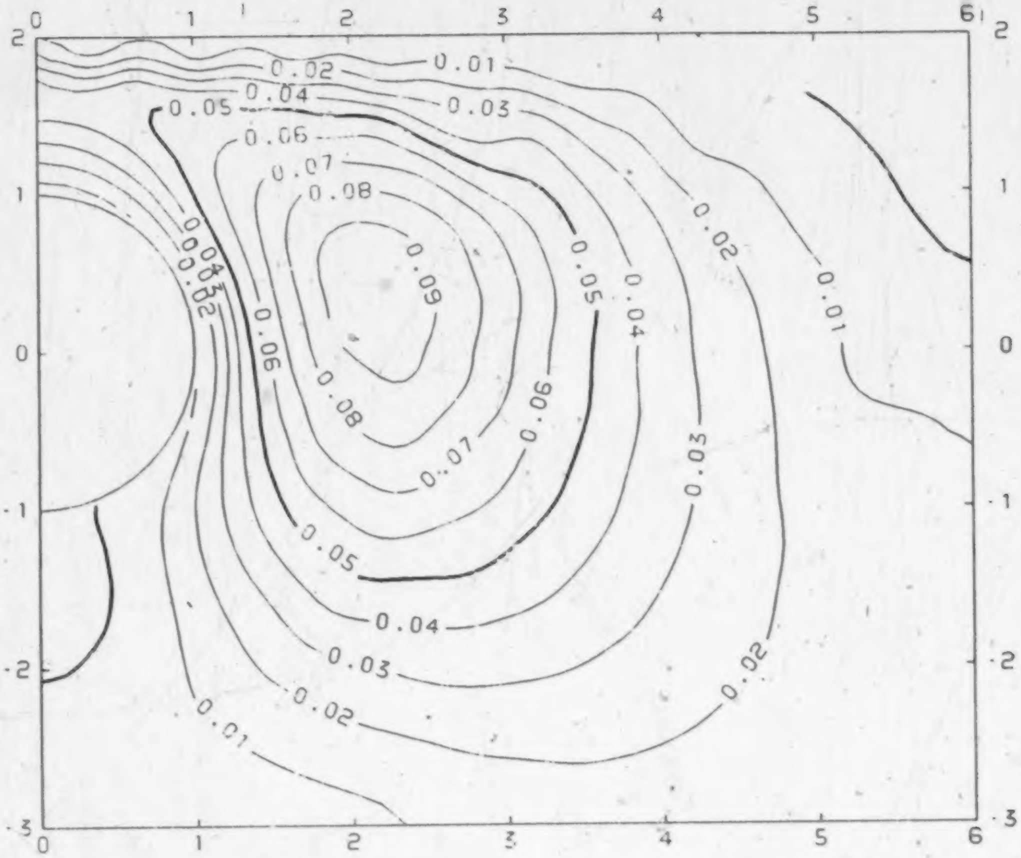

Figure 5.39 Unsealed Tunnel in NCC, û in (ξ,η), ESR=0, T=0.01

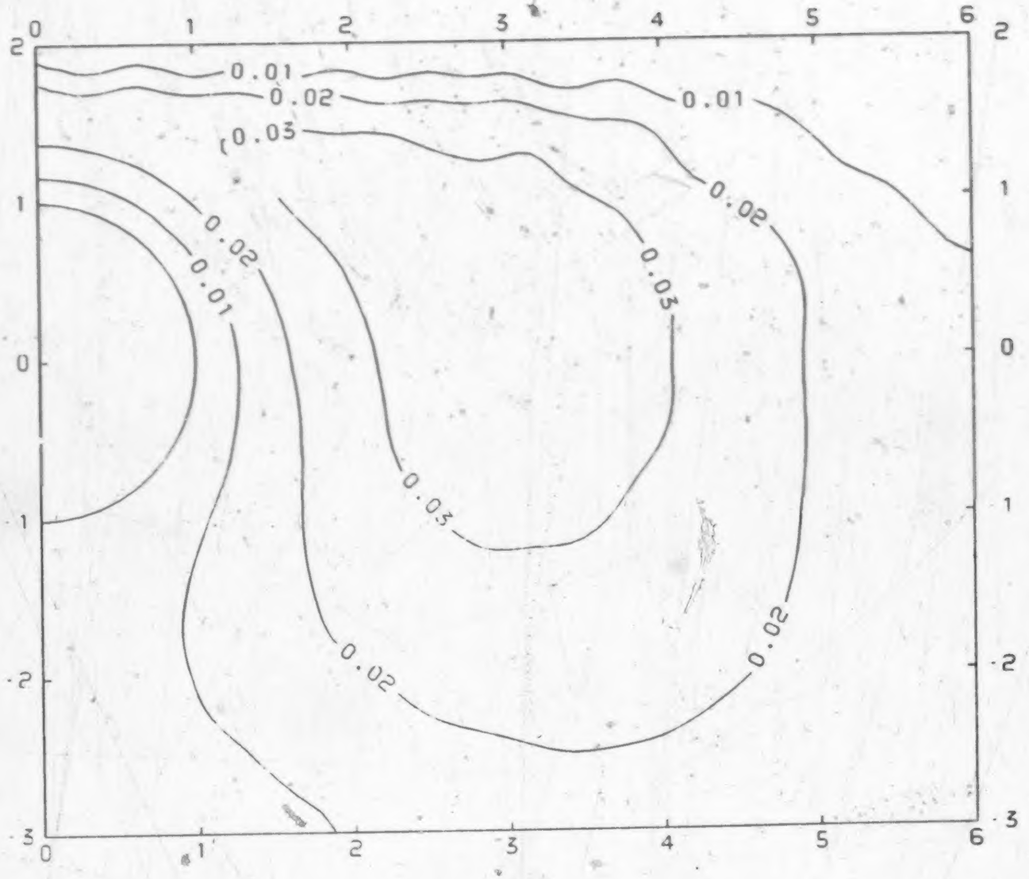

Figure 5.40 Unsealed Tunnel in NCC, $\hat{u}$ in (ξ,η), ESR=0, T=0.1

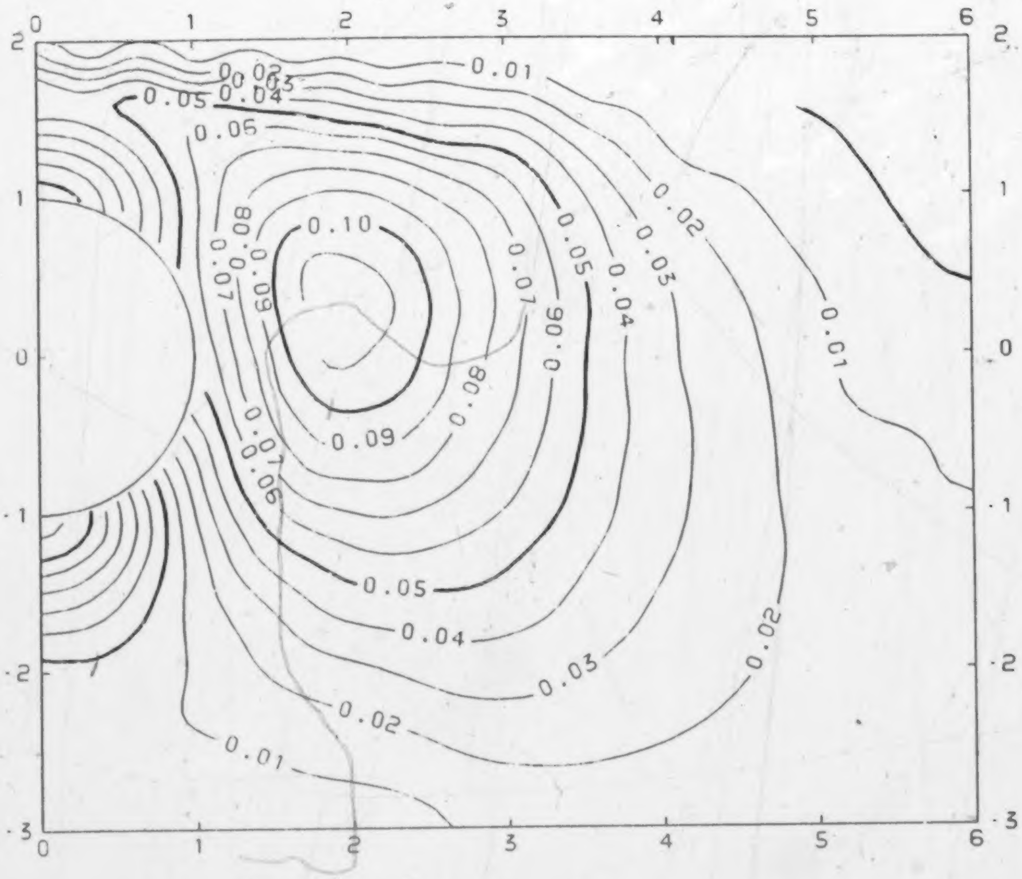

Figure 5.41 Sealed Tunnel in NCC, $\hat{u}$ in (ξ,η), ESR=0, T=0.001

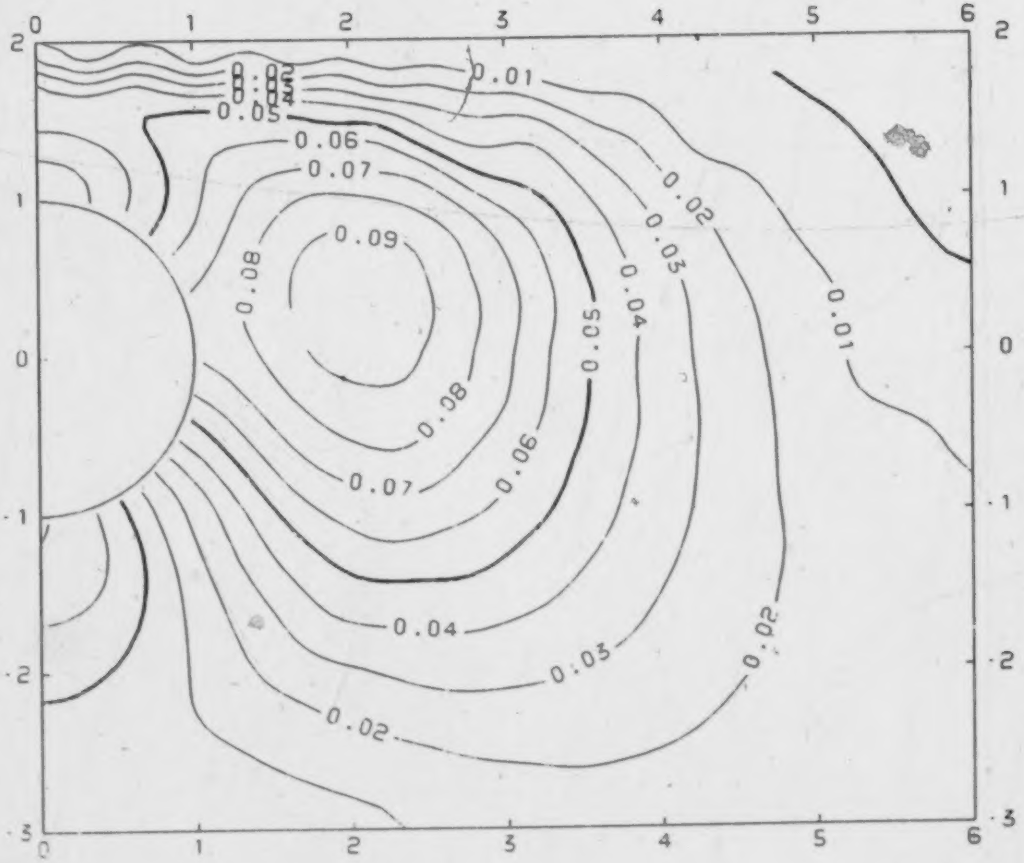

Figure 5.42 Sealed Tunnel in NCC, $\hat{u}$ in (ξ,η), ESR=0, T=0.01

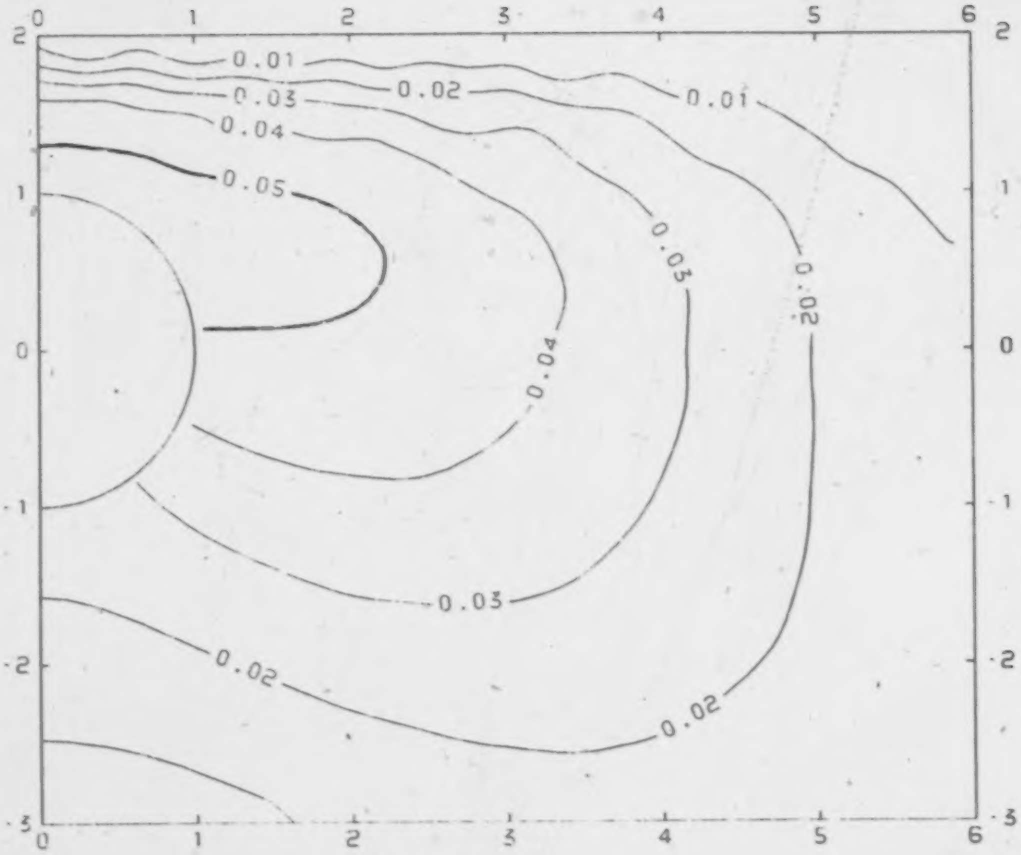

Figure 5.43 Sealed Tunnel in NCC, û in (ξ,η), ESR=0, T=0.1

Einstein et al. (1979) published these ranges for supported tunnels. In soft ground tunnelling, E_s/E_l ranges from 10^{-4} to 10^{-3} for steel or cast iron supports, whereas for concrete supports it ranges from 10^{-3} to 10^{-2}, where E_l is the liner modulus and E_s is that of soil. The small to medium diameter (3-6 m) tunnels with prefabricated concrete or cast iron elements and cast in place concrete liners have a t/R value of 0.075, which belongs to the upper range (t is the liner thickness and R the tunnel radius) . The cast in place concrete tunnels with medium to large diameter (6-9 m) have a t/R value of approximately 0.05, and for the whole range of diameters (3-9 m) with fabricated steel liner plates or steel sets, the range of t/R is 0.025 to 0.01.

To account for the influence of the support system on pore pressure around supported tunnels, a quantity called Effective Stiffness Ratio (ESR) was introduced in section 5.3.5. Using the practical ranges it was found that for fabricated steel liner plates or steel sets, for the whole range of tunnel diameters (3-9 m), ESR varies between 0.004 and 1.5, whereas for cast in place concrete tunnels with medium to large diameter (6-9 m), ESR has a range of 0.02 to 2.3. ESR varies from 0.1 to 3.9 for the prefabricated concrete or cast iron elements in cast in place concrete tunnels with small diameters (3-6 m). Therefore, ESR has an approximate practical range of 10^{-3} to 10^{0}. On this basis, it was decided, to examine the pore pressure behaviour of shallow tunnels with ESR values, 10^{-3}, 10^{-2}, 10^{-1} and 10^{0}. It must be noted, however, that the ESR range computed using the initial modulus as the soil modulus has to be smaller than this range.

The same average tunnel geometries and soil properties (section 5.5.1) used in the preceding unsupported tunnel analysis were employed to investigate the supported tunnels. The cross-sectional area and the second moment of area of the liner were selected in conformity with the average value (0.05) of the practical range of t/R. The initial pore water pressure distribution due to the excavation of the tunnel was computed as explained previously. The non-dimensionalized pore pressure diagrams shown in Figures 5.54 to 5.70 show the influence of ESR on initial pore pressure.

In order to verify the validity of the Effective Stiffness Ratio (ESR) concept, the parameters in ESR were varied in a logical manner in different combinations in their practical ranges.

5.5.2.1 SOIL MODULUS, LINER MODULUS AND PORE PRESSURE

As discussed in section 5.5.1, the soil modulus can be characterized by E_i/σ_{1c}. Therefore, in this analysis, E_i was changed fourfold to correspond with the practical range of E_i/σ_{1c}, 200 to 800. At the same time, E_l, the liner modulus was changed accordingly to maintain the ESR value. The resulting pore pressure distributions were compared with the pore pressure distribution corresponding to the average parameters (section 5.5.1). Not surprisingly, for the same ESR (for different values in its practical range, 10^{-3} and 10^{0}) the initial pore pressure distribution was the same. For ESR=10^{-3}, Figures 5.44 and 5.45 show the pore pressure diagrams corresponding to E_l/σ_{1c}=200 and 800, respectively.

5.5.2.2 A_l, I_l, SOIL MODULUS AND PORE PRESSURE

Since the soil modulus can be characterized by E_i/σ_{1c} (section 5.5.1), E_i was varied within the practical range of E_i/σ_{1c} (200 to 800), while these changes were compensated by changing A_l and I_l to maintain the same ESR value (A_l and I_l are liner cross-sectional area and the second moment area of the cross-section respectively). The resulting pore pressure distributions were compared with the pore pressure distribution corresponding to the average parameters (section 5.5.1). As expected, in its full practical range, for a given ESR value the pore pressure distribution was the same. For ESR=10^{-2}, Figures 5.46 and 5.47 show the pore pressure diagrams corresponding to E_i/σ_{1c}=200 and 800, respectively.

5.5.2.3 K_0 AND PORE PRESSURE

In this numerical simulation, the variation of the initial pore pressure with changing K_0 was investigated. The K_0 value was changed (in steps of 0.05) within a practical range between 0.5 and 0.8, keeping all other parameters at their average values. At the same time, the liner modulus was changed accordingly to keep the

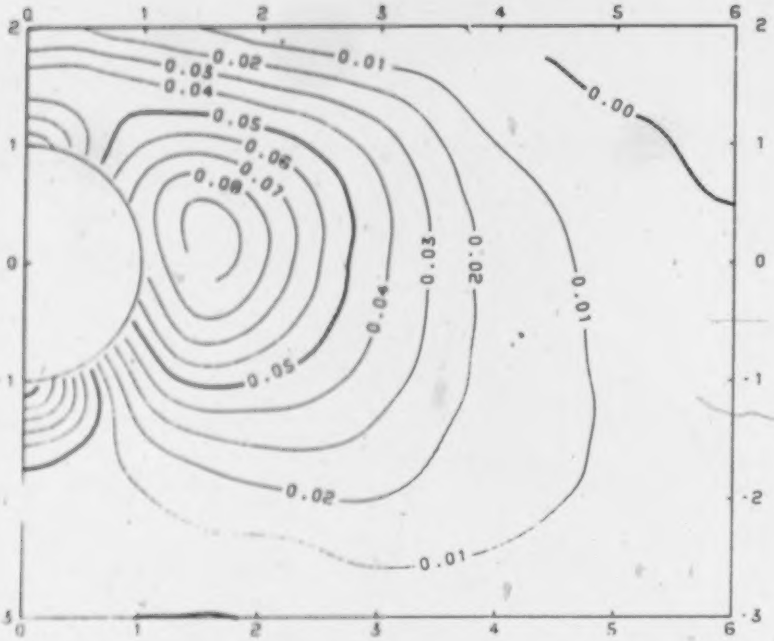

Figure 5.44 Normalized Pore Pressure, ESR=10^{-3}, E_i/σ_{1c}=200; E_1 Decreased

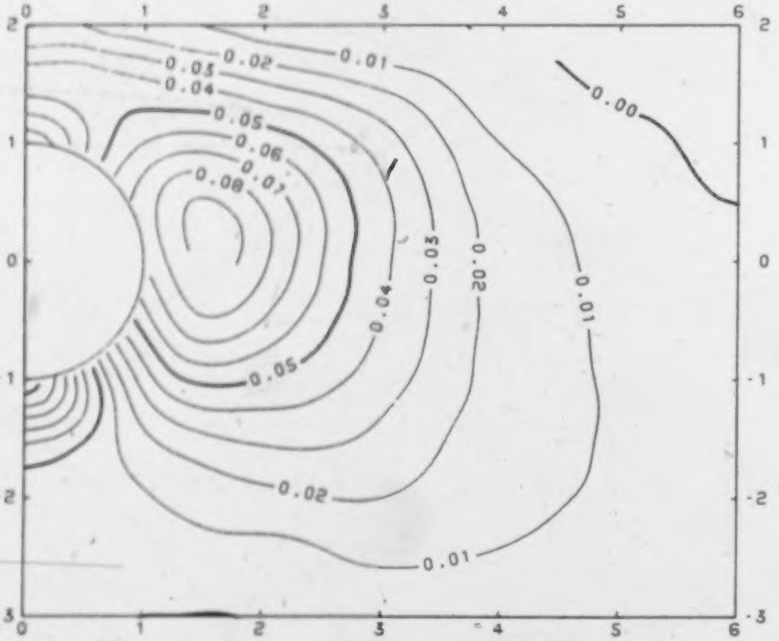

Figure 5.45 Normalized Pore Pressure, ESR=10^{-3}, E_i/σ_{1c}=800; E_1 Increased

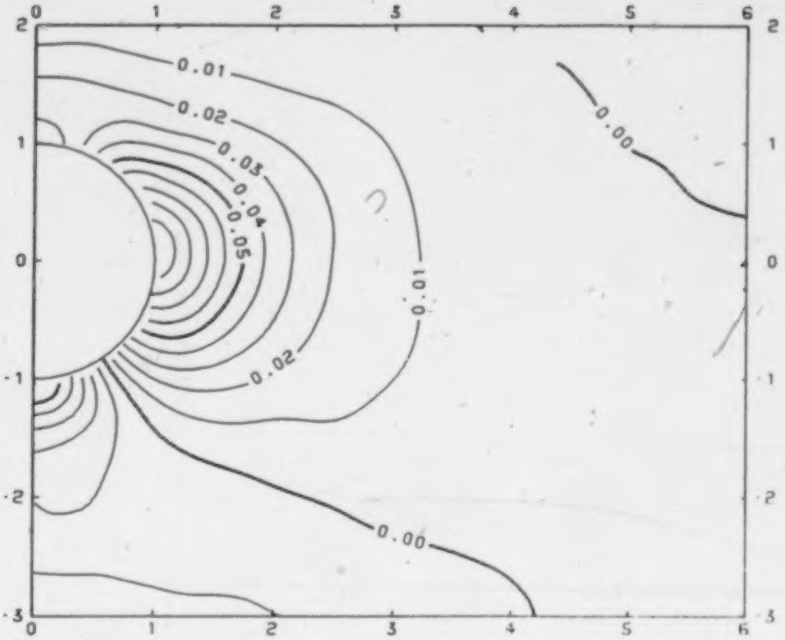

Figure 5.46 Normalized Pore Pressure, ESR=10^{-2}, E_i/σ_{1c}=200; I_1, A_1 Decreased

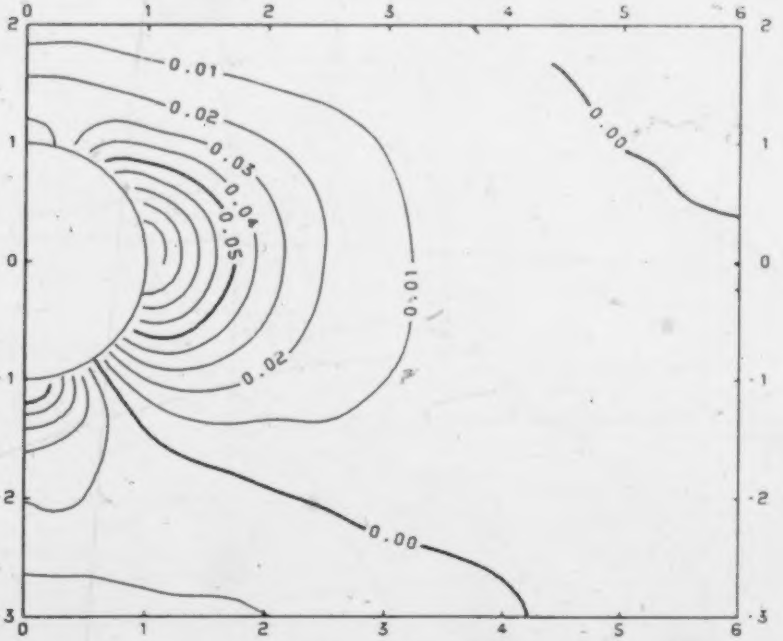

Figure 5.47 Normalized Pore Pressure, ESR=10^{-2}, E_i/σ_{1c}=800; I_1, A_1 Increased

same ESR value. As before, the resulting normalized pore pressure distributions were compared with the distribution corresponding to the average parameters (section 5.5.1), and the deviations were computed. These computations were made for the full practical range of ESR, 10^{-3} to 10^{0}. Not surprisingly, the maximum deviations correspond to extreme K_0 values. In the range of ESR noted, the 95% probable maximum deviation (defined in section 5.5) computed was within 5%. Figures 5.48 and 5.49 show the normalized pore pressure distributions for ESR=0.1 and corresponding to K_0=0.5 and 0.8, respectively.

5.5.2.4 TUNNEL DIAMETER AND PORE PRESSURE

The influence of the tunnel diameter on ESR and hence on the initial pore pressure generation is examined in this section. The tunnel diameter was changed within the practical range of 3 to 9 m, maintaining the other parameters at average values (section 5.5.1) except that the liner modulus E_l was varied accordingly to maintain the same ESR value. As before, the resulting pore pressure distributions were compared with the distribution corresponding to the average parameters. Not surprisingly, in the full practical range of ESR, there were no deviations in the pore pressures. For ESR=10^{-2}, Figures 5.50 and 5.51 show the normalized pore pressure diagrams corresponding to D=3m and 9m, respectively.

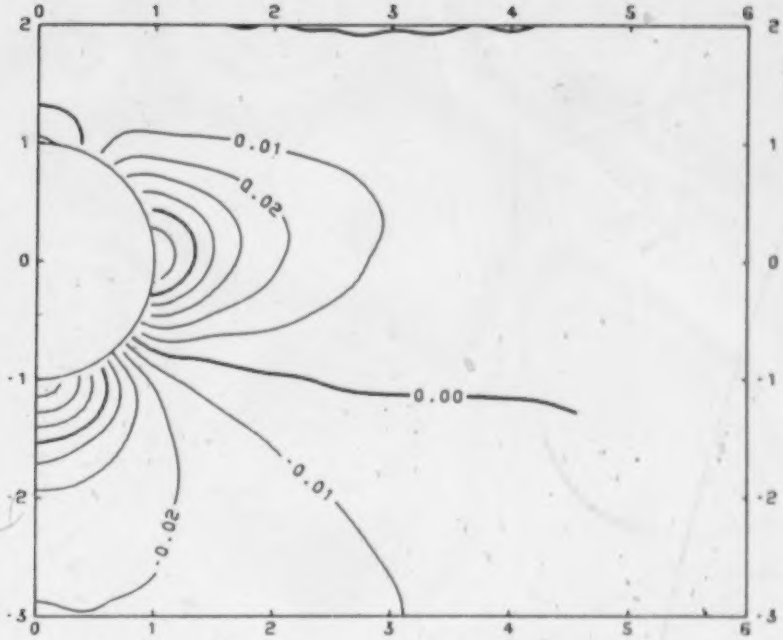

Figure 5.48 Normalized Pore Pressure, ESR=10^{-1}, K_0=0.5

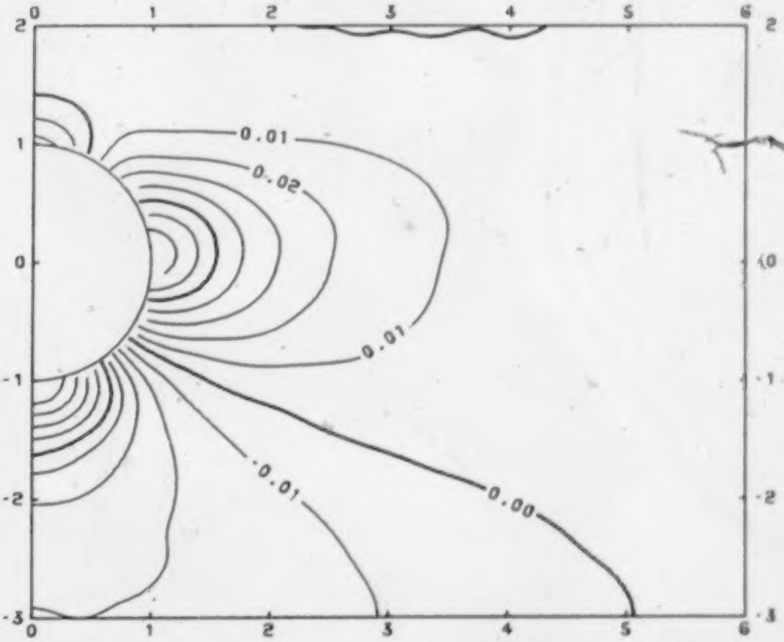

Figure 5.49 Normalized Pore Pressure, ESR=10^{-1}, K_0=0.8

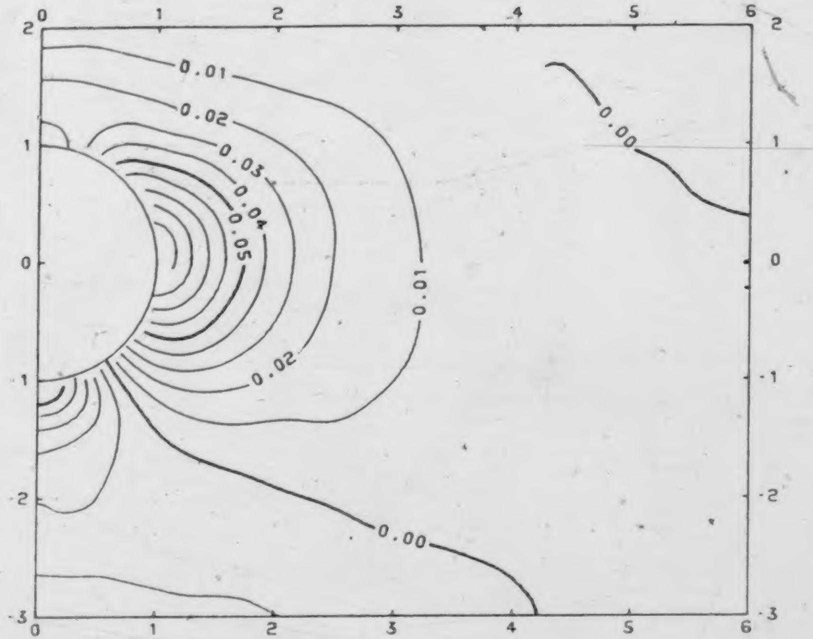

Figure 5.50 Normalized Pore Pressure, ESR=10^{-2}, D=3m

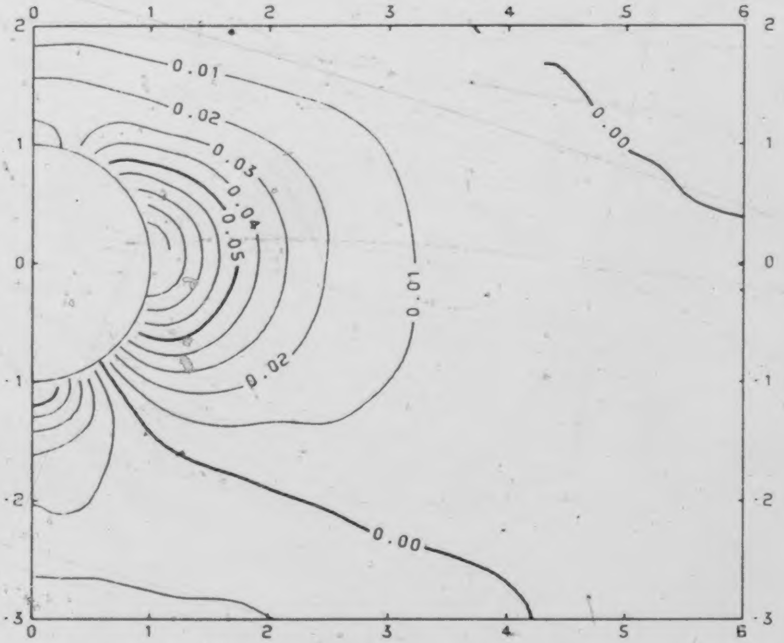

Figure 5.51 Normalized Pore Pressure, ESR=10^{-2}, D=9m

5.5.2.5 t/R AND PORE PRESSURE

From the expression for ESR, it is clear that t/R has a direct influence on ESR and hence on the initial pore pressure (R is the tunnel radius and t is the liner thickness). To investigate the influence of t/R ratio on the initial pore pressure generation, t/R was varied within the practical range of 0.03 to 0.07, maintaining all other parameters at average values (section 5.5.1). While t/R was being varied (in steps of 0.01), the liner modulus E_1 was changed accordingly to maintain the same ESR value. The initial pore pressure distributions obtained were compared with the distribution corresponding to the average parameters. This was done for the full practical range of ESR (10^{-3} to 10^{0}), and the percentage deviations were computed as before. As expected, the extreme deviations were obtained for the extreme values of t/R. The 95% probable maximum deviation (defined in section 5.5) was less than 5% for the practical range of ESR values. Figures 5.52 and 5.53 show the pore pressure diagrams for ESR=0.1 that correspond to t/R 0.03 and 0.07 respectively.

5.5.2.6 FURTHER COMMENTS ON SUPPORTED TUNNELS

The above analyses were performed on supported tunnels having liners of rectangular cross-sections. However, Einstein et al. (1979) found that the liner shape has little influence on the stress and displacement behaviour around a tunnel. As explained in

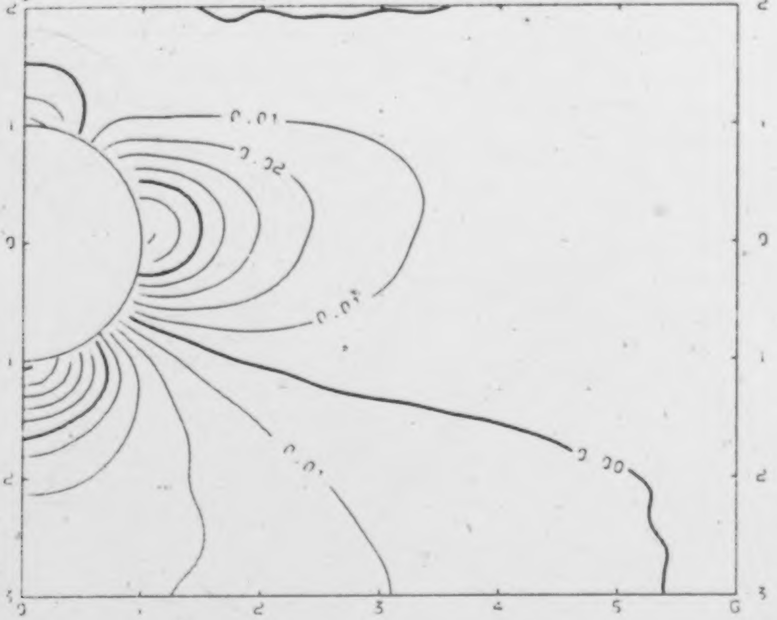

Figure 5.52 Normalized Pore Pressure, ESR=10^{-1}, t/R=0.03

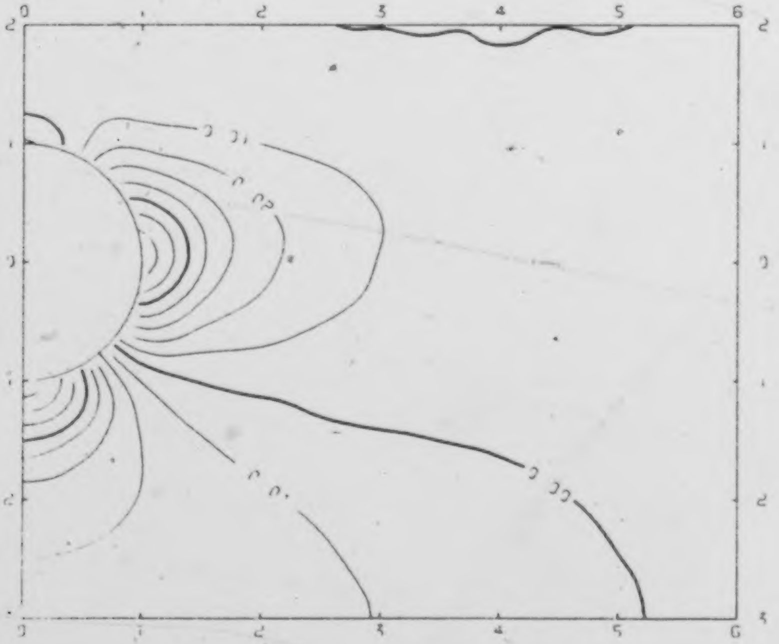

Figure 5.53 Normalized Pore Pressure, ESR=10^{-1}, t/R=0.07

the previous sections, the pore pressure generation is directly related to stress change around the tunnel. Therefore, it is reasonable to assume that the influence of the shape of the liner on pore pressure generation is also insignificant. The normalized pore pressure diagrams for tunnels having ESR values, 0, 10^{-3}, 10^{-2} and 10^{-1} are shown in Figures 5.37 to 5.43 and 5.54 to 5.70.

5.5.3 UNSUPPORTED TUNNELS IN OVERCONSOLIDATED CLAY

Before examining the pore pressure behaviour around tunnels in overconsolidated clays, it is important to understand the overconsolidated clay behaviour. The overconsolidated clay characteristics in many aspects are different from that of normally consolidated clays, therefore, it is reasonable to expect this difference to be reflected in pore pressure behaviour around tunnels driven in this type of soil. A comprehensive parametric analysis was undertaken to study and understand this behaviour. The soils chosen had a range of overconsolidation ratios from 5 to 15. This avoids the transition region of lightly overconsolidated clays which show both over and normally consolidated clay characteristics. The values of OCR chosen are considered to fall within the heavily overconsolidated range.

As pointed out earlier, (section 5.5) in a parametric study such as this, it is practically essential that the values of parameter be restricted to their practical range

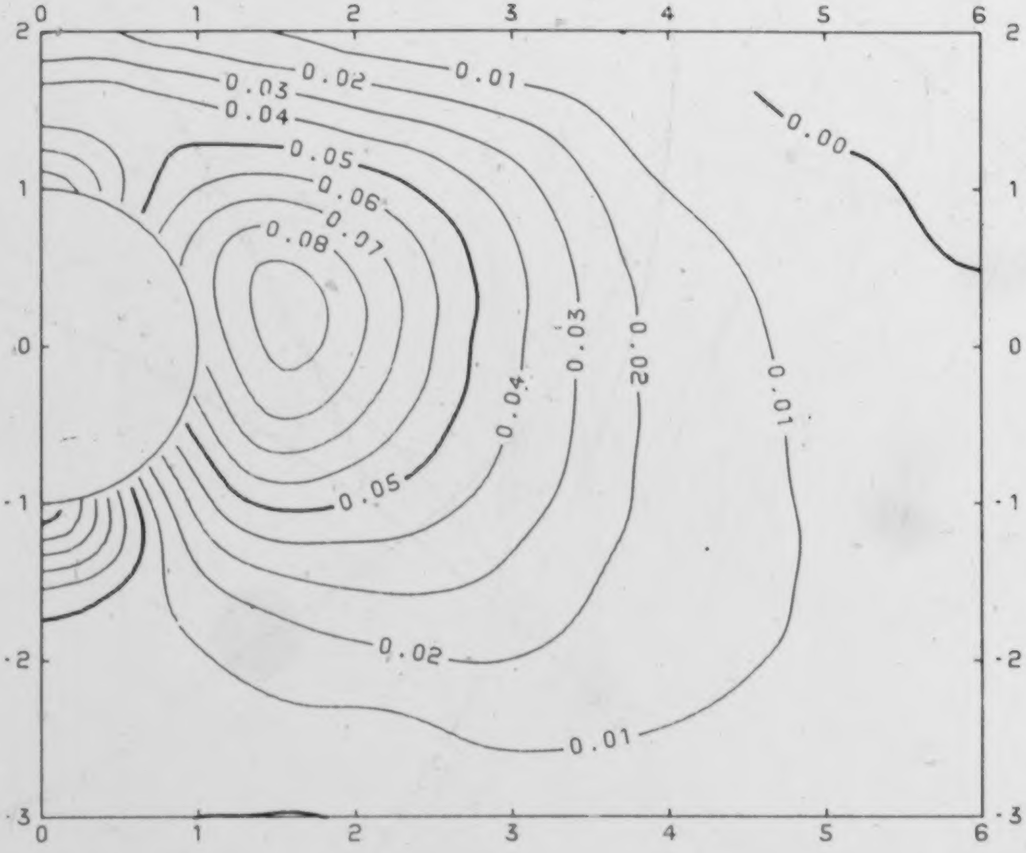

Figure 5.54 Unsealed Tunnel in NCC; $\hat{u}$ in (ξ,η), ESR=10^{-3}, T=0

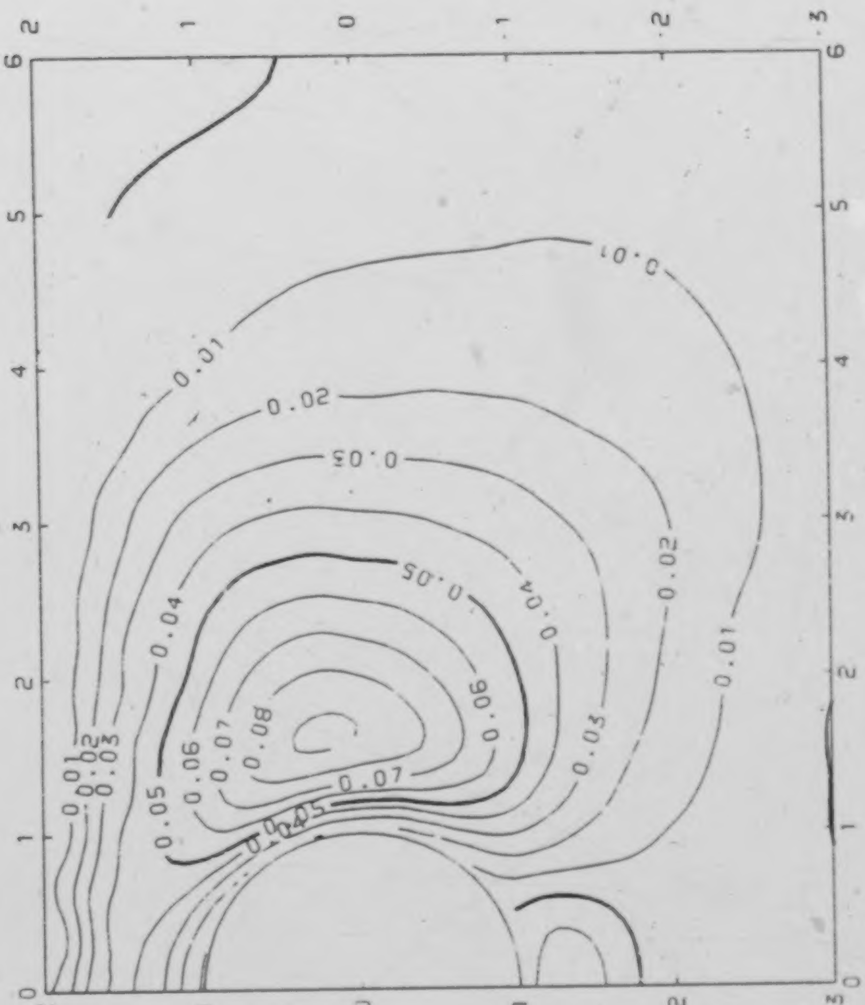

Figure 5.55 Unsealed Tunnel in NCC; $\bar{u}$ in (ξ,η), ESR=10^{-3}, T=0.001

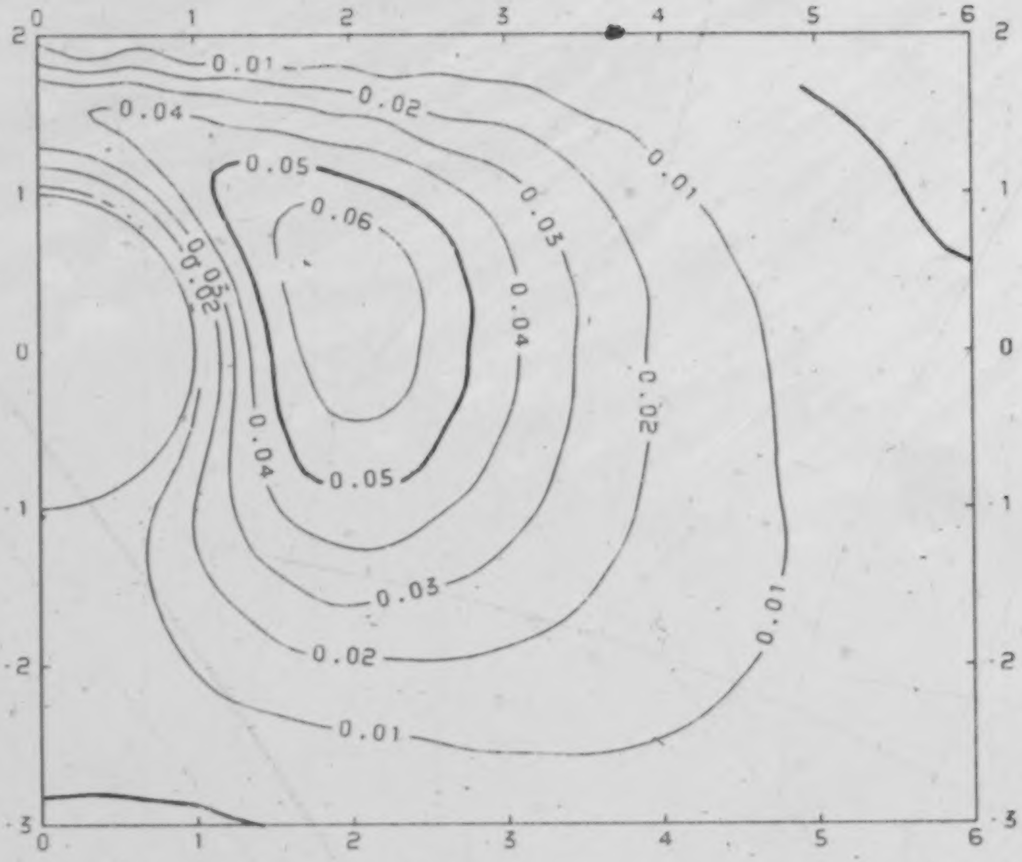

Figure 5.56 Unsealed Tunnel in NCC; $\hat{u}$ in (ξ,η), ESR=10^{-3}, T=0.01

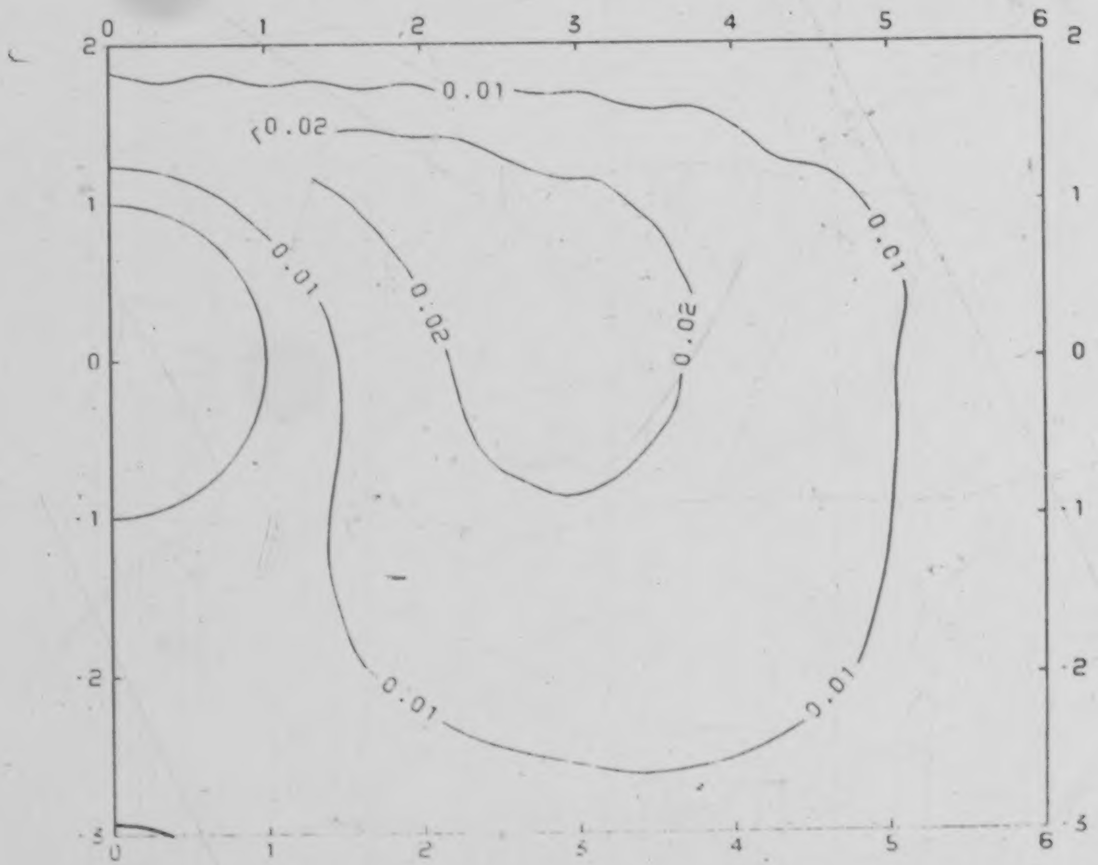

Figure 5.57 Unsealed Tunnel in NCC; $\hat{u}$ in (ξ,η), ESR=10^{-3}, T=0.1

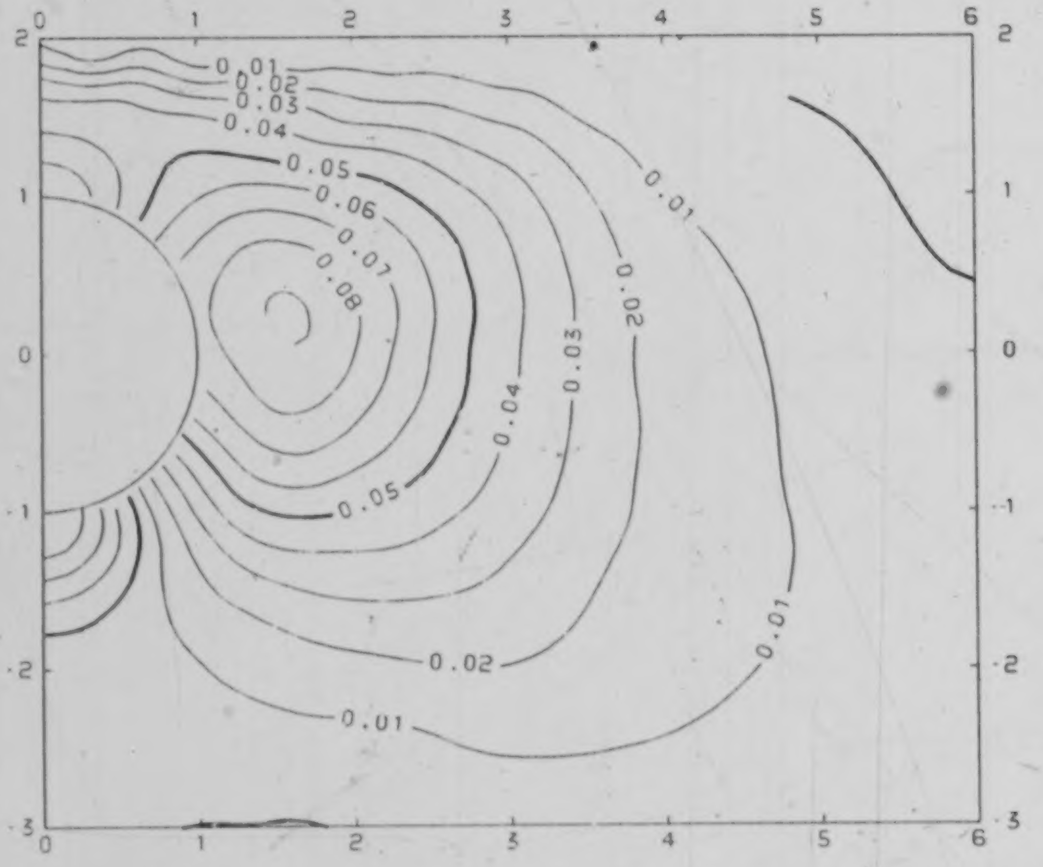

Figure 5.58 Sealed Tunnel in NCC; $\hat{u}$ in (ξ,η), ESR=10^{-3}, T=0.001

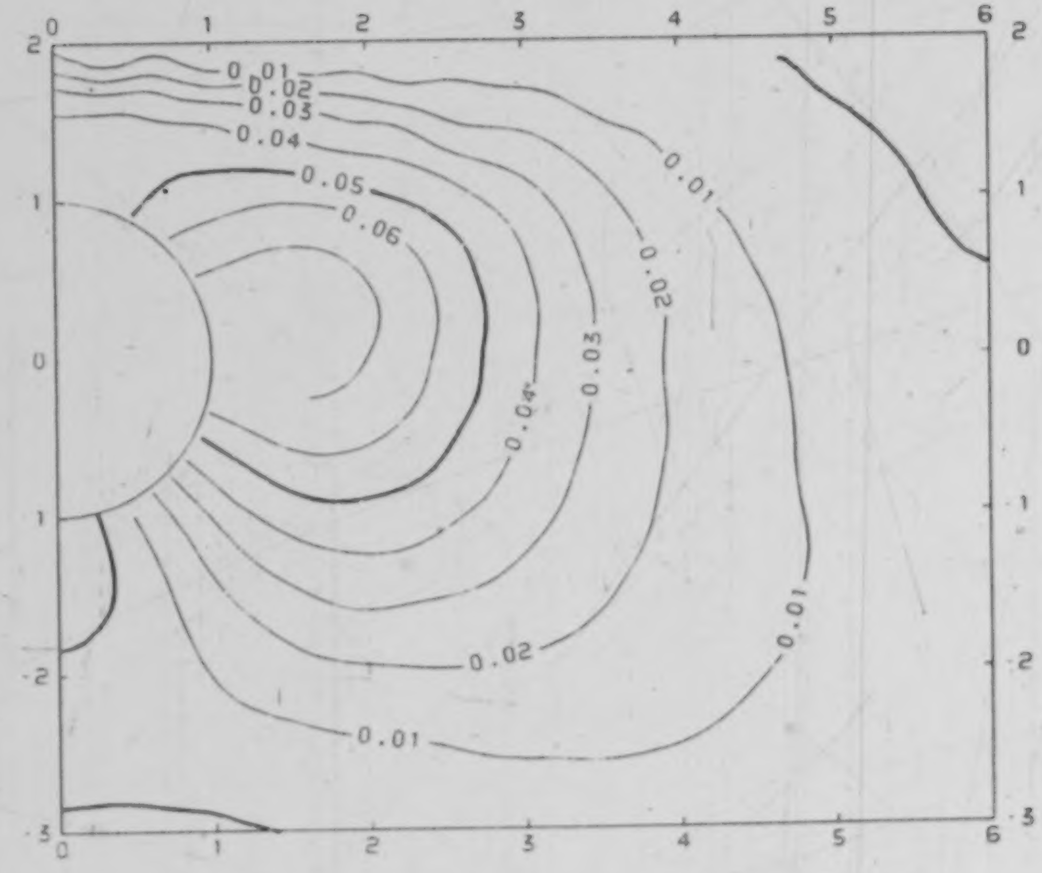

Figure 5.59 Sealed Tunnel in NCC; $\hat{u}$ in (ξ,η), ESR=10^{-3}, T=0.01

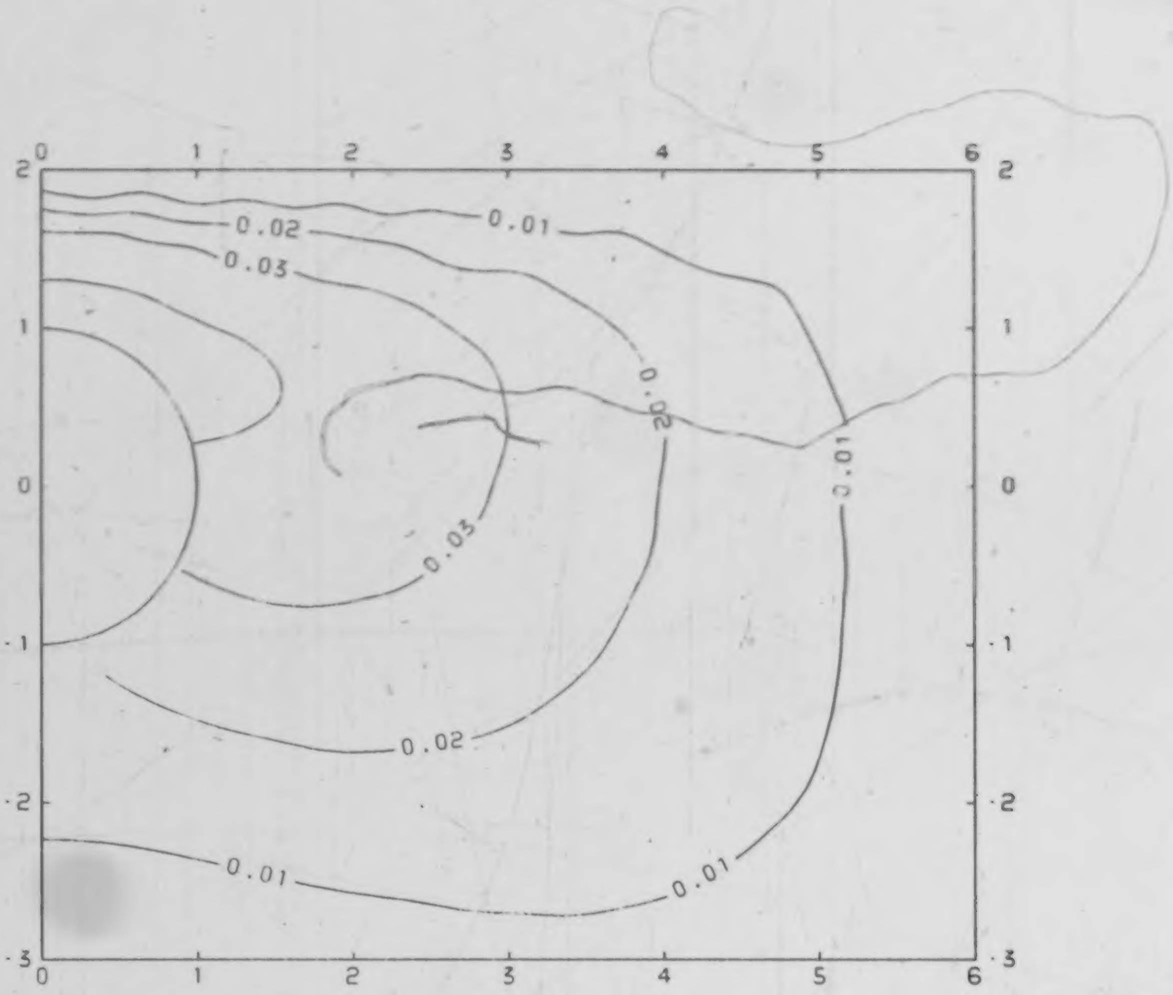

Figure 5.60 Sealed Tunnel in NCC; $\hat{u}$ in (ξ,η), ESR=10^{-3}, T=0.1

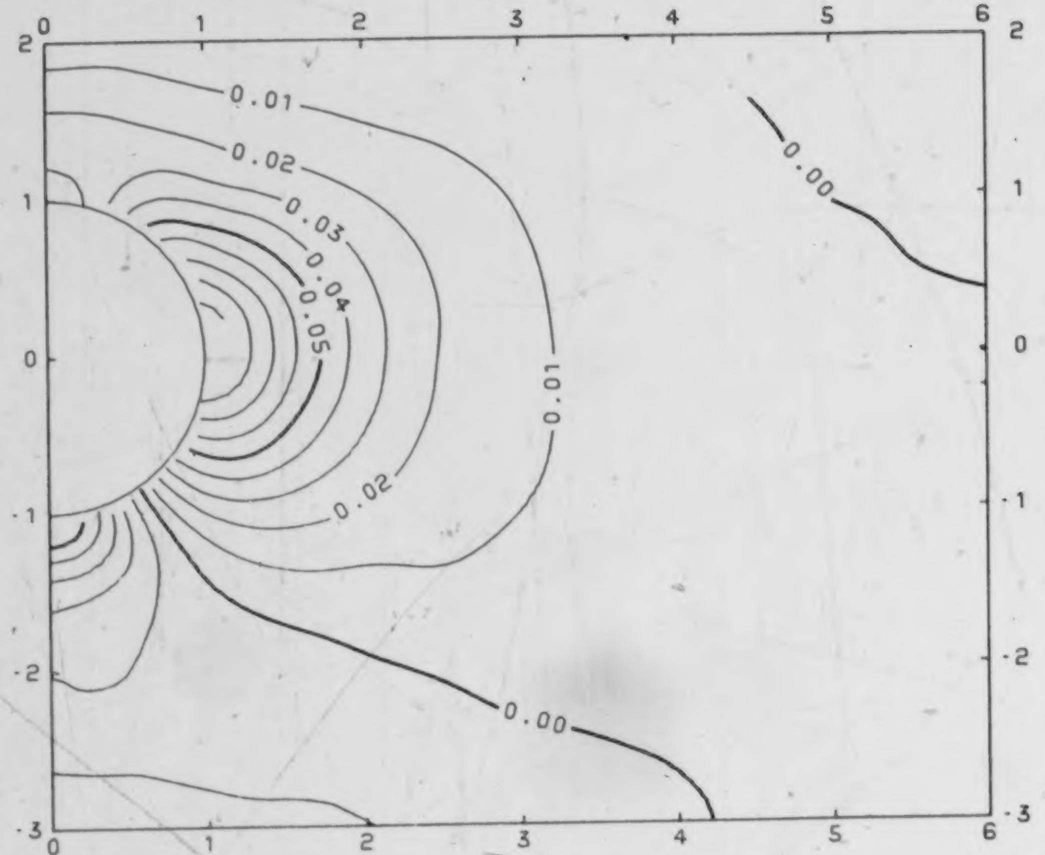

Figure 5.61 Unsealed Tunnel in NCC; $\hat{u}$ in (ξ,η), ESR=10^{-2}, T=0

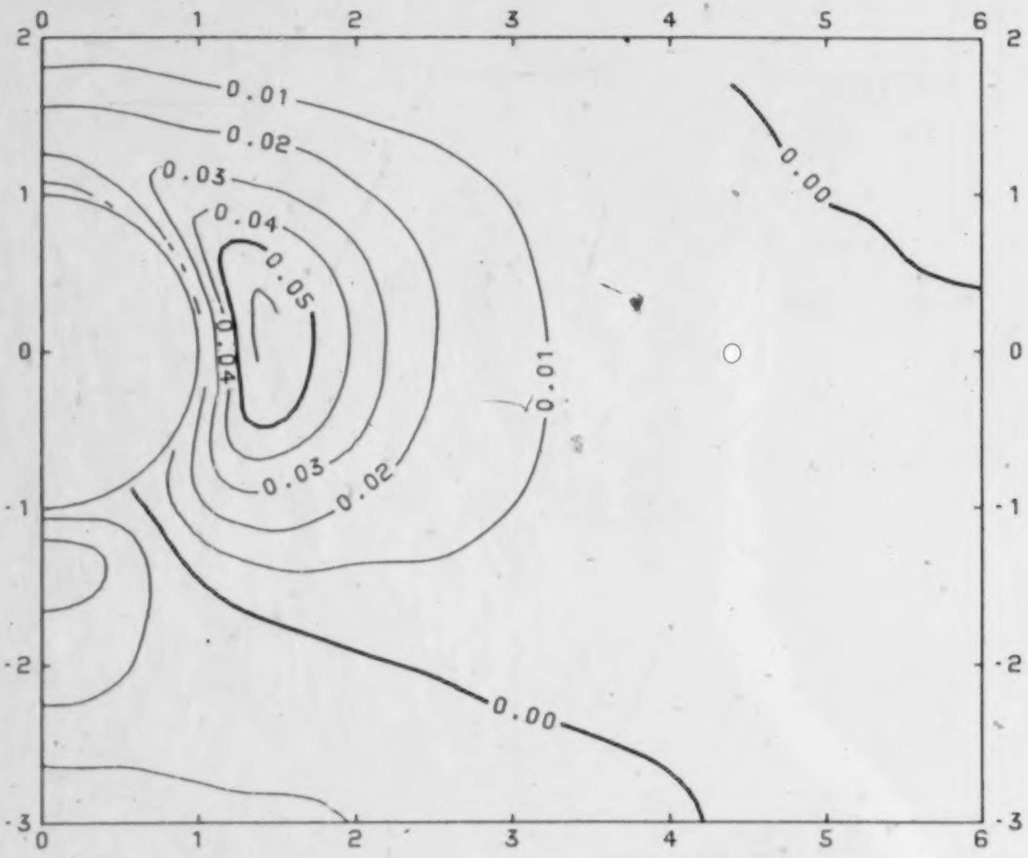

Figure 5.62 Unsealed Tunnel in NCC; $\hat{u}$ in (ξ,η), ESR=10^{-2}, T=0.001

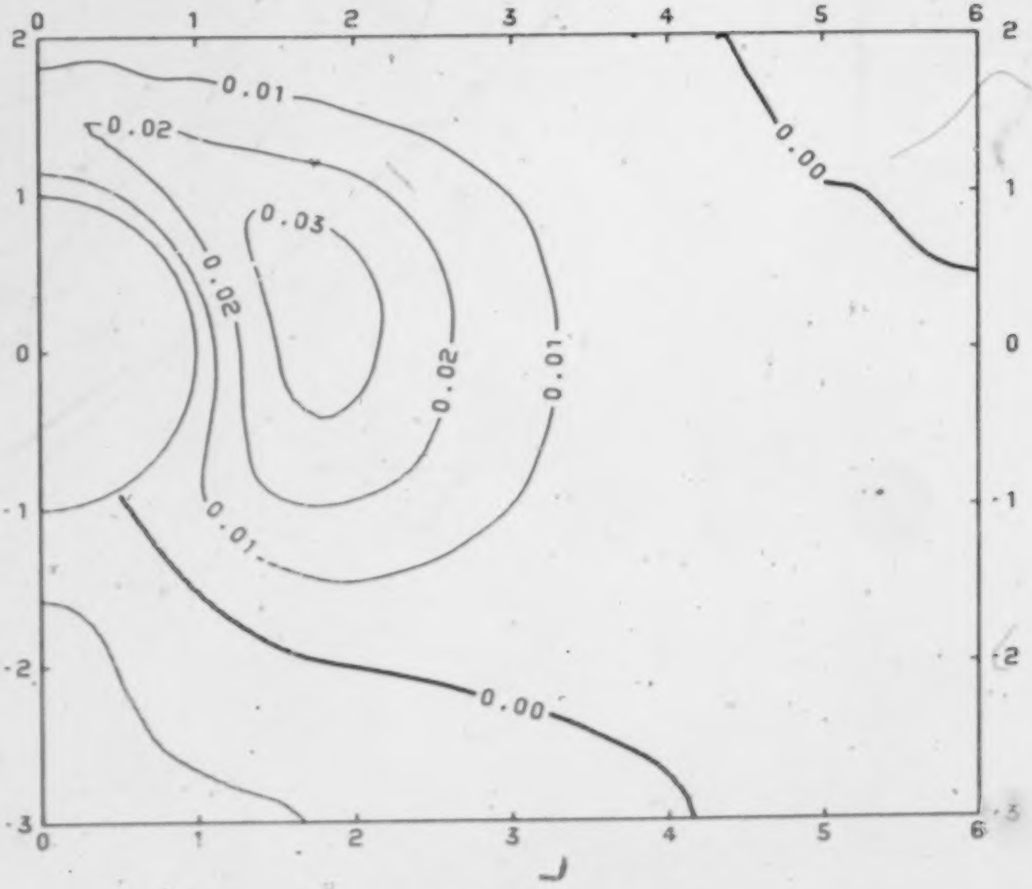

Figure 5.63 Unsealed Tunnel in NCC; $\bar{u}$ in (ξ,η), ESR=10^{-2}, T=0.01

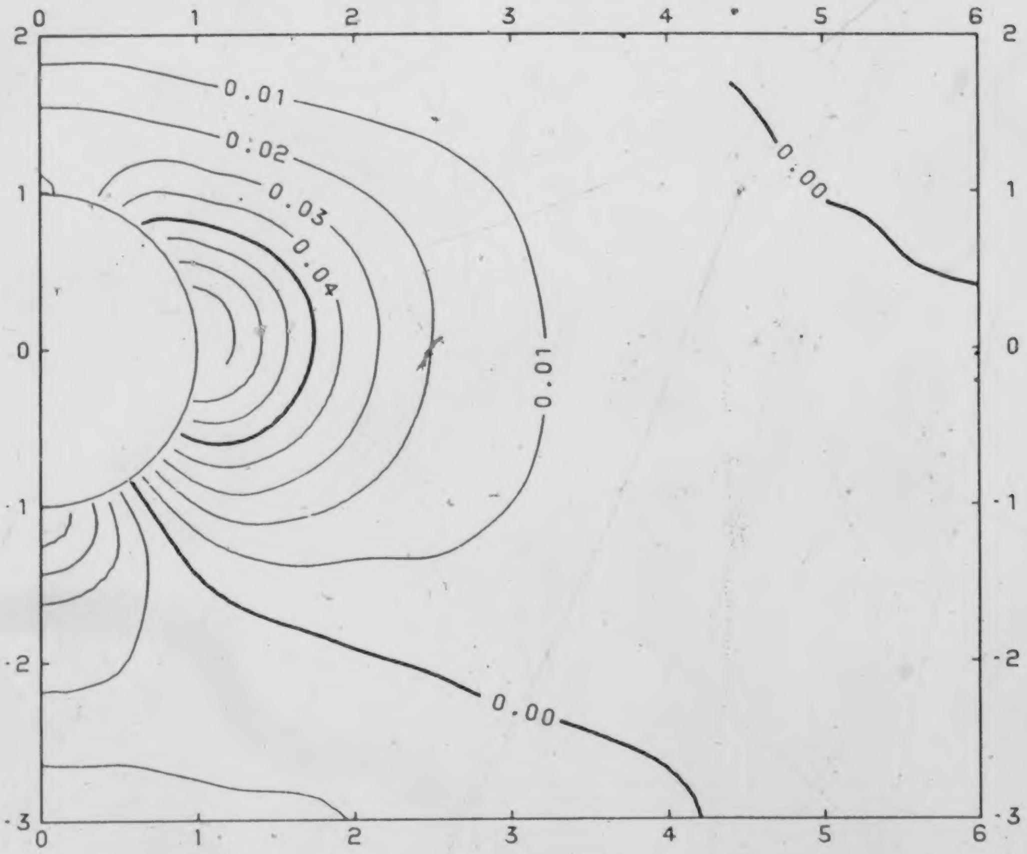

Figure 5.64 Sealed Tunnel in NCC; $\hat{u}$ in (ξ,η), ESR=10^{-2}, T=0.001

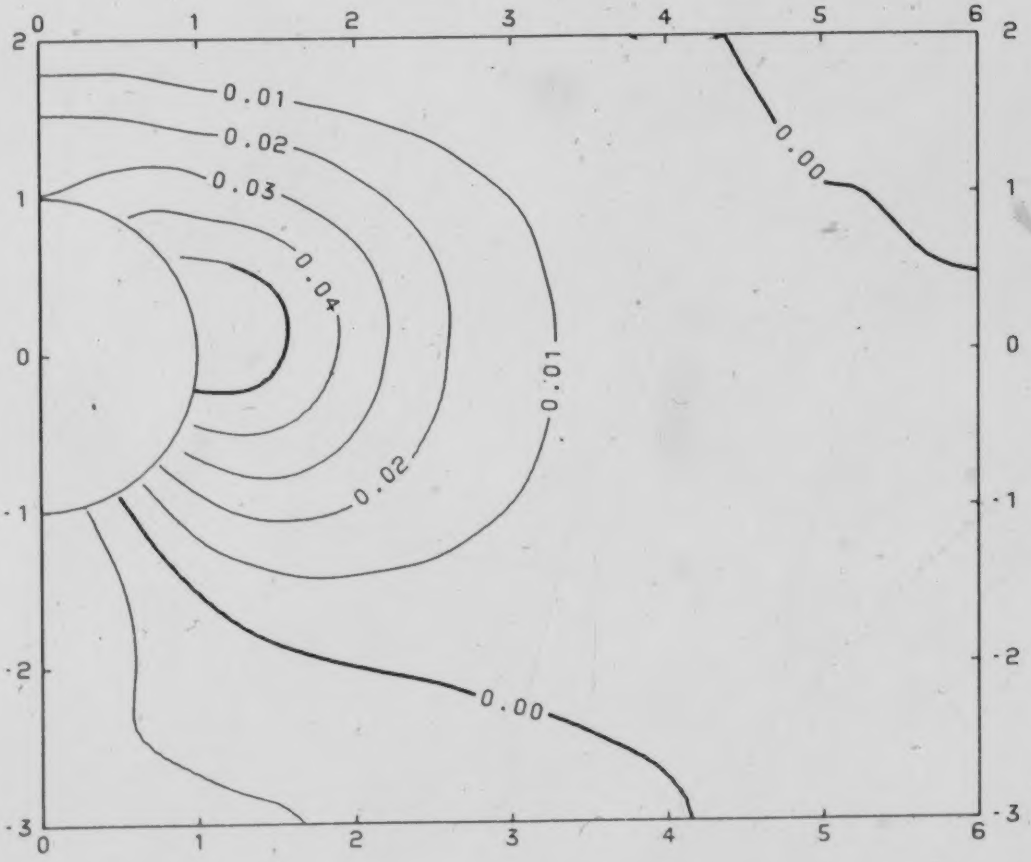

Figure 5.65 Sealed Tunnel in NCC; $\hat{u}$ in (ξ,η), ESR=10^{-2}, T =0.01

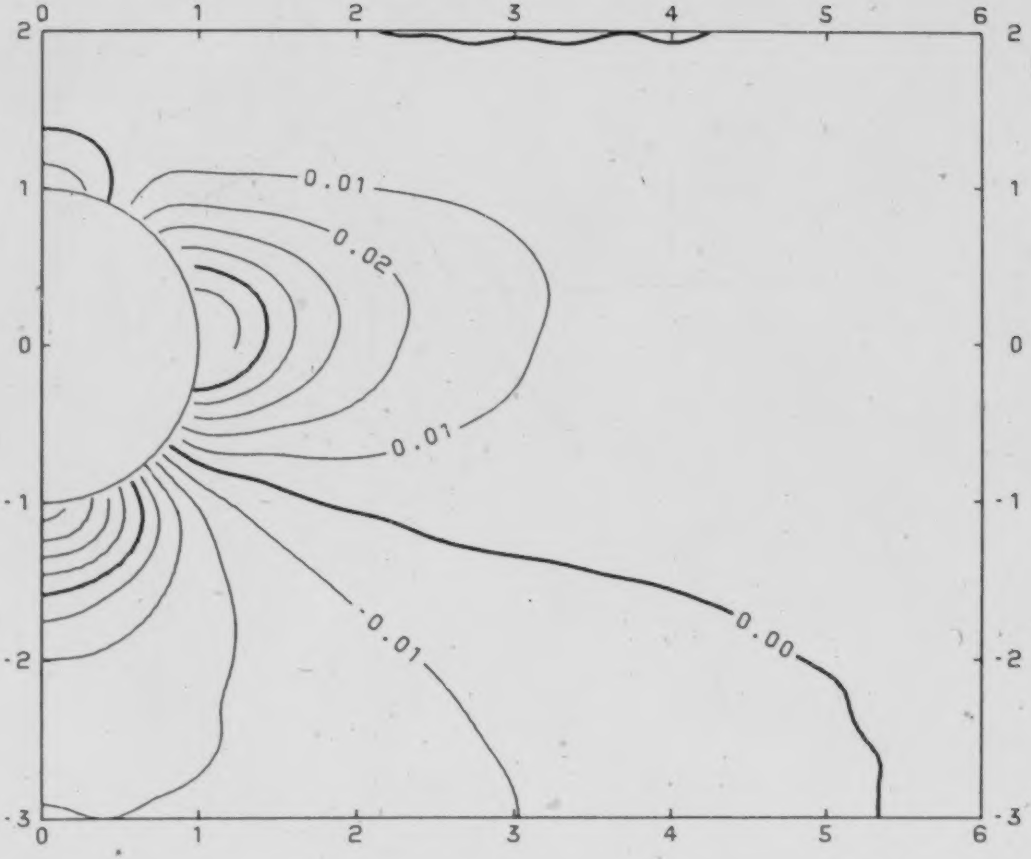

Figure 5.66 Unsealed Tunnel in NCC; û in (ξ,η), ESR=10^{-1}, T=0

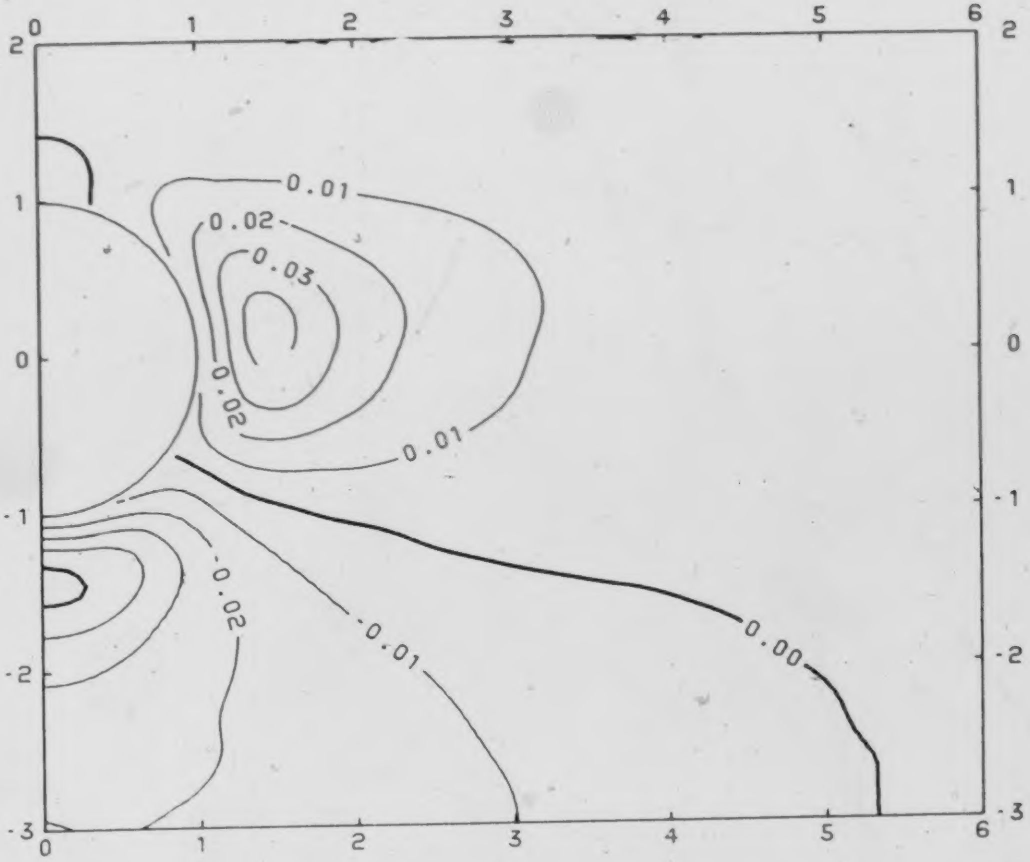

Figure 5.67 Unsealed Tunnel in NCC; û in (ξ,η), ESR=10^{-1}, T=0.001

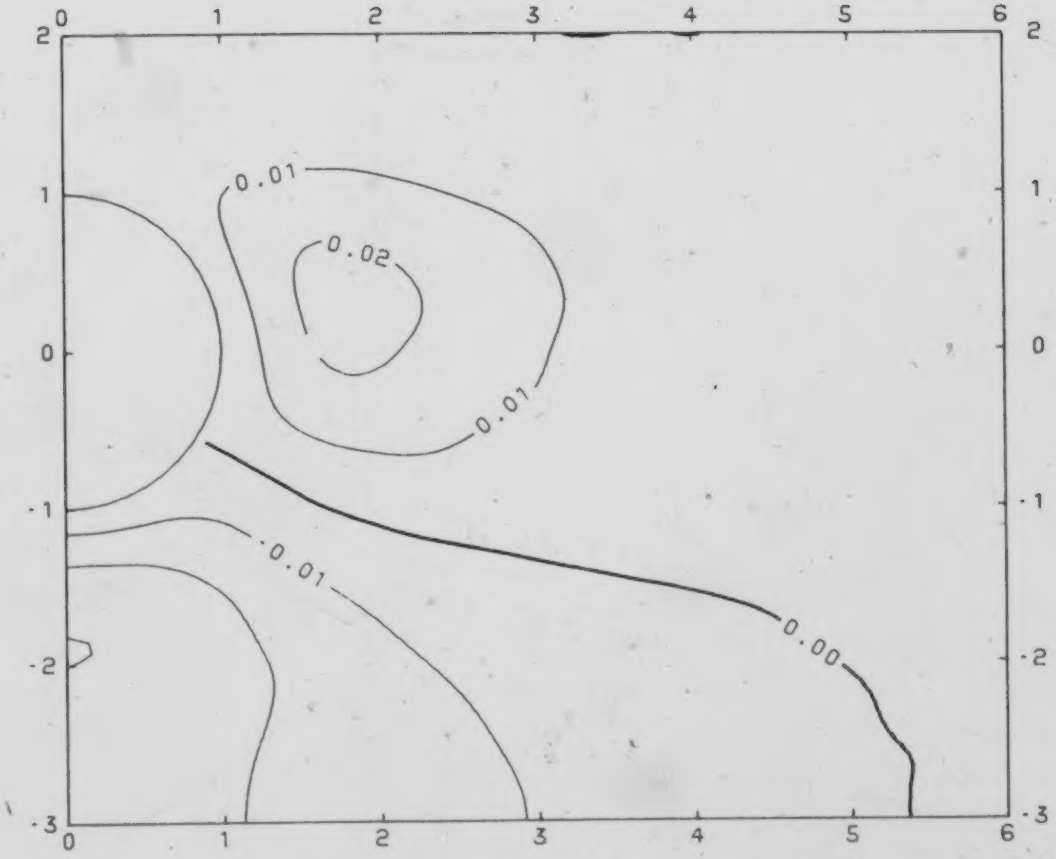

Figure 5.68 Unsealed Tunnel in NCC; $\hat{u}$ in (ξ,η), ESR=10^{-1}, T=0.01

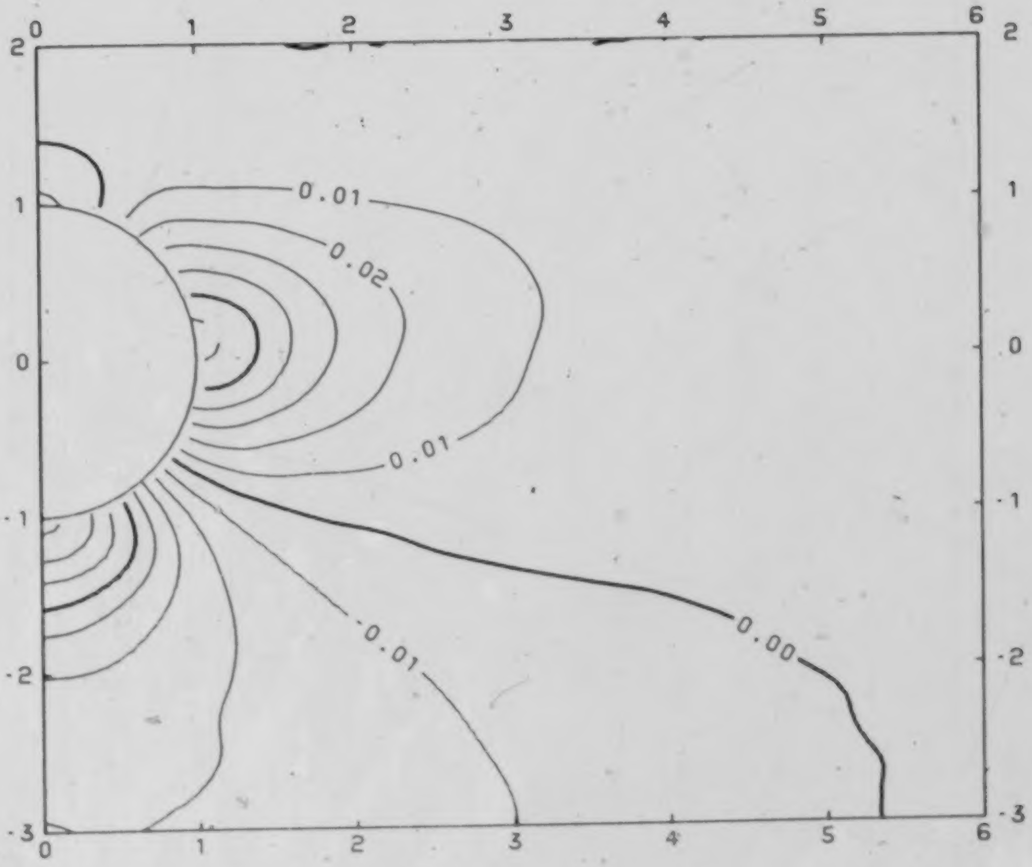

Figure 5.69 Sealed Tunnel in NCC; $\hat{u}$ in (ξ,η), ESR=10^{-1}, T=0.001

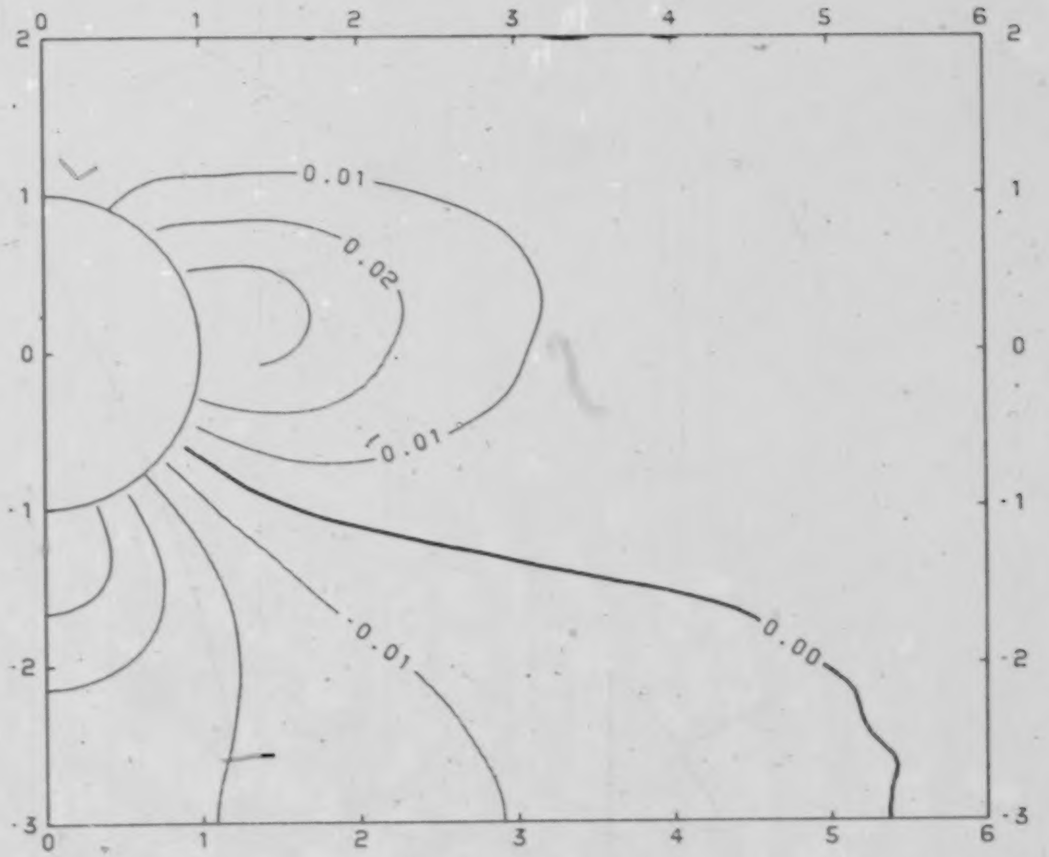

Figure 5.70 Sealed Tunnel in NCC; $\hat{u}$ in (ξ,η), ESR=10^{-1}, T=0.01

(Table 5.1). As in the normally consolidated case, the variation of the pore pressure distribution around the tunnel with varying parameters was compared with the pore pressure distribution corresponding to their average values, viz., H/D = 1.8, $E_i/\sigma_{1c}^{\frac{1}{2}}$ = 28.5 GPa$^{\frac{1}{2}}$, K_0 = 1.5, $s_u/\sigma_{1c}^{\frac{1}{2}}$ =33 kPa$^{\frac{1}{2}}$ and D=6 m .

5.5.3.1 MODULUS AND PORE PRESSURE

Hardin and Drnevich (1972) found a relationship among the initial shear modulus, void ratio, overconsolidation ratio and plasticity index. This formula, expressed in terms of non-dimensional quantities is:

$$G_i/P_a = 320.85\frac{(2.973-e)^2}{1+e}(OCR)^K\left[\frac{\sigma_m}{P_a}\right]^{\frac{1}{2}} \qquad [5.16]$$

where,

G_i	is initial shear modulus,
e	is void ratio,
K	is a parameter that depends on plasticity index,
σ_m	is mean normal stress and
P_a	is atmospheric pressure.

This formula was developed using the results of dynamic tests, and in some cases it underestimates the in situ dynamic modulus by a factor of upto 10. Desai and Christian (1977) recommend this formula to determine the initial modulus G_i for the hyperbolic model. It must be noted that in this thesis, it was used only to obtain an approxiamte range for G_i values.

A void ratio range of 0.5 to 1.7 (Hardin and Drnevich, 1972) was chosen for this analysis. Hence, the value of the expression, $(2.973-e)^2/(1+e)$, (Equation 5.16) ranges from 0.6 to 4.1. For soils having a plasticity index greater than 20%, the parameter K, (Equation 5.16) varies from 0.18 to 0.5 (Hardin and Drnevich, 1972). For the parametric ranges noted and for the chosen range of OCR (5 to 15), it can be shown that OCR^K lies between 1.34 and 3.87. Therefore, Equation 5.16 yields a lower bound of 225 and an upperbound of 5070, for $(G_1/P_a)/(\sigma_m/P_a)^{\frac{1}{2}}$ in the same parameter ranges. The logarithmic mean value of this range is 1100. Hence, for the undrained conditions, the $E_1/\sigma_{1c}^{\frac{1}{2}}$ average can be shown to be 28.5, with a range of 6 to 136 in units of $GPa^{\frac{1}{2}}$. The initial pore pressure distributions corresponding to the extreme values were computed and compared with the distribution corresponding to the average parameters (section 5.5.3). As expected, no pore pressure deviation was found for these distributions. The pore pressure diagrams corresponding to $E_1/\sigma_{1c}^{\frac{1}{2}} = 6\ GPa^{\frac{1}{2}}$ and $136\ GPa^{\frac{1}{2}}$ are shown in Figures 5.71 and 5.72, respectively.

5.5.3.2 STRENGTH AND PORE PRESSURE

The pore pressure variation with strength is investigated in this section. Seed et al., (1970)

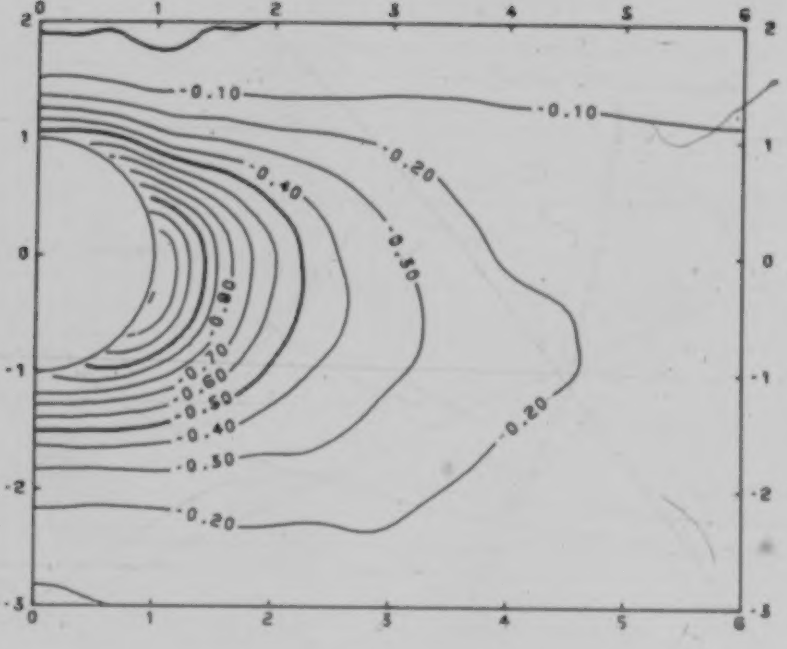

Figure 5.71 Normalized Pore Pressure, $E_i/\sigma_{1c}^{\frac{1}{2}}$ =6 $\mathrm{GPa}^{\frac{1}{2}}$

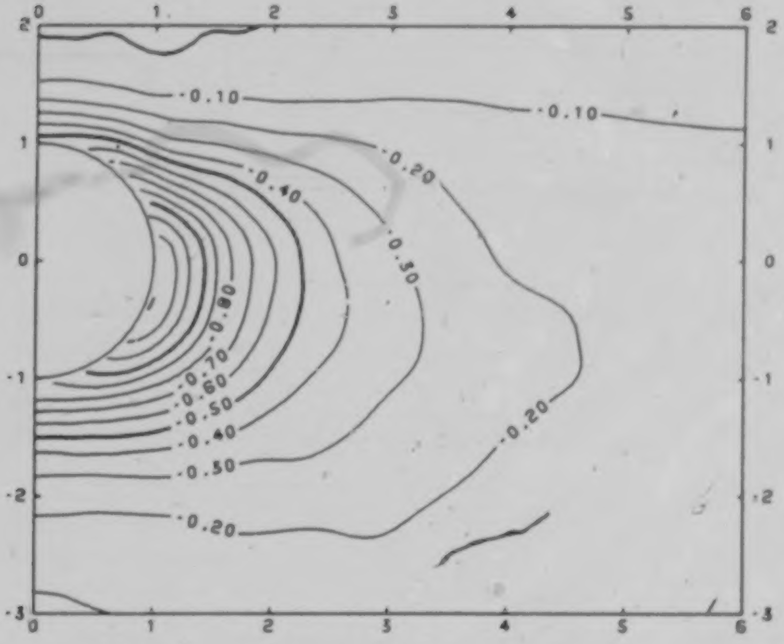

Figure 5.72 Normalized Pore Pressure, $E_i/\sigma_{1c}^{\frac{1}{2}}$ =136 $\mathrm{GPa}^{\frac{1}{2}}$

collected data from twelve researchers and recorded the G_i/s_u variation in one plot. From this plot it can be seen that the majority of G_i/s_u points lie between 100 and 1000. Hence, using the values computed for G_i from the expression given in equation 5.16, it can be shown that $s_u/\sigma_{1c}^{\frac{1}{2}}$ varies between 10 and 100 in units of kPa $^{\frac{1}{2}}$. It has a logarithmic mean value of 33 kPa $^{\frac{1}{2}}$.

To investigate the variation of pore pressure behaviour with strength, as in the earlier cases, the strength was varied within the above range, keeping all the other parameters at average values (section 5.5.3). The resulting pore pressure distributions were computed and the deviation with respect to the pore pressure distribution corresponding to the average parameters was assessed. As expected, the deviations were not relatively substantial, and the extreme deviations took place for the extreme values of strength. As explained in the normally consolidated case, this behaviour is not surprising in the upper ranges of the strength values. Overconsolidated clays, in general, belong to the upper ranges of the strength values of clay. The 95% probable, maximum deviations corresponding to $s_u/\sigma_{1c}^{\frac{1}{2}}$ = 10 kPa $^{\frac{1}{2}}$ and 100 kPa $^{\frac{1}{2}}$ are 9% and 6%, respectively. The computation of these percentage deviations are described in section 5.5.

As discussed in normally consolidated clays, the pore pressure tends to increase with increasing strength. Figures 5.73 and 5.74 show the normalized pore pressure diagrams corresponding to 10 kPa $^{\frac{1}{2}}$ and 100 kPa $^{\frac{1}{2}}$, respectively.

5.5.3.3 K_0 AND PORE PRESSURE

The influence of K_0 on pore pressure is examined in this section. As stated earlier, the development of a normalization procedure for K_0 is difficult, as there are no closed form solutions that can be used as guidelines. The influence of K_0 on initial pore pressure in overconsolidated clays is assumed to be similar to that in normally consolidated clays (section 5.5.1.4). Therefore, a normalization factor of the form $1/(\lambda_1+\lambda_2K_0)$ was postulated for the overconsolidated case too. Keeping all the other parameters at their average values (section 5.5.3), the K_0 was varied from 1.25 to 1.75 in steps of 0.25. These K_0 values fall within the range of K_0 values for heavily overconsolidated clays (Table 5.1). The initial pore pressure distributions were computed for each of these K_0 values and the deviations were computed with respect to the pore pressures corresponding to the average parameters. By trial and error, it was found that λ_1=-0.5 and λ_2=1 yield the best fit normalization factor. As expected, the extreme deviations occurred for the extreme values of K_0. The 95% probable maximum deviation (defined in section 5.5) for K_0=1.25 and 1.75 are 9% and 8%, respectively.

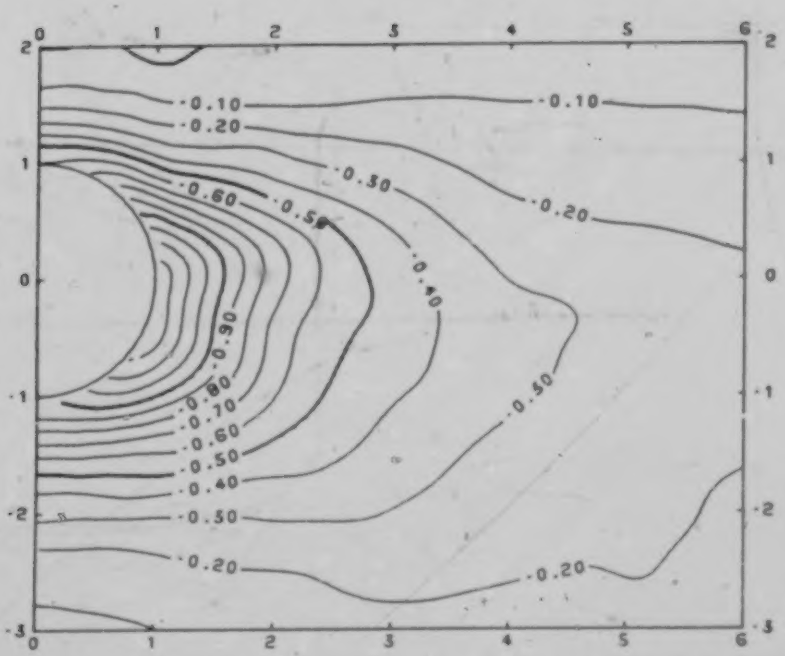

Figure 5.73 Normalized Pore Pressure, $s_u/\sigma_{1c}^{\frac{1}{2}}$ =10 kPa$^{\frac{1}{2}}$

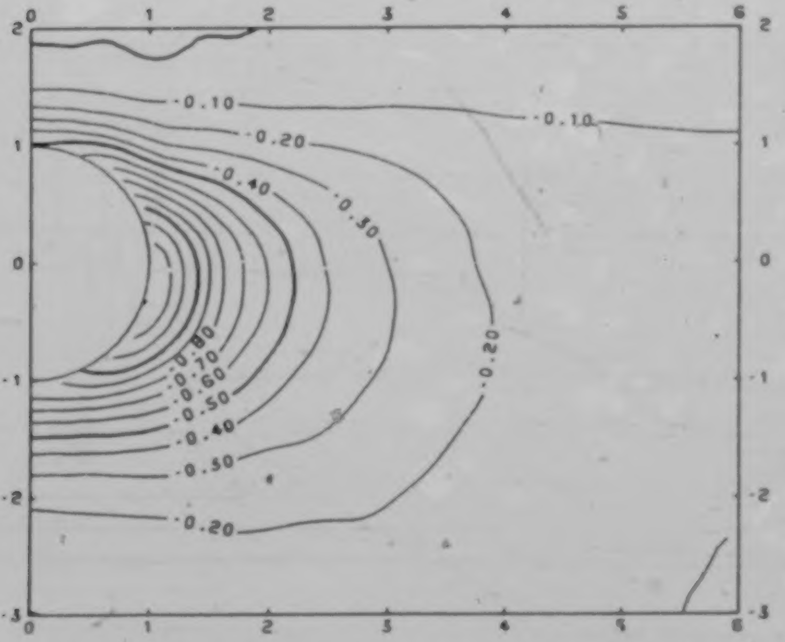

Figure 5.74 Normalized Pore Pressure, $s_u/\sigma_{1c}^{\frac{1}{2}}$ =100 kPa$^{\frac{1}{2}}$

As K_0 increases, the pore pressures decrease in this range of K_0 of overconsolidated clays. As explained in section 5.5.1.4, a larger K_0 amounts to a greater degree of arching, which tends to produce a concentration of higher positive pore pressures. These pore pressures are counterbalanced by the larger negative pore pressures developed due to higher stress relief and increased shear stress magnitudes. Clearly, in this case, the effects of stress relief and shear stresses appear to dominate. Figures 5.75 and 5.76 show the normalized pore pressure diagrams corresponding to K_0=1.25 and 1.75, respectively.

5.5.3.4 HENKEL'S COEFFICIENT α AND PORE PRESSURE

As in the normally consolidated case, the pore pressure coefficient has a direct influence on the initial pore pressure generation. To examine the pore pressure behaviour with variation of the Henkel coefficient, within the practical range (Table 5.1) it was changed from -0.6 to -0.2 in steps of 0.1, and the other parameters were kept at their average values (section 5.5.3). The pore pressure distribution for each case was computed and the deviations with respect to the pore pressures corresponding to the average parameters were assessed. Similar to the normally consolidated case, several attempts were made to normalize the pore pressure distribution with respect to α. A normalization

Table 5.1 Practical Ranges of Parameters used

NORMALLY CONSOLIDATED CLAYS		
K_0	(3)	0.5 to 0.8 for PI>15
E_i/σ_v	(5)	200 to 800
s_u/σ_v	(3,5)	0.3 to 0.7
a (Henkel)	(1)	0.12 to 0.48

OVER CONSOLIDATED CLAYS		
c'	(4)	5 to 25 kPa
OCR		5 to 15
K_0	(3)	1 to 2
G_i/s_u	(6)	100 to 1000
ϕ^0	(4)	5 to 20
c_v m^2/month	(3)	0.1 to 10
a (Henkel)	(1)	-0.6 to -0.2

GEOMETRY AND STIFFNESS PARAMETERS (2)	
D	3 to 6 m small to medium 6 to 9 m medium to large
H/D	1 to 3; shallow tunnels

	E_s/E_l	t/R
Steel or Cast Iron supports in soft ground: fabricated steel liner plates(D, 3 to 9 m)	10^{-4} to 10^{-3}	.025 to .01
Concrete supports in soft ground; cast in place concrete. (D, 3 to 6 m)	10^{-3} to 10^{-2}	.065 to .0375
Pre fabricated concrete or cast iron elements(D, 3 to 6 m)	10^{-3} to 10^{-2}	.075 to .0625

Clough and Schmidt, 1981 (1); Einstein and Schwartz, 1979 (2); Lambe and Whitman, 1979 (3); Mitchel, 1983 (4); Samarasekera, 1982 (5); Seed and Idriss, 1970 (6).

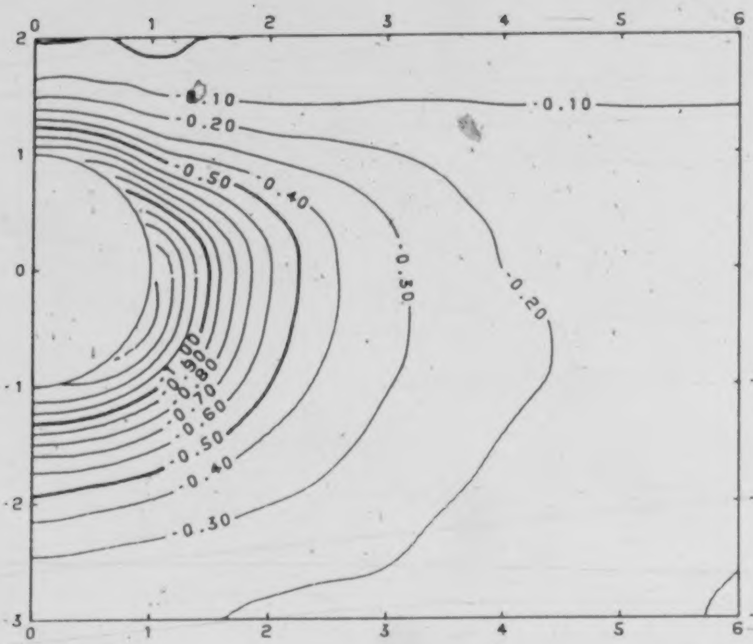

Figure 5.75 Normalized Pore Pressure, K_0=1.25

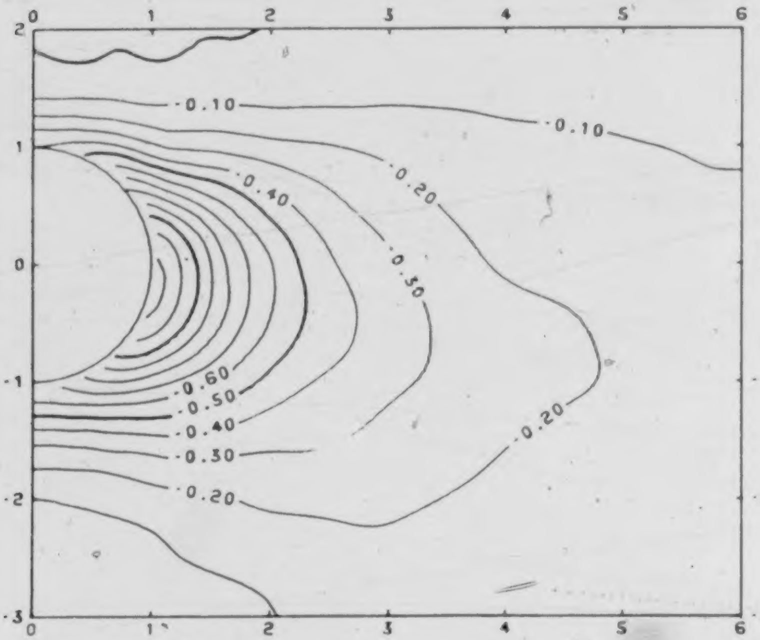

Figure 5.76 Normalized Pore Pressure, K_0=1.75

factor of the form $1/(\lambda_1+\lambda_2 a)$ was postulated, and by trial and error it was found that $\lambda_1=4/30$ and $\lambda_2=-1$ yielded the best fit normalization factor. The extreme deviations correspond to the extreme values of a. The 95% probable maximum deviation (defined in section 5.5) for $a=-0.2$ and -0.6 were 7% and 5%, respectively. Figures 5.77 and 5.78 show the normalized pore pressure diagrams corresponding to $a = -0.2$ and -0.6, respectively. With decreasing a, the pore pressures tend to decrease.

5.5.3.5 H/D AND PORE PRESSURE

The pore pressure variation with H/D ratio, and whether or not the coordinate non-dimensionalization (section 5.3.2) provides a unique pore pressure diagram in (ξ,η) plane, are investigated in this section. In this analysis, the H/D ratio was chosen within the defined limits of shallow tunnels, viz., $1<H/D<3$ (section 5.5). The other parameters were maintained at their average values (section 5.5.3). The pore pressure distribution was obtained for H/D values 1, 1.25, 1.60, 2.0, 2.25, 2.50 and 3.0, and results were compared with the pore pressure distribution corresponding to the average parameters. Then the percentage deviations were assessed, and the extreme deviations correspond to the extreme values of H/D. The 95% probable maximum deviations corresponding to H/D=1 and 3 are 5% and 4%, respectively. Figures 5.79 and 5.80 show the pore

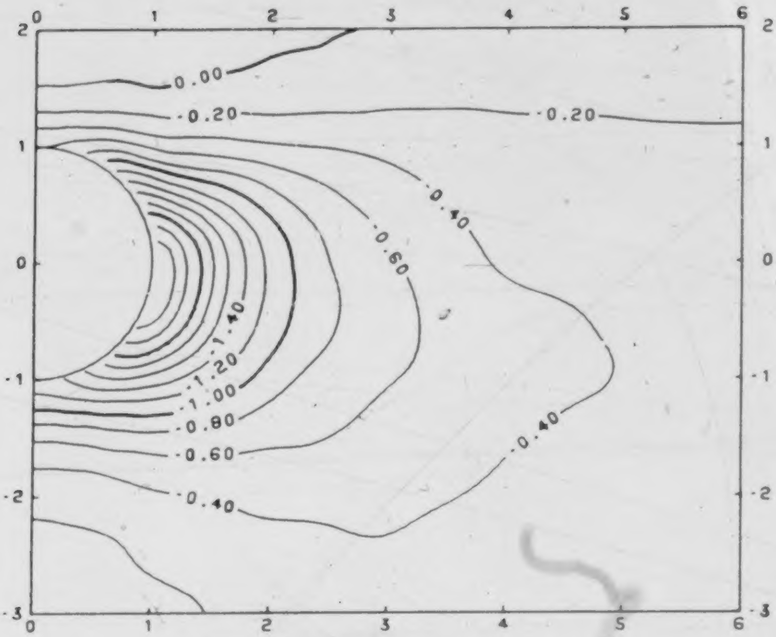

Figure 5.77 Normalized Pore Pressure, a=-0.2

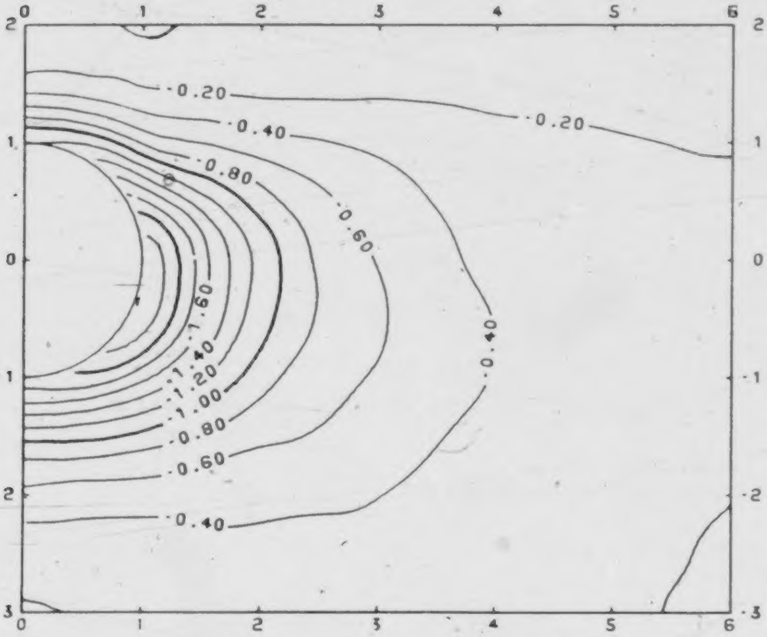

Figure 5.78 Normalized Pore Pressure, a=-0.6

pressure distributions corresponding to H/D=1 and 3, respectively.

5.6 PORE WATER PRESSURE DIAGRAMS

The above parametric analysis justified the postulated normalization and non-dimensionalization procedures developed for the study of generation and dissipation of pore pressures around shallow tunnels constructed in both normally and overconsolidated clays. The use of a newly defined quantity ESR, was also found to be successful in characterizing the pore pressure distribution around supported tunnels. It must be noted that the unsupported tunnels correspond to ESR=0.

Figures 5.37 to 5.43 and 5.54 to 5.70 provide approximate design diagrams or a classification system for estimating the pore pressure generation and dissipation behaviour. These diagrams are for ESR values of, 0, 10^{-3}, 10^{-2} and 10^{-1} at T=0, 0.001, 0.01 and 0.1, for both sealed and unsealed tunnels in normally consolidated clay. Figures 5.81 to 5.87 provide pore pressure diagrams for both sealed and unsealed unsupported tunnels in overconsolidated clays for the same (as above) time factors. The tunnels are assumed to be well above the water table. For sealed tunnels however, the water table may also be assumed to be at the ground surface. The diagrams are presented in their non-dimensionalized and normalized form. The pore pressure u(x,y,t) around a tunnel constructed in clay of known OCR

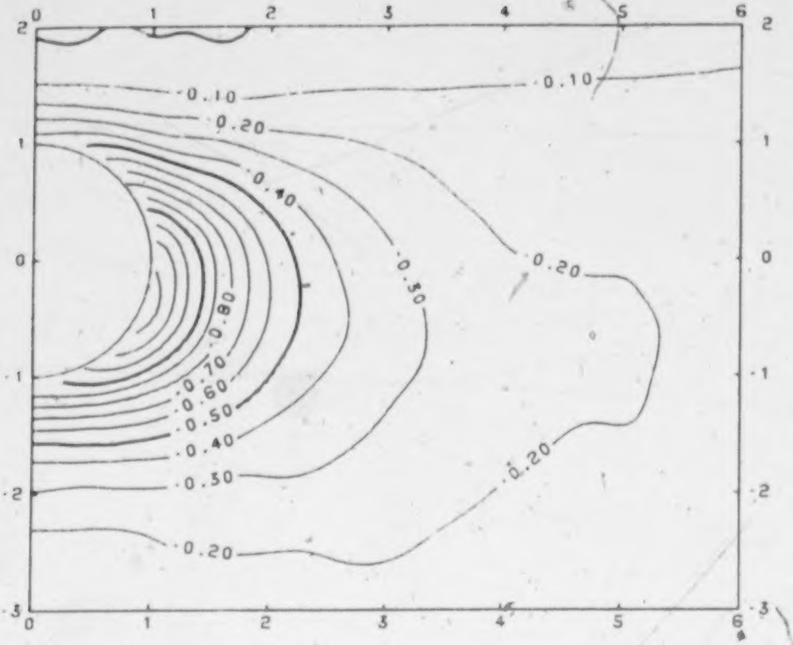

Figure 5.79 Normalized Pore Pressure, H/D=1

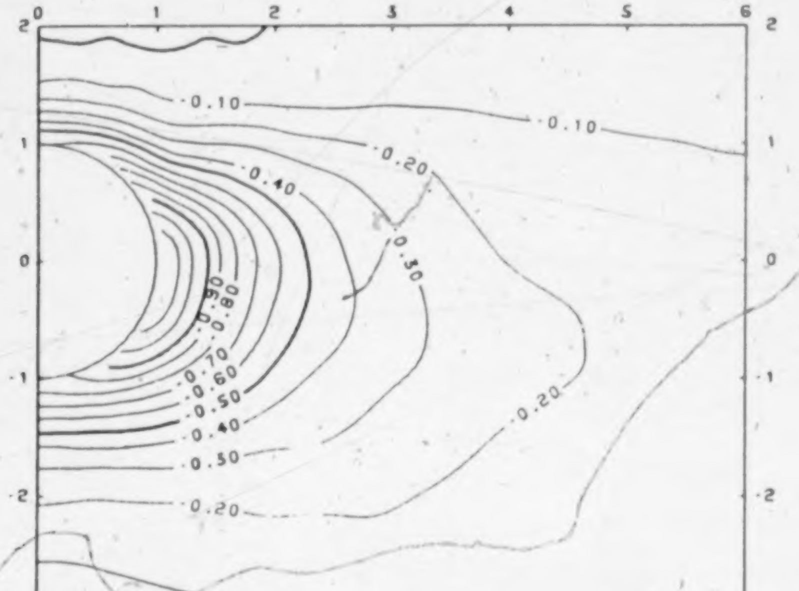

Figure 5.80 Normalized Pore Pressure, H/D=3

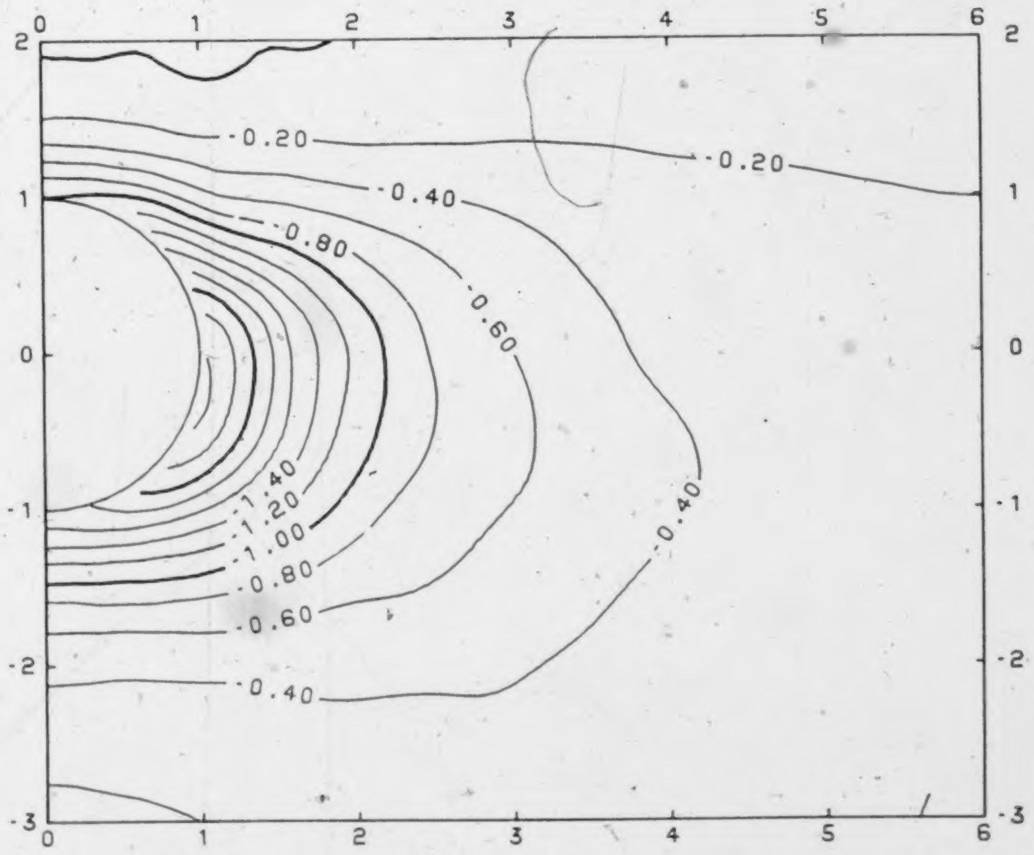

Figure 5.81 Unsealed Tunnel in OCC, $\hat{u}$ in (ξ,η), T=0

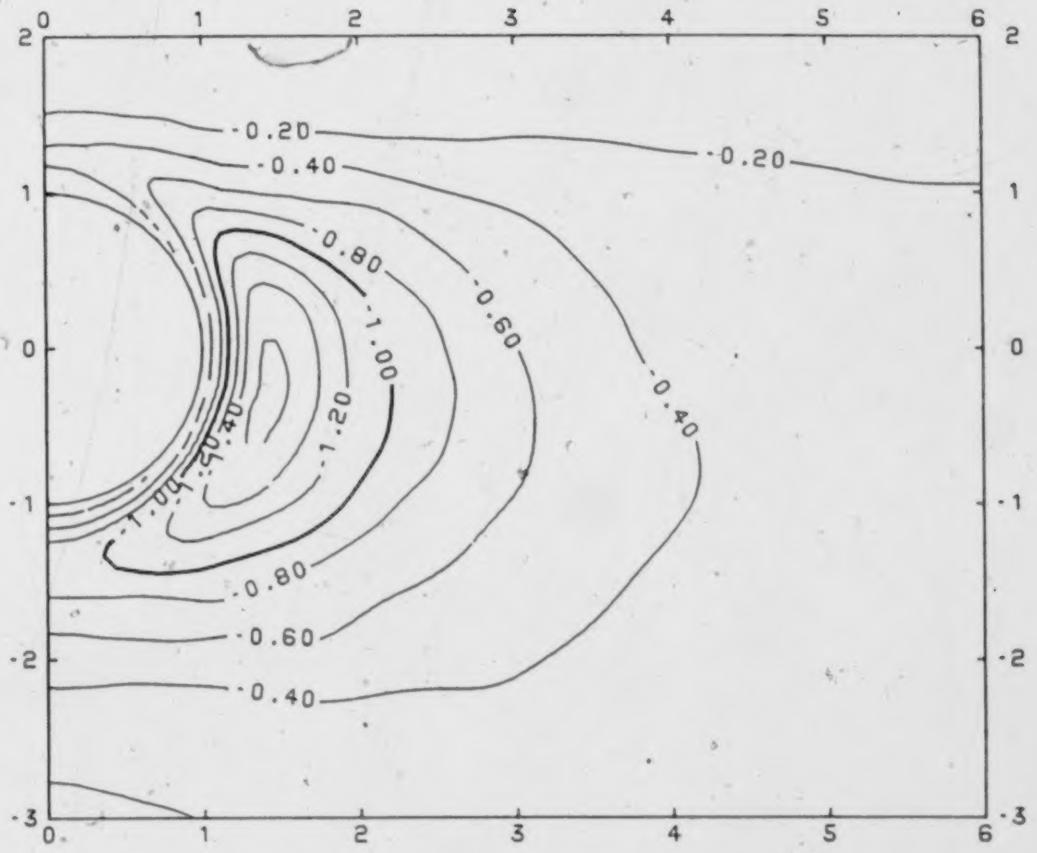

Figure 5.82 Unsealed Tunnel in OCC, $\hat{u}$ in (ξ,η), T=0.001

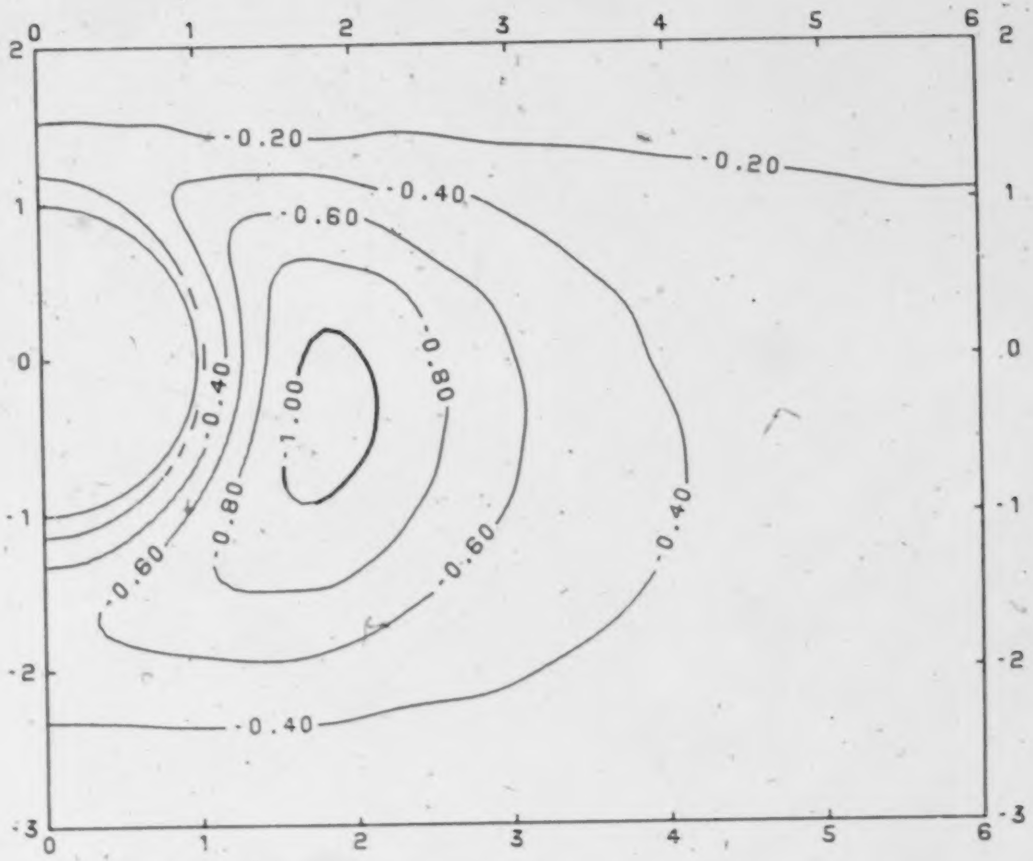

Figure 5.83 Unsealed Tunnel in OCC, û in (ξ,η), T=0.01

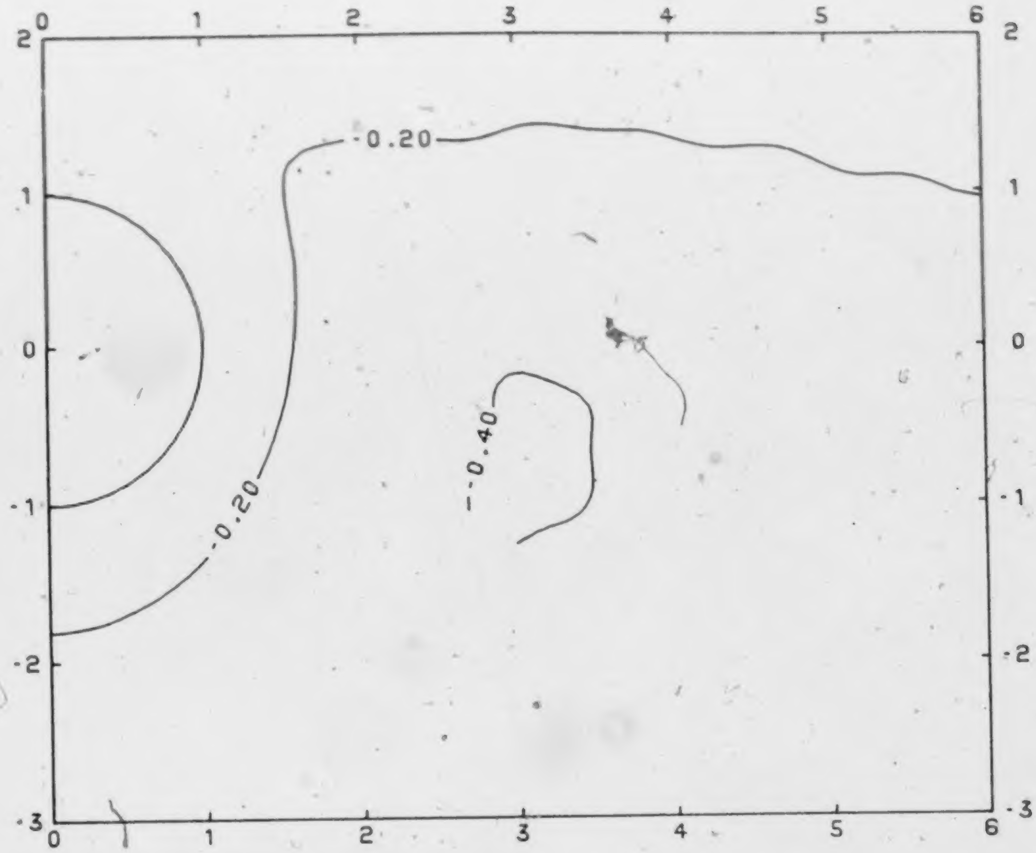

Figure 5.84 Unsealed Tunnel in OCC, $\hat{u}$ in (ξ,η), T=0.1

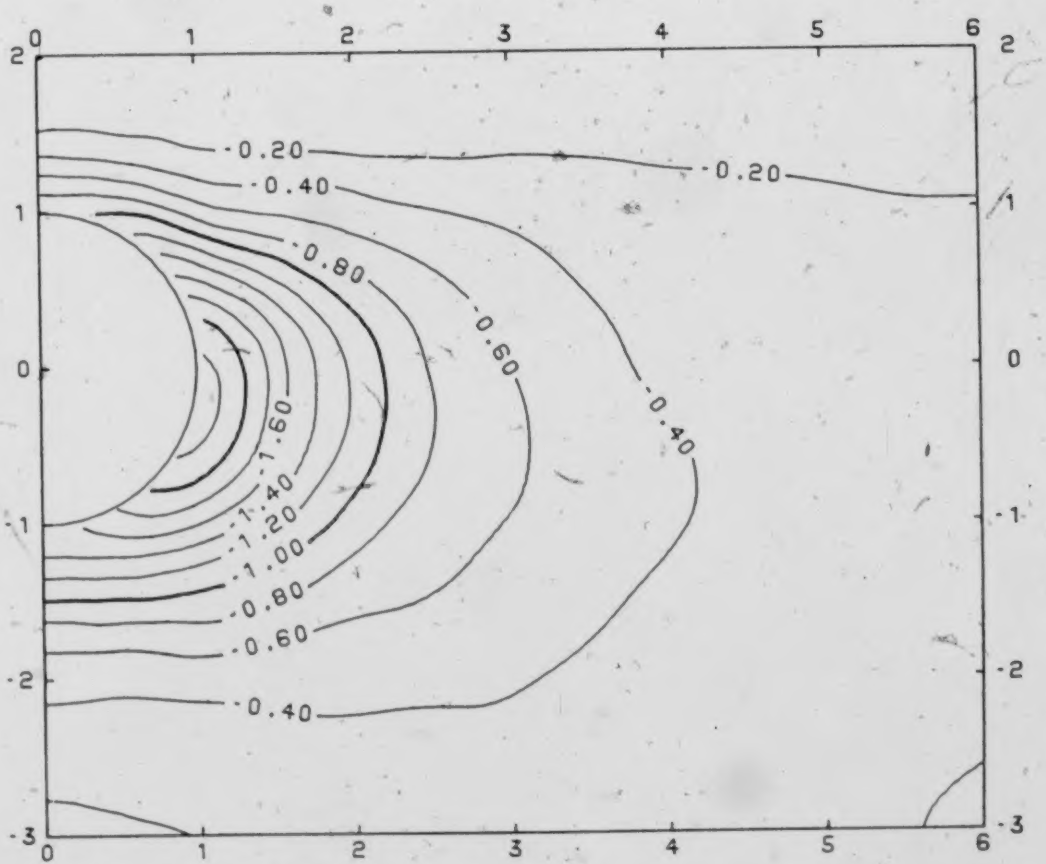

Figure 5.85 Sealed Tunnel in OCC, $\hat{u}$ in (ξ,η), T=0.001

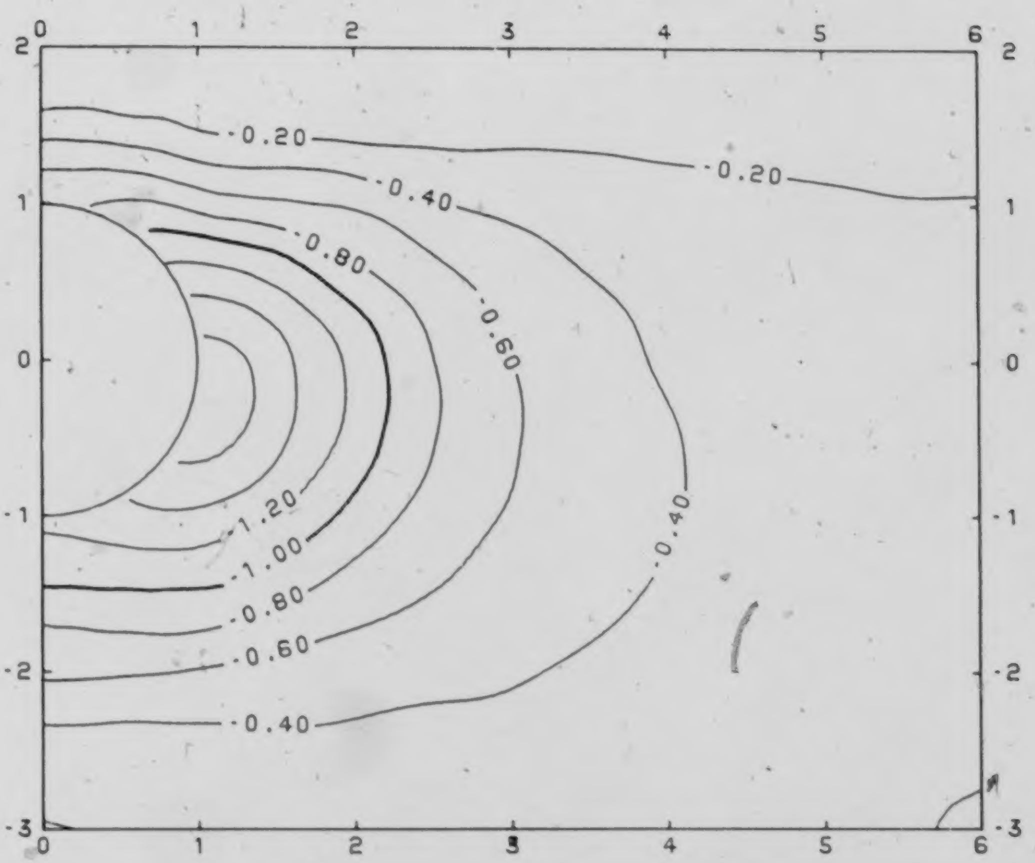

Figure 5.86 Sealed Tunnel in OCC, û in (ξ,η), T=0.01

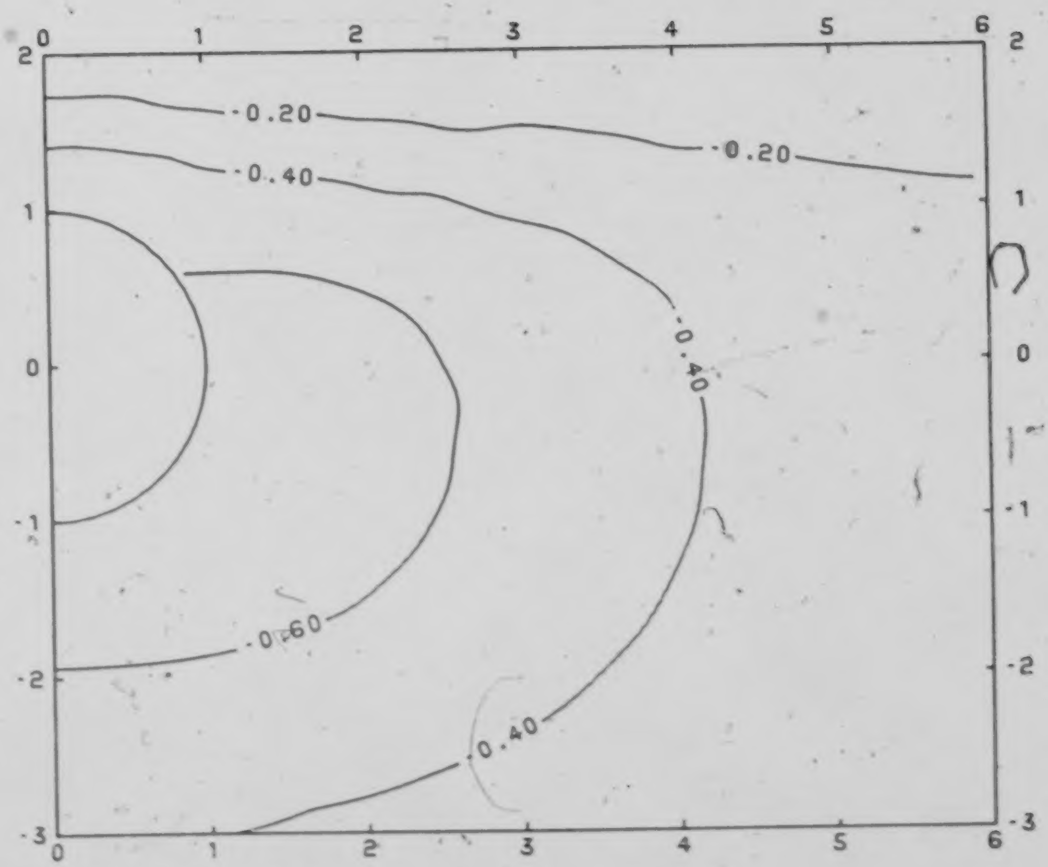

Figure 5.87 Sealed Tunnel in OCC, $\hat{u}$ in (ξ,η), T=0.1

and, with given a, c_v, H_c, D, K_0, γ, x, y, ESR and, time t after construction, can be estimated approximately using these diagrams. The (x,y) coordinates must be transformed into non-dimensional (ξ,η) (Figure 5.2) plane using the transformation given in Equations 5.10 and 5.11. Then the normalized pore pressures obtained from the diagrams can be transformed back to the actual pore pressures by multiplying by $\gamma H_c(1-0.6K_0)(1+10a)$ for normally consolidated clay. The multiplication factor for tunnels constructed in over-consolidated clay is $\gamma H_c(K_0-0.5)(4/30-a)$. Qualitative three-dimensional figures of pore pressure around unsupported and supported tunnels in normally consolidated clay, corresponding to the average parameters are shown in Figures 5.88 and 5.89. The 3-D image for pore pressure behaviour around an unsupported tunnel constructed in an over-consolidated clay with average parameters is shown in Figure 5.90. Since these 3-D figures are easier to visualize, they can be used to get a better qualitative understanding of the nature of pore pressure distribution around tunnels.

5.7 SUMMARY AND CONCLUSIONS

A parametric study was undertaken to examine the pore pressure variation behaviour around tunnels by varying different parameters within practical ranges. A summary of the parametric analysis is given in Table 5.2. A general non-dimensionalization and normalization procedures were postulated to develop approximate but concise design

Table 5.2 Summary of Parametric Analysis on Pore Pressure

IN NORMALLY CONSOLIDATED CLAY

UNSUPPORTED TUNNELS	
RANGE OF THE PARAMETER VARRIED	NORMALIZING FACTOR
s_u/σ_v; 0.4 to 0.7	1
E_i/σ_v; 200 to 800	1
Henkel's coefficient a; 0.12 to 0.48	$1/(1+10a)$
K_0; 0.5 to 0.8	$1/\overline{(1-0.6K_0)}$
H/D; 1.25 to 2.75	see section 5.3.2
D m, H m and γ kN/m^3; 3 to 9, 3.75 to 24.75 and 5 to 10	$1/\gamma H_c$
D m, H m, c_v m^2/MONTH and t; 3 to 9, 3.75 to 24.75, 0.1 to 10.0	$c_v t/H^2$

SUPPORTED TUNNELS; ESR VARIED FROM 10^{-1} to 10^{-3}	
RANGE OF THE PARAMETER VARIED	PORE PRESSURE DISTRIBUTION APPROXIMATELY SAME FOR A GIVEN ESR
E_i/σ_v varied from 200 to 800; E_l, A_l and I_l varied to maintain a given ESR	
K_0; 0.5 to 0.8	
D; 3 m to 9 m	
t/R; 0.03 to 0.07	

UNSUPPORTED TUNNELS IN OVERCONSOLIDATED CLAY	
RANGE OF PARAMETER VARIED	NORMALIZING FACTOR
$s_u/\sigma_v^{\frac{1}{2}}$ kPa$^{\frac{1}{2}}$; 10 to 100	1
$E_i/\sigma_v^{\frac{1}{2}}$ GPa$^{\frac{1}{2}}$; 6 to 136	1
Henkel's coefficient a; -0.60 to -0.20	$1/(4/30-a)$
K_0; 1.25 to 1.75	$1/(K_0-0.5)$
H/D; 1 to 3	see section 5.3.2

diagrams or a classification system for estimating the pore pressure behaviour around tunnels. These postulates were justified by the results of the parametric study.

In a normally consolidated clay, the pore pressures generated around a tunnel excavation is not very sensitive to the s_u/σ_{1c} value when it is greater than 0.4. In an overconsolidated clay the strength values are higher and thus, the same insensitivity was observed. In both normally and overconsolidated clays the initial pore pressures are insensitive to the changes in E_i/σ_{1c}^n ratio. The pore pressures are dependent to a greater extent on the pore pressure coefficient a, and to a lesser extent on K_0. With increasing a, pore pressure tends to increase, whereas with increasing K_0, it tends to decrease. The proposed coordinate non-dimensionalization procedure was successful in helping develop a concise set of pore pressure diagrams representing many different tunnel geometries. The pore pressure dissipation rate was found to be nearly independent of the tunnel diameter, but dependent on the depth of cover H. The time factor $T=c_v t/H^2$, was found to be capable of describing the pore pressure dissipation behaviour in both sealed and unsealed tunnels.

A non-dimensional quantity called Effective Stiffness Ratio (ESR) was postulated to account for tunnel support system in the study of pore pressure behaviour around tunnels. The general effect of increasing ESR is to reduce the magnitude of the initial pore pressures and to shift the

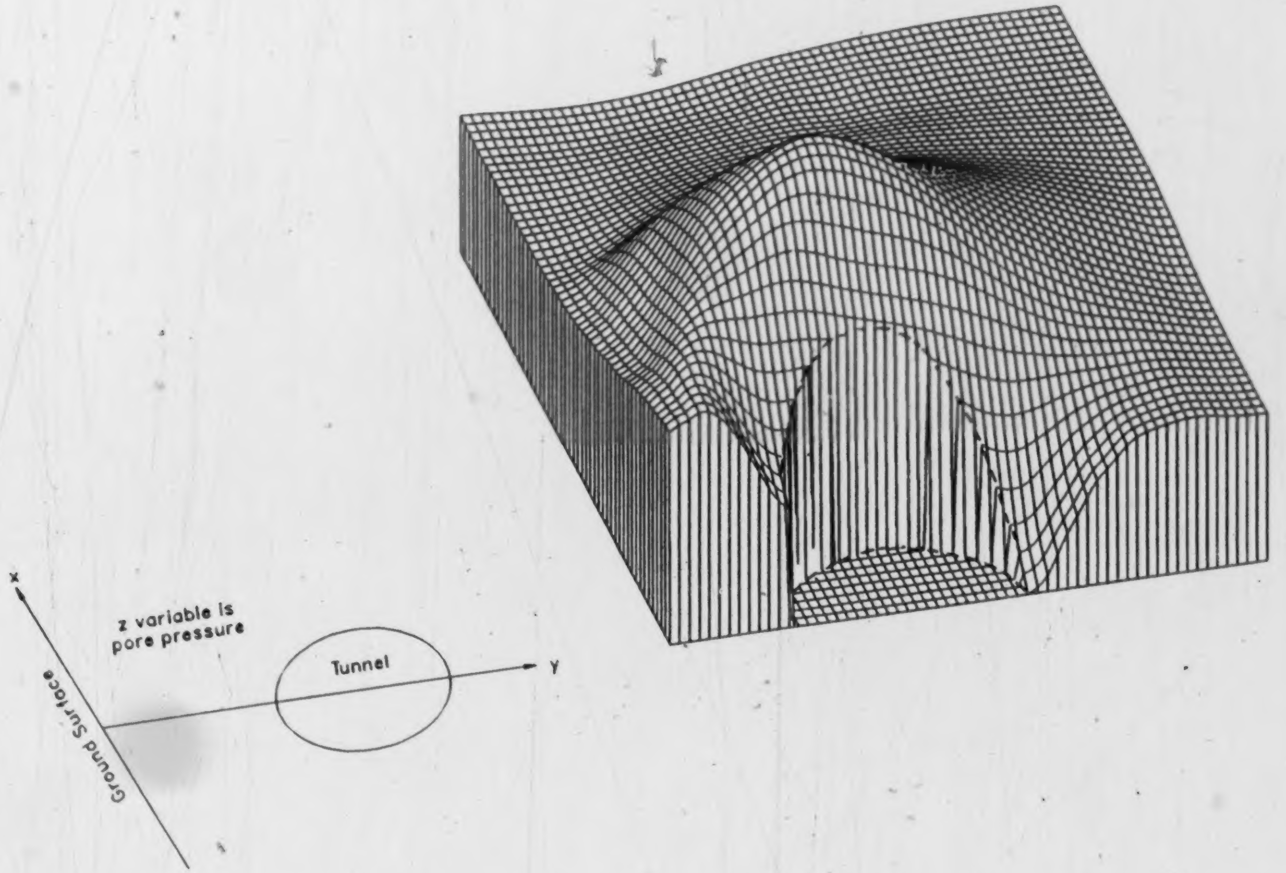

Figure 5.88 3-D Image of Pore Pressure around an Unsupported Tunnel in NC Clay

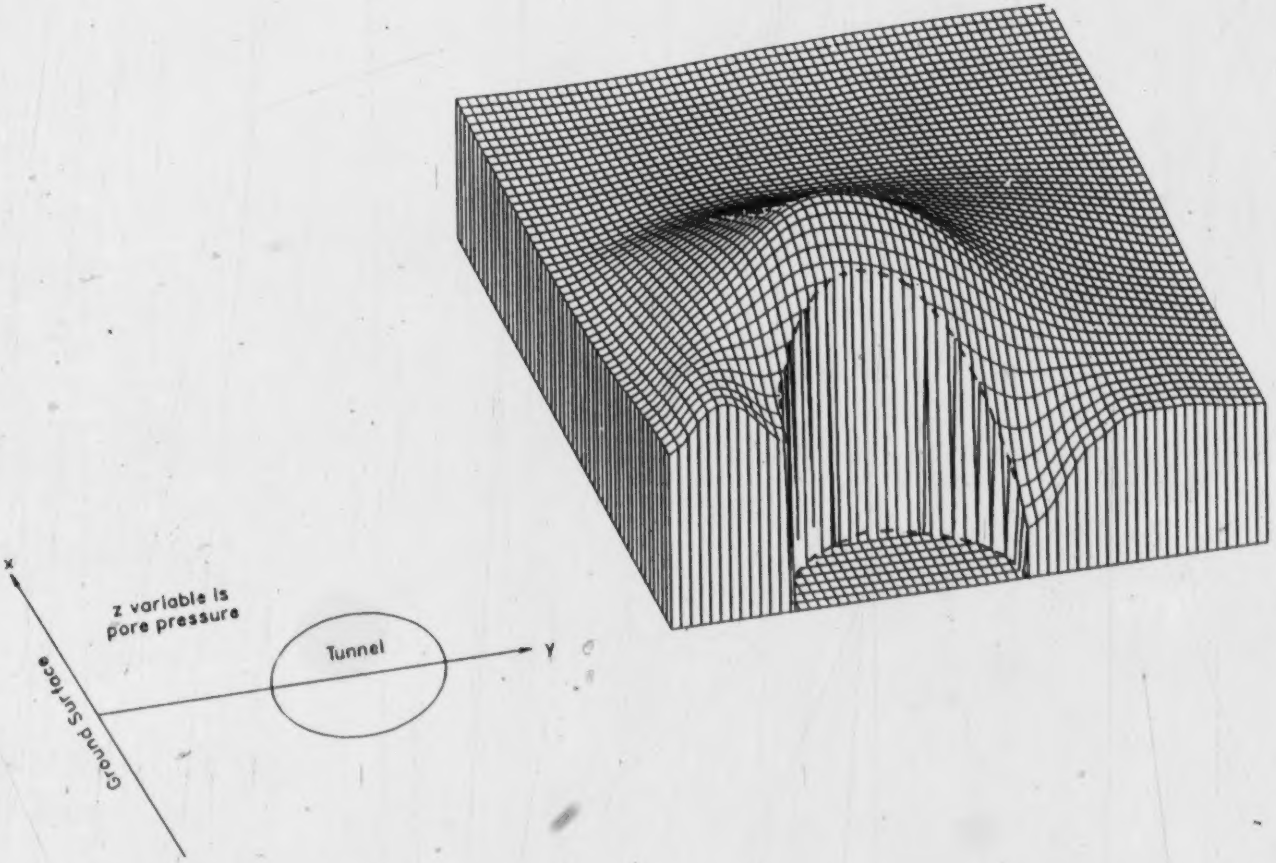
x
z variable is
pore pressure
Tunnel
Y
Ground Surface

Figure 5.89 3-D Image of Pore Pressure around a Supported Tunnel in NC Clay

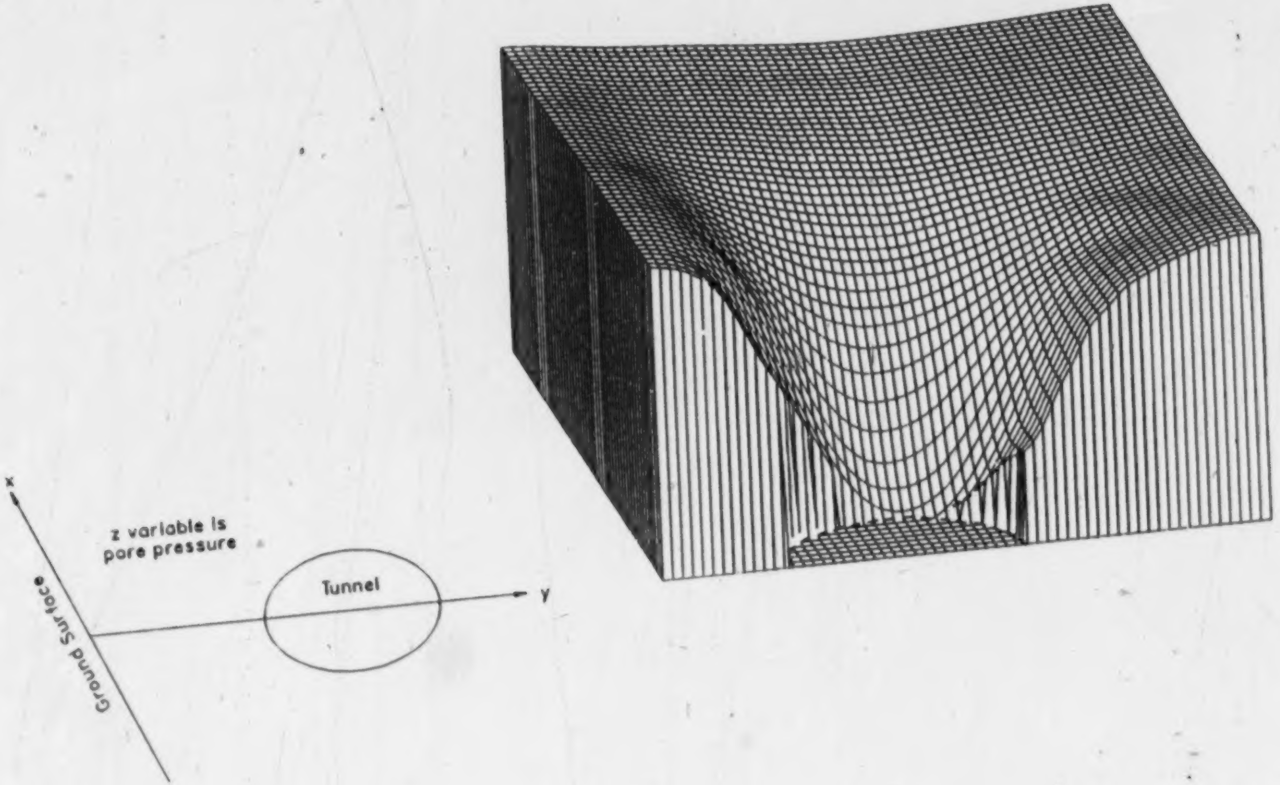

Figure 5.90 3-D Image of Pore Pressure around an Unsupported Tunnel in OC Clay

peak (point of maximum pore pressure) towards the center of the tunnel in a normally consolidated clay. For values of ESR greater than 0.1, the pore pressure generation around the tunnel was found to be marginal.

The normalized and non-dimensionalized pore pressure diagrams for both sealed and unsealed tunnels at T values, 0, 0.001, 0.01 and 0.1 are provided for ESR 0, 10^{-3}, 10^{-2} and 10^{-1} which (i.e. ESR) belong to their practical range. This non-dimensionalization and normalization procedure can be considered as numerical semi-empiricism, and it is a practical alternative when the closed form solutions are not possible. The pore pressure diagrams in overconsolidated clays are for unsupported tunnels only. Note that ESR=0 corresponds to an unsupported tunnel. These diagrams provide a very simple and straightforward tool for estimating the approximate pore pressure generation and dissipation behaviour around shallow tunnels excavated in both normally and overconsolidated clays. Knowing the OCR and with given a, c_v, H_c, D, K_0, γ, x, y, ESR and, time t after construction, the pore pressure u(x,y,t) can be easily and quickly estimated for both sealed and unsealed tunnels from the given pore pressure diagrams.

It can be clearly seen that the typical pore water pressures developed around a significant region of an unsupported shallow tunnel driven in a normally consolidated clay is positive, whereas in overconsolidated clay it is negative. This conclusion has an important implication for the stability of tunnels. The stiffer tunnel supports reduce the pore pressure generation significantly.

Finally, and most important, this study aids in understanding with greater confidence, the pore pressure behaviour around shallow tunnels constructed in normally and overconsolidated clays. The pore pressure diagrams developed can be used as a guideline in planning field instrumentation. These diagrams can also be used in preliminary designs to decide which characteristics need to be explored and established in greater detail. For preliminary design, these diagrams can be employed to make estimates of the change in factors of safety, and surface settlements due to pore pressure dissipation.

6. STABILITY EVALUATION OF UNSUPPORTED SHALLOW TUNNELS IN OVERCONSOLIDATED CLAYS USING A NEW APPROACH

6.1 TUNNEL STABILITY

In tunnel construction there are various ways of providing immediate internal support. For example, the internal support can be in the form of structural members or in the form of fluid pressure. However, whether any form of immediate internal support should be provided at all is a very important cost consideration. In addition, such a decision can have a major influence on the rate of construction. In many cases, the most important factors involved in making the decision to provide any form of immediate internal support, are the required safety and the tolerable ground displacement. A major factor that governs the safety is the unsupported stability of the excavated tunnel. The lower and upper bound closed form solutions have been used to evaluate tunnel stability.

In using the upper bound theorem, various failure mechanisms have been employed. Some of the more widely used failure mechanisms are shown in Figures 6.1 and 6.2.

Mechanism A (Figure 6.2) is the simplest and is referred to as "roof" mechanism, and B (Figure 6.1) is referred to as "roof and sides" mechanism. Both mechanisms have been deduced from model tunnel tests at Cambridge University (Cairncross, 1973). To define each mechanism only one variable parameter (x or θ) is necessary, whereas for

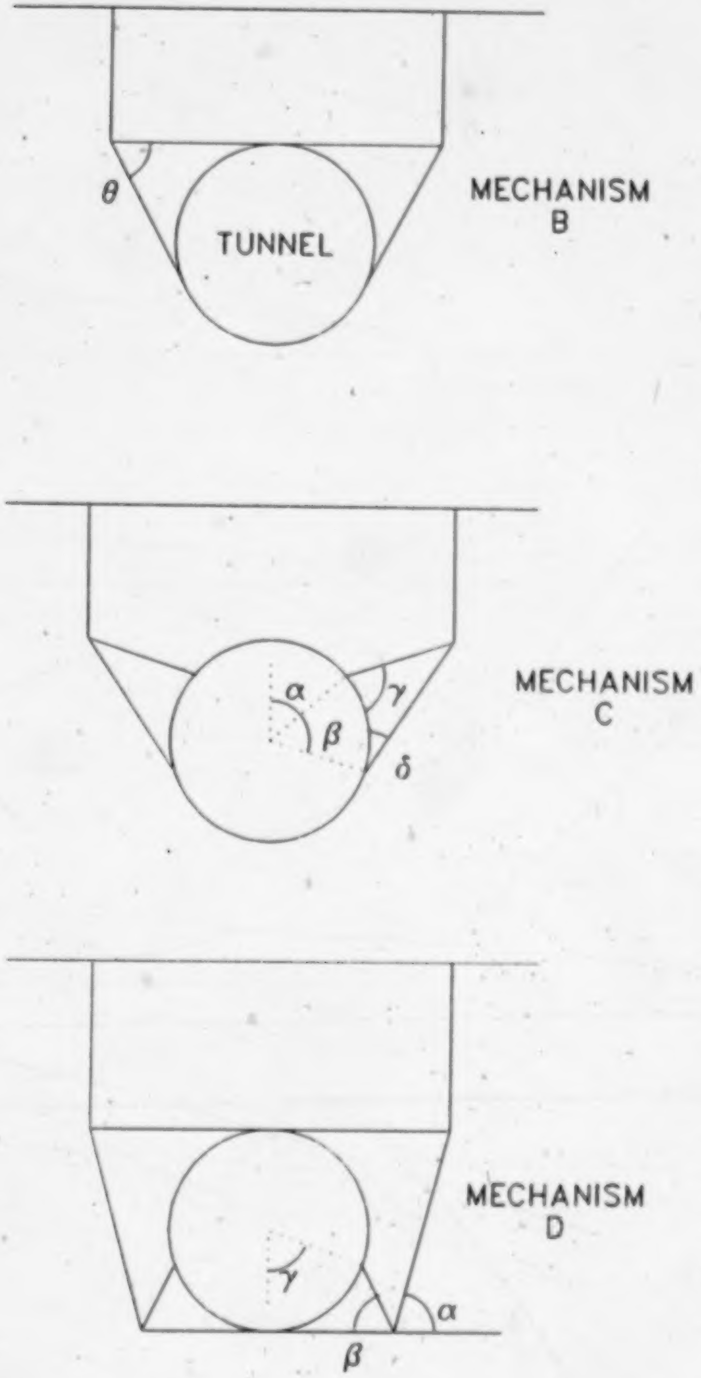
θ
TUNNEL
MECHANISM
B
α
γ
β
δ
MECHANISM
C
MECHANISM
D
γ
α
β

Figure 6.1 Some Failure Mechanisms of Shallow Tunnels

mechanism C (Figure 6.1) four variable parameters are necessary. It can be clearly seen that the mechanisms A and B are subsets of mechanism C. Mechanism D (Figure 6.1) referred to as "roof sides and bottom" (Davis et al., 1980) requires three variables for its definition.

In most cases, the stability of the tunnel is analysed only for the initial undrained situation. This is the usual practice for both upper and lower bound solutions. The implication is that once the tunnel is stable under the initial condition, it will be stable until some form of supports, whether primary or secondary, are installed.

The preceding is common design practice in clay materials. The $\phi=0$ analysis is used to investigate the stability of clay foundations. It is assumed that the pore pressures dissipate and the foundation becomes more stable. Therefore, the most critical condition is assumed to be the condition of no drainage. However, with overconsolidated clays this assumption may not be valid. In most cases, for both upper and lower bound solutions, the soil is idealized as a perfectly elastic plastic material with constant strength and moduli values. In soils however, in addition to nonhomogeneity, the strength is dependent on effective stresses. When the pore pressures dissipate, the effective stresses change, and so does the soil strength. The stability analysis of slopes in geotechnical engineering practice accommodates this important soil behaviour by making an indirect arbitrary assumption on the stress distribution.

6.2 INADEQUACY IN CURRENT PRACTICE

Section 5.2 discussed the inadequacy of the closed form solutions for the stress and deformation analysis around tunnels. These same arguments are valid for the closed form solutions obtained using lower and upper bound theorems. As stated earlier, in the upper bound solution for the initial undrained conditions ($\phi=0$), usually the strength is assumed to be constant with depth. As discussed in section 5.2, this assumption is not necessarily valid either with normally consolidated clays or with overconsolidated clays. Generally, in both cases the strength increases with depth.

Other inaccuracies can be attributed to the fundamental assumption involved in the design philosophy. This assumption implies that the stability of the clay structure either increases or remains the same with time, which is not accurate for overconsolidated clays. From the analyses in sections 5.5.1 and 5.5.3 it was found that around a tunnel constructed in a normally consolidated clay, there are substantial regions of positive pore pressure, whereas in an overconsolidated clay negative pore pressures constitute a significant region. In a tunnel constructed in a normally consolidated clay, these positive pore water pressures dissipate over time, and therefore, in general, stability increases. However, in a tunnel driven in an overconsolidated clay, with time, the pore pressures increase and the strength deteriorates, thus decreasing the stability. This is a very important phenomenon, and under these conditions the undrained (initial) stability may be of less practical importance. The undrained stability may serve as a starting point for an in depth analysis of long term stability. This phenomenon is one of the most important factors that governs the stand up time because the stand up time is directly related to the delayed stability of the unsupported tunnel. In the next section, a new design procedure is proposed to overcome these limitations in current design practice.

6.3 NEW APPROACH FOR STABILITY OF SOIL STRUCTURES AND APPLICATION FOR TUNNELS

As pointed out in the previous section, unlike in normally consolidated clays, the stability of a tunnel in an overconsolidated clay deteriorates with time. In some cases, current design practice does not take this factor into account. In this section an attempt will be made to develop a new design procedure that overcomes this problem and the other limitations of the methods of stability analysis (mentioned earlier) used in geotechnical engineering.

The following paragraphs describe the basics of the proposed method of stability analysis which will be explained using the applications to tunnel stability. The basic theory is a combination of finite element models and the concepts of limit equilibrium method applied in soil mechanics. This approach overcomes the major limitations (mentioned in the previous section) in current design practice. This new procedure is applicable in general to geotechnical engineering stability problems. However, only the stability analysis of shallow tunnels in overconsolidated clays were considered in this thesis.

For the stability of an earth structure, the factor of safety F, will be defined as (Figure 6.3):

$$\tau dl = \frac{c'dl}{F} + \frac{\tan\phi'(\sigma - u)dl}{F} \qquad [6.1]$$

Making the usual assumption of slope stability that the factor of safety is the same everywhere, and by integrating the Equation 6.1, it can be easily shown that:

$$F = \frac{\int_0^L c'dl + \int_0^L \tan\phi'(\sigma - u)dl}{\int_0^L \tau dl} \qquad [6.2]$$

The next step of this analysis is to choose a failure mechanism for the limit equilibrium solution. By closely examining the failure modes in the model test results of Cairncross (1973) and Mair (1979), the author came to the conclusion that mechanism A (Figure 6.2) although not a perfect idealization, is an important starting point for applying the new approach to investigate the pore pressure effects on tunnel stability. Figure 6.4 shows a typical failure mode of the six models tested to failure by Mair (1979). All these models were within an H/D ratio of 1 and 3. These H/D ratios fall within the range of shallow tunnels (defined in section 5.5).

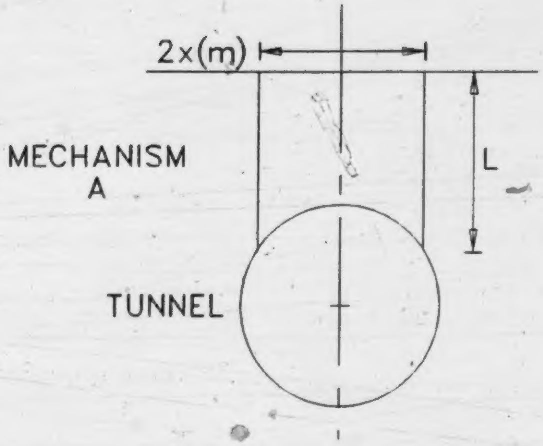
2x(m)
MECHANISM
A
L
TUNNEL

Figure 6.2 A Simple Failure Mechanism for Shallow Tunnels

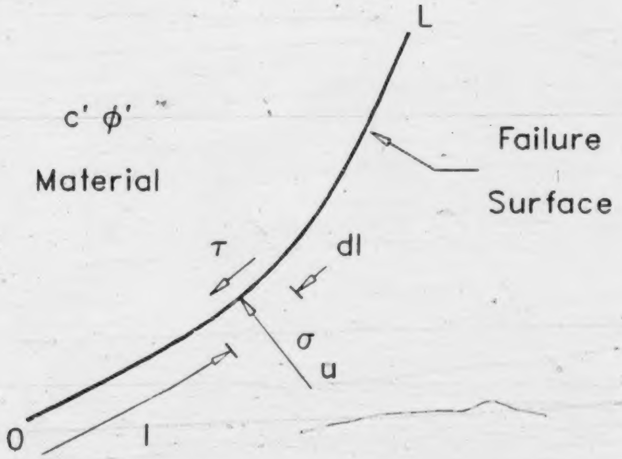
L
c' ϕ'
Material
Failure
Surface
τ
dl
σ
u
O
l

Figure 6.3 Definition of Factor of Safety

As stated earlier, in usual slope stability analyses in geotechnical engineering practice, it is not possible to compute factor of safety without making a direct or indirect assumption about the stress distribution. This assumption provides sufficient equations to evaluate the factor of safety. By using different arbitrary assumptions, many methods of slope stability analysis have been derived. Further, it allows the more realistic drained parameters to be used in the stability analysis. However, if the stress field is known to an acceptable degree of accuracy, the need to make such arbitrary assumptions does not arise.

In our analysis, more realistic finite element models (Chapter 3) were used to determine the stress distribution as well as the pore pressure distribution. These stress and pore pressure distributions together with the drained soil properties were used in Equation 6.2 to estimate the factor of safety. The finite element model eliminates the problem of inaccurate stress estimates and overcomes other limitations (section 5.2) in closed form solutions stated in section 6.2. As mentioned in sections 5.5.3.1 and 5.5.3.2, the strength and modulus distribution are considered parabolic with depth, and the K_0 stress field is taken into account. The effects of K_0 and the variations of in situ stresses with depth were also considered in the numerical simulation of the tunnel excavation. Consequently, the proposed method of analysis uses a more realistic stress distribution. Therefore, the results can be expected to be more reliable. This needs to be confirmed by field applications.

Using the new method of stability analysis described above, a parametric study of the stability of shallow tunnels in overconsolidated clays is carried out in the sections to follow.

6.4 FACTORS INFLUENCING TUNNEL STABILITY

Before starting a parametric study to investigate the stability of tunnels constructed in overconsolidated clay, it is important to identify the factors that may have significant effects on tunnel stability. Making use of the fundamental principles of soil behaviour and the results of the analysis of Chapter 5, it was assumed that the stability of a tunnel at a given time is dependent on the geometry, the total stresses, the pore water pressures and the strength parameters. On a more quantitative basis, the parameters H_c, D, (Figure 5.2a) K_0, γ, c', ϕ, c_v and t can be expected to have a significant influence on tunnel stability. Due to the large number of parameters involved, as was done throughout Chapter 5, and for the reasons discussed in section 5.3, it is more logical to present the results of the parametric study in a concise form using non-dimensional quantities. Taking into consideration the failure mechanism proposed in section 6.2, the following non-dimensionalization procedure was adopted. As seen in Chapter 5, c_vt/H^2 appropriately gives the state of pore pressure distribution at a given time t. From the discussions and results of Chapter 5, it is reasonable to consider H/D ratio to have an influence on the stability of the tunnel. The quantity γH_c is a measure of the stress relief that takes place during the excavation of the tunnel for a given K_0. Therefore, $c'/(\gamma H_c)$ can be considered to have a significant influence on stability. In overconsolidated clays, the cohesion is relatively large. Keeping in mind that the lower the cohesion, the less stable is the tunnel, it is preferable that the lower range of cohesion have a more sensitive scale on the non-dimensionalized plane than the upper range. To satisfy this condition, $\gamma' H_c/c'$ was chosen to be a non-dimensional quantity for the study of tunnel stability. An additional non-dimensional strength parameter, ϕ', was also chosen. In the next section, the new method of stability analysis proposed in the previous section and the concepts discussed in this section are applied to tunnels constructed in overconsolidated clays.

6.5 TIME-STABILITY-STRENGTH (TSS) CURVES FOR ESTIMATING STABILITY VARIATION DUE TO PORE PRESSURE DISSIPATION

The new approach proposed for stability analysis in section 6.3 and the non-dimensional quantities developed in section 6.4 for tunnel stability are applied in a parametric analysis. In this study the influence of pore pressure dissipation on unsupported shallow tunnels constructed in overconsolidated clays is examined. An attempt is made to use the results of this study to develop concise, but approximate design diagrams or a form of classification system. These diagrams will be used to understand and quantify the behaviour of delayed stability in unsupported tunnels constructed in overconsolidated clays.

The stress and pore pressure values needed to compute factors of safety from Equation 6.2 were obtained using the finite element models selected in Chapter 3. The stability computations were carried out as outlined in section 6.3. A typical shallow tunnel situation was considered, viz., $H/D=1.8$, $s_u/\sigma^{\frac{1}{2}}=70$ kPa$^{\frac{1}{2}}$, $E_i/\sigma^{\frac{1}{2}}=310$ kPa$^{\frac{1}{2}}$, and $K_0=0.8$. Using the finite element techniques previously noted, the stress and pore water pressure distribution were obtained for each T = 0, 0.001, 0.01 and 0.1. For a given T value and for different mechanisms defined by the distance x (m) (Figure 6.2), the stress and pore water pressure distribution on the failure planes were computed. The typical practical ranges for c' and ϕ' in overconsolidated clays are, 5 to 25 kPa and 5^0 to 20^0 (Table 5.1), respectively. A value for c', 15 kPa and a value for ϕ', 10^0 were chosen within this limit, and using the stress and pore water pressure distribution computed at T=0 for different failure planes (different x values), the factors of safety were computed. The factors of safety for x=0.45 and 2.00 were found to be 2.19 and 1.23, respectively. In calculating the factors of safety, the definition given in section 6.3.1 was used. To integrate the appropriate terms in the expression for factor of safety, cubic spline functions were used. In computing the pore water pressure integral, the spline functions were fitted to the dissipated pore pressure (Figure 6.5). The integral of the current pore pressure can be obtained by subtracting the integral of the initial pore pressure as follows:

$$\int_0^L u(t)dl = \int_0^L u(0)dl - \int_0^L \Delta u(t)dl \qquad [6.3]$$

where, $\Delta u(t)$ is the dissipated pore pressure at time t. Using this procedure, for T = 0, instead of calculating the factor of safety, the ϕ' necessary for incipient failure for a given c' and a given failure plane (x) was computed. Then the c' and ϕ' values were changed within their practical ranges and the correlation between the two quantities was found. Similar correlations of c' and ϕ' obtained for different failure planes (x=0.45, 0.85, 1.40, 1.80 and 2.00) are drawn on a $\gamma L/c'$ versus ϕ' plot and is shown in Figure 6.6, where L (Figure 6.2) is the length of the failure plane. To obtain the critical solution or the solution closest to the real solution in this spanning set, the envelope of all the curves must be found. In this case it happened to be the curve corresponding to x = 2.00. It is also worth noting that as ϕ' tends to zero, $H_c\gamma/c'$ reaches a value of 5.5.

A similar analysis was undertaken for each T = 0.001, 0.01 and 0.1. For each case, the critical solution was found from the envelope of a spanning set, and these envelopes are plotted in Figure 6.7. This Figure shows a substantial

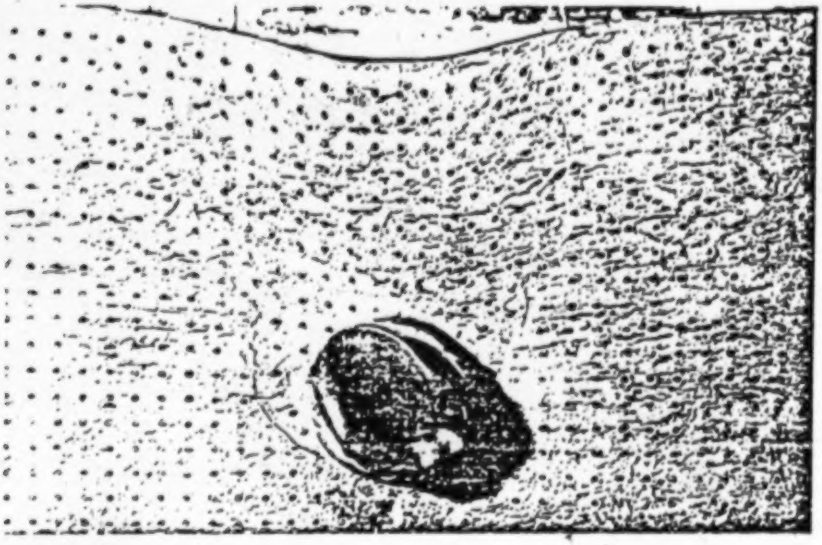

Figure 6.4 A Typical Failure Mode in a Model Test

(after Mair, 1979)

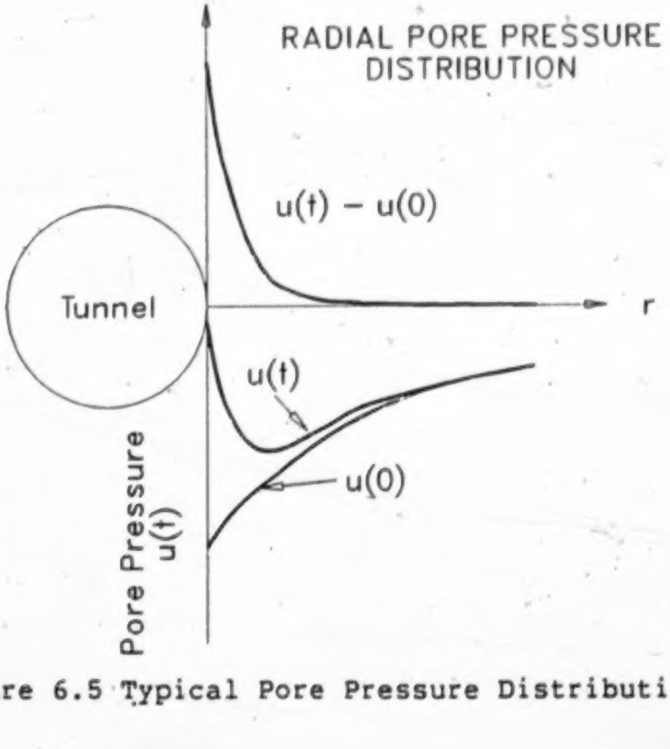

Figure 6.5 Typical Pore Pressure Distributions

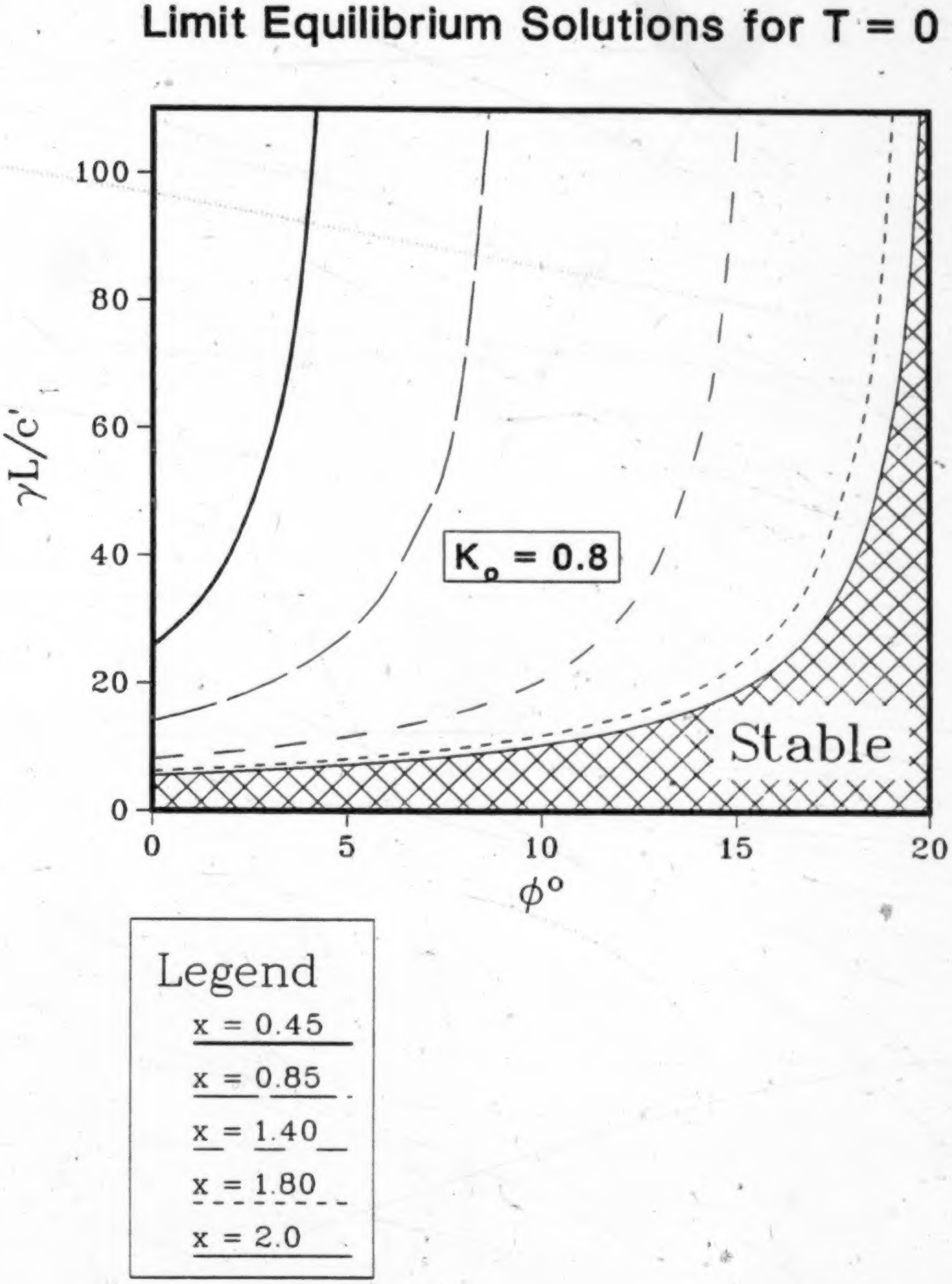

Figure 6.6 Limit Equilibrium Solutions for Different Failure Planes

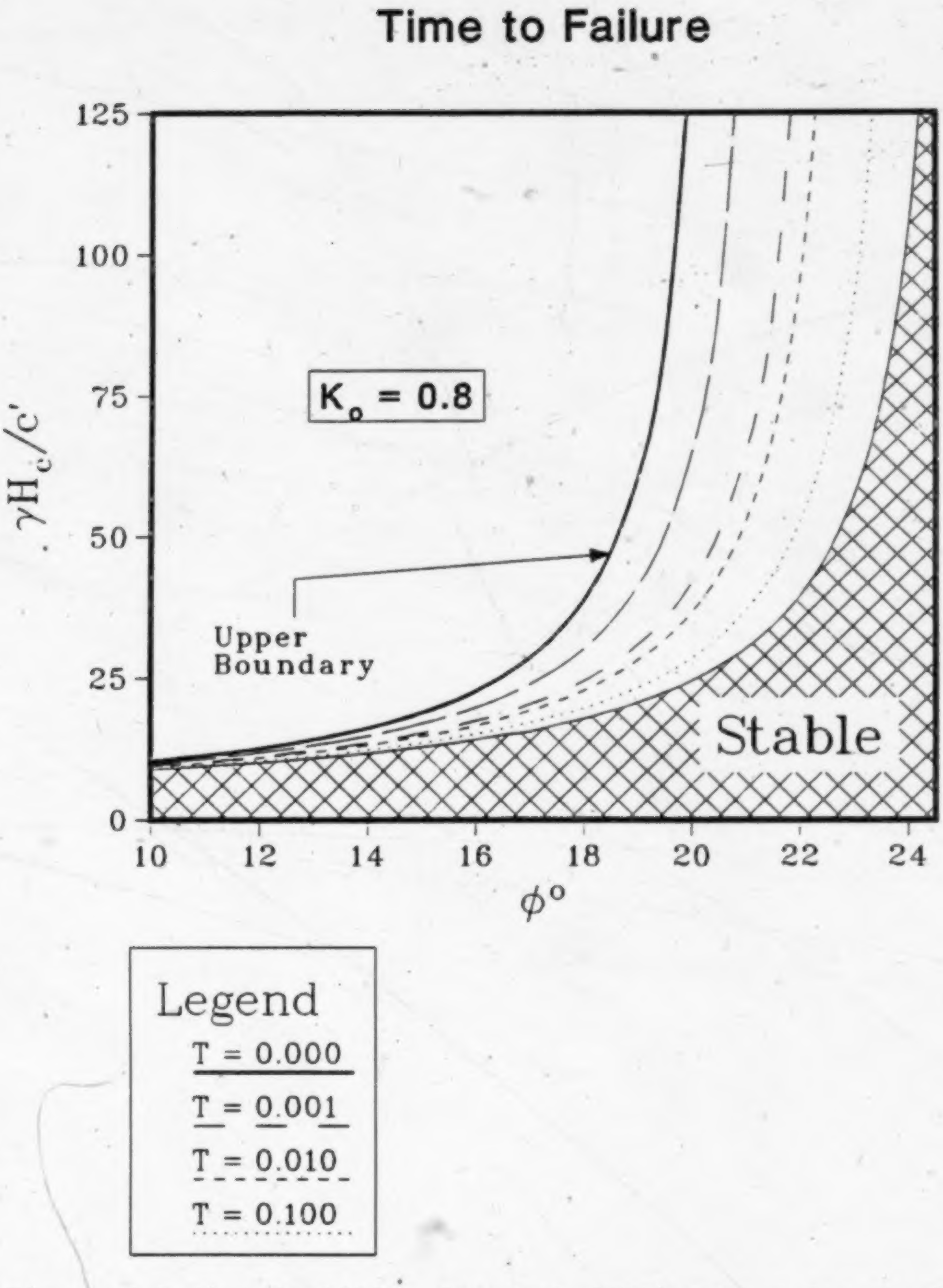

Figure 6.7 Time-Stability-Strength (TSS) Curves for K_0 =0.8, H/D=1.8

difference among the curves, $T = 0, 0.001, 0.01$ and 0.1 indicating the deterioration of stability. In other words, the initial undrained stability that is considered (in usual practice) to remain unaltered may be more of a theoretical and mathematical state that lasts only an instant. It can be clearly seen that the stability decreases with time. For a tunnel of 3 m diameter and H/D ratio 1, constructed in a soil having a coefficient of consolidation 9.3 m^2/MONTH; $T = 0.001$ translates to be nearly half an hour. The reduction in $H_c\gamma/c'$ corresponding to $T=0$ and $T=0.001$ is 65% for $\phi'=14.5^0$. This proves a very important fact. The initial undrained stability of a tunnel in overconsolidated clay can be of little or no practical value. That is, under such circumstances the pore water pressures around the tunnel dissipate rapidly and substantially, softening the soil around the tunnel considerably below the initial undrained strength. Similarly, with time, the negative pore water pressures dissipate further and the stability decreases accordingly. These results are shown on $(\gamma H_c/c', \phi')$ plot in Figure 6.7. This diagram clearly shows the influence of pore water pressure dissipation on the stability of tunnels constructed in overconsolidated clays.

Figure 6.7 also shows, for all constant T curves, as ϕ' increases, $H_c\gamma/c'$ increases more rapidly. That is, the rate of increase in stability increases with ϕ'. With increasing ϕ', the gap between any two adjoining curves also increases. That is, as ϕ' increases, both the stability and the influence of pore water pressure on stability increase. This behaviour is compatible with the Mohr Coulomb criterion and the effective stress principle. This plot also shows that the factor of safety decreases with time, but the rate of decrease is higher in the initial stages. The states that lie in the shaded area are stable (factor of safety >1) at all times whereas, the states that lie above the upper boundary are unstable and need immediate support. From Figure 6.7, it is easy to predict the time at which the tunnel becomes unstable. Therefore, this chart provides an estimate of the longest time the tunnel can stand without having any form of internal support. That is, supports must be provided before the time indicated by the chart is elapsed.

It was expected that K_0 would have some influence on stability. To investigate this influence, two other K_0 values (1.2 and 1.5) in the overconsolidated range were chosen. By following the same procedure that was used to obtain Figure 6.7, Figures 6.8 and 6.9 were obtained for $K_0 = 1.2$ and 1.5, respectively. Figures 6.7 to 6.9 will be referred to as TSS (Time-Stability-Strength) curves in this thesis. These figures clearly show how the stability of a tunnel constructed in overconsolidated clay increases with K_0. For example, for a stable tunnel, for $\phi'=11^0$, at T=0, the $H_c\gamma/c'$ value for $K_0=1.5$ must be at most 100, whereas for $K_0=0.8$, $H_c\gamma/c'$ should not exceed 10. As one would expect, for all three cases, as ϕ' tends to zero, $H_c\gamma/c'$ reaches a

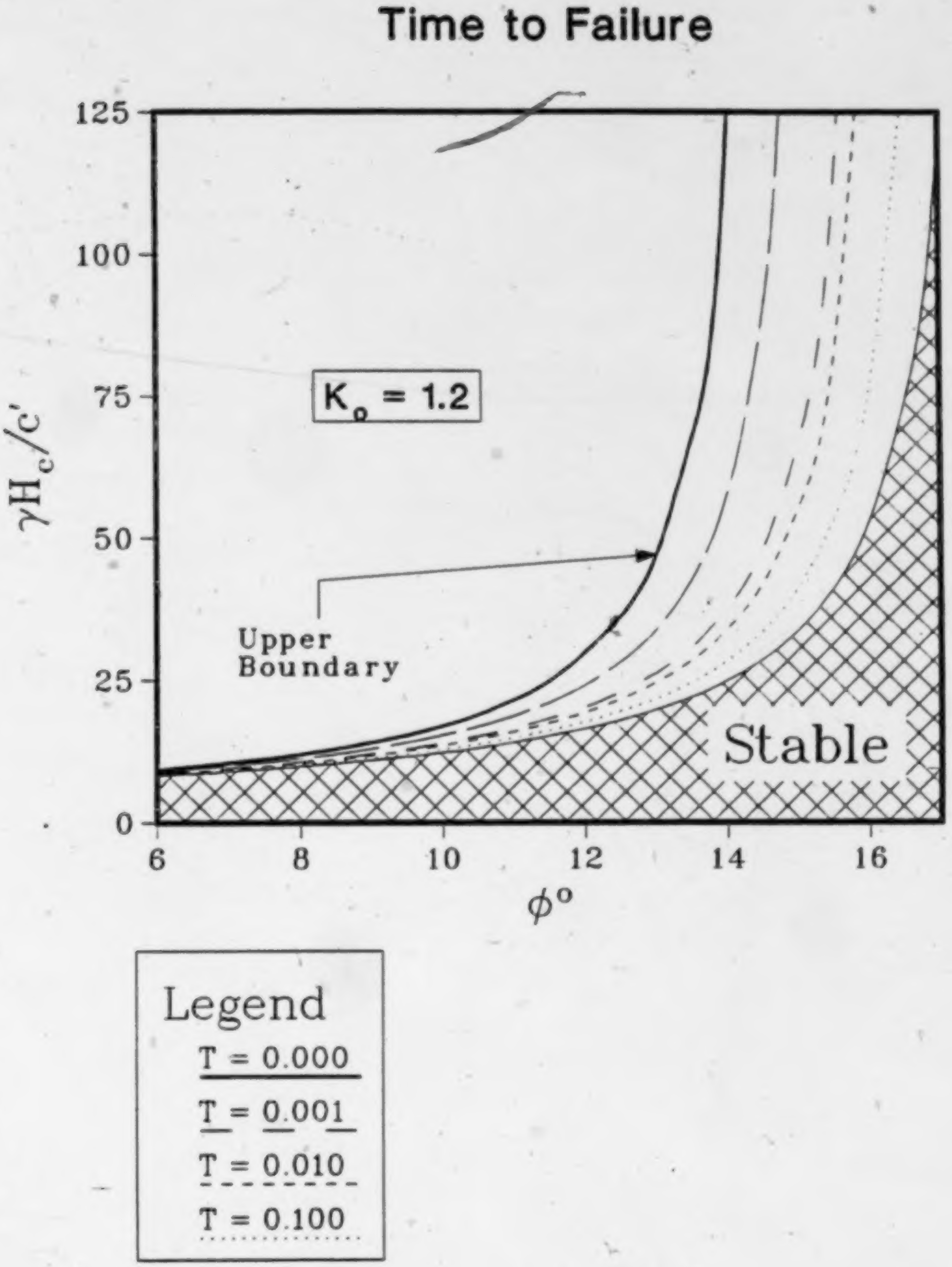

Figure 6.8 Time-Stability-Strength (TSS) Curves for K_0=1.2, H/D=1.8

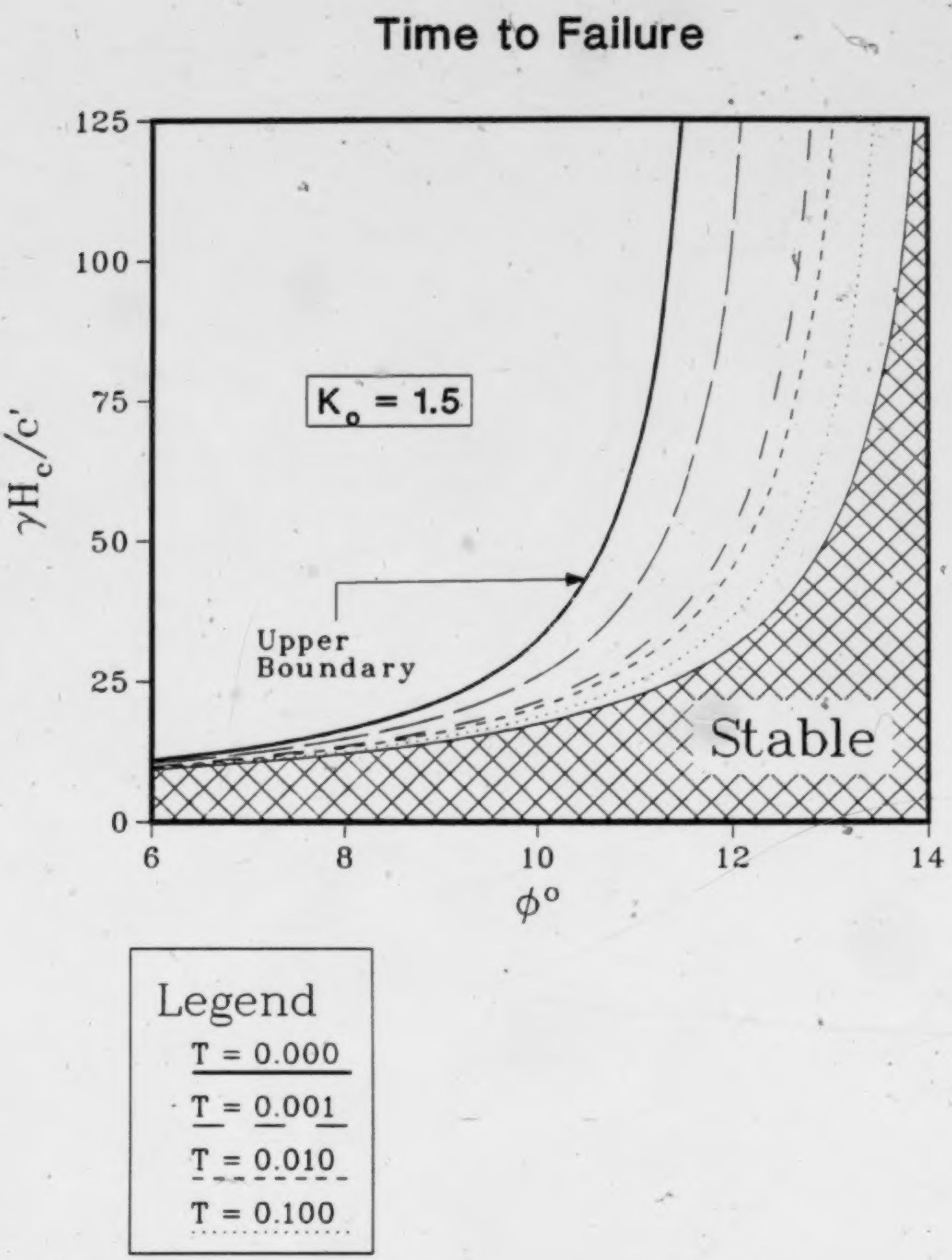

Figure 6.9 Time-Stability-Strength (TSS) Curves for K_0=1.5, H/D=1.8

value of 5.5. This result is especially interesting because Broms et al. (1967) found similar results in both experimental and field data for the tunnel face. They found that if $H_c\gamma/s_u$ lies between 6 and 8, the tunnel face is stable. Note also that for the practical ranges of the parameters under consideration (Table 5.1), $\gamma H_c/c'$ lies between 3 and 125. This range was used when developing the TSS curves.

For a given tunnel geometry and given soil properties (c',ϕ',c_v), the TSS diagrams can be used as a guideline to estimate the approximate time (an upper limit) it takes for the tunnel to become unstable after construction.

6.6 SUMMARY AND CONCLUSIONS

The present study showed that the assumption that the critical conditions occur under the initial undrained state is not valid for tunnels constructed in overconsolidated clays. The closed form upper bound solutions assume that the material is homogeneous. The limit equilibrium approach used in stability analysis of slopes make a direct or indirect arbitrary assumption concerning the stress distribution. These assumptions impose limitations on the currently available methods of stability analysis. To overcome these limitations, a new method of stability analysis that combines the limit equilibrium theory and finite element models was proposed. The finite element model solves the problem of determining the stress field accurately. It also computes the pore pressure dissipation behaviour to a reasonably accurate degree. These finite element models are described in detail in Chapter 3. The known pore pressure values allow the generally more accurate drained parameters to be used in the limit equilibrium solution to evaluate stability. Using this procedure, the change in stability with time may be studied with more confidence. Although this approach is applicable to the stability analysis of any geotechnical engineering structure, the method was applied in a parametric study to investigate the change in stability due to pore pressure dissipation of shallow tunnels constructed in overconsolidated clays. $H_c\gamma/c'$, ϕ' and the time factor $T=c_vt/H^2$ were used to present the results of the parametric analysis in a concise form. Curves that relate these quantities and the stability of the tunnel were developed from the results of the study. To study stability, three sets of such Time-Stability-Strength (TSS) curves were obtained for three different K_0 values.

The analysis showed that the initial undrained stability condition of an unsupported tunnel constructed in overconsolidated clay is a mathematical state that lasts only an infinitesimally small time. Stability was found to decrease with time. Therefore, the often performed undrained analysis may be considered as a starting point. The above analysis also showed that under certain circumstances, the initial undrained stability has little practical significance. The pore water pressure dissipation plays a major role in determining the variation of global stability of an unsupported tunnel with time. This is one of the most important factors that determine the stand-up time of a tunnel. If the soil properties and the geometry are known, the TSS diagrams may be used to estimate the elapsed time (after construction) before some form of supports are necessary. These diagrams can be used as a guideline to estimate how long the immediate supports can be delayed before the tunnel becomes unstable. Figures 6.7 to 6.9 show that with time, the factor of safety decreases and the rate of decrease is greater in the initial stages than in the final stages. The differences in the three sets of curves (Figures 6.7 to 6.9) show that the tunnel stability generally increases with increasing K_0. The analysis shows that $H_c\gamma/c'$ reaches a value of 5.5 as ϕ' tends to zero for all three K_0 values.

It must be emphasized that this study is only a first step towards understanding the variation in stability with time, of shallow tunnels constructed in overconsolidated clays. The three-dimensional effects have been disregarded. The stability diagrams given are for the case of H/D=1.8, and if they are to be used for other H/D ratios, proper engineering judgement must be used.

7. SUMMARY AND CONCLUSIONS

The conventional design procedures do not make accurate predictions of soil movements or of failure. In large projects, increased accuracy of predictions has major economic benefits and to make such predictions, a large number of sophisticated material models have been developed for soils. These material models, in general, predict the laboratory soil behaviour accurately. Also the finite element methods can be used to attain high numerical accuracies in solving boundary value problems. However, when these material models combined with finite element methods are applied to practical problems, they generally fail to make correspondingly accurate field predictions. The sophisticated models do not seem to have an overwhelming advantage over the conventional methods.

To solve this paradox, a detailed review was made of each step of modern geotechnical engineering design. In general, modern design includes laboratory/field tests, determination of parameters, material models and numerical models. It was concluded that material models are forms of curve fitting (using a kinematic model) for laboratory data. The laboratory parameters are at best only a consistent measure of the real parameters. Numerical models also generally represent a consistent measure of the continuum model. The continuum model always gives only an idealized measure of the real behaviour. Each of these models form only one link in the complete chain of modern design. The inadequacies in each link of the chain make the predictions inaccurate. On the basis of these facts and as a logical extension to curve fitting in material models, a new design concept, the Solution Oriented Model (SOM) was postulated.

This extends the curve fitting procedure to the whole chain of models taken as a unit. The basic concepts are;

$$\text{OBSERVATIONS} = \text{SOM}\left[\lambda_1\Phi_1,\ ..\ \lambda_k\Phi_k,\ ..\ \lambda_n\Phi_n\right]$$

where, Φ_1, .. Φ_k, .. Φ_n are design parameters. λ_1, .. λ_k, .. λ_n are parameters that must be computed by curve fitting with the observations. The Φ parameters must be selected using engineering judgement. In certain cases the SOM function may contain merely one parameter, such as modulus. In design, this approach accommodates "engineering judgement" in a rational manner. For wider applicability and efficiency, it is encouraged and recommended that only simple numerical and material models be used.

Simple numerical and material models are employed to analyse the deformation and pore pressure behaviour of clays. These models compute the initial undrained stresses and strains using a finite element method that utilizes an improved hyperbolic material model. These undrained stresses are used in Henkel's 3-D pore pressure formula to estimate the initial pore pressures. To compute the pore pressure dissipation behaviour, the initial pore pressures are used in a finite element model that employs uncoupled consolidation theory. To evaluate the additional settlement, these pore pressure values are used in a finite element program that incorporates the Cam Clay model. This proposed procedure was applied to three different case histories. The predictions of pore pressures and settlements compare reasonably well with the observations.

A parametric study was undertaken to investigate the pore pressure behaviour around supported and unsupported shallow tunnels constructed in normally consolidated clays. A non-dimensional quantity called Effective Stiffness Ratio (ESR) was defined to account for the support system. For unsupported tunnels ESR=0. A similar study was done for unsupported tunnels constructed in overconsolidated clays. The effects of H/D, D, K_0, E_s, s_u, α, γ and ESR on pore pressure generation and dissipation behaviour was investigated. The effects of D, t, R, A_1, I_1, E_1, E_s and K_0 on pore pressure around supported tunnels were investigated. A time factor $T=c_v t/H^2$ was defined to study the pore pressure dissipation behaviour. Only the practical ranges of parameters were considered and the normalized results are presented in a concise form using non-dimensional quantities to facilitate simplicity and usage. A shallow tunnel is defined as a tunnel where $H/D<3$, but on practical considerations a lower limit of $H/D>1$ was also used. These diagrams can be used to understand the pore pressure behaviour around tunnels. Given ESR, α, K_0, D, H/D, (x,y), c_v, and t, the pore pressure at a point P(x,y), at a time t after construction, can be easily and approximately estimated using the above diagrams.

As can be expected, the variation of the pore pressure coefficients influenced both the magnitude and the distribution of the pore pressure to the largest extent. The results of the parametric study clearly showed that in normally consolidated clays the pore pressures tend to be largely positive, and in overconsolidated clays they are negative. This implies that with time, the tunnels constructed in normally consolidated clays tend to become more stable, whereas the tunnels driven in overconsolidated clays tend to be more unstable. The results of a second parametric study quantifies this fact. A new method of stability analysis that combines finite element procedure and the limit equilibrium theory was incorporated in the analysis. These results are also given in a concise form and they can be used to estimate the decrease in global stability of tunnels constructed in overconsolidated clays. These results may be used to understand the influence of pore pressure on the stability of tunnels and estimate the stand-up time approximately.

These diagrams can also be considered as an approximate classification system and may be used in preliminary designs to make estimates of pore pressure, stability and settlement. They may also be used to help plan instrumentation programs or to decide which characteristics need to be explored and established in greater detail. Throughout the whole analysis, two dimensional models were used.

BIBLIOGRAPHY

ARGYRIS, J. H. and Willam, K. J. "Some considerations for the Evaluation of Finite Element Models" Second International Conference on Structural Mechanics in Reactor Technology, Berlin, September, 1973.

ATKINSON, J. H. and POTTS, D. M. "Subsidence above Shallow Tunnels in Soft Ground", Journal of the Geotechnical Engineering Division, ASCE, Vol. 103, pp. 307-325, 1977.

BELSHAW, D. J. and PALMER, J. H. L. "Results of a Programme of Instrumentation involving a Precast Segmented Concrete-lined Tunnel in Clay", Canadian Geotechnical Jourrnal, Vol. 15, No. , pp. 573-583, 1978.

BROMS, B. B. and BENNERMARK, H. Stability of Clay at Vertical Openings. Journal of Soil Mechanics and Foundations Division, ASCE, Vol. 93, No. SM1, Proc. Paper 5063 pp. 71-94, January 1967.

BURLAND, J. B. "Deformation of Soft Clay", Ph.D. Thesis, Cambridge University, 1967.

BURNS, J. Q. and RICHARD, R. M. Attenuation of Stresses for Buried Cylinders, Proceedings, Symposium on Soil-Structure Interaction. Tucson, Ariz., pp. 378-392, 1964.

CAIRNCROSS, A. M. Deformations Around Model Tunnels in Stiff Clay. Ph.D. Thesis, University of Cambridge. 1973.

CHAN, D. H. and MORGENSTERN, N. R. "Progressive Deformation of the Edmonton Convention Center" Canadian Geotechnical Journal, Vol. 24, pp. 430-440, 1987.

CHAN, D. H. "Finite Element Analysis of Strain Softening Material" Ph.D. Thesis, University of Alberta, 1985.

CHANG, C. S. and DUNCAN, J. M. "Consolidation Analysis for Partly Saturated Clay by Using an Elastic-Plastic Effective Stress-Strain Model" International Journal for Numerical and Analytical Methods in Geomechanics, Vol. 7, No. 1, pp. 39-55, 1983.

CLOUGH, G. W. and HANSEN, L. A. "Clay Anisotropy and Braced Wall Behaviour" Journal of the Geotechnical Engineering Division, ASCE, Vol. 107, No. GT7, Proc. Paper 16391 pp. 893-913, July, 1981.

CLOUGH, G. W. and MANNA, A. I. "Lessons Learned in Finite Element Analysis of Temporary Excavations in Soft Clay" 2 nd International Conference on Numerical Methods in Geomechanics, Blacksburg, Virginia, U.S.A., Vol. 1, pp. 496-510, June, 1976.

CLOUGH, G. W. and SCHMIDT, B., "Design and Performance of Excavations and Tunnels in Soft Clay" Developments in Geotechnical Engineering 20, Elsevier Scientific Publishing Company, Amsterdam, Netherlands, pp. 557-634, 1981.

CLOUGH, G. W., SHIRASUNA, T. and FINNO, R. J. "Finite Element Analysis of Advanced Shield Tunnelling in Soils" Proceedings, 5th International conference on Numerical Methods in Geomechanics, Nagoya, pp. 1167-1174, 1985.

CORDING, E. J. and HANSMIRE, W. H. "Tunnels in Soils-General Report" Proceedings, Session IV, 5th Pan American Congress of Mechanical and Foundation Engineering, Buenos Aires, p. 63, 1975.

DAVIS, E. H. "Theories of Plasticity and the Failure of Soil Masses" Soil Mechanics Selected Topics, (Ed. I. K. LEE), Butterworths, 1968.

DAVIS, E.H., GUNN, M. J., MAIR, R. J. and SENEVIRATNE, H. N. The Stability of Shallow Tunnels and Underground Openings in Cohesive Material. Geotechnique, London, England, Vol. 30, No. 4, pp. 397-416, 1980.

DAVIS, E. H. and POULOS, H. G., "Rate of settlement under Two and Three Dimensional Consolidations", Geotechnique, London, England, Vol. 12, No. 1, pp. 95-114, March, 1972.

DeLORY, F. A., and LAI, H-W, "Variation in Undrained Shearing Strength by Semiconfined Tests", Canadian Geotechnical Jourrnal, Vol. 8, No. , pp. 538-545, 1971.

DESAI, C. S. and ABEL, J. F. "Introduction to Finite Element Method" Van Nostrand Reinhold Company.

DESAI, C. S. and CHRISTIAN, J. T., "Numerical Metthods in Geotechnical Engineering", McGraw-Hill Book

Company, pp.83 , 1977.

DiMAGGIO, F. L. and SANDLER, I. S. Journal of the Engineering Mechanics Division, ASCE, Vol. 97, No. EM3, pp. 935-950, June, 1971.

DUNCAN, J. M. and DUNLOP, P. "The Significance of Cap and Base Restraint" Journal of Soil Mechanics and Foundations Division, ASCE, Vol. 94, No. SM1, Proc. Paper 5768 pp. 271-290, January, 1968.

DUNCAN, J. M. and DUNLOP, P. "Behaviour of Soils in Simple Shear Tests" Proceedings of the 7th International Conference on Soil Mechanics and Foundations Engineering, Vol. 1, Sociedad Mexicana de Mecanica de Suelos, Mexico, 1969, pp. 101-109.

DUNLOP, P., DUNCAN, J. M. and SEED, H. B., "Finite Element Analyses of Slopes in Soil", Report No. TE 68-3, University of California, Berkeley, California, 1968.

EIGENBROD, K. D., "Progressive Failure in Overconsolidated Clays and Mudstones", PhD Thesis, Dept. of Civil Eng., University of Alberta, Canada, 1972.

EINSTEIN, H. B. and SCHWARTZ, W. C., 1979, Simplified Analysis for Tunnel Supports. Journal of the Geotechnical Engineering Division, GT4, pp. 499-518, April, 1979.

EISENSTEIN, Z. "Computer Analysis in Earth Dam Engineering - State of the Art Report" Proceedings of Speciality Session No. 12, 9th International Conference on Soil Mechanics and Foundation Engineering, Tokyo, pp. 77-122, 1977.

EISENSTEIN, Z., "Application of Finite Element Method to Analysis of Earth Dams", State of the Art Report, First Brazilian Seminar on Application of Finite Element Method in Soil Mechnics, Universidade Federal do Rio de Janeiro, Sept., 1974.

EISENSTEIN, Z. "Behaviour of Deep Excavations in Soils" Brazilian Association for Soil Mechanics, Sao Paulo, Brazil, pp. 93-152, April 1981.

EISENSTEIN, Z. "The Contribution of Numerical Analysis to Design of Shallow Tunnels" Proceedings, International Symposium on Numerical Models in Geomechanics, Zurich, Sept. 1982.

EISENSTEIN, Z., "Tunnelling" CIVE 692, University of Alberta, 1984.

EISENSTEIN, Z. and BRANCO, P. "Observational Method Applied to Ground Control at the Edmonton LRT Tunnels" Canadian Tunneling, No. 1, pp. 51-66, 1985.

EISENSTEIN, Z. and BRANDT, J. R. T. "Soil-Concrete Interaction Test Facility, Proceeidngs, 15th International Congress on Large Dams, ICOLD, Lausanne, Q. 56, R. 7, pp. 153-172, June, 1985.

EISENSTEIN, Z., El-NAHHAS, F. and THOMSON, S. "Strain Field around a Tunnel in Stiff Soil" Proceedings, 10th International Conference on Soil Mechanics and Foundation Engineering, Stockholm, Vol. 1, pp. 283-288, June 1981.

EISENSTEIN, Z., El-NAHHAS, F. and THOMSON, S. "Pressure Displacement Relations in Systems of Tunnel Lining" Proceedings, 6th Panam Conference on Soil Mechanics, Lima, pp. 85-94, Dec. 1979.

EISENSTEIN, Z., HEINZ, H. and NEGRO, A. "On Three-Dimensional Ground response to Tunnelling" ASCE Geotech III, Tunnelling in Soils and Rocks, Atlanta, USA, pp. 107-127, May 1984.

EISENSTEIN, Z., HEINZ, H. and NEGRO, A. "Multiple Stage Excavation Schemes for Large Openings in Soft Ground" Procedings, International Congress on Large Underground Openings, Firenze, 1986.

EISENSTEIN, Z., KRISHNAYYA, A. V. G. and LAW, S. T. C. "Analysis of Consolidation in Cores of Earth Dams" Proceedings of the EF Conference on Numerical Methods in Geomechanics, Blacksburg, Virginia, USA, pp. 1089-1105, June, 1976.

EISENSTEIN, Z., and LAW, S. T. C. "Analysis of Consolidation Behaviour in Mica Dam" Journal of the Geotechnical Engineering Division, ASCE, Vol. 103, No. GT8, Proc. Paper 13161 pp. 879-895, August, 1977.

EISENSTEIN, Z. and MEDEIROS, L. V. "A Deep Retaining Structure in Till and Sand-Part II - Performance and Analysis" Canadian Geotechnical Journal, Vol. 20, No. 1, pp. 131-140, 1980.

EISENSTEIN, Z. and MORRISON, N. A. "Predictions of Foundation Deformation Using an In Situ Pressure Probe" Canadian Geotechnical Journal, Vol. 10, pp. 193-210, 1973.

EISENSTEIN, Z. and NAYLOR, D. J. "Static Analysis of Embankment Dams" Report by International Commission on Large Dams, Paris, 1984.

EISENSTEIN, Z. and NEGRO, A. "Excavations and Tunnels in Tropical Soils (General Report), Proceedings, 1st Int. Conference on Geomechanics of Tropical Lateritic and Saprolitic Soils, Brassilia, Vol. 4, pp. 299-333, Feb., 1985.

EISENSTEIN, Z. and NEGRO, A. "Comprehensive Design Method for Shallow Tunnels" Proceedings, ITA/AITES, Prague, Czechoslovakia, Sept. 1985.

EISENSTEIN, Z. and SORENSEN, K. L. "Tunnelling for the South LRT Extension in Edmonton", Alberta, Proceedings, 6th Annual Tunnelling Conference, Niagara Falls, Canada, pp. 29-31, 1986.

EISENSTEIN, Z. and THOMSON, S. "Geotechnical Performance of a Tunnel in Till", Canadian Geotechnical Journal, Vol. 15, pp. 332-345, 1978.

EISENSTEIN, Z., VERSKI, I., BURMAN, R. and ZALSZUPIN, R. "Analysis of Closely Adjacent Shafts" Proceedings, 4th International Conference on Numerical Methods in Geomechanics, Edmonton, Canada, Vol 3, pp. 1193-1202, 1983.

FELIPPA, C. A. and CLOUGH, R. W. "The Finite Element Method in Solid Mechanics" Numerical Solution of Field Problems in Continuum Physics, SIAM-AMS Proceedings, Vol. 2, American Mathematical Society, Providence, R. I., 1970.

FINN, W. D. L. and BHATIA, S. "Endochronic Theory of Sand Liquefaction", Proceedings of the Seventh World Conference on Earthquake Engineering, Istanbul, Turkey, pp. 149-155, September, 1980.

FINNO, R. J. and CLOUGH, G. W. "Evaluation of Soil Response to EPB Shield Tunneling" Journal of the Geotechnical Engineering Division, ASCE, Vol. 111, No. GT2, Proc. Paper 19486 pp. 155-173, 1985.

GHABOUSSI, J., RANKEN, R. E. and KARSHENAS, M. "Analysis of Subsidence oover Soft Ground Tunnels" Proceedings, International Conference on Evaluation and Prediction of Subsidence", ASCE, Pensacola, Florida, pp. 182-196, 1978.

GIODA, G. "Some Remarks on Back Analysis and Characterization Problems in Geomechnics" 5 th

International Conference on Numerical methods in Geomechnics, pp. 47-61, April, 1985.

GIODA, G. and JURINA, L. "Identification of Earth Pressure on Tunnel Liners" Proceedings, 10 th International Conference on Soil Mechanics and Foundation Engineering, Stockholm, pp. 301-304, 1981.

GIRIJAVALLABHAN, C. V., and REESE, L. C. "Finite Element Method for Problems in Soil Mechanics", Journal of Soil Mechanics and Foundations Division, ASCE, Vol. 94, No. SM2, Proc. Paper 5864 pp. 473-4, March, 1968.

HARDIN, B. O. AND DRNEVICH, V. P., "Shear Modulus and Damping in Soils: Design Equations and Curves" Journal of Soil Mechanics and Foundations Division, ASCE, Vol. 98, No. SM7, Proc. Paper 9006 pp. 667-692, July, 1972.

HEINZ H. K., "Application of New Austrian Tunnelling Method in Urban Areas" M.Sc. Thesis, University of Alberta, Canada, 1984.

HENKEL, D. J., "The Shear Strength of Saturated Remolded Clays" Proceedings, Research Conference on Shear Strength of Cohesive Soils, Soil Mechanics and Foundations Division, ASCE, University of Colorado, pp. 533-554, June, 1960.

HOEG, K. Stress against Underground Structural Cylinders, Journal of the Soil Mechanics and Foundations Division, July, SM4, pp. 833-858, 1968.

HRUDEY, T. M. "Introduction to the Finite Element Method" CIVE 665, University of Alberta, 1983.

HRUDEY, T. M. "Advanced Topics in the Finite Element Method" CIVE 667, University of Alberta, 1985.

JOHNSTON, P. R. and CLOUGH, G. W. "Development of a Design Technology for Ground Support for Tunnels in Soil, Volume 1, Time Dependent Response due to Consolidation in Clays" US Department of Transportation, Urban Mass Transportation Administration, 1983.

KANKARE, E., "Failure at Kimola Floating Canal in Southern Finland", Proceedings, 7th International Conference on Soil Mechanics and Foundation Engineering, Vol. 2, Mexico, pp. 609-616, 1969a.

KANKARE, E., "Geotechnical Properties of the Clays at the

Kimola Canal Area with Special Reference to the Slope Stability", The State Institute for Technical Research, Finland, Helsinki, Publ. 152, 1969b.

KIEKBUSCH, M. and SCHUPPENER, B., "Membrane Penetration and Its Effects on Pore Pressures", Journal of the Geotechnical Engineering Division, ASCE, Vol. 103, No. GT11, Proceedings Paper 13331, pp. 1267-1279, November, 1977.

KONDNER, R. L., "Hyperbolic Stress Strain Response: Cohesive Soils", Journal of Soil Mechanics and Foundations Division, ASCE, Vol. 89, No. SM1, Proc. Paper pp. 115-143, January, 1963.

KRISHNAYYA, A. V. G., "Finite Element Consolidation Programme for Two Dimensional Problems" User Manual, Soil Mechanics No. 22, Department of Civil Engineering, University of Alberta, 1973.

KULHAWY, F. H. "Finite Element Modelling Criteria for Underground Openings in Rock" International Journal of Rock Mechanics and Mineral Sciences, II, pp. 465-472, 1974.

KULHAWY, F. H. "Embankments and Excavations. In: Numerical Methods in Geotechnical Engineering" Edited by Desai, C. S. and Christian, J. T., McGraw Hill, pp.528-555, 1977.

KULHAWY, F. H. and DUNCAN, J. M. "Stresses and Movements in Oroville Dam", Journal of the Soil Mechanics and Foundations Engineering Division, ASCE, Vol. 98, No. SM7, pp. 653-665, 1972.

KULHAWY, F. H., DUNCAN, J. M. and SEED, H. B. "Nonlinear Soil Structure Interaction Programme" coded first by Kulhawy and then by Ozawa, Y.; further modified to include Soil Structure Interaction by Booker, J. R. and Byrne, P. M., coded by Dickens, J., University of California, Berkeley, USA, 1969.

KUPPER, A. M. A. G., "Characteristicas Tensao x Deformacao x Resistencia De Uma Amostra Da Argila Vermelha Do Terciario De Sao Paulo" Tese De Mestrado, Departmento De Engenharia Civil, Pontificia Universidade Catolica do Rio de Janeiro, Brazil, 1983.

LADD, C. C. and FOOTT, R. "New Design Procedure for Stability of Soft Clays", Journal of the Geotechnical Engineering Division, ASCE, Vol.

100, No. GT7, Proc. Paper 10664 pp. 763-786, July, 1974.

LADE, P. V. and DUNCAN, J. M. "Elastoplastic Stress-Strain Theory for Cohesionless Soil", Journal of the Geotechnical Engineering Division, ASCE, Vol. 101, No. GT10, Proc. Paper 11670 pp. 1037-1053, October, 1975.

LAMBE, T. W. "Predictions in Soil Engineering" Geotechnique 23, pp.149-202, 1973.

LAMBE, T. W. and WHITMAN, R. V. Soil Mechanics. John Wiley & Sons Inc., 1979.

-LEDESMA, A., GENS, A. and ALONSO, E. E. "Identification of Parameters in a Tunnel Excavation Problem" 2 nd International Symposium on Numerical Methods in Geomechnics, Ghent, pp. 333-344, 1986.

LEE, K. M. and ROWE, R. K. "The Effect of Elastic Anisotropy on Settlements Induced by Tunnelling" CANCAM 85, Vol. 1, pp. 323-324, 1985.

LEKHNITSKII, S. G. Radial Distribution for Stresses in a Wedge and in a Half Plane with Variable Modulus. Journal of Applied Mathematics and Mechanics. Vol. 26, Part 1, pp. 146-151, 1962.

LO, K. Y. and ROWE, R. K. "Prediction of Ground Subsidence due to Tunnelling in Clays", Research Report GEOT-10-82, Faculty of Engineering Science, University of Western Ontario, London, Ontario, 1982.

LO, K. Y., NG, M. C. and ROWE, R. K. "Predicting Settlement due to Tunnelling in Clays", In tTunnelling in Soil and Rock, Proceedings, Geotechnical Engineering Division, ASCE-GEOTECH'84, Atlanta, GA, pp. 46-76, 1984.

MAIR, J. M. Centrifugal Modeling of Tunnel Construction in Soft Clay. Ph.D. Thesis, University of Cambridge. 1979.

MARTIN, G. F. and FINN, W. D. L., "Effects of System Compliance on Liquefaction Tests" Journal of the Geotechnical Engineering Division, ASCE, Vol. 104, No. GT4, Proceedings Paper 13667, pp. 463-479, April, 1978.

MASLIYAH, J. "Numerical Solutions of Engineering Problems" CHE 674, University of Alberta, 1984.

McNEICE, G. M. and Marcal, P. V. "Optimization of Finite Element Grids Based on Minimum Potential Energy" Journal of Engineering for Industry, Transactions of the ASME, pp. 186-190, February, 1973.

MELOSH, R. J. and MARCAL, P. V., "An Energy Basis for Mesh Refinement of Structural Continua" International Journal for Numerical Methods in Engineering Vol. 11, pp. 1083-1091, 1977.

MITCHELL, R. J., "Earth Structures Engineering" Allen and Unwin Inc., pp. 79, 1983.

MOHRAZ, B., HENDRON, A. J., RANKEN, R. E. and SALEM, M. H. "Liner-Medium Interaction in Tunnels" Journal of the Construction Division, ASCE, Vol. 101, No. CO1, Porc. Paper 11174, pp. 127-141, March, 1975.

MORGENSTERN, N. R. "Construction in Difficult Soils - Commentary and Case Histories" Proceedings, Conference on Difficult Soils, Canadian Society for Civil Engineering, Thunder Bay, 1982.

MORGENSTERN, N. R. "Factors Affecting the Selection of Shear Strength Parameters in Slope Stability Analysis" Proceedings, International Conference on Landslides New Delhi, Vol. 2, pp.83-93, 1980.

MORGENSTERN, N. R. "Slopes and Excavations - General Report" Proceedings, 9th International Conference on Soil Mechanics and Foundation Engineering, Tokyo, Vol. 3, pp. 317-324, 1977.

MURRAY, D. W., "Introduction to the Finite Element Method" CIVE 665, University of Alberta, 1983.

MURRAY, D. W., "Advanced Topics in the Finite Element Method" CIVE 667, University of Alberta, 1985.

NEGRO, A., "Design of Shallow Tunnels in Soft Ground" Ph.D. Thesis, University of Alberta, Canada, 1988.

NEGRO, A. and EIZENSTEIN, Z., "Ground Control Techniques Compared in Three Brazilian Water Tunnels", Parts 1, 2 and 3, Tunnels and Tunnelling, pp. 11-14, 52-54, 48-50, Dec. 1981.

NEGRO, A., EIZENSTEIN, Z. and HEINZ, H. "Prediction of Radial Displacements at the Face of Shaallow Tunnels" Proceedings, 2nd International Symposium on Numerical Models in Geomechanics, Delft, April, 1986.

NG, R. M. C, "Ground Reaction and Behaviour of Tunnels in Soft Clays", PhD. Thesis, University of Western Ontario, London, Canada, 1984.

PALMER, J. H. L. and BELSHAW, D. J., "Deformations and Pore Pressures in the Vicinity of a Precast, Segmented, Concrete-lined Tunnel in Clay", Canadian Geotechnical Jourrnal, Vol. 17, No. , pp. 174-184, 1980.

PECK, R. B., "Art and Science in Subsurface Engineering" Geotechnique 12, No. 1, 1962.

PECK, R. B., "Deep Excavations and Tunnelling in Soft Ground" Proceedings, 7th International Conference on Soil Mechanics and Foundation Engineering, Mexico City, pp. 225-290, 1969.

PECK, R. B., "Judgement in Geotechnical Engineering: the Professional Legacy of Ralph B. Peck" Wiley, New York, 1984.

PECK, R. B. "Advantages and Limitations of the Observational method in Applied Soil Mechanics" Geotechnique 19, No. 2, pp. 171-187, 1969.

PECK, R. B., HENDRON, A. J. and MOHRAZ, B. State of the Art of Soft-Ground Tunneling, Proceedings, First Rapid Excavation and Tunneling Conference, American Institute of Mining, Metallurgical and Petroleum Engineers, Vol. 1, pp. 259-286, 1972.

PREVOST, J. H., "Field and Constitutive Equations for a Two Phase Medium for Analysis of the Behaviour of In-situ Soil Deposits", Proceedings of the Seventh World Conference on Earthquake Engineering, Istanbul, Turkey, pp. 1-8, September, 1980.

RANKEN, R. E. and GHABOUSSI, J. "Tunnel Design Considerations: Analyses of Stress and Deformations around Advancing Tunnels" Report UILU-ENG75-2016 (NTIS National Technical Information Service, US Department of Commerce, Springfield, VA 22161), 1975.

RAYMOND, G. P. and TOWNSEND, D. L., "The Effect of Sampling on the Undrained Soil Properties of a Leda Soil", Canadian Geotechnical Jourrnal, Vol. 8, No. , pp. 546-557, 1971.

ROSCOE, K. H. and BURLAND, J. B. "On Generalized Stress-strain Behaviour of Wet Clays" Engineering Plasticity, Cambridge University

Press, pp. 535-609, 1968.

ROSCOE, K. H., SCHOFIELD, A. N. and THURAIRAJAH, A. "Yielding of Clays in States Wetter than Critical", Geotechnique, London, England, Vol. 13, No. , pp. 211-240, 1963.

ROSCOE, K. H., "Laboratory Shear Testing of Soils", Symposium on Laboratory Shear Testing of Soils, Ottawa, Canada, pp. 111-128, 1963.

ROWE, R. K. "The Predictions of Deformations caused by Soft Ground Tunnelling - Recent Trends" Canadian Tunnelling, 1986.

ROWE, R. K. and KACK, G. J. "A Theoretical Examination of the Settlements Induced by Tunnelling: Four Case Histories" Canadian Geotechnical Journal, Vol. 20, pp. 299-314, 1983.

ROWE, R. K., LO, K. Y. and KACK, G. J. "The Prediction of Subsidence above Shallow Tunnels in Soft Soil" Proceedings, Symposium on Implementation of Computer Procedures and Stress-Strain Laws in Geotechnical Engineering, pp. 266-280, 1981.

ROWE, R. K., LO, K. Y. and KACK, G. J. "A Method of Estimating Surface Settlement above Tunnels Constructed in Soft Ground", Canadian Geotechnical Jourrnal, Vol. 20, No. 1, pp. 11-22, 1983.

SAMARASEKERA, L., "Nonlinear Elastic Stress-Strain Model for Anisotropically Consolidated Clay" M.A.Sc. Thesis, University of British Columbia, Canada, 1982.

SCHKADE, A. F. "Solution Techniques for Large Systems of Stiffness Equations" M.S. Thesis, Department of Aerospace Engineering, The University of Texas, Austin, January 1969.

SCHMERTMANN, J. H., "Estimating the True Consolidation Behaviour from Laboratory Test Results", Proc., ASCE, 79, 1953.

SCOTT, C. R. An Introduction to Soil Mechanics and Foundations, Applied Science Publishers Ltd. pp. 171, 1980.

SEED, H. B. and IDRISS, I. M. "Soil Moduli and Damping Factors of Dynamic Response Analyses" EERC-70-10, Earthquake Engineering Research Center, College of Engineering, University of

California Berkeley, 45 pp., December, 1970.

SHEPHARD, M. S. "Finite Element Grid Optimization - A Review" The third National Congress on Pressure Vessels and Piping, San Francisco, California, The Pressure Vessel and Piping Division, ASME, pp. 1-13, June 1979.

SHEPHARD, M. S., Gallagher, R. H. and Abel, J. F. "Experience with Interactive Computer Graphics for the Synthesis of Optimal Finite Element Meshes" The Third National Congress on Pressure Vessels and Piping, San Francisco, California, The Pressure Vessel and Piping Division, ASME, pp. 61-73, June 1979.

SIMON, R. M., CHRISTIAN, J. T. and LADD, C. C., "Analysis of Undrained Behaviour of Loads on Clay" Proceedings, Conference on Analysis and Design in Geotechnical Engineering, ASCE, Austin, Texas, pp. 51-84, June 1974.

SKEMPTON, A. W., "The Pore Pressure Coefficients A and B" Geotechnique 4, No. 4, pp. 143-147, 1954.

SOWERS, G. B. and SOWERS, G. F., "Failures of Bulkhead and Excavation Bracing, Civ. Eng., Vol. 37, No. 1, pp. 72-77, 1967.

TAN, T. Y. and CLOUGH, G. W. "Ground Control for Shallow Tunnels by Soil Grouting" Journal of the Geotechnical Engineering Division, ASCE, Vol. 106, GT9, pp. 1037-1057, 1980.

TERZAGHI, K., "Theoretical Soil Mechanics", John Wiley & Sons, Inc., New York, 1943.

THOMSON, S. and KJARTANSON, B. H. "A Study of Delayed Failure in a Cut Slope in Stiff Clay" Canadian Geotechnical Journal, Vol. 22, pp. 286-297, 1985.

THOMSON, S. and MORGENSTERN, N. R. "Factors Affecting Distribution of Landslides along Rivers in Southern Alberta" Canadian Geotechnical Journal, Vol. 14, No. 4, pp. 508-523, 1977.

THOMSON, S. and SCHULZ, T. "Settlement Study of an Open Pit Mine Backfill in Western Canada" 3rd International Conference on Ground Movements and Structures, UWIST, Cardiff, Wales, Vol. 3, pp. 480-495, 1984.

THOMSON, S. and SONNENBERG, R. "Settlement Observations of

Open Pit Mine Backfill" 39th Canadian Geotechnical Conference, Ottawa, August, 1986.

THOMSON, S. and TIEDEMANN "A Review of Factors Affecting Landslides in Urban areas" Canadian Geotechnical Society, Speciality Conference on Slope Stability Problems in Urban Areas, Bulletin Association of Engineering Geologists, XIX, pp. 55-65, 1980

TURCKE, D. J. "Characteristics of piecewise approximations in Numerical Analysis" The third National Congress on Pressure Vessels and Piping, San Francisco, California, The Pressure Vessel and Piping Division, ASME, pp. 15-26, June 1979.

TURCKE, D. J. and McNEICE, G. M. "Application of Grid Selection Procedures for Improved Finite element Stres Analysis" Proceedings, International Conference on Vehicle Structural Mechanics, Detroit Michigan, Society of Automotive Engineers, Inc., pp. 205-216, March 1974.

USBR, U.S. Department of Interior, "Design of Small Dams", A Water Resources Technical Publication, United States Government Printing Office, Washington, 1977.

VAID, Y. P. "Effect of Consolidation History and Stress Path on Hyperbolic Stress Strain Relations" Soil Mechanics Series, No. 54, University of British Columbia, Vancouver, Canada, December 1981.

VAID, Y. P. and CAMPANELLA, R. G. "Time Dependent Behaviour of Undisturbed Clay" Journal of the Geotechnical Engineering Division, ASCE, Vol. 103, No. GT7, Proceedings Paper 13065, pp. 693-709, July 1977.

VAID, Y. P. and CAMPANELLA, R. G. "Triaxial and Plane Strain Behaviour of Natural Clays" Journal of the Geotechnical Engineering Division, ASCE, Vol. 100, No. GT3, Proceedings Paper 10421, pp. 207-224, March 1974.

WARD, W. H. and PENDER, M. J. "Tunnelling in Soft Ground-General Report" Preprint, 20th International Conference on Soil Mechanics and Foundation Engineering, Stockholm, 1981.

WEI, R. L., "Constitutive Laws of Normally Consolidated Clay" Proceedings, 10 th International Conference on Soil Mechanics and Foundation Engineering, Stockholm, Vol. 1, pp. 269-272, 1981.

WEI, R. L., "The Plastic Potential of Normally Consolidated Clay" Journal of Hydraulic Engineering, Beijing, 6, pp. 9-20, 1964.

WHITE, R. N. "Optimum Solution Techniques fo Finite Difference Equations" Proceedings, ASCE, J. ST Dn, Vol. 89, ST4, August, 1963.

YAMAGAMI, T. and UETA, Y. "Elasto-plastic Uncoupled Procedure for Consolidation Analysis and its Comparison with Coupled Procedures" 5 th International Conference on Numerical Methods in Geomechanics, Nagoya, pp. 605-612, April, 1985.

ZIENKIEWICZ, O. C., "Finite Element Method" McGraw-Hill Book Co., 1977.

APPENDIX A

THEORY OF REAL FINITE ELEMENT ANALYSIS

Total potential energy of the system can be written in the form:

$$\Pi = \sum_{k=1}^{m} \frac{1}{2} <r>[K]\{r\} - <R>\{r\} \qquad [A.1]$$

where,

[K] = $\int_v [B]^T[D][B]dv$,

{r} the nodal displacement vector,

{R} the nodal load vector and

m number of elements in the mesh.

For potential energy to be a minimum:

$$\frac{\partial \Pi}{\partial r_i} = 0 \quad i = 1, n \qquad [A.2]$$

and

$$\frac{\partial \Pi}{\partial x_j} = 0 \quad j = 1, n \qquad [A.3]$$

where,

n is the total degrees of freedom

Equation A.2 implies:

$$K_{ij}r_j - R_i = 0 \quad i = 1, n \qquad [A.4]$$

where,

K_{ij} = [K] and

R_i = {R}.

and A.3 implies that:

$$\frac{1}{2} <r> \frac{\partial [K]}{\partial x_j} \{r\} - \frac{\partial <R>}{\partial x_j} \{r\} = 0 \quad j = 1, n \qquad [A.5]$$

The Equations A.4 and A.5 describe a true finite element analysis. These equations compute both the nodal displacements as well as nodal coordinates for optimum potential energy. Consequently, the coordinates of the mesh are changed, as opposed to having fixed coordinates in a conventional finite element analysis.

APPENDIX B

EFFECTIVE STIFFNESS RATIO FORMULATIONS

As explained in section 5.3.5, the pore pressures generated around a tunnel excavation, in a very broad sense depend on the stiffness ratio of the soil mass to the liner. This stiffness ratio is called the Effective Stiffness Ratio. As the stiffness is inversely proportional to the strain, the effective stiffness ratio is defined as;

$$\frac{\text{Characteristic ground strain}}{\text{Characteristic strain of support}} \qquad [B.1]$$

In the following sections an attempt will be made to quantify the broad qualitative meaning of the above definition.

SYMMETRIC LOADING

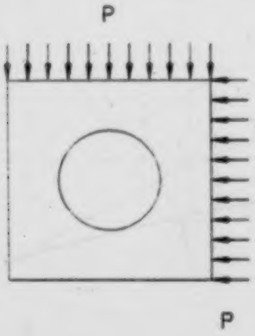

Under the symmetric loading shown, the strain in the soil mass can be shown to be equal to

$$2(1 - \nu^2)P/E_s$$

Where,

E_s is soil modulus

ν is Poisson's ratio of soil

The strain in the liner can be proved to be equal to;

$$(1 - \nu_1^2)PR/A_1E_1$$

Where,

E_1 is the liner modulus

ν_1 is the liner Poisson's ratio

R is the tunnel radius

ANTI-SYMMETRIC LOADING

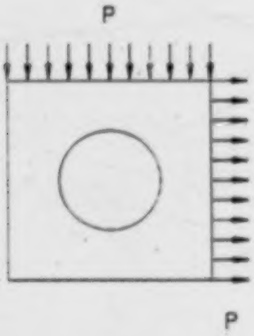

For the above anti-symmetric loading the ground strain can be shown equal to,

$$4(1 - \nu^2)P/E_s$$

where as the liner strain is equal to,

$$(1 - \nu_1^2)PR^3/6I_1E_1$$

GENERAL K_0 LOADING

The general K_0 soil loading can be divided into a symmetric and an anti-symmetric loading systems as shown below. Using the results of the previous two sections, the characteristic strain of the ground around a tunnel of radius R constructed in K_0 consolidated soil was defined as;

$$2(1 - \nu^2)\sigma_v(1+K_0)/2E_{cs} + 4(1 - \nu^2)\sigma_v(1-K_0)/2E_{cs}$$

Where,

E_{cs} is the characteristic soil modulus; E_s or E_i may be used

The characteristic strain of the liner under K_0 loading conditions was defined as;

$$(1 - \nu_1^2)\sigma_v(1+K_0)R/2A_1E_1 + (1 - \nu_1^2)\sigma_v(1-K_0)PR^3/12I_1E_1$$

Therefore by the definition of Effective Stiffness Ratio,

$$ESR = \{2(1-\nu^2)(3-K_0)E_1/(1-\nu_1^2)E_{cs}R\}/\{(1+K_0)/A_1+(1-K_0)R^2/6I_1\}$$

(Some concepts of Einstein et al., 1979, have been used in the above derivation)

Note that for our analysis in Chapter 5, E_i is taken as the characteristic soil modulus E_{cs}.

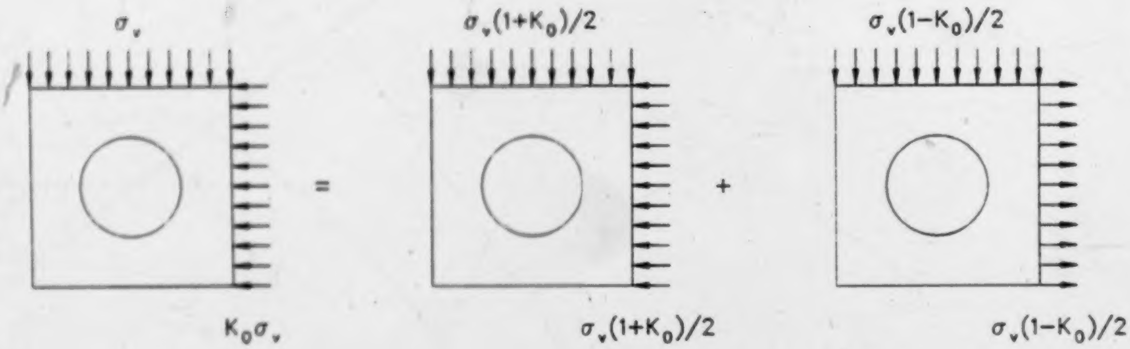
σ_v
$\sigma_v(1+K_0)/2$
$\sigma_v(1-K_0)/2$
=
+
$K_0\sigma_v$
$\sigma_v(1+K_0)/2$
$\sigma_v(1-K_0)/2$